ANALYSIS OF THIN-WALLED CYLINDRICAL COMPOSITE SHELL STRUCTURES SUBJECT TO AXIAL AND BENDING LOADS: CONCEPT DEVELOPMENT, ANALYTICAL MODELING, AND EXPERIMENTAL VERIFICATION

by

STHANU MAHADEV

Presented to the Faculty of the Graduate School of

The University of Texas at Arlington in Partial Fulfillment

of the Requirements

for the Degree of

DOCTOR OF PHILOSOPHY

THE UNIVERSITY OF TEXAS AT ARLINGTON

August 2015

Acknowledgements

This work could not have been completed without the indispensable support and encouragement of numerous people to whom I would like to earnestly convey my appreciation and thanks.

First and foremost, I would like to express my fervent and most profoundly heart-felt gratitude to my dissertation advisors: Dr. Wen Chan and Dr. D. Stefan Dancila, for devoting their invaluable time to provide me with their undivided guidance, academic, professional support and constant encouragement. I am indebted to them for the plentiful enlightening discussions and inspiring critiques that occurred amidst my graduate student life at UTA. I am also grateful to my distinguished professors; Dr. Andrew Makeev, Dr. Ashfaq Adnan, Dr. Kent Lawrence, and Dr. Seiichi Nomura for their willingness to serve as my dissertation academic committee.

Additionally, I would like to show my cordial appreciation to my amiable lab colleagues and friends: Vishnu Sreeram, Martin Kora, Deedee, Bastiaan, Julia Cline, Sarvi , Brian Shonkwiler and Jan Czarina Domingo Ocampo for their dedicated technical and emotional support.

I sincerely thank my mother, Dr. Vanitha Moorthy and my cherished brother Sthanu Mukunda for showering their unconditional love, support and sacrifices to enable and facilitate my achievements so far.

May 14, 2015

Abstract

ANALYSIS OF THIN-WALLED CYLINDRICAL COMPOSITE SHELL STRUCTURES SUBJECT TO AXIAL AND BENDING LOADS: CONCEPT DEVELOPMENT, ANALYTICAL MODELING, AND EXPERIMENTAL VERIFICATION

Sthanu Mahadev, PhD

The University of Texas at Arlington, 2015

Supervising Professors: Wen Chan & D. Stefan Dancila

Several studies have focused on the modeling and response characterization of composite structural members, with particular emphasis on thin-walled cylindrical composite shells. This class of shell configurations is explored to determine their mechanical response in primary aerospace structural members. The present work is focused on formulating a modified composite shell theory prognosis methodology for investigating the structural response of thin-walled cylindrical shell type composite configurations under axial and bending loads, respectively. The prime motivation to develop this theory arises from its capability to generate simple yet accurate closed-form analytical results that can efficiently charecterize cylindrical composite shell constructions.

This work shows the development of a novel mathematical framework to predict key structural characteristics such as axial stiffness, bending stiffness, and centroid for thin walled composite shells. Longitudinal components of ply-stresses are analytically computed through the global stiffness matrix model for cylindrical composite tubes under thermomechanical environments. An ANSYS based FE routine is employed to compare against the analytical results. This concept development is further extended to analyze thin-walled, open cross-section, curved composite shells characterized by circumferential

arc angle, thickness-to-mean radius ratio, and total laminate thickness, respectively. The potential of this methodology is used to analytically identify the location of the centroid for such cross-sections. Ply stress variations for curved cylindrical shells are analytically examined under the application of centroidal tensile and bending loadings respectively. In-plane ply-stress estimations determined by the present model show excellent agreement in comparison with FEM results.

The present work also incorporates the design and manufacturing of a novel ad-hoc test-fixture set-up to experimentally characterize the extension-bending behavior in open cross-section curved composite strips. Seven symmetric, balanced curved composite test specimens are fabricated. This investigation introduces a new testing methodology to measure longitudinal surface strain fields and predict the centroid location via implementing a non-contact, full field strain measurement technique, Digital Image Correlation (DIC). Experimental measurements are compared against analytical results. This work is shown to essentially capture the mechanical response of cylindrical shells by providing an efficient and effective mathematical tool for structural engineers.

Table of Contents

List of Illustrations

List of Tables

Chapter 1

BRIEF LITERATURE SURVEY ON LAMINATED COMPOSITE SHELL THEORIES

Over the past several decades, fiber-reinforced composite materials have played an increasingly significant role in numerous mechanical and aerospace structural applications, and continue to represent the preferred material option due to superior specific mechanical properties such as stiffness-to-weight ratio, low-density characteristics, coupled with significant improvements in fatigue resistance as opposed to metal structure counterparts. Extensive research have demonstrated their core potential as more than just mere lightweight substitutes to conventional materials. Although representing a challenge for analysis, their fundamental anisotropic nature allows for additional degrees of freedom for structural design.

Continued research efforts have been devoted in recent years towards the design, development, and manufacturing of efficient composite members such as thin-walled curved/cylindrical tubular shells, columns, and beams. An accurate evaluation of their primary mechanical properties such as axial stiffness, bending stiffness, and ply stresses are warranted to achieve a conceptual yet broad understanding of the structural response to deformations, loads and mechanical vibrations.

Thin-walled composite shell constructions as fundamental structural elements occupy a pivotal position in the application of a wide array of structures. Specifically, thin walled shell structural members such as closed and open cross-section composite tubes are being increasingly used in the petrochemical and marine industry. They exhibit superior structural performance characteristics by greatly lowering overall weight and largely improving the specific strength and stiffness as opposed to metallic materials. Structural applications of shell structures are noticed in construction of large-span roofs, liquid-

retaining structures such as thin-walled pipes, ducts and water tanks, containment shells of nuclear power plants, concrete arched domes, rotating turbine disks, pressure vessels etc. Their increasing use in typical aerospace applications includes manufacturing of thin-walled curved aircraft skins, wings and fuselages for aerodynamic bodies, missiles, air-breathing engine cowlings, rockets and morphing structures for satellites. Structural footprint of shell engineering also spans across in the field of biomechanics; composite prosthetics is being actively explored to optimize foot biomechanics in below-knee amputee patients.

Vardhan and Bhaskar [1] developed a set of three dimensional elasticity equations for finite length, cross-ply cylindrical shells that were characterized by simply-supported type boundary conditions across both ends and subjected to transverse loading. Upon the implementation of satisfying displacement functions, appropriate ordinary differential equations were formulated and consequently ply-stresses were presented. Fan and Ding [2] expanded upon the method of initial functions (MIF) to analyze thin, moderately thick and thick cylindrical shells by solving for a set of displacement function operators in the form of Maclaurin series. Their numerical analysis consisted of dividing an arbitrary layer into several thin plies that showed a faster convergence rate and better ply stress results.

Yuan [3] developed a set of analytical elasticity solutions for laminated composite cylindrical shells subjected to cylindrical bending. A set of partial differential equations based on Lekhnitskii's stress function approach was generated to determine the stresses and displacements in composite cylinders. His study was done on +45 degree off-axis uni-directional plies, [+45/-45] un-symmetric and $[+45/-45]_s$ angle-ply fiber reinforced laminated shells. Ren [4] formulated an elasticity solution in the form of a convergent series for anisotropic laminated circular cylindrical shells that are simply supported under axisymmetric loads. His numerical results concluded that the displacement results from

the composite shell theory were in good agreement with his analytical values and the anisotropic lamination had a significant influence towards the stress distributions along the thickness direction. His approach can also be utilized to analyze the axisymmetric deformation of laminated shells under tangential loading conditions.

Cho, Kim and Min-Ho [5] were successful in formulating a higher-order shell theory applicable to symmetric laminated composites shells. Upon implementing a combination of zig-zag linearly varying in-plane displacement field and a globally varying cubic displacement field, equilibrium equations and boundary conditions were derived that was consistent with a curvature based coordinate system. Their shell theory was in good agreement with those of exact elasticity solutions.

Wu and Chen [6] recently derived a higher-order mathematical model to predict the displacements and stresses in laminated cylindrical shell panels; in addition the thermally induced bending was also considered in their analysis. Bhaskar and Ganapathysaran [7] proposed a set of baseline elasticity solutions for analyzing thin-walled laminated composite shells subjected to localized bending moments. By adopting a cylindrical coordinate system, coupled ordinary differential equations were developed by Taylor series expansions. A comparison on localized deformation and stress results were made with respect to FEM data respectively. Qatu et al. [8] performed a comprehensive research in the last decade (2000–2010) on the static structural behavior of laminated composite shells.

Shu [9] proposed a closed form analytical solution based on a shell theory in combination with Love's first-order geometric approximation [8 cited by Qatu] for shallow composite cylindrical shells. This derived theory indicated improvements in the in-plane displacement (u, v) distributions across the structure by ensuring the continuity of inter-laminar transverse shear stresses and zero transverse shear strains on the surface. The

theory contained the same dependent unknown and the same order of governing equations as in the first-order shear deformation theories. Without the necessity for shear correction factors, the theory was able to predict more accurate responses than first-order theory and some higher-order theories. Furthermore, the solutions showed good agreement with elasticity solutions based on the literature. Hodges and Yu [10] were successful in developing strip-beam and composite shell properties that can be derivable from classical lamination theory. Their model utilizes the variational-asymptotic method to charectersize the mechanical response of such structures. Sectional constants calculations were made while no ad-hoc assumptions were imposed. This apporach offers the capability to provide highly accurate solutions however the methodology is computationally intensive.

Recently, Chan and Demirhan [11] developed a simple closed-form expression for evaluating bending stiffness in laminated composite tubes. The influence of curvature effects on bending stiffness was investigated by conducting a parametric study on tubes of varying radius and laminate stacking sequence.

With the objective on developing an effective and efficient analytical model to charecterize the structural behavior of thin-walled composite shells under axial and bending loadings while significantly reducing computational efforts, this work focuses on formulating a simple linear analytical model to investigate closed composite tubes and open cross-sectioned shells, respecively.

Chapter 2

RESEARCH OBJECTIVES & SCOPE OF STUDY

2-1 Motivation

Over the recent years, structural constructions constituting composite materials have garnered attention in the aerospace industry for continually demonstrating superior mechanical characteristics as opposed to conventional counterparts. Materialistically tailored high performance composite materials can offer the possibility to develop new structural elements while striving to mitigate the demerits of a monolithic equivalent. Their enhanced ability to resist loads under various dynamic loading conditions while preserving their essential mechanical attributes such as durability and reduced maintenance, improved corrosion-resistance, anisotropy and heterogeneity have escalated them to become the frontrunners in material evolution. With particular focus on thin-walled, closed and open (circular) cross-sectioned cylindrical shells, several decades of considerable research have produced a plethora of analytical and numerical models that served to conduct mechanical investigations on the structural response while identifying their key physical characteristics.

Primary governing equations that influenced the mechanics of a composite material when subjected to various static loading environments, additionally introduced mathematical complexities and computational challenges, consequently precluding the scope of a model's development and implementation. Next generation of researchers was scientifically motivated to alleviate the analytical constraints witnessed with precursor mathematical solution procedures and strived towards establishing improved membrane theories and higher order composite shell theories. These approximation techniques served as a principal avenue to further characterize such configurations. Furthermore,

substantial research efforts have been dedicated towards examining the linear free vibration, geometrically non-linear vibration, stability, vibro-acoustic, fracture, delamination, natural frequency and modal shape, and buckling characteristics of cylindrical composite shells as opposed to investigations conducted on the static mechanical response of such structures when subjected to various localized loadings in/about the radial, longitudinal and circumferential directions. Growing demand to incorporate such structures on to various industrial applications have generated renewed scientific research initiatives that seek to gain a better understanding into the mechanical challenges that need to be overcome on their path towards practical implementation.

The principal interest of this research is to formulate a novel analytical framework that:

- Relies upon the fundamentals of Extended Classical Lamination Theory.
- Represents the ability to generate a simple, closed-form solution procedure that associates a fully evolved loads-strain-curvature based constitutive relationship.
- Significantly reduces the time constraint for structural engineers in capturing a first-hand understanding of the mechanical aspects of cylindrical shells.
- Embodies the potential to perform a parametric investigation on such composite members by varying geometric variables based on an intended structural application.
- Indicates the capability to be extended as a computational algorithm for numerical approximation techniques.
- Substantiates the predicted results in comparison to experimentally generated data.

2-2 Scope of the Present Research

A fundamental need is realized to propose, model and develop a simplified, closed-form analytical formulation that is able to full well predict and characterize the mechanical response of thin-walled, closed and open cross-sectioned fiber reinforced cylindrical shell configurations. The current work strives to accomplish specific objectives that are commensurate with the conceptual understanding of their structural behavior. Therefore, breadth of this study can be strategically categorized to have three constituents.

Part-I primarily deals with the macromechanical elastic response investigation of closed, circularly cross-sectioned laminated cylindrical tubes (Figure 2-1).

- Formulation of a closed-form mathematical theory to evaluate equivalent axial and bending stiffness.
- Generation of global stiffness expressions (in terms of Extensional stiffnesses A_{ij}, Coupling stiffnesses B_{ij}, Bending stiffnesses D_{ij} and a set of new higher order stiffnesses E_{ij}) that unifies the relationship between in-plane mechanical and hygro-thermally induced moments to reference plane strains and curvatures.
- Examination of graphical trends involving analytically computed equivalent bending stiffness and axial stiffness results as a function of tube radius.
- Analyses of longitudinal stress distributions on a ply-by-ply basis as a function of circumferential arc angle are conducted. Influence of a thermo-mechanical loading environment on tubular ply stresses are specifically considered.
- Implementation of an ANSYS based finite element approach to substantiate analytical estimations.

Part-II focuses on the macromechanical elastic response investigation of curved, circularly open cross-sectioned cylindrical shells (Figure 2-2).

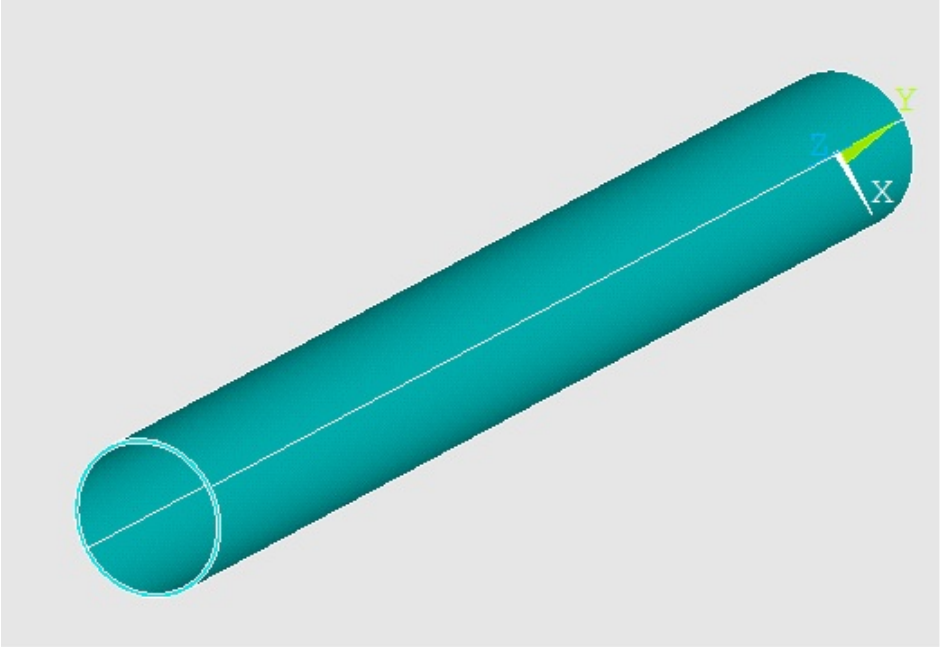

Figure 2-1 Generalized Composite Tube Schematic- ANSYS Model

- Formulation of a simple, closed-form mathematical framework that govern the mechanical characteristics of composite cylindrical shells.
- Generation of global stiffness expressions (in terms of Extensional stiffnesses A_{ij}, Coupling stiffnesses B_{ij}, Bending stiffnesses D_{ij} and a set of new higher order stiffnesses E_{ij}) that unifies the relationship between in-plane mechanical and hygro-thermally induced moments to reference plane strains and curvatures.
- Development of a closed-form expression to predict the centroidal location that essentially decouples the extension-bending deformation mode in such structures subjected to longitudinal tension or longitudinal bending type loading conditions.
- Analyses of longitudinal stress distributions on a ply-by-ply basis as a function of circumferential arc angle are performed. Influence of a thermo-mechanical loading environment on ply stresses are specifically considered.

- Conduct parametric investigations by considering specific geometric and materialistic design variables such as total laminate thickness-to-mean radius of curvature (t/R_m) ratio, mean radius of curvature R_m, circumferential arc angle etc. Influence of ply stresses distribution patterns are examined and interpreted for each of these parameters.
- Employing of a finite element approach to substantiate analytical estimations of ply stresses and centroidal point.

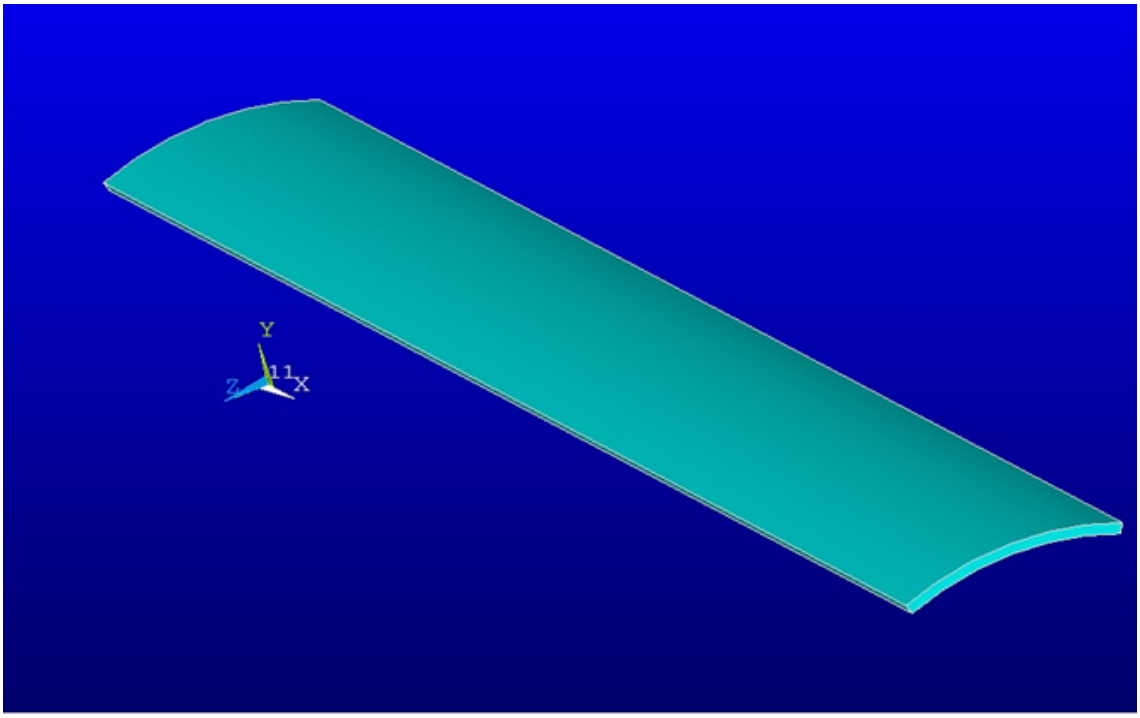

Figure 2-2 Generalized Curved Cylindrical Shell Schematic-ANSYS Model

Part-III emphasizes on an experimental investigation of curved, circularl open cross-sectioned cylindrical shells (Figure 2-3).

- Modeling, design and fabrication of a novel ad-hoc test apparatus to conduct a surface strain based structural response characterization.

- Fabrication of curved cylindrical shell coupons utilizing an autoclave molding based manufacturing procedure.
- Implementation of an accurate surface strain and displacement field measurement technique.
- Interpretation of quantified in-plane strains utilizing a non-contact based full field Digital Image Correlation (DIC) technique.
- Experimentally determine the centroid location for a set of symm-balanced, open cross-sectioned, curved composite coupons.
- Comparison of experimental data with analytical results.

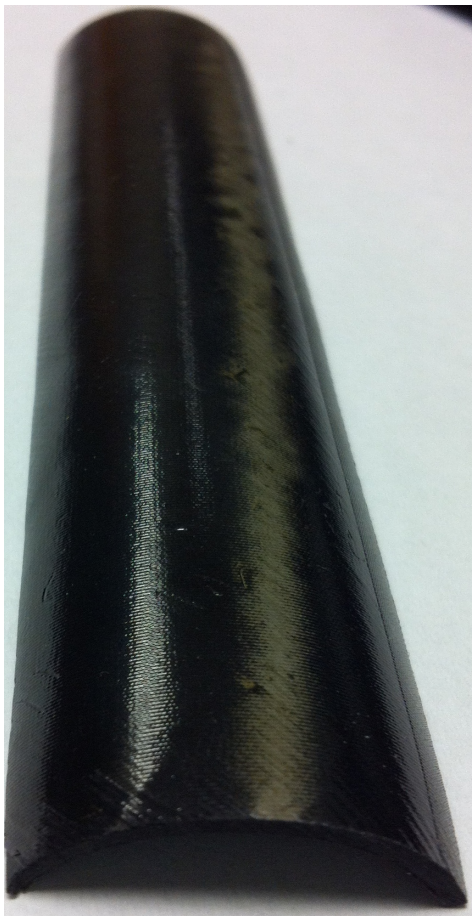

Figure 2-3 Curved Cylindrical Composite Shell Coupon

Chapter 3

BASIC OVERVIEW OF COMPOSITE LAMINATION THEORY

3-1 Lamina Constitutive Equation

Fundamentally, a *lamina* or ply is characterized as a single layer (planar or curved in cross-section) of unidirectional fibers or woven fabric in a matrix. The lamina is an orthotropic material with their principal material axes (Fig 3-1) oriented along the direction of the fibers (longitudinal), normal to the fibers in the plane of the lamina (in-plane transverse) and normal to the plane of the lamina that constitutes the thickness direction. These principal axes are designated as 1, 2 and 3 respectively. A *laminate*, in composite terminology; is made up of two or more unidirectional laminae or plies stacked together at arbitrary orientations. Laminae can consist of plies with tailored material properties and non-uniform thickness. As the orientation of the principal material axes alter from ply-to-ply, it is increasingly convenient to analyze laminates via utilizing a fixed global coordinate system (x, y and z) that is able to primarily characterize the orientation of each stacked ply, ply stacking sequence and eventually perform comprehensive surface stress-strain analyses. In essence, these two typical coordinate systems as shown in Figure 3-1 are utilized to perform a micromechanical analysis and further scaled to a macromechanics based laminate investigation. A thin-walled unidirectional lamina is generally assumed to be under a state of plane stress. Hence stress-strain relations as indicated in Eq. 3.1 and Eq. 3.2 are applicable. Stress-relief along the thickness direction is observed by imposing a plane-stress type boundary condition. This reduced constitutive relationship (Eq 3.1 and Eq. 3.2) relates the in-plane stress components with the in-plane strain components along the principal material axes.

$$\sigma_3 = \tau_{13} = \tau_{23} = 0$$

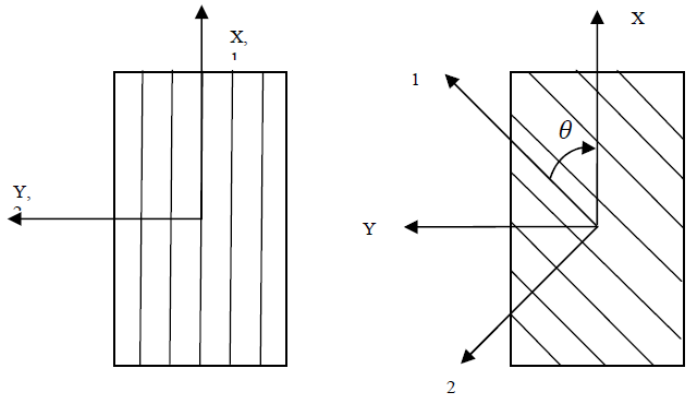

Figure 3-1 Local and Global Coordinate System Schematic for a Lamina

$$[\varepsilon]_{1-2} = [S]_{1-2}[\sigma]_{1-2}$$

$$\begin{bmatrix}\varepsilon_1\\ \varepsilon_2\\ \gamma_{12}\end{bmatrix} = \begin{bmatrix}S_{11} & S_{12} & 0\\ S_{12} & S_{22} & 0\\ 0 & 0 & S_{66}\end{bmatrix}\begin{bmatrix}\sigma_1\\ \sigma_2\\ \tau_{12}\end{bmatrix} \tag{3.1}$$

$$\begin{bmatrix}\sigma_1\\ \sigma_2\\ \tau_{12}\end{bmatrix} = \begin{bmatrix}Q_{11} & Q_{12} & 0\\ Q_{12} & Q_{22} & 0\\ 0 & 0 & Q_{66}\end{bmatrix}\begin{bmatrix}\varepsilon_1\\ \varepsilon_2\\ \gamma_{12}\end{bmatrix} \tag{3.2}$$

Where,

$\varepsilon_1 \; and \; \varepsilon_2$ = In-plane strains in 1 and 2 directions respectively

γ_{12} = In-plane shear strain in the 1-2 plane.

$[S]_{1-2}$ = Reduced compliance matrix in 1-2 coordinate system

$[Q]_{1-2}$ = Reduced stiffness matrix in 1-2 coordinate system

$$S_{11} = \frac{1}{E_1} \; ; \; S_{22} = \frac{1}{E_2} \; ; \; S_{12} = -\frac{\upsilon_{12}}{E_2} = -\frac{\upsilon_{21}}{E_1} \; ; \; S_{66} = \frac{1}{G_{12}}$$

$$Q_{11} = \frac{E_1}{1-\upsilon_{12}\upsilon_{21}} \; ; \; Q_{22} = \frac{E_2}{1-\upsilon_{12}\upsilon_{21}} \tag{3.3}$$

$$Q_{12} = \frac{\upsilon_{21}E_1}{1-\upsilon_{12}\upsilon_{21}} = \frac{\upsilon_{12}E_2}{1-\upsilon_{12}\upsilon_{21}} \; ; \; Q_{66} = G_{12}$$

Stiffness/compliance relations as shown in Eqns. (3.1) and (3.2) are typically expressed in terms of engineering constants (Eq. 3.3). Therefore, as far as the in-plane stress-strain relations are concerned, a single orthotropic lamina can be fully distinguished by four independent constants: -

a) Four reduced stiffnesses Q_{11},Q_{22},Q_{12} and Q_{16} respectively.

b) Four compliances S_{11} , S_{22} , S_{12} and S_{66} respectively.

c) Four engineering constants E_1,E_2,υ_{12} and G_{12} respectively.

3.2 Transformation of Elastic Parameters and Stress-Strain Relations

The relationship establishing a mathematical interaction between the transformed compliances as a function of the principal lamina compliances is given by:

$$[\bar{S}]_{x-y} = [T_\varepsilon(-\theta)][S]_{1-2}[T_\sigma(\theta)] \tag{3.4}$$

The relationship of the reduced stiffness matrix in x-y coordinate system and 1-2 co-ordinate system is as follows:

$$[\bar{Q}]_{x-y} = [T_\sigma(-\theta)][Q]_{1-2}[T_\varepsilon(\theta)] \tag{3.5}$$

where

$[\bar{S}]_{x-y}$ = Transformed compliance matrix in x-y coordinate system

$[\bar{Q}]_{x-y}$ = Transformed stiffness matrix in x-y coordinate system

$[\bar{S}]_{1-2}$ = Reduced compliance matrix in 1-2 coordinate system

$[\bar{Q}]_{1-2}$ = Reduced stiffness matrix in 1-2 coordinate system

$$[T_\varepsilon(\theta)] = \begin{bmatrix} m^2 & n^2 & mn \\ n^2 & m^2 & -mn \\ -2mn & 2mn & m^2-n^2 \end{bmatrix}$$

$$[T_\sigma(\theta)] = \begin{bmatrix} m^2 & n^2 & 2mn \\ n^2 & m^2 & -2mn \\ -mn & mn & m^2-n^2 \end{bmatrix} \tag{3.6}$$

$$m = cos\theta \; ; \; n = sin\theta$$

where θ = angle measured positive counterclockwise from the global x-axis to the 1-axis and $[T_\varepsilon(\theta)]$ and $[T_\sigma(\theta)]$ are the associated transformation matrices for strain and stress respectively.

Reviewing the stress-strain relations in Eq. 3.1 and Eq. 3.2, it can be deduced that, when the lamina is loaded only in tension or compression along the principal material axes, there is no shear strains induced. Similarly, when the lamina is loaded under pure shear τ_{12} on the principal plane (1-2) only a shear strain γ_{12} is produced on the 1-2 plane. Thus, no coupling exists between normal stresses and shear deformation and between shear stresses and normal strains. This is not the case when the lamina is loaded along arbitrary axes x and y that are oriented at an angle θ. Then, the stress-strain relationship manifest in the form,

$$\begin{bmatrix}\sigma_x\\ \sigma_y\\ \tau_{xy}\end{bmatrix} = \begin{bmatrix}Q_{xx} & Q_{xy} & Q_{xs}\\ Q_{yx} & Q_{yy} & Q_{ys}\\ Q_{sx} & Q_{sy} & Q_{ss}\end{bmatrix}\begin{bmatrix}\varepsilon_x\\ \varepsilon_y\\ \gamma_{xy}\end{bmatrix}$$

or in brief

$$[\sigma]_{x-y} = [\bar{Q}]_{x-y}\,[\varepsilon]_{x-y} \tag{3.7}$$

where

$$\begin{bmatrix}Q_{xx} & Q_{xy} & Q_{xs}\\ Q_{yx} & Q_{yy} & Q_{ys}\\ Q_{sx} & Q_{sy} & Q_{ss}\end{bmatrix} = [T_\sigma(-\theta)]\begin{bmatrix}Q_{11} & Q_{12} & 0\\ Q_{21} & Q_{22} & 0\\ 0 & 0 & Q_{66}\end{bmatrix}[T_\varepsilon(\theta)]$$

Therefore, the transformed stress-strain relations can be obtained either by direct inversion (Eq. 3.7) or by transformation of the stress-strain relations referred to the principal material axes. Similarly, the transformed strain-stress relations can be shown respectively.

3-3 Review of Classical Lamination Theory (CLT)

Fundamentally, the structural response of a multidirectional laminate is a function of the mechnical properties and stacking sequence of the individual plies. This theory is able to predict the behavior of a laminate when the following hypotheses and restrictions are in full agreement:

1. Each layer of the laminate is quasi-homogeneous and orthotropic.
2. The laminate is thin with its lateral dimensions much larger than its thickness and is loaded in its plane only, i.e., the laminate and its layer (except for their edges) are in a state of plane stress ($\sigma_z = \tau_{xz} = \tau_{yz} = 0$).
3. All displacements are small compared with the thickness of the laminate ($|u|, |v| \text{ and } |w| < t_{laminate}$).
4. Displacements are continuous throughout the laminate.
5. In-plane displacements vary linearly through the thickness of the laminate, i.e., u and v displacements in the x and y directions are linear functions of z.
6. Straight lines normal to the middle surface remain straight and normal to that surface after deformation. This implies that transverse shear strain γ_{xz} and γ_{yz} are negligible.
7. Strain-displacement and stress-strain relations are linear.
8. Normal strains ε_z are negligible (as opposed to in-plane strains ε_x and ε_y).

In principle, classical lamination theory can be used to generate stress-strain relations for any arbitrary layer within a laminate and further develop general load-deformation relations that relate the in-plane forces and moments to mid-plane strains and curvatures. Figure 3-2 shows a section of the laminate normal to y-axis before and after deformation.

The x-y plane is equidistant from the top and bottom surfaces of the laminate respectively.

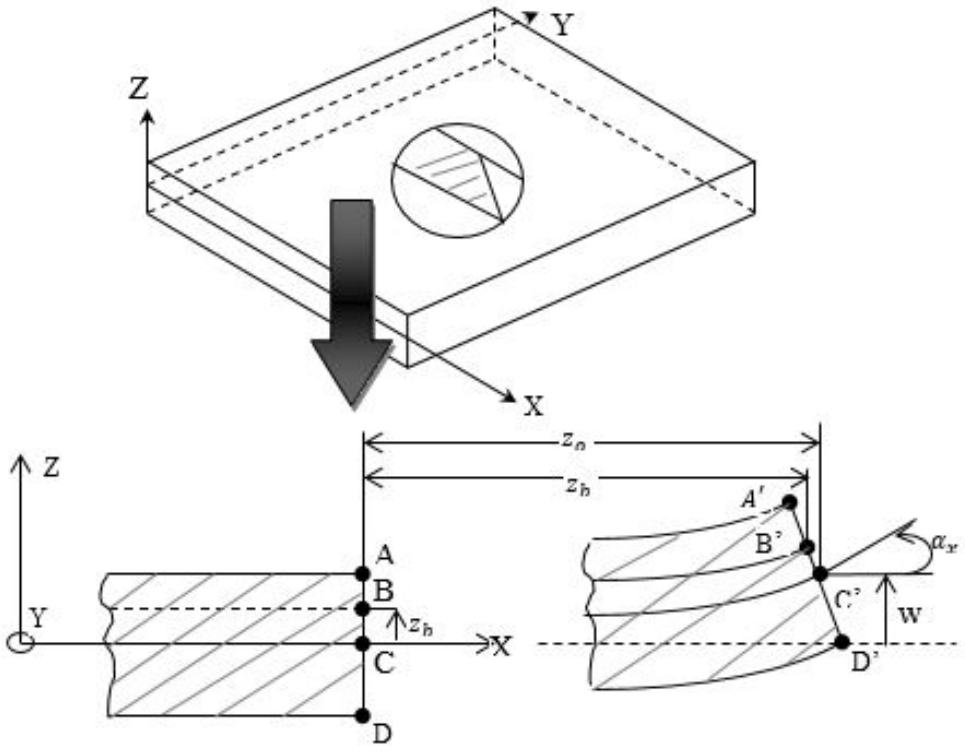

Figure 3-2 Laminate section before (ABCD) and after (A'B'C'D') deformation

The reference plane (x-y) of laminated plate is located at the mid-plane of the plate as shown in Figure 3-2. Reference plane displacements in the x-y plane can be shown as

$$u_0 = u_0(x,y);\ v_0 = v_0(x,y);\ w_0 = w_0(x,y) \tag{3.8}$$

and in general,

$$u = u_0 - z\frac{\partial w}{\partial x}\ ; v = v_0 - z\frac{\partial w}{\partial y} \tag{3.9}$$

where, z is the through-the-thickness coordinate of a general point in the cross section. For small displacements, the classical strain-displacement relations of elasticity (Eq. 3.10) yields generalized relations for ε_x, ε_y and γ_{xy} respectively.

$$\varepsilon_x = \frac{\partial u}{\partial x} = \frac{\partial u_0}{\partial x} - z\frac{\partial^2 w}{\partial x^2}$$

$$\varepsilon_y = \frac{\partial v}{\partial y} = \frac{\partial v_0}{\partial y} - z\frac{\partial^2 w}{\partial y^2} \tag{3.10}$$

$$\gamma_{xy} = \frac{\partial u}{\partial y} + \frac{\partial v}{\partial x} = \frac{\partial u_0}{\partial y} + \frac{\partial v_0}{\partial x} - 2z\frac{\partial^2 w}{\partial x \partial y}$$

Noting that the strain components on the reference plane are expressed as:

$$\varepsilon_x^0 = \frac{\partial u_0}{\partial x}\ ;\ \varepsilon_y^0 = \frac{\partial v_0}{\partial y}\ ;\ \gamma_{xy}^0 = \frac{\partial u_0}{\partial y} + \frac{\partial v_0}{\partial x} \tag{3.11}$$

And the curvatures of the laminate as:

$$\kappa_x = -\frac{\partial^2 w}{\partial x^2}\ ;\ \kappa_y = -\frac{\partial^2 w}{\partial y^2}\ ;\ \kappa_{xy} = -2\frac{\partial^2 w}{\partial x \partial y} \tag{3.12}$$

we can relate the strains at any point in the laminate (Fig. 3-3) to the reference plane strains and the laminate curvatures as follows:

$$\begin{bmatrix} \varepsilon_x \\ \varepsilon_y \\ \gamma_{xy} \end{bmatrix} = \begin{bmatrix} \varepsilon_x^0 \\ \varepsilon_y^0 \\ \gamma_{xy}^0 \end{bmatrix} + z \begin{bmatrix} \kappa_x \\ \kappa_y \\ \kappa_{xy} \end{bmatrix} \tag{3.13}$$

The stresses of the kth layer in the laminate can be written as

$$\left[\sigma_{x-y}\right]_{k^{th}} = \left[\bar{Q}_{x-y}\right]_{k^{th}} \left[\varepsilon_{x-y}\right]_{k^{th}}$$

i.e. (3.14)

$$\left[\sigma_{x-y}\right]_{k^{th}} = \left[\bar{Q}_{x-y}\right]_{k^{th}} \left(\left[\varepsilon^0{}_{x-y}\right]_{k^{th}} + z_{k^{th}} \left[\kappa_{x-y}\right]\right)$$

Because of the discontinuous variation of the transformed stiffness matrix from layer to layer, stresses can vary discontinuously from layer to layer. Typically for a laminate subjected to axial/flexural bending, a linear strain variation through thickness is observed. As a consequence, it is more convenient to deal with the integrated effect of these stresses on the laminate. In-plane stresses acting on a layer k of the laminate (Fig 3-3) can be expressed in terms of resultant forces and moments respectively.

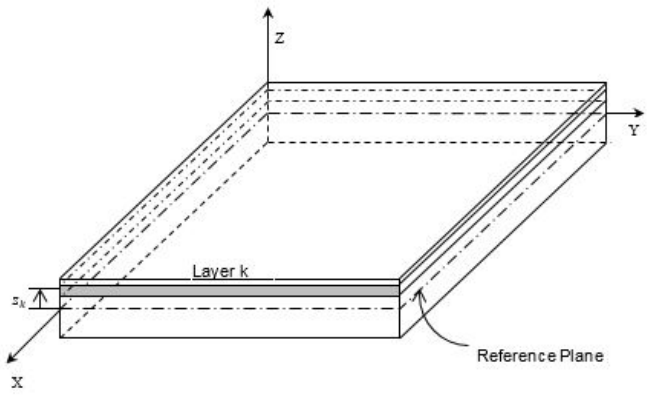

Figure 3-3 Layer k within Laminate

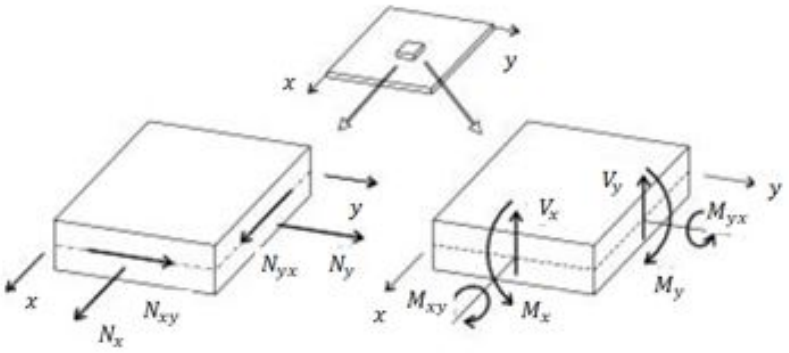

Figure 3-4 Element of Single Layer with Resultant Force and Moments

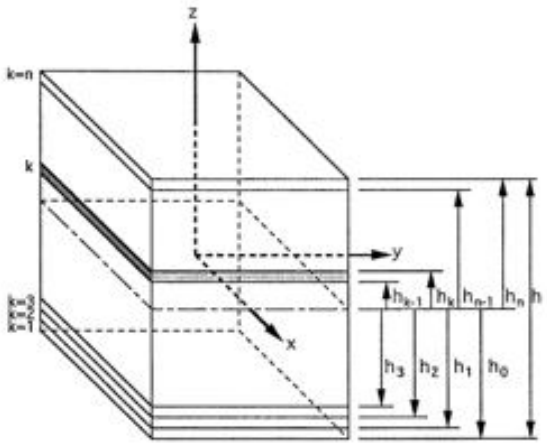

Figure 3-5 Multidirectional Laminate with Coordinate Notation of Individual Plies

In the case of a multi-layered laminate, the total force and moment resultants (Fig. 3-4) are acquired by summing the effects of all layers. Thus, for a multi-directional laminate consisting of n number of arbitrarily oriented laminae (Fig. 3-5) , the force and moment resultants are obtained as

$$\begin{bmatrix} N_x \\ N_y \\ N_{xy} \end{bmatrix} = \sum_{k=1}^{n} \int_{h_{k-1}}^{h_k} \begin{bmatrix} \sigma_x \\ \sigma_y \\ \tau_{xy} \end{bmatrix}_k dz \quad (\frac{lb}{in})$$

$$\begin{bmatrix} M_x \\ M_y \\ M_{xy} \end{bmatrix} = \sum_{k=1}^{n} \int_{h_{k-1}}^{h_k} \begin{bmatrix} \sigma_x \\ \sigma_y \\ \tau_{xy} \end{bmatrix}_k zdz \quad (\frac{lb-in}{in}) \tag{3.15}$$

where

z = Through-the thickness coordinate of a point in the cross-section

t = Layer thickness

N_x , N_y = Normal forces per unit length

N_{xy} = Shear forces per unit length

M_x , M_y = Bending moments per unit length

M_{xy} = Twisting moment per unit length

Integrating Eq. 3-15 with aid of Eq. 3.14, a general expression relating in-plane forces and moments to reference palne strains and curvatures is developed and shown as:

$$\begin{bmatrix} [N]_{3x1} \\ [M]_{3x1} \end{bmatrix}_{6x1} = \begin{bmatrix} [A]_{3x3} & [B]_{3x3} \\ [B]_{3x3} & [D]_{3x3} \end{bmatrix}_{6x6} \begin{bmatrix} [\varepsilon^0]_{3x1} \\ [\kappa]_{3x1} \end{bmatrix}_{6x1}$$

or in expanded form as:

$$\begin{bmatrix} N_x \\ N_y \\ N_{xy} \\ M_x \\ M_y \\ M_{xy} \end{bmatrix} = \begin{bmatrix} A_{11} & A_{12} & A_{16} & B_{11} & B_{12} & B_{16} \\ A_{12} & A_{22} & A_{26} & B_{12} & B_{22} & B_{26} \\ A_{16} & A_{26} & A_{66} & B_{16} & B_{26} & B_{66} \\ B_{11} & B_{12} & B_{16} & D_{11} & D_{12} & D_{16} \\ B_{12} & B_{22} & B_{26} & D_{12} & D_{22} & D_{26} \\ B_{16} & B_{26} & B_{66} & D_{16} & D_{26} & D_{66} \end{bmatrix} \begin{bmatrix} \varepsilon_x^0 \\ \varepsilon_y^0 \\ \gamma_{xy}^0 \\ \kappa_x \\ \kappa_y \\ \kappa_{xy} \end{bmatrix} \tag{3.16}$$

It should be noted that Figure 3-4 represents the positive convection for all resultant forces and moments. The constitutive relationship (Eq. 3-16) is typically expressed in terms of three laminate stiffness matrices [A], [B], and [D] , which are implicit functions of the laminate geometry, material properties and stacking sequence of the individual plies. The simplified expressions for the average elastic parameters of the multi-directional laminate can be denoted by

$$[A] = \sum_{k=1}^{n} \left[\bar{Q}_{x-y}\right]_k (h_k - h_{k-1})$$

$$[B] = \frac{1}{2} \sum_{k=1}^{n} \left[\bar{Q}_{x-y}\right]_k \left({h_k}^2 - {h_{k-1}}^2\right) \tag{3.17}$$

$$[D] = \frac{1}{3} \sum_{k=1}^{n} \left[\bar{Q}_{x-y}\right]_k \left({h_k}^3 - {h_{k-1}}^3\right)$$

where [A] is the extensional stiffness matrix that relates the in-plane loads to the in-plane strains, [B] is the extension-bending coupling matrix that relates in-plane loads to cruvatures and moments to in-plane strains and [D] is the bending stiffness matrix that relates moments to curvatures respectively. It is also known that matrices [A],[B] and [D] are symmetrical matrices respectively. Since multidirectional laminates are charecterized by stress discontunities from ply-t-ply, its is more convenient to work with strains, which are contineous through the thickness. Hence Eqn. 3.16 can be rewritten by performing a matrix inversion and expressed in a brief form as follows

$$\begin{bmatrix} \varepsilon^0 \\ \kappa \end{bmatrix} = \begin{bmatrix} a & b \\ b^T & d \end{bmatrix} \begin{bmatrix} N \\ M \end{bmatrix} \tag{3.18}$$

When a multidirectional laminate is subjected to mechanical ([N], [M]) and hygrothermal loading ($\Delta T, \Delta c$), the resultant loads, moments and the stresses can be rewritten. Fundamentally, total strain induced in a composite structure is a combination of

$$\{\varepsilon_{total}\} = \{\varepsilon_{mechanical}\} + \{\alpha\}\Delta T + \{\beta\}\Delta C \tag{3.19}$$

Ply mechanical stresses can be related to mechanical and thermal strains through the reduced stiffness matrices and is given by

$$\left\{\sigma_{mechanical}\right\}_k = \left[\bar{Q}_{x-y}\right]_k * (\{\varepsilon_{total}\} - \{\alpha\}_k \Delta T - \{\beta\}_k \Delta C) \tag{3.20}$$

Eqn. 3.20 can be expanded in a matrix form and can be shown as

$$\begin{pmatrix} \sigma_x \\ \sigma_y \\ \tau_{xy} \end{pmatrix}_k = \begin{pmatrix} \bar{Q}_{11} & \bar{Q}_{12} & \bar{Q}_{16} \\ \bar{Q}_{21} & \bar{Q}_{22} & \bar{Q}_{26} \\ \bar{Q}_{61} & \bar{Q}_{62} & \bar{Q}_{66} \end{pmatrix}_k * \left(\begin{pmatrix} \varepsilon^o_x \\ \varepsilon^o_y \\ \gamma^o_{xy} \end{pmatrix} + z * \begin{pmatrix} \kappa_x \\ \kappa_y \\ \kappa_{xy} \end{pmatrix} - \begin{pmatrix} \alpha_x \\ \alpha_y \\ \alpha_{xy} \end{pmatrix}_k * \Delta T - \begin{pmatrix} \beta_x \\ \beta_y \\ \beta_{xy} \end{pmatrix}_k * \Delta C \right) \tag{3.21}$$

Resultant mechanical and hygrothermal loadings can be related to the mid-plane strains and curvatures through the stiffness matrices by

$$\begin{pmatrix} \bar{N} + N^T + N^H \\ \bar{M} + M^T + M^H \end{pmatrix} = \begin{pmatrix} A & B \\ B & D \end{pmatrix} * \begin{pmatrix} \varepsilon_0 \\ \kappa \end{pmatrix}$$
$$\begin{pmatrix} \varepsilon_0 \\ \kappa \end{pmatrix} = \begin{pmatrix} a & b \\ b^T & d \end{pmatrix} * \begin{pmatrix} \bar{N} + N^T + N^H \\ \bar{M} + M^T + M^H \end{pmatrix} \tag{3.22}$$

it is known that matrices [a] and [d] are symmetric and [b] matrix is not generally symmetrical. However, the global stiffness matrix shows an overall symmetryChapter 4 deals with developing an analytical methodology for thin-walled cylindrical composite tubes while utilizing an extended lamination theory approach to characterize key structural properties such as axial stiffness, bending stiffness and ply stress distributions respectively.

Chapter 4

STIFFNESS AND PLY-STRESS INVESTIGATION OF THIN WALLED, CYLINDRICAL COMPOSITE TUBE CONFIGURATIONS

4-1 Stiffness Model Formulation for Cylindrical Composite Tubes

A novel closed-form analytical methodology for estimating the equivalent axial and bending stiffnesses in thin-walled fiber-reinforced circular composite tubes subjected to a hygrothermomechanical loading environment is initially developed. A borad preliminary understanding into the mechanical behavior of composite tubes is achieved through this model development. The composite tube (Fig 4-1) represents a circular cross-section with an inner radius R_i and outer radius R_o respectively. Longitudinal span of the tube is assumed to be be one order of magnitude larger in comparison to its geometric radius. Plane stress conditions are assumed throughout for this geometrically linear-elastic analysis. Charecteristic stiffness (axial and bending) data are predicted utilizing the composite shell theory approach and compared against the stiffness results achieved using the conventional smear protery approach and composite plate theory approach.

4-1-1 Composite Smear-Property Approach

The conventional stiffness evaluation approach utilizes the smeared modulus of the composite ply lay-up to mechanically characterize the stiffness properties of a typical composite structural configuration. Smear modulus is essentially multiplied with cross-section area and structural moment of inertia to obtain an effective first-level estimation of the equivalent axial and bending stiffness respectively. Via smear property approach, equivalent axial stiffness (EA) and bending stiffness (EI) for a fiber-reinforced tube can be shown as

$$(EA)_{equivalent} = E_x \pi.(R_o^{\ 2} - R_i^{\ 2})$$
$$(EI)_{equivalent} = E_x \frac{\pi}{4}.(R_o^{\ 4} - R_i^{\ 4}) \qquad (4.1)$$

where, the smeared modulus is denoted by $E_x = \frac{1}{a_{11}t}$ and a_{11} is the extensional compliance term and t is the total thickness of the composite laminate.

4-1-2 Composite Laminate Plate Theory (CLPT) Approach

Laminated plate theory is the fundamental design tool for evaluating multidirectional laminates when experimental data are not immediately available for mechanical investigation. Primary governing hypotheses defining this theory are based on preservation of plane stress conditions and the assumption of strain-linearity-through-thickness. Key benefits of laminated plate theory include:

- used in situations where a uniform in-plane loading or bending is achieved.
- used to analyze stress fields free from localized stress concentrations.
- feasible to be supplemented with a failure-criteria theory to identify first ply failure.
- extraction of viable solution procedures via allowing for multi-design analyses.
- streamlined implementation onto various computational approximation packages.

Underlying mechanics of composite laminated plate theory is applied towards evaluating the axial and bending stiffness characteristics of a generalized composite tube structure. An infinitesimal rectangular plate element sectioned out (Figure 4-1) from the cylindrical tube cross-section is considered. Plane stress conditions are preserved in this differential element. A cartesian coordinate system is designated to characterize the geometric attributes of the cylindrical tube. The length of the tube is defined along the global x' axis and the cross-section of the tube is along the y'-z' plane. The focused infinitesimal plate section inclines at an angle θ with respect to the vertically oriented z' axis of the tube.

Initially, the section is rotated about x' to be aligned with y' axis. Parallel-axis theorem is subsequently implemented to translate the stiffness of the rotated plate section by a distance $R_m.\cos\theta$, where R_m is the tube mean-radius respectively.

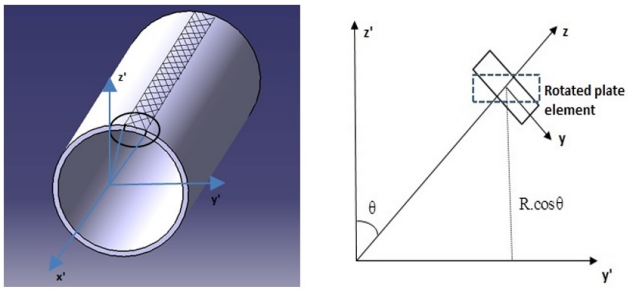

Figure 4-1 Composite Tube Schematic & 2-D Infinitesimal Plate Element

Plane stress transformation matrices associated with rotations about elemental x-axis and z-axis coordinates are given by

$$\left[T_\sigma(\theta)\right]_x = \begin{pmatrix} 1 & 0 & 0 \\ 0 & m_1^2 & 0 \\ 0 & 0 & m_1 \end{pmatrix} \qquad \left[T_\varepsilon(\theta)\right]_z = \begin{pmatrix} m_2^2 & n_2^2 & m_2 n_2 \\ n_2^2 & m_2^2 & -m_2 n_2 \\ -2m_2 n_2 & 2m_2 n_2 & m_2^2 - n_2^2 \end{pmatrix}$$

$$\left[T_\varepsilon(\theta)\right]_x = \begin{pmatrix} 1 & 0 & 0 \\ 0 & m_1^2 & 0 \\ 0 & 0 & m_1 \end{pmatrix} \qquad \left[T_\sigma(\theta)\right]_z = \begin{pmatrix} m_2^2 & n_2^2 & 2m_2 n_2 \\ n_2^2 & m_2^2 & -2m_2 n_2 \\ -m_2 n_2 & m_2 n_2 & m_2^2 - n_2^2 \end{pmatrix} \tag{4.2}$$

where $m_1 = \cos\theta, m_2 = \cos\beta$ and $n_2 = \sin\beta$ respectively.

Initially, for conducting a β rotation about z-axis, the reduced-stiffness matrix is multiplied with the z-rotation transformation equation (Eq. 4.1.2) and can be shown as

$$[\bar{Q}'(\beta)]_x = [T_\sigma(-\beta)]_z.[Q_{1-2}].[T_\varepsilon(\beta)]_z \tag{4.3}$$

For performing a θ rotation on the plate element about x'-axis, the transformed-reduced stiffness is further multiplied with the x-rotation transformation equation (Eq. 4.2) associated with x-axis as denoted by

$$[\bar{Q}''(\theta)]_x = [T_\sigma(\theta)]_x.[\bar{Q}'(\beta)]_x.[T_\varepsilon(-\theta)]_x \tag{4.4}$$

Assuming θ to be the rotation angle about x'-axis and β to be the fiber-orientation angle about z axis, the transformed stiffness matrices incorporating two rotation-transformation matrices for the infinitesimal plate element are obtained (Eq. 4.4). Additionally the stiffness matrices $\left[\hat{A}\right]$, $\left[\hat{B}\right]$ and $\left[\hat{D}\right]$ for the differential tube element are generated as indicated in Eqns. (4.5) and (4.6) respectively.

$$[\bar{Q}"]_k = [T_\sigma(-\beta)]_z.[T_\sigma(\theta)]_x.[Q_{1-2}].[T_\varepsilon(-\theta)]_x.[T_\varepsilon(\beta)]_z \tag{4.5}$$

$$\left[\hat{A}\right] = \sum_{k=1}^{n} \int_{z_{k-1}}^{z_k} [\bar{Q}"]_k \, dz" = \sum_{k=1}^{n} [\bar{Q}"]_k * (z"_k - z"_{k-1})$$

$$\left[\hat{B}\right] = \sum_{k=1}^{n} \int_{z_{k-1}}^{z_k} [\bar{Q}"]_k z" dz" = \frac{1}{2}\sum_{k=1}^{n} [\bar{Q}"]_k * (z"^2_k - z"^2_{k-1}) \tag{4.6}$$

$$\left[\hat{D}\right] = \sum_{k=1}^{n} \int_{z_{k-1}}^{z_k} [\bar{Q}"]_k z"^2 dz" = \frac{1}{3}\sum_{k=1}^{n} [\bar{Q}"]_k * (z"^3_k - z"^3_{k-1})$$

where $\left[\hat{A}\right]$, $\left[\hat{B}\right]$ and $\left[\hat{D}\right]$ are the doubly-rotated and transformed extensional stiffness per unit width, extension-bending coupling stiffness per unit width and the coupling stiffness per unit width for the differential tube element respectively. In order to determine the global stiffness matrices for the integral composite tube structure, stiffness-per-unit-width expressions denoted in Eq. (4.6) are further integrated through the circumference of the tube over the entire θ domain as indicated in Eq. (4.7).

$$\left[\bar{A}\right] = \int_0^{2\pi} \left[\hat{\hat{A}}\right]_k R_m.d\theta = \int_0^{2\pi} \left[\hat{A}\right]_k R_m.d\theta$$

$$\left[\bar{B}\right] = \int_0^{2\pi} \left[\hat{\hat{B}}\right]_k R_m.d\theta = \int_0^{2\pi} \left(\left[\hat{B}\right]_k + R_m Cos\theta * \left[\hat{A}\right]_k\right) * R_m.d\theta \tag{4.7}$$

$$\left[\bar{D}\right] = \int_0^{2\pi} \left[\hat{\hat{D}}\right]_k R_m.d\theta = \int_0^{2\pi} \left(\left[\hat{D}\right]_k + 2*(R_m Cos\theta) * \left[\hat{B}\right]_k + (R_m Cos\theta)^2 * \left[\hat{A}\right]_k\right) * R_m.d\theta$$

where matrices $\left[\bar{A}\right]$, $\left[\bar{B}\right]$ and $\left[\bar{D}\right]$ are the respective global stiffness matrices of the composite tube structure constructed utilizing the mechanics of laminated plate theory. Thus the effective axial stiffness and bending stiffness of the composite tube are given by

$$\bar{A}_x = \frac{1}{\bar{a}_{11}} \text{ and } \bar{D}_x = \frac{1}{\bar{d}_{11}} \tag{4.8}$$

where $\bar{a}_{11}$ is the (1,1) extensional compliance term and $\bar{d}_{11}$ is the (4,4) bending compliance term obtained from the global $\begin{bmatrix} \bar{A}_{3*3} & \bar{B}_{3*3} \\ \bar{B}_{3*3} & \bar{D}_{3*3} \end{bmatrix}$ matrix inversion respectively.

4-1-3 Composite Laminate Shell Theory (CLST) Approach

In the laminated shell approach, an infinitesimal composite cylindrical tube element acquiring a specific ply stacking sequence is assumed for global stiffness matrix evaluation. As indicated in Figure 4-2, the composite shell theory based approach incorporates the influence of the shell curvature towards characterizing the mechanical aspects of a composite tube configuration. An infinitesimal shell element is targeted to develop an analytical expression for the transformed stiffnesses per unit width.

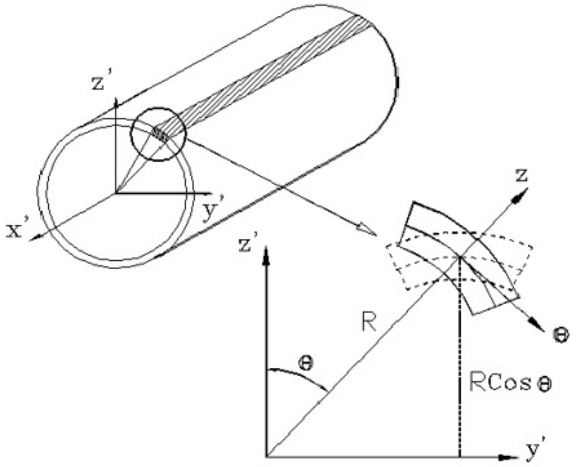

Figure 4-2 Composite Shell Element Schematic

Considering $N_x^{"},N_y^{"},N_{xy}^{"}$ and $N_{yx}^{"}$ to be the applied resultant mechanical loads per unit width while $M_x^{"},M_y^{"},M_{xy}^{"}$ and $M_{yx}^{"}$ to be the applied resultant moments per unit width acting on the composite tube differential element; axial, transverse and shear stresses can be associated to resultant force and moment components by

$$\begin{aligned}
N_x^{"} &= \sum_{k=1}^{n} \int_{z_k}^{z_{k-1}} \sigma_x^k (1+\frac{z"}{R_m}).dz" & M_x^{"} &= \sum_{k=1}^{n} \int_{z_k}^{z_{k-1}} \sigma_x^k (1+\frac{z"}{R_m}).z".dz" \\
N_y^{"} &= \sum_{k=1}^{n} \int_{z_k}^{z_{k-1}} \sigma_y^k .dz" & M_y^{"} &= \sum_{k=1}^{n} \int_{z_k}^{z_{k-1}} \sigma_y^k .z".dz" \\
N_{xy}^{"} &= \sum_{k=1}^{n} \int_{z_k}^{z_{k-1}} \tau_{xy}^k (1+\frac{z"}{R_m}).dz" & M_{xy}^{"} &= \sum_{k=1}^{n} \int_{z_k}^{z_{k-1}} \tau_{xy}^k (1+\frac{z"}{R_m}).z".dz" \\
N_{yx}^{"} &= \sum_{k=1}^{n} \int_{z_k}^{z_{k-1}} \tau_{yx}^k .dz" & M_{yx}^{"} &= \sum_{k=1}^{n} \int_{z_k}^{z_{k-1}} \tau_{yx}^k .z".dz"
\end{aligned} \tag{4.9}$$

where $\left(1+\frac{z^{"}}{R_m}\right)$ is the cylindrical shell curvature factor that influences the longitudinal and shear stress components. The fundamental necessity to seek expressions describing the relations of forces and moments to the laminate deformation is due to the typical discontinuous variation of stresses witnessed from layer to layer within the composite tube. Hence, for convenience in dealing with the integrated effect of these stresses on the composite laminate, the stresses acting on any arbitrary layer (Eqn. 4.10) located a distance z_k from the reference plane can be replaced by resultant forces and moments as shown in Eqn. (4.9) respectively.

An important assumption made in regards to the geometry of the composite tube is the existence of a uni-curvature around the circumference. Curvature is assumed to be absent along the y' plane as the tube span is substantially larger compared to tube mean-radius. It should be noted that, although expressions involving $N_{xy}^{"}$ and $M_{xy}^{"}$ are not

identical to expressions involving N''_{xy} and M''_{xy}, $\tau^k_{xy} = \tau^k_{yx}$ for all cases respectively. Furthermore, transverse shear stress effects are ignored since the laminate wall thickness assumed to be small.

Generally, in the case of a multilayer composite laminate such as a thin-walled circular composite tube configuration comprising of a specified ply lay-up and laminate stacking sequence, amount of mechanical stresses $\begin{Bmatrix} \sigma^k_x \\ \sigma^k_y \\ \tau^k_{xy} \end{Bmatrix}$ encountered in each ply can be mathematically expressed by relating mechanical strains (difference of reference plane strains and curvatures with hygrothermal strains) with their corresponding transformed stiffness parameters respectively. Eqn. (4.10) represents the relation between the in-plane mechanical stresses to mechanical strains in terms of transformed stiffness matrices.

$$\begin{pmatrix} \sigma_x \\ \sigma_y \\ \tau_{xy} \end{pmatrix}_k = \begin{pmatrix} \overline{Q}''_{11} & \overline{Q}''_{12} & \overline{Q}''_{16} \\ \overline{Q}''_{21} & \overline{Q}''_{22} & \overline{Q}''_{26} \\ \overline{Q}''_{61} & \overline{Q}''_{62} & \overline{Q}''_{66} \end{pmatrix}_k * \left(\begin{pmatrix} \varepsilon^o{}_x \\ \varepsilon^o{}_y \\ \gamma^o{}_{xy} \end{pmatrix} + z * \begin{pmatrix} \kappa_x \\ \kappa_y \\ \kappa_{xy} \end{pmatrix} - \begin{pmatrix} \alpha_x \\ \alpha_y \\ \alpha_{xy} \end{pmatrix}_k * \Delta T - \begin{pmatrix} \beta_x \\ \beta_y \\ \beta_{xy} \end{pmatrix}_k * \Delta C \right) \tag{4.10}$$

where, $\overline{Q}''_{ij}$ is the transformed-reduced stiffness matrix obtained after incorporating two transformation matrix operations on the reduced principal-axes stiffness matrix. Upon introducing Eqn. (4.10) into each of the resultant force-moment equations (Eq. 4.9), a broader understanding can be gained via generating a set of fully expanded expressions (Eqns. 4.11-4.18) that relates in-plane mechanical loadings (forces and moments) to in-plane reference strains and curvatures respectively. Here the stiffnesses $\left[Q\right]^k_{x,y}$, reference plane strains $\left\{\varepsilon^o\right\}_{x,y}$ and curvatures $\left\{\kappa\right\}_{x,y}$ are taken outside the integration

operation since they are not functions of z''. Of these quantities only stiffnesses are unique to each layer k, whereas the reference plane strains and curvatures refer to the entire laminate and are the same for all the plies constituting the composite tube.

$$N_x^{"} = \left\{\sum_{k=1}^{n}\int_{z_k}^{z_{k-1}} \begin{pmatrix} \overline{Q}_{11}^{"} & \overline{Q}_{12}^{"} & \overline{Q}_{16}^{"} \end{pmatrix} * \left(1+\frac{z^{"}}{R_m}\right) dz^{"}\right\} * \begin{pmatrix} \varepsilon_x^o \\ \varepsilon_y^o \\ \gamma_{xy}^o \end{pmatrix} + \left\{\sum_{k=1}^{n}\int_{z_k}^{z_{k-1}} \begin{pmatrix} \overline{Q}_{11}^{"} & \overline{Q}_{12}^{"} & \overline{Q}_{16}^{"} \end{pmatrix} * \left(1+\frac{z^{"}}{R_m}\right) * z^{"}.dz^{"}\right\} * \begin{pmatrix} \kappa_x \\ \kappa_y \\ \kappa_{xy} \end{pmatrix}$$
$$- \left\{\sum_{k=1}^{n}\int_{z_k}^{z_{k-1}} \begin{pmatrix} \overline{Q}_{11}^{"} & \overline{Q}_{12}^{"} & \overline{Q}_{16}^{"} \end{pmatrix} * \begin{pmatrix} \alpha_x \\ \alpha_y \\ \alpha_{xy} \end{pmatrix} * \left(1+\frac{z^{"}}{R_m}\right) dz^{"}\right\} * \Delta T - \left\{\sum_{k=1}^{n}\int_{z_k}^{z_{k-1}} \begin{pmatrix} \overline{Q}_{11}^{"} & \overline{Q}_{12}^{"} & \overline{Q}_{16}^{"} \end{pmatrix} * \begin{pmatrix} \alpha_x \\ \alpha_y \\ \alpha_{xy} \end{pmatrix} * \left(1+\frac{z^{"}}{R_m}\right) dz^{"}\right\} * \Delta C$$

(4.11)

$$N_y^{"} = \left\{\sum_{k=1}^{n}\int_{z_k}^{z_{k-1}} \begin{pmatrix} \overline{Q}_{12}^{"} & \overline{Q}_{22}^{"} & \overline{Q}_{26}^{"} \end{pmatrix} * dz^{"}\right\} * \begin{pmatrix} \varepsilon_x^o \\ \varepsilon_y^o \\ \gamma_{xy}^o \end{pmatrix} + \left\{\sum_{k=1}^{n}\int_{z_k}^{z_{k-1}} \begin{pmatrix} \overline{Q}_{12}^{"} & \overline{Q}_{22}^{"} & \overline{Q}_{26}^{"} \end{pmatrix} * z^{"}.dz^{"}\right\} * \begin{pmatrix} \kappa_x \\ \kappa_y \\ \kappa_{xy} \end{pmatrix}$$
$$- \left\{\sum_{k=1}^{n}\int_{z_k}^{z_{k-1}} \begin{pmatrix} \overline{Q}_{12}^{"} & \overline{Q}_{22}^{"} & \overline{Q}_{26}^{"} \end{pmatrix} * \begin{pmatrix} \alpha_x \\ \alpha_y \\ \alpha_{xy} \end{pmatrix} * dz^{"}\right\} * \Delta T - \left\{\sum_{k=1}^{n}\int_{z_k}^{z_{k-1}} \begin{pmatrix} \overline{Q}_{12}^{"} & \overline{Q}_{22}^{"} & \overline{Q}_{26}^{"} \end{pmatrix} * \begin{pmatrix} \alpha_x \\ \alpha_y \\ \alpha_{xy} \end{pmatrix} * dz^{"}\right\} * \Delta C$$

(4.12)

$$N_{xy}^{"} = \left\{\sum_{k=1}^{n}\int_{z_k}^{z_{k-1}} \begin{pmatrix} \overline{Q}_{16}^{"} & \overline{Q}_{26}^{"} & \overline{Q}_{66}^{"} \end{pmatrix} * \left(1+\frac{z^{"}}{R_m}\right) dz^{"}\right\} * \begin{pmatrix} \varepsilon_x^o \\ \varepsilon_y^o \\ \gamma_{xy}^o \end{pmatrix} + \left\{\sum_{k=1}^{n}\int_{z_k}^{z_{k-1}} \begin{pmatrix} \overline{Q}_{16}^{"} & \overline{Q}_{26}^{"} & \overline{Q}_{66}^{"} \end{pmatrix} * \left(1+\frac{z^{"}}{R_m}\right) z^{"}.dz^{"}\right\} * \begin{pmatrix} \kappa_x \\ \kappa_y \\ \kappa_{xy} \end{pmatrix}$$
$$- \left\{\sum_{k=1}^{n}\int_{z_k}^{z_{k-1}} \begin{pmatrix} \overline{Q}_{16}^{"} & \overline{Q}_{26}^{"} & \overline{Q}_{66}^{"} \end{pmatrix} * \begin{pmatrix} \alpha_x \\ \alpha_y \\ \alpha_{xy} \end{pmatrix} * \left(1+\frac{z^{"}}{R_m}\right) dz^{"}\right\} * \Delta T - \left\{\sum_{k=1}^{n}\int_{z_k}^{z_{k-1}} \begin{pmatrix} \overline{Q}_{16}^{"} & \overline{Q}_{26}^{"} & \overline{Q}_{66}^{"} \end{pmatrix} * \begin{pmatrix} \alpha_x \\ \alpha_y \\ \alpha_{xy} \end{pmatrix} * \left(1+\frac{z^{"}}{R_m}\right) dz^{"}\right\} * \Delta C$$

(4.13)

$$M_x^{"} = \left\{\sum_{k=1}^{n}\int_{z_k}^{z_{k-1}} \begin{pmatrix} \overline{Q}_{11}^{"} & \overline{Q}_{12}^{"} & \overline{Q}_{16}^{"} \end{pmatrix} * \left(1+\frac{z^{"}}{R_m}\right) .z^{"} dz^{"}\right\} * \begin{pmatrix} \varepsilon_x^o \\ \varepsilon_y^o \\ \gamma_{xy}^o \end{pmatrix} + \left\{\sum_{k=1}^{n}\int_{z_k}^{z_{k-1}} \begin{pmatrix} \overline{Q}_{11}^{"} & \overline{Q}_{12}^{"} & \overline{Q}_{16}^{"} \end{pmatrix} * \left(1+\frac{z^{"}}{R_m}\right) * z^{"2}.dz^{"}\right\} * \begin{pmatrix} \kappa_x \\ \kappa_y \\ \kappa_{xy} \end{pmatrix}$$
$$- \left\{\sum_{k=1}^{n}\int_{z_k}^{z_{k-1}} \begin{pmatrix} \overline{Q}_{11}^{"} & \overline{Q}_{12}^{"} & \overline{Q}_{16}^{"} \end{pmatrix} * \begin{pmatrix} \alpha_x \\ \alpha_y \\ \alpha_{xy} \end{pmatrix} * \left(1+\frac{z^{"}}{R_m}\right) z^{"} dz^{"}\right\} * \Delta T - \left\{\sum_{k=1}^{n}\int_{z_k}^{z_{k-1}} \begin{pmatrix} \overline{Q}_{11}^{"} & \overline{Q}_{12}^{"} & \overline{Q}_{16}^{"} \end{pmatrix} * \begin{pmatrix} \alpha_x \\ \alpha_y \\ \alpha_{xy} \end{pmatrix} * \left(1+\frac{z^{"}}{R_m}\right) z^{"} dz^{"}\right\} * \Delta C$$

(4.14)

$$M_y^{"} = \left\{ \sum_{k=1}^{n} \int_{z_k}^{z_{k-1}} \begin{pmatrix} \overline{Q}_{12}^{"} & \overline{Q}_{22}^{"} & \overline{Q}_{26}^{"} \end{pmatrix} * z^{"} dz^{"} \right\} * \begin{pmatrix} \varepsilon_x^o \\ \varepsilon_y^o \\ \gamma_{xy}^o \end{pmatrix} + \left\{ \sum_{k=1}^{n} \int_{z_k}^{z_{k-1}} \begin{pmatrix} \overline{Q}_{12}^{"} & \overline{Q}_{22}^{"} & \overline{Q}_{26}^{"} \end{pmatrix} * z^{"2} . dz^{"} \right\} * \begin{pmatrix} \kappa_x \\ \kappa_y \\ \kappa_{xy} \end{pmatrix}$$

$$- \left\{ \sum_{k=1}^{n} \int_{z_k}^{z_{k-1}} \begin{pmatrix} \overline{Q}_{12}^{"} & \overline{Q}_{22}^{"} & \overline{Q}_{26}^{"} \end{pmatrix} * \begin{pmatrix} \alpha_x \\ \alpha_y \\ \alpha_{xy} \end{pmatrix} * z^{"} dz^{"} \right\} * \Delta T - \left\{ \sum_{k=1}^{n} \int_{z_k}^{z_{k-1}} \begin{pmatrix} \overline{Q}_{12}^{"} & \overline{Q}_{22}^{"} & \overline{Q}_{26}^{"} \end{pmatrix} * \begin{pmatrix} \alpha_x \\ \alpha_y \\ \alpha_{xy} \end{pmatrix} * z^{"} dz^{"} \right\} * \Delta C$$

(4.15)

$$M_{xy}^{"} = \left\{ \sum_{k=1}^{n} \int_{z_k}^{z_{k-1}} \begin{pmatrix} \overline{Q}_{16}^{"} & \overline{Q}_{26}^{"} & \overline{Q}_{66}^{"} \end{pmatrix} * \left(1 + \frac{z^{"}}{R_m} \right) z^{"} dz^{"} \right\} * \begin{pmatrix} \varepsilon_x^o \\ \varepsilon_y^o \\ \gamma_{xy}^o \end{pmatrix} + \left\{ \sum_{k=1}^{n} \int_{z_k}^{z_{k-1}} \begin{pmatrix} \overline{Q}_{16}^{"} & \overline{Q}_{26}^{"} & \overline{Q}_{66}^{"} \end{pmatrix} * \left(1 + \frac{z^{"}}{R_m} \right) z^{"2} . dz^{"} \right\} * \begin{pmatrix} \kappa_x \\ \kappa_y \\ \kappa_{xy} \end{pmatrix}$$

$$- \left\{ \sum_{k=1}^{n} \int_{z_k}^{z_{k-1}} \begin{pmatrix} \overline{Q}_{16}^{"} & \overline{Q}_{26}^{"} & \overline{Q}_{66}^{"} \end{pmatrix} * \begin{pmatrix} \alpha_x \\ \alpha_y \\ \alpha_{xy} \end{pmatrix} * \left(1 + \frac{z^{"}}{R_m} \right) z^{"} dz^{"} \right\} * \Delta T - \left\{ \sum_{k=1}^{n} \int_{z_k}^{z_{k-1}} \begin{pmatrix} \overline{Q}_{16}^{"} & \overline{Q}_{26}^{"} & \overline{Q}_{66}^{"} \end{pmatrix} * \begin{pmatrix} \alpha_x \\ \alpha_y \\ \alpha_{xy} \end{pmatrix} * \left(1 + \frac{z^{"}}{R_m} \right) z^{"} dz^{"} \right\} * \Delta C$$

(4.16)

$$N_{yx}^{"} = \left\{ \sum_{k=1}^{n} \int_{z_k}^{z_{k-1}} \begin{pmatrix} \overline{Q}_{16}^{"} & \overline{Q}_{26}^{"} & \overline{Q}_{66}^{"} \end{pmatrix} * dz^{"} \right\} * \begin{pmatrix} \varepsilon_x^o \\ \varepsilon_y^o \\ \gamma_{xy}^o \end{pmatrix} + \left\{ \sum_{k=1}^{n} \int_{z_k}^{z_{k-1}} \begin{pmatrix} \overline{Q}_{16}^{"} & \overline{Q}_{26}^{"} & \overline{Q}_{66}^{"} \end{pmatrix} * z^{"} . dz^{"} \right\} * \begin{pmatrix} \kappa_x \\ \kappa_y \\ \kappa_{xy} \end{pmatrix}$$

$$- \left\{ \sum_{k=1}^{n} \int_{z_k}^{z_{k-1}} \begin{pmatrix} \overline{Q}_{16}^{"} & \overline{Q}_{26}^{"} & \overline{Q}_{66}^{"} \end{pmatrix} * \begin{pmatrix} \alpha_x \\ \alpha_y \\ \alpha_{xy} \end{pmatrix} * dz^{"} \right\} * \Delta T - \left\{ \sum_{k=1}^{n} \int_{z_k}^{z_{k-1}} \begin{pmatrix} \overline{Q}_{16}^{"} & \overline{Q}_{26}^{"} & \overline{Q}_{66}^{"} \end{pmatrix} * \begin{pmatrix} \alpha_x \\ \alpha_y \\ \alpha_{xy} \end{pmatrix} * dz^{"} \right\} * \Delta C$$

(4.17)

$$M_{yx}^{"} = \left\{ \sum_{k=1}^{n} \int_{z_k}^{z_{k-1}} \begin{pmatrix} \overline{Q}_{16}^{"} & \overline{Q}_{26}^{"} & \overline{Q}_{66}^{"} \end{pmatrix} * z^{"} dz^{"} \right\} * \begin{pmatrix} \varepsilon_x^o \\ \varepsilon_y^o \\ \gamma_{xy}^o \end{pmatrix} + \left\{ \sum_{k=1}^{n} \int_{z_k}^{z_{k-1}} \begin{pmatrix} \overline{Q}_{16}^{"} & \overline{Q}_{26}^{"} & \overline{Q}_{66}^{"} \end{pmatrix} * z^{"2} . dz^{"} \right\} * \begin{pmatrix} \kappa_x \\ \kappa_y \\ \kappa_{xy} \end{pmatrix}$$

$$- \left\{ \sum_{k=1}^{n} \int_{z_k}^{z_{k-1}} \begin{pmatrix} \overline{Q}_{16}^{"} & \overline{Q}_{26}^{"} & \overline{Q}_{66}^{"} \end{pmatrix} * \begin{pmatrix} \alpha_x \\ \alpha_y \\ \alpha_{xy} \end{pmatrix} * z^{"} dz^{"} \right\} * \Delta T - \left\{ \sum_{k=1}^{n} \int_{z_k}^{z_{k-1}} \begin{pmatrix} \overline{Q}_{16}^{"} & \overline{Q}_{26}^{"} & \overline{Q}_{66}^{"} \end{pmatrix} * \begin{pmatrix} \alpha_x \\ \alpha_y \\ \alpha_{xy} \end{pmatrix} * z^{"} dz^{"} \right\} * \Delta C$$

(4.18)

In view of Eqns. (4.11) through (4.18), each of the resultant load and moment expressions can be integrated and expanded to arrive at the following analytical expressions given by:

$$\begin{pmatrix} N_x'' \\ N_y'' \\ N_{xy}'' \\ N_{yx}'' \end{pmatrix} = \begin{bmatrix} A_{11}+\frac{B_{11}}{R_m} & A_{12}+\frac{B_{12}}{R_m} & A_{16}+\frac{B_{16}}{R_m} \\ A_{12} & A_{22} & A_{26} \\ A_{16}+\frac{B_{16}}{R_m} & A_{26}+\frac{B_{26}}{R_m} & A_{66}+\frac{B_{66}}{R_m} \\ A_{16} & A_{26} & A_{66} \end{bmatrix} * \begin{pmatrix} \varepsilon_x^o \\ \varepsilon_y^o \\ \gamma_{xy}^o \end{pmatrix} + \begin{bmatrix} B_{11}+\frac{D_{11}}{R_m} & B_{12}+\frac{D_{12}}{R_m} & B_{16}+\frac{D_{16}}{R_m} \\ B_{12} & B_{22} & B_{26} \\ B_{16}+\frac{D_{16}}{R_m} & B_{26}+\frac{D_{26}}{R_m} & B_{66}+\frac{D_{66}}{R_m} \\ B_{16} & B_{26} & B_{66} \end{bmatrix} * \begin{pmatrix} \kappa_x \\ \kappa_y \\ \kappa_{xy} \end{pmatrix}$$
$$- \begin{pmatrix} N_x^{T''}+N_x^{H''}+\frac{M_x^{T''}}{R_m}+\frac{M_x^{H''}}{R_m} \\ N_y^{T''}+N_y^{H''} \\ N_{xy}^{T''}+N_{xy}^{H''}+\frac{M_{xy}^{T''}}{R_m}+\frac{M_{xy}^{H''}}{R_m} \\ N_{yx}^{T''}+N_{yx}^{H''} \end{pmatrix} \tag{4.19}$$

$$\begin{pmatrix} M_x'' \\ M_y'' \\ M_{xy}'' \\ M_{yx}'' \end{pmatrix} = \begin{bmatrix} B_{11}+\frac{D_{11}}{R_m} & B_{12}+\frac{D_{12}}{R_m} & B_{16}+\frac{D_{16}}{R_m} \\ B_{12} & B_{22} & B_{26} \\ B_{16}+\frac{D_{16}}{R_m} & B_{26}+\frac{D_{26}}{R_m} & B_{66}+\frac{D_{66}}{R_m} \\ B_{16} & B_{26} & B_{66} \end{bmatrix} * \begin{pmatrix} \varepsilon_x^o \\ \varepsilon_y^o \\ \gamma_{xy}^o \end{pmatrix} + \begin{bmatrix} D_{11}+\frac{E_{11}}{R_m} & D_{12}+\frac{E_{12}}{R_m} & D_{16}+\frac{E_{16}}{R_m} \\ D_{12} & D_{22} & D_{26} \\ D_{16}+\frac{E_{16}}{R_m} & D_{26}+\frac{E_{26}}{R_m} & D_{66}+\frac{E_{66}}{R_m} \\ D_{16} & D_{26} & D_{66} \end{bmatrix} * \begin{pmatrix} \kappa_x \\ \kappa_y \\ \kappa_{xy} \end{pmatrix}$$
$$\begin{pmatrix} M_x^{T''}+M_x^{H''}+L_x^{T''}+L_x^{H''} \\ M_y^{T''}+M_y^{H''} \\ M_{xy}^{T''}+M_{xy}^{H''}+L_{xy}^{T''}+L_{xy}^{T''} \\ M_{yx}^{T''}+M_{yx}^{H''} \end{pmatrix} \tag{4.20}$$

Eq. 4.19 denotes the resultant force-deformation relations for a differential tube element in full form and Eq. 4.20 denotes the resultant moment-deformation relations for a differential tube element in full form respectively. The generalized expressions for the averaged elastic parameters comprising the multi-directional, tubular composite laminate are given by:

$$\left[A_{ij}\right] = \sum_{k=1}^{n} \int_{z_{k-1}}^{z_k} [\overline{Q}_{ij}]_k \, dz'' = \sum_{k=1}^{n} [\overline{Q}_{ij}]_k * (z_k'' - z_{k-1}'')$$

$$\left[B_{ij}\right] = \sum_{k=1}^{n} \int_{z_{k-1}}^{z_k} [\overline{Q}_{ij}]_k z'' \, dz'' = \frac{1}{2} * \sum_{k=1}^{n} [\overline{Q}_{ij}]_k * (z_k''^2 - z_{k-1}''^2) \tag{4.21}$$

$$\left[D_{ij}\right] = \sum_{k=1}^{n} \int_{z_{k-1}}^{z_k} [\overline{Q}_{ij}]_k z''^2 \, dz'' = \frac{1}{3} * \sum_{k=1}^{n} [\overline{Q}_{ij}]_k * (z_k''^3 - z_{k-1}''^3)$$

$$\left[E_{ij}\right] = \sum_{k=1}^{n} \int_{z_{k-1}}^{z_k} [\overline{Q}_{ij}]_k z''^3 \, dz'' = \frac{1}{4} * \sum_{k=1}^{n} [\overline{Q}_{ij}]_k * (z_k''^4 - z_{k-1}''^4)$$

These elastic parameters physically signify and represent the mechanical characteristics of a multidirectional composite tube by emerging as critically dependent functions of the tube's mean radius of curvature, rotation angle θ and fiber orientation angle β in addition to the basic structural geometry, material properties and stacking sequence of the individual plies. These newly derived expressions can further be combined into one expression explicitly relating the in-plane mechanical forces and moments and thermally induced forces and moments to reference plane strains and curvatures.

Eq. (4.22) represents the constitutive equation for a multidirectional, thin-walled, closed cross-section, composite tube. Influence of curvature factor is noticeable on each of the formulated elemental stiffness matrix components. Hygrothermal strains induce thermal loading and moments, which add upon mechanical load terms. Fundamentally, when the infinitesimal composite tube element is assumed to be subjected to thermal and moisture loadings, hygrothermal forces and moments are induced due to the increased cross-sectional area present above the circumferential mid-plane of the composite tube. Furthermore, these additional hygrothermal load and moment terms are influenced by the presence of shell curvature-factor $\left(1 + \frac{z''}{R_m}\right)$. Newly developed stiffnesses, hygrothermally

induced longitudinal and shear stress resultants are highlighted in red respectively (Eq. 4.19, Eq. 4.20 and Eq. 4.22).

$$\begin{pmatrix} N_x' + N_x^{T'} + N_x^{H'} + \frac{M_x^{T'}}{R_m} + \frac{M_x^{H'}}{R_m} \\ N_y' + N_y^{T'} + N_y^{H'} \\ N_{xy}' + N_{xy}^{T'} + N_{xy}^{H'} + \frac{M_{xy}^{T'}}{R_m} + \frac{M_{xy}^{H'}}{R_m} \\ M_x' + M_x^{T'} + M_x^{H'} + L_x^{T'} + L_x^{H'} \\ M_y' + M_y^{T'} + M_y^{H'} \\ M_{xy}' + M_{xy}^{T'} + M_{xy}^{H'} + L_{xy}^{T'} + L_{xy}^{H'} \\ N_{yx}' + N_{yx}^{T'} + N_{yx}^{H'} \\ M_{yx}' + M_{yx}^{T'} + M_{yx}^{H'} \end{pmatrix} = \begin{bmatrix} A_{11} + \frac{B_{11}}{R_m} & A_{12} + \frac{B_{12}}{R_m} & A_{16} + \frac{B_{16}}{R_m} & B_{11} + \frac{D_{11}}{R_m} & B_{12} + \frac{D_{12}}{R_m} & B_{16} + \frac{D_{16}}{R_m} \\ A_{12} & A_{22} & A_{26} & B_{12} & B_{22} & B_{26} \\ A_{16} + \frac{B_{16}}{R_m} & A_{26} + \frac{B_{26}}{R_m} & A_{66} + \frac{B_{66}}{R_m} & B_{16} + \frac{D_{16}}{R_m} & B_{26} + \frac{D_{26}}{R_m} & B_{66} + \frac{D_{66}}{R_m} \\ B_{11} + \frac{D_{11}}{R_m} & B_{12} + \frac{D_{12}}{R_m} & B_{16} + \frac{D_{16}}{R_m} & D_{11} + \frac{E_{11}}{R_m} & D_{12} + \frac{E_{12}}{R_m} & D_{16} + \frac{E_{16}}{R_m} \\ B_{12} & B_{22} & B_{26} & D_{12} & D_{22} & D_{26} \\ B_{16} + \frac{D_{16}}{R_m} & B_{26} + \frac{D_{26}}{R_m} & B_{66} + \frac{D_{66}}{R_m} & D_{16} + \frac{E_{16}}{R_m} & D_{26} + \frac{E_{26}}{R_m} & D_{66} + \frac{E_{66}}{R_m} \\ A_{16} & A_{26} & A_{66} & B_{16} & B_{26} & B_{66} \\ B_{16} & B_{26} & B_{66} & D_{16} & D_{26} & D_{66} \end{bmatrix} * \begin{pmatrix} \varepsilon_x^0 \\ \varepsilon_y^0 \\ \gamma_{xy}^0 \\ \kappa_x \\ \kappa_y \\ \kappa_{xy} \end{pmatrix}$$

(4.22)

For gaining a broad physical understanding, each of the highlighted load resultants denoted by $\frac{M_x^{T''}}{R_m}, \frac{M_x^{H''}}{R_m}, \frac{M_{xy}^{T''}}{R_m}, \frac{M_{xy}^{H''}}{R_m}, L_x^{T''}, L_x^{H''}, L_{xy}^{T''}$ and $L_{xy}^{H''}$ are expanded and represented in Eqns. (4.23) through (4.30) respectively. Symmetry of the individual stiffness matrix components becomes vanished upon the introduction of curvature effect. Upon gradually increasing the value of tube mean-radius R towards infinity, stiffness matrix of the thin-walled laminated composite shell element gets reduced to the typical composite plate element stiffness equation.

$$\frac{M_x^{T'}}{R_m} = \frac{1}{2R_m} * \left\{ \sum_{k=1}^{n} \begin{pmatrix} \bar{Q}_{11}''(z^2{}_k - z^2{}_{k-1}) & \bar{Q}_{12}''(z^2{}_k - z^2{}_{k-1}) & \bar{Q}_{16}''(z^2{}_k - z^2{}_{k-1}) \end{pmatrix} * \begin{pmatrix} \alpha_x \\ \alpha_y \\ \alpha_{xy} \end{pmatrix} \right\} * \Delta T$$

$$\frac{M_x^{H'}}{R} = \frac{1}{2R_m} * \left\{ \sum_{k=1}^{n} \begin{pmatrix} \bar{Q}_{11}''(z^2{}_k - z^2{}_{k-1}) & \bar{Q}_{12}''(z^2{}_k - z^2{}_{k-1}) & \bar{Q}_{16}''(z^2{}_k - z^2{}_{k-1}) \end{pmatrix} * \begin{pmatrix} \beta_x \\ \beta_y \\ \beta_{xy} \end{pmatrix} \right\} * \Delta C$$

(4.23-4.24)

$$\frac{M_{xy}^{T}}{R_m} = \frac{1}{2R_m} * \left\{ \sum_{k=1}^{n} \left(\bar{Q}_{16}^{"}(z^2{}_k - z^2{}_{k-1}) \quad \bar{Q}_{26}^{"}(z^2{}_k - z^2{}_{k-1}) \quad \bar{Q}_{66}^{"}(z^2{}_k - z^2{}_{k-1}) \right) * \begin{pmatrix} \alpha_x \\ \alpha_y \\ \alpha_{xy} \end{pmatrix} \right\} * \Delta T$$

$$\frac{M_{xy}^{H}}{R_m} = \frac{1}{2R_m} * \left\{ \sum_{k=1}^{n} \left(\bar{Q}_{16}^{"}(z^2{}_k - z^2{}_{k-1}) \quad \bar{Q}_{26}^{"}(z^2{}_k - z^2{}_{k-1}) \quad \bar{Q}_{66}^{"}(z^2{}_k - z^2{}_{k-1}) \right) * \begin{pmatrix} \beta_x \\ \beta_y \\ \beta_{xy} \end{pmatrix} \right\} * \Delta C$$

(4.25-4.26)

$$L_x^{T} = \frac{1}{3R_m} * \left\{ \sum_{k=1}^{n} \left(\bar{Q}_{11}^{"}(z^3{}_k - z^3{}_{k-1}) \quad \bar{Q}_{12}^{"}(z^3{}_k - z^3{}_{k-1}) \quad \bar{Q}_{16}^{"}(z^3{}_k - z^3{}_{k-1}) \right) * \begin{pmatrix} \alpha_x \\ \alpha_y \\ \alpha_{xy} \end{pmatrix} \right\} * \Delta T$$

$$L_x^{H} = \frac{1}{3R_m} * \left\{ \sum_{k=1}^{n} \left(\bar{Q}_{11}^{"}(z^3{}_k - z^3{}_{k-1}) \quad \bar{Q}_{12}^{"}(z^3{}_k - z^3{}_{k-1}) \quad \bar{Q}_{16}^{"}(z^3{}_k - z^3{}_{k-1}) \right) * \begin{pmatrix} \beta_x \\ \beta_y \\ \beta_{xy} \end{pmatrix} \right\} * \Delta C$$

(4.27-4.28)

$$L_{xy}^{T} = \frac{1}{3R_m} * \left\{ \sum_{k=1}^{n} \left(\bar{Q}_{16}^{"}(z^3{}_k - z^3{}_{k-1}) \quad \bar{Q}_{26}^{"}(z^3{}_k - z^3{}_{k-1}) \quad \bar{Q}_{66}^{"}(z^3{}_k - z^3{}_{k-1}) \right) * \begin{pmatrix} \alpha_x \\ \alpha_y \\ \alpha_{xy} \end{pmatrix} \right\} * \Delta T$$

$$L_{xy}^{H} = \frac{1}{3R_m} * \left\{ \sum_{k=1}^{n} \left(\bar{Q}_{16}^{"}(z^3{}_k - z^3{}_{k-1}) \quad \bar{Q}_{26}^{"}(z^3{}_k - z^3{}_{k-1}) \quad \bar{Q}_{66}^{"}(z^3{}_k - z^3{}_{k-1}) \right) * \begin{pmatrix} \beta_x \\ \beta_y \\ \beta_{xy} \end{pmatrix} \right\} * \Delta C$$

(4.29-4.30)

Translation of the elemental stiffness matrices (Eq. 4.21) to the global coordinate system is conducted by implementing parallel-axes theorem concepts and is given by

$$\left[\hat{A}\right] = \left[A\right]$$

$$\left[\hat{B}\right] = \left[B\right] + R_m * \cos\theta * \left[A\right] \tag{4.31}$$

$$\left[\hat{D}\right] = \left[D\right] + 2 * (R_m * \cos\theta) * \left[B\right] + (R_m * \cos\theta)^2 * \left[A\right]$$

$$\left[\hat{E}\right] = \left[E\right] + 3 * (R_{mm} * \cos\theta) * \left[D\right] + 3 * (R_m * \cos\theta)^2 * \left[B\right] + (R_m * \cos\theta)^3 * \left[A\right]$$

where $\left[\hat{A}\right],\left[\hat{B}\right],\left[\hat{D}\right]$ and $\left[\hat{E}\right]$ are the translated elemental stiffness matrices per width for the differential tube element respectively. Each of the stiffness terms on the right–hand side of Eqn. (4.22) constitutes a 3*3 matrix, that is extracted from Eqn. (4.21). Global stiffness matrices for the entire laminated composite tube cross-section incorporating the curvature factor is obtained by performing an integration of the elastic stiffness constituents for the infinitesimal element over the entire circumference of the tube $(0$ to $2\pi)$, as shown in Eqn. (4.32)

$$\left[\overline{A}\right]=\int_0^{2\pi}\left[\hat{A}\right]*R_m d\theta=\int_0^{2\pi}\left[A\right]*R_m d\theta$$

$$\left[\overline{B}\right]=\int_0^{2\pi}\left[\hat{B}\right]*R_m d\theta=\int_0^{2\pi}\left(\left[B\right]+R_m*\mathrm{Cos}\theta*\left[A\right]\right)*R_m d\theta \tag{4.32}$$

$$\left[\overline{D}\right]=\int_0^{2\pi}\left[\hat{D}\right]*R_m d\theta=\int_0^{2\pi}\left(\left[D\right]+2*(R_m\mathrm{Cos}\theta)*\left[B\right]+(R_m\mathrm{Cos}\theta)^2*\left[A\right]\right)*R_m d\theta$$

$$\left[\overline{E}\right]=\int_0^{2\pi}\left[\hat{E}\right]*R_m d\theta=\int_0^{2\pi}\left(\left[E\right]+3*(R_m\mathrm{Cos}\theta)*[D]+3*(R_m\mathrm{Cos}\theta)^2*\left[B\right]+(R_m\mathrm{Cos}\theta)^3*\left[A\right]\right)*R_m d\theta$$

Upon observing the formulated global stiffness matrix terms (Eq. 4.25), it is indicative that they are primarily dependent on the element rotation angle and fiber orientation angles. Since multidirectional laminates such as the cylindrical composite tube configuration are typically charecterized by stress discontinuities from ply to ply, it is preferable to work with surface strains, which are continuous through the thickness. For this reason, inversion of the load-deformation and moment deformation relations indicated in Eqns. (4.19 and 4.20) yields the following relation.

$$\left\{\begin{array}{c}\overline{N}\\ \overline{M}\end{array}\right\}_{6*1}=\left[\begin{array}{cc}\overline{A} & \overline{B}\\ \overline{B} & \overline{D}\end{array}\right]_{6*6}*\left\{\begin{array}{c}\varepsilon^o_{x,y}\\ \kappa_{x,y}\end{array}\right\}_{6*1} \tag{4.33}$$

$$\begin{Bmatrix} \varepsilon_0'' \\ \kappa_0'' \end{Bmatrix}_{6*1} = \begin{pmatrix} \bar{a} & \bar{b} \\ \bar{b}^T & \bar{d} \end{pmatrix}_{6*6} * \begin{Bmatrix} \bar{N} \\ \bar{M} \end{Bmatrix}_{6*1} \tag{4.34}$$

where $\left[\bar{a}\right]$, $\left[\bar{b}\right]$ and $\left[\bar{d}\right]$ are the global laminate compliance matrices associated with a thin-walled cylindrical composite tube, obtained by a direct inversion of the 6*6 global stiffness matrices $\left[\bar{A}\right]$, $\left[\bar{B}\right]$ and $\left[\bar{D}\right]$ matrices respectively. The equivalent axial and bending stiffness of the laminated composite tube utilizing a thin-walled Laminated Composite Shell Theory approach is given by

$$\bar{A}_x = \frac{1}{\bar{a}_{11}} \text{ and } \bar{D}_x = \frac{1}{\bar{d}_{11}} \tag{4.35}$$

where $\bar{a}_{11}$ is the (1,1) term and $\bar{d}_{11}$ is the (4,4) element term obtained from the global $\begin{bmatrix} \bar{A}_{3*3} & \bar{B}_{3*3} \\ \bar{B}_{3*3} & \bar{D}_{3*3} \end{bmatrix}$ matrix inversion. In essence, the constitutive relationship generated for the laminated composite tube entails the effects of shell curvature factor and influence of thermal & moisture concentrations across the entire volume and can be effectively utilized to conduct a geometrically linear hygrothermoelastic analyses. The formulated mathematical model primarily seeks to obtain approximate (not exact) yet accurate closed-form solutions thus offering the potential to deliver a broad-spectrum understanding on the physical response of thin-walled closed cross section composite tube configurations.

4-2 Finite Element Modeling of Cylindrical Composite Tubes

An ANSYS based geometrically linear FEA approach [12] has been used to computationally model and simulate the structural response of a thin-walled, multidirectional laminated composite tube configuration. Building upon the model,

equivalent axial and bending stiffness are numerically computed and the variation of longitudinal stresses along the circumferential contour induced by an applied bending moment is investigated. A six ply symmetric-balanced configuration with a $\left[\pm 45/0\right]_s$ laminate stacking sequence is assumed. Table 1 lists the composite material properties of IM6/3501-6 graphite-epoxy system [13]. A constant length of 10 inches and a uniform cross-sectional thickness of the tube are assumed throughout the analysis. Composite tube mean-radius R_m is varied incrementally in steps of 0.2 inch from 0.1 inch to 2.5 inches respectively. The tube cross section is assumed to have a constant Poisson's ratio of 0.329.

Table 4-1 Mechanical Properties for IM6-3501-6 Composite Material System

Property	Value
E_{11}	$24.8*10^{6}$ psi
E_{22}	$1.41*10^{6}$ psi
υ_{12}	0.329
G_{12}	$0.9*10^{6}$ psi
t_{ply}	0.0052 inches
α_1	$-0.5*10^{-6}$ in/in/ ^{o}F
α_2	$15*10^{-6}$ in/in/ ^{o}F

The subsequent paragraphs discusses the structural modeling aspects of a multidirectional composite tube design. Figure 4-3 illustrates the discretization of the tube structure performed utilizing a 8-noded structural shell labelled as SHELL 281 [12]. The core purpose behind adopting this element is due to its superior adaptability demonstrated towards analyzing thin to moderately-thick composite shell structures. This element basically consists of eight nodes that define its geometry and curvature. Each node provides six degrees of freedom; three translations in the x, y and z axes, and rotations about the x, y and z axes.

SHELL 281 is well-suited for conducting geometrically linear, large-rotation and/or large strain based analyses. Their accuracy in computationally designing layered composite shells is governed by the first order shear deformation theory. Additionally this shell element possesses the capability to characterize structural behavior influenced by the presence of transverse shear deformations and interlaminar shear stresses located at inter-ply boundaries. SHELL281 can be additionally associated with elastoplastic, creep, or hyperelastic material properties. This element works best with full Newton-Raphson solution scheme. Stress stiffening can further be included for conducting several geometrically nonlinear analyses by invoking the “Non-linear-geometry” feature in its element structural tree.

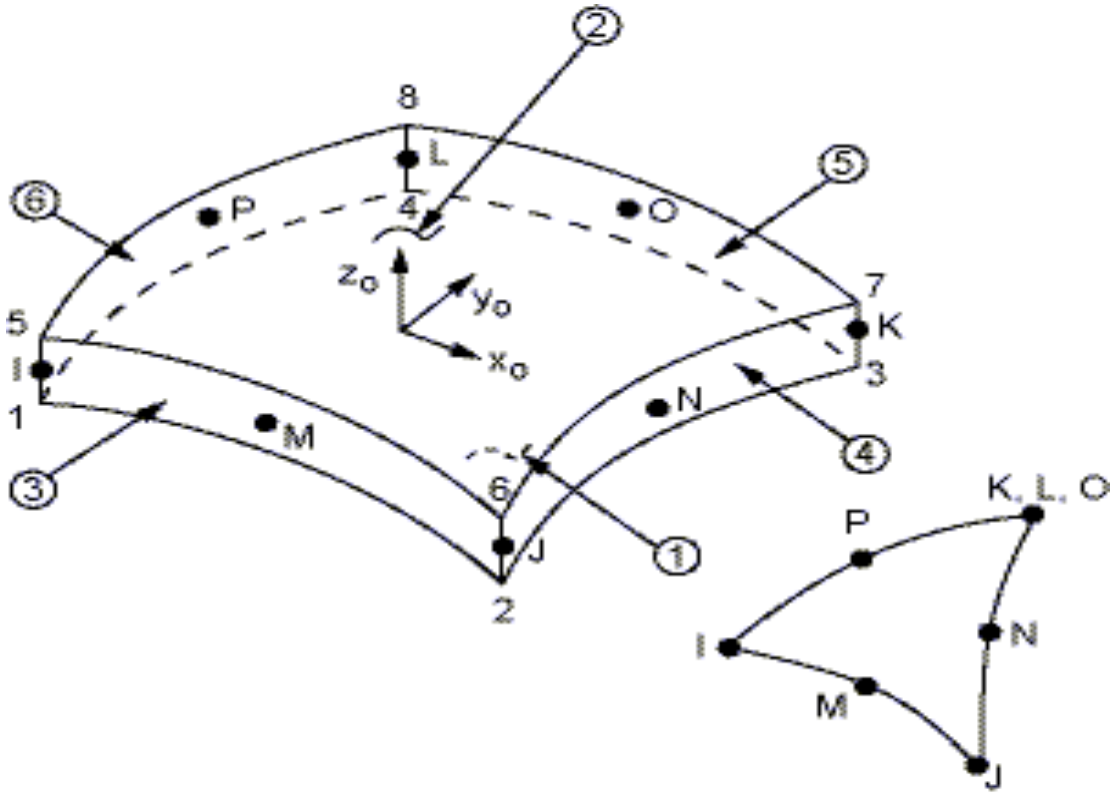

Figure 4-3 SHELL-281 Element Schematic and Nodal Structure [12]

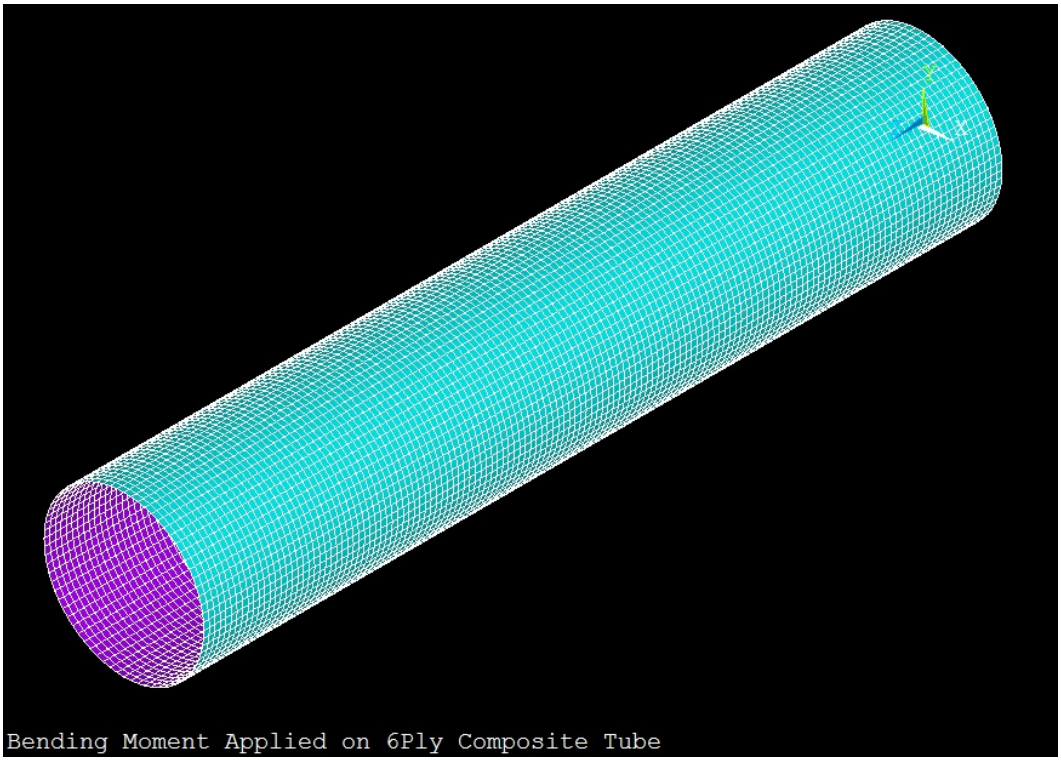

Figure 4-4 Discretized Model of Composite Tube

The assumed composite ply lay-up and stacking sequence are designated to the solid model. A global mesh density in the order of 198620 elements (Fig. 4-4) is established based on a mesh-convergence study to execute a linearly-static finite element analysis. Furthermore, much attention has been devoted towards preserving an appreciable aspect-ratio (<100 in terms of the ratio of maximum to minimum integration point surface areas in all elements adjacent to a node). A cantilevered bar type configuration is simulated on the FE platform via creating a solid model of a thin-walled composite tube, restricting all degrees-of-freedom along the circumferential nodes defining the left edge and eventually applying concentrated loadings (force and moment) on the free edge (Fig. 4-5).

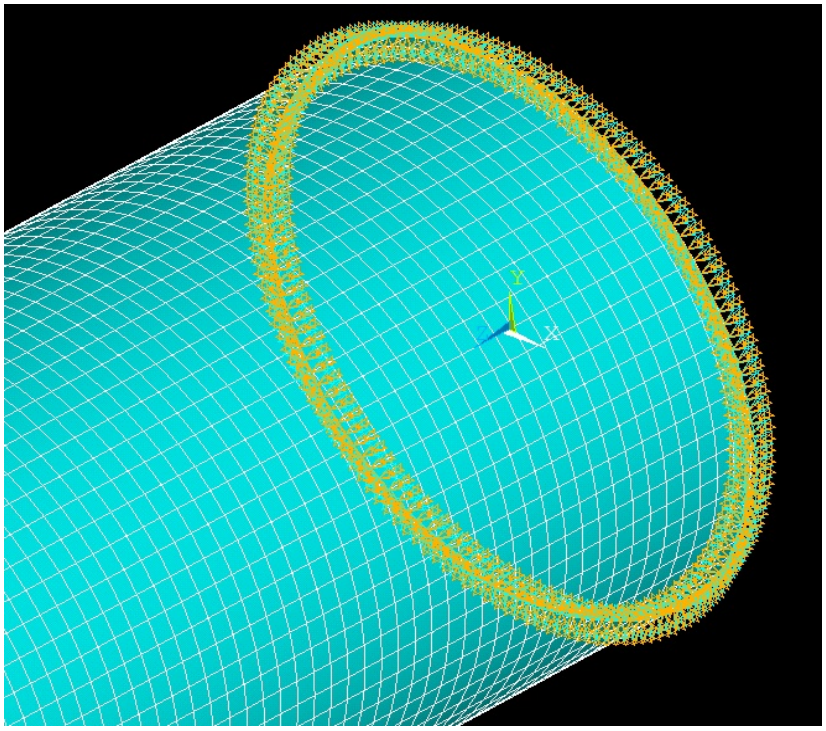

Figure 4-5 Cantilevered Bar Type Simulation

Fundamentally, in order to ensure uniform longitudinal cross-sectional deformation along x'-axis under the influence of a finite tension loading applied at the centroidal point and a pure bending deformation at the free end about y'-axis (oriented along tube mean-radius) under the application of a concentrated bending moment, a multi-point constraint about the centroidal node-point is effectively generated. A concentrated axial force of 10 lbs and bending moment of 10 in-lbs are applied on/about the centroidal axis of the tube to evaluate its axial stiffness and bending stiffness properties respectively. The "multi-point constraint" feature [12] offers a vital avenue to couple the degrees of freedom of a set of nodes (slave nodes) with respect to a parent node (PILOT node). The flexibility in terms of degrees of freedom provided to the target node basically governs the mechanical response of its slave nodes.

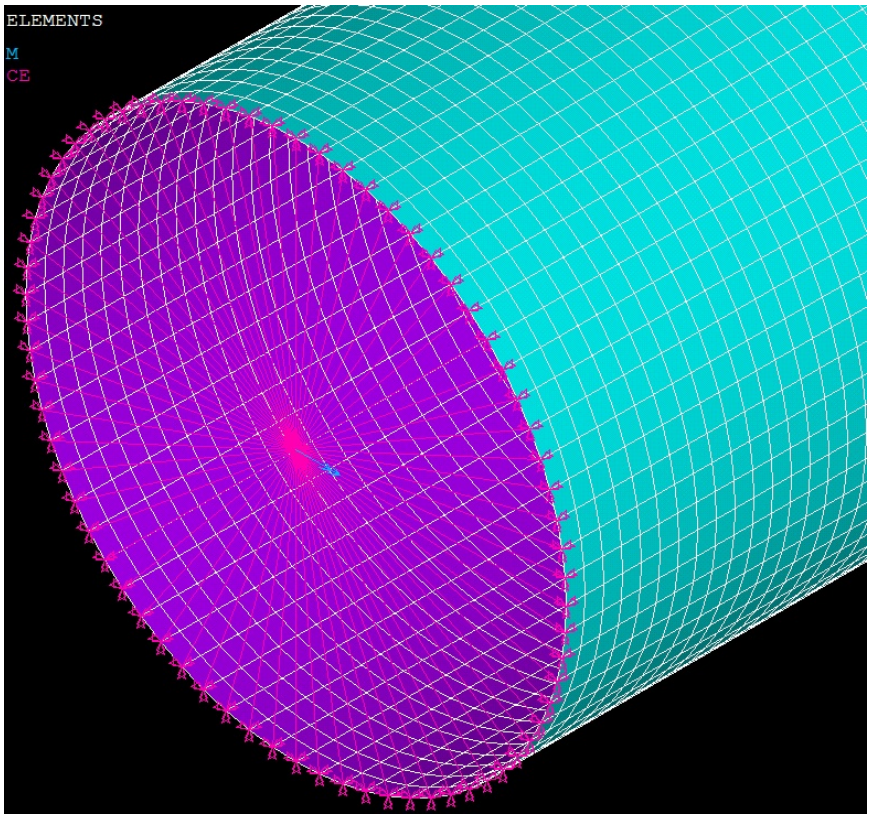

Figure 4-6 Multi-point Constraint Employed at Free Edge

Conceptually, a rigid region can be associated with areas or volumes within the constructed solid model by automatically generating constraint equations that mathematically relates nodes in the isolated region of interest. Circumferential nodes along the unconstrained free edge of the composite tube are identified before this command is implemented. Generated constraint equations are based on small deflection theory. Multiple rigid lines are created that interlink the SLAVE nodes (free-end nodes surrounding the centroidal node) to the PILOT node (centroidal node). Six equations are generated for each pair of constrained nodes in 3-D space. These equations essentially define the six rigid body motions in global cartesian space (three in-plane translations and three in-plane rotations). Influence of edge effects on nodal displacement and strain

computations are obviated by considering two cross sections located at 50% and 75% (5 in, 7.5 in) of the composite tube geometric length. Average extensional strains at nodes $\varepsilon_x^{'}$ are subsequently computed by subtracting axial displacements generated at 75%L and 50%L along the longitudinal axis of the tube and further dividing the result with the difference between the lengths of two node stations. Consequently, equivalent axial stiffness is numerically computed and can be mathematically shown as

$$\varepsilon_x^{'} = \frac{u_{75\%L} - u_{50\%L}}{2.5}$$
$$(EA)_{FEM} = P_{applied} * \varepsilon_x^{'} \tag{4.36}$$

where, u is the longitudinal displacement and P is the centroidally applied finite extensional load. The curvature induced in the presence of a centroidally concentrated bending moment is essentially required to numerically obtain the equivalent bending stiffness of the composite tubular cross-section. Curvature κ_x of deformed tube is determined by considering nodal displacements of three arbitarily selected nodal points along longtitudinal axis of the tube (Appendix A). Fundamentally utilizing simple geometry, the radius of the curve adjoining the three nodal points is computed and further the curvature of the curve is calculated by taking its inverse. Consequently, for a centroidally applied finite bending moment M, the effective bending stiffness in x-direction can be numerically computed and can be related to the induced curvature κ_x by

$$D_{xx}^{FEM} = \frac{M_{applied}}{\kappa_{x(computed)}} \tag{4.37}$$

Following section deals with evaluating the bending stiffness and axial stiffness charectersitics for closed cross-sectioned cylindrical composite tube configurations.Finite element results are used to compare with analytical results.

4-3 Stiffness Data Analysis and Result Interpretation

The validity of result data generated and recorded through FEA analyses are fundamentally investigated by initially developing an isotropic cylindrical tube configuration and comparing numerical results with analytically generated solution. Effective bending stiffness for an isotropic cylindrical tube cross-section is essentially given by

$$D_{isotropic} = (EI)_{isotropic} = E * \frac{\pi}{4} * (R_o^{\,4} - R_i^{\,4}) \tag{4.38}$$

where, E is elastic modulus, I is moment of inertia, R_o and R_i are outer and inner radii of the linearly-elastic, thin-walled, isotropic cylindrical tube respectively. Geometric properties assumed for isotropic tube cross section are shown in Table 4-2. Bending stiffnesses are compared against analytical estimations and finite element results. Acquired data are recorded and shown in Table 4-3. Equivalent Error percentage differences between the two distinct approaches are observed to fall within 1.5%. These preliminary results are able to physically demonstrate the correctness in mechanical design and modeling aspects of the FE model utilizing an isotropic material system.

Table 4-2 Assumed Geometric Properties of Isotropic Tube Cross Section

Property	Value
Elastic modulus, E	$3*10^{7}$ psi
Poisson's ratio, υ	0.3
Bending moment M (in-lbs.)	20
Tube length (in)	10
t_{ply}	0.005 inches
Tube mean-radius, R_m	Varying from 2.6" to 0.1"
Element type	SHELL 281

Further FEA is extended to a thin-walled multidirectional laminated cylindrical tube cross section characterized by material properties of a IM6/3501-6 graphite-epoxy composite material system as shown in Table 4-1.

Table 4-3 Bending Stiffness Comparison: Analytical vs. FEM (Isotropic Case)

Tube Radius (in)	Analytical EI (lb-in^2)	FEM EI (lb-in^2)	% error diff
2.6	1.31E+08	1.30E+08	0.77
2.2	7.89E+07	7.82E+07	0.89
1.8	4.27E+07	4.23E+07	0.95
1.4	1.97E+07	1.95E+07	1.03
1	6.92E+06	6.84E+06	1.14
0.8	3.43E+06	3.39E+06	1.18
0.6	1.37E+06	1.35E+06	1.22
0.4	3.66E+05	3.61E+05	1.26
0.2	3.33E+04	3.29E+04	1.33

Analytically formulated mathematical expressions (utilizing Eqs. 4.1-4.35) are solved using MATLAB to generate stiffness predictions for equivalent axial and bending stiffnesses respectively. The influence of shell curvature factor $\left(1+\frac{z''}{R_m}\right)$ while predicting equivalent axial and bending stiffnesses for a thin-walled fiber-reinforced circular composite tube cross-section is analyzed. The composite tube mean-radius of curvature R_m is parametrically varied from 2.5 inches to 0.1 inch in increments of 0.2 inches respectively. Table 4-4 illustrates the predicted comparison data for the equivalent bending stiffness results generated via utilizing the mechanics of three previously described mathematical models with respect to the computationally produced stiffness data. ANSYS based axial stiffness and bending stiffness estimations are used to compare $\left(\%\text{error} = \left(\frac{(EI)_{fem} - (EI)_{ana}}{(EI)_{fem}}\right) * 100\right)$ against the data for equivalent bending

stiffness results computed utilizing the three previously developed analytical approaches respectively. As represented in Table 4-4, equivalent bending stiffness model predictions utilizing the laminated composite shell theory approach show excellent agreement in comparison to FEA results and demonstrate significantly higher accuracy in providing bending stiffness estimations as opposed to the bending stiffness model estimations developed using composite plate theory and conventional smear property approach. In general, error percentage difference in bending stiffness estimations generated between FEM results and shell model data are witnessed to be less than 2% and reduces as tube mean-radius is incrementally increased.

Table 4-4 Effect of Curvature Factor on Eq. Bending Stiffness (Composite Case)

Radius (in)	FEM Results ($lb\text{-}in^2$)	Smear Property ($lb\text{-}in^2$), (% diff)	Shell Approach ($lb\text{-}in^2$), (% diff)
2.5	1.578 E+07	1.573 E+07	1.575 E+07
2.3	1.231 E+07	1.223 E+07	1.224 E+07
2.1	9.367 E+06	9.294 E+06	9.303 E+06
1.9	6.934 E+06	6.867 E+06	6.874 E+06
1.7	4.954 E+06	4.904 E+06	4.910 E+06
1.5	3.392 E+06	3.357 E+06	3.361 E+06
1.3	2.198 E+06	2.174 E+06	2.178 E+06
1.1	1.328 E+06	1.308 E+06	1.315 E+06
0.9	7.341 E+05	7.101 E+05	7.270 E+05
0.7	3.506 E+05	3.291 E+05	3.469 E+05
0.5	1.311 E+05	1.167 E+05	1.296 E+05
0.3	3.001 E+04	2.367 E+04	2.649 E+04
0.1	1.460 E+03	6.380 E+02	1.441 E+03

Bending stiffness estimations generated by assuming the infinitesimal tube section to be a plate element indicate an error percentage difference of less than 3.5% to begin with (for R_m=2.5 in) and peaks to approximately 33% for the case of a composite tube with 0.1 inch mean-radius. Significant disparity in bending stiffness estimations are observed in comparison between FEM results and conventional smear property based results. Error percentage difference initiates at approximately 4.5% for the case of a composite tube with 2.5 inch mean-radius and escalates to approximately 55% for the case of a 0.1 inch mean radius composite tube. Figure 4-7 represents the plot of percentage error variation between three analytical based approaches in comparison with finite element result as a function of composite tube mean-radius R_m.

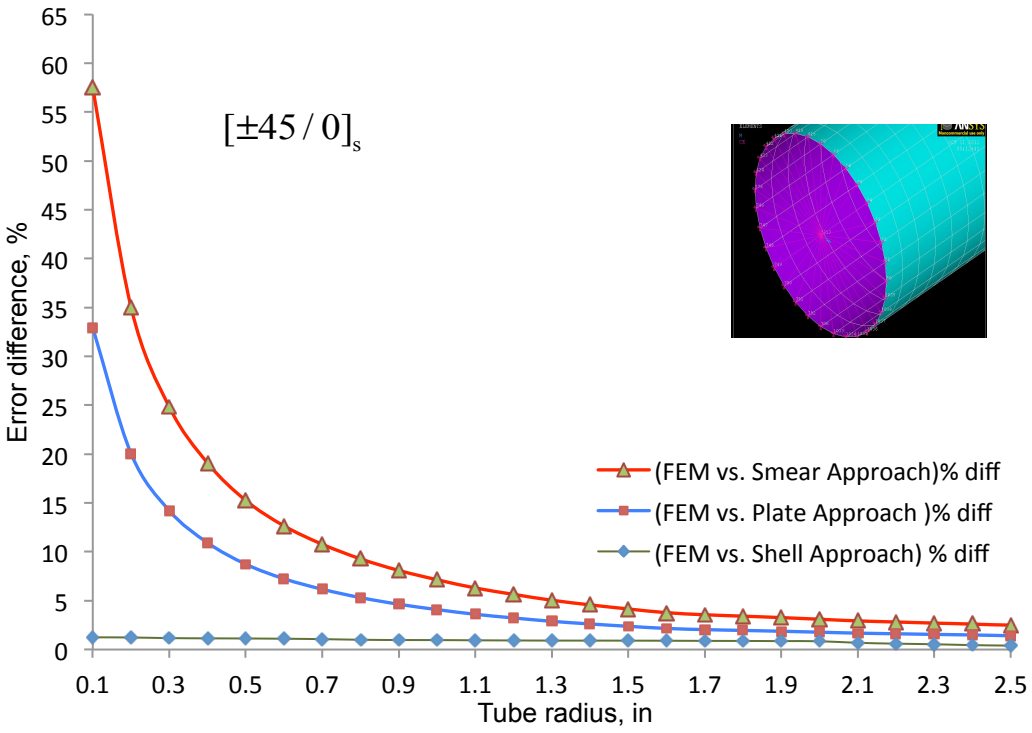

Figure 4-7 Combined Equivalent Bending Stiffness % Error diff as a Function of Tube Mean-radius R_m

Based upon the results of this initial investigation, it is observed that analytical expressions developed via thin-walled laminated composite shell theory approach that effectively incorporates the influence of shell-curvature factor in its resultant load and global stiffness matrix formulations exhibits encouraging results and is in very good agreement with the FEM based numerical results. Furthermore, this study also indicates that the role of $\left(1+\frac{z''}{R_m}\right)$ critically governs the bending stiffness estimations for smaller tube mean-radius regimes (0.1 in<R_m<1.0 in). Essentially, the physical significance of shell curvature factor greatly diminishes for composite tubes with fairly large radii (R_m>2 in). Asymtotically, if the tube mean-radius of curvature R_m is assumed to approach a value of infinity, the global stiffness model (Eq. 4.1.23) developed for charecterizing the stiffness response of thin-walled composite tubes gets reduced to the generalized global stiffness model expression associated with a rectangular composite plate.

Similarly, the effect of shell curvature factor on the equivalent axial stiffness of a thin-walled laminated composite tube configuration is examined by parameterizing R_m from 2.5 inches to 0.1 inch in increments of 0.2 inch respectively Figure 4-7 depicts the error percentage difference associated with the equivalent axial stiffness comparisons performed for FEM vs. Shell, FEM vs. Plate and FEM vs. Smear model as a function of tube mean-radius. Conducting sequential increments in values of tube mean-radius to generate equivalent axial stiffness predictions by implementing three mathematically distinct stiffness models does not present a significant variation among each analytical estimations in comparison with FEM data. Essentially, the equivalent stiffness results obtained numerically and analytically collapse on top of each other indicating a closely matched axial stiffness value for any specifically chosen radius of shell curvature. Based upon the results of this initial investigation, it therefore appears that the mechanical

response characterization of a class of thin-walled, multidirectional fiber-reinforced composite tube configurations based on equivalent bending stiffness estimations are critically governed by the influence of tube curvature and mean-radius while exhibiting no significant effect towards analyzing the axial stiffness predictions.

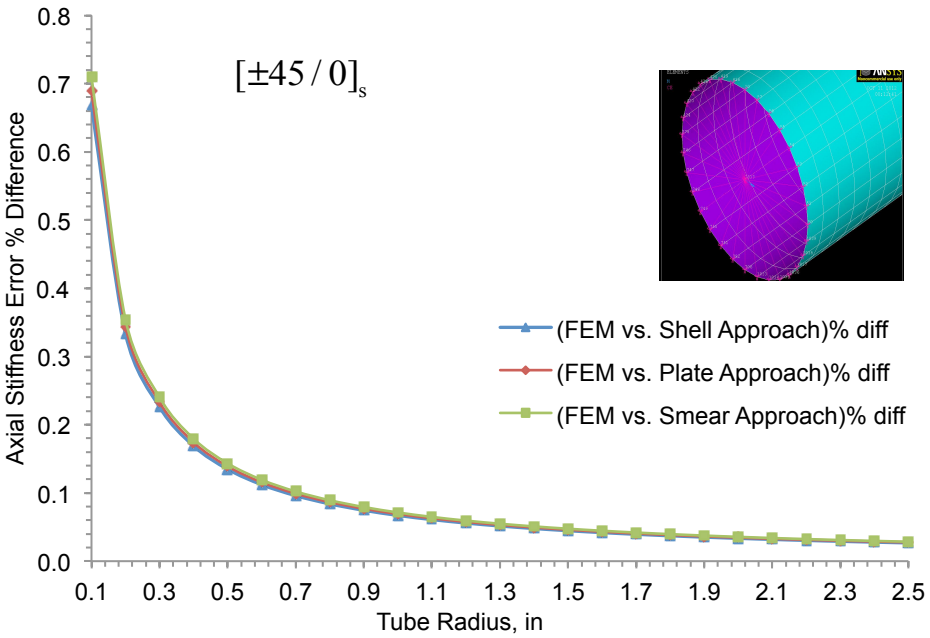

Figure 4-8 Combined Equivalent Axial Stiffness % Error diff as a Function of Tube Mean-Radius R_m

Table 4-5 represents the analytically computed equivalent axial and bending stiffness predictions based on the thin-walled modified shell theory approach for a 6-ply symmetric-balanced multi-directional cylindrical composite tube with a $\left[\pm 45/0\right]_{symm}$ tacking sequence that is preferentially thin-walled and closed cross-sectioned in nature. A general comparison of stiffness data made on small tube mean-radii indicate that the effect of shell-curvature factor is more influential towards governing the bending stiffness response as opposed to the extensional stiffness response. For tube radii ($0.1<R_m<0.5$), bending stiffnesses are observed to be one order of magnitude lower as opposed to the

predicted axial stiffness results. On the contrary, for a specified large tube-radius (R_m>2.0), bending stiffness values show a significantly larger stiffness magnitude in comparison to the axial stiffness results. In principle, the influence of shell-curvature begins to diminish for tubes with relatively large tube mean-radius as each individual element constituting the tube cross-section can be allowed to be approximated as a thin-walled plate. Additionally, for a composite tube that is classified under a small tube-radius regime (0.1<R_m<0.5), the pre-assumed composite tube structural characteristics render the tube configuration to be more compliant to bending as opposed to tension loading. However, for laminated cylindrical tubes classified under a larger tube-radius regimes,(R_m>2.0) an antithetical stiffness response can be observed.

Table 4-5 Bending and Axial Stiffness Predictions: Laminated Shell Theory Approach

Tube Mean-Radius (in)	Bending Stiffness (lb-in^2)	Axial Stiffness (lb)
2.5	1.575 E07	4.625 E06
2.3	1.224 E07	4.255 E06
2.1	9.303 E06	3.885 E06
1.9	6.874 E06	3.515 E06
1.7	4.910 E06	3.145 E06
1.5	3.361 E06	2.775 E06
1.3	2.178 E06	2.405 E06
1.1	1.315 E06	2.035 E06
0.9	7.370 E05	1.655 E06
0.7	3.469 E05	1.295 E06
0.5	1.296 E05	9.251 E05
0.3	2.649 E04	5.550 E05
0.1	1.441 E03	1.850 E05

4-4 Ply-per Ply In-plane Stress Recovery for Multidirectional Composite Tubes

Furthermore, in order to acquire a better understanding on the mechanical behavior of these thin-walled fiber-reinforced composite tubes, a structural response characterization in terms of ply-stresses is conducted. The thin-walled, circular cross-section, closed composite tube configuration is subjected to an uniform temperature-differential and/or to a finite bending moment concentrated about its cross-sectional centroidal point to investigate the longitudinal stress distribution patterns across the tube circumference. Constitutive equations that fundamentally relate the resultant applied loads and moments to induced mid-plane strains-curvatures are given by

$$\left\{ \begin{array}{c} \bar{N} \\ \bar{M} \end{array} \right\}_{6*1} = \left[\begin{array}{cc} \bar{A} & \bar{B} \\ \bar{B} & \bar{D} \end{array} \right]_{6*6} * \left\{ \begin{array}{c} \varepsilon^{o}_{x,y} \\ \kappa_{x,y} \end{array} \right\}_{6*1} \tag{4.39}$$

This equation represents the abbreviated version of the generalized constitutive equation based on classical lamination theory.

$$\begin{gathered} \left\{ \begin{array}{c} \varepsilon^{"}_{0} \\ \kappa^{"}_{0} \end{array} \right\} = \left(\begin{array}{cc} \bar{a} & \bar{b} \\ \bar{b}^{T} & \bar{d} \end{array} \right) * \left\{ \begin{array}{c} \bar{N} \\ \bar{M} \end{array} \right\} \\ \left(\begin{array}{cc} \bar{a} & \bar{b} \\ \bar{b}^{T} & \bar{d} \end{array} \right) = \left[\begin{array}{cc} \bar{A}^{"} & \bar{B}^{"} \\ \bar{B}^{"} & \bar{D}^{"} \end{array} \right]^{-1} \end{gathered} \tag{4.40}$$

Where, $\bar{N}$ and $\bar{M}$ are the resultant hygrothermomechanical forces and moments referenced with respect to the global coordinate system of composite tube. For a specified composite ply lay-up consisting of a pre-defined stacking sequence, corresponding global stiffness matrices are initally determined. Additionally, under the application of a specific finite combination of loads that include mechanical and thermal loads, the associated mid-plane strain and curvatures can further be evaluated. Based on for any arbitrarily oriented ply located at the newly developed constitutive relationship

based on extended lamination theory principles (composite shell theory approach), distance z_k from centroidal axis of the laminate, corresponding in-plane ply strains can be computed by

$$\left\{\varepsilon\right\}_{k^{th}layer} = \left\{\varepsilon_0^{"}\right\} + z"_k . \left\{\kappa_0^{"}\right\} \tag{4.41}$$

Incorporating the translational distance parameter $R_m.Cos\theta$, resultant in-plane surface strains (in x-y global coordinate) for an arbitrary ply located at a specific vertical distance from the global horizontal axis can be computed and is shown as

$$\left\{\varepsilon_{x-y}^{total}\right\}_k = \left\{\varepsilon_o^{"}\right\} + \left((R + z"_k) * \cos\theta\right) * \left\{\kappa"\right\} \tag{4.42}$$

Under the influence of hygrothermal strains, in-plane ply mechanical strains can be determined and can be shown as

$$\left\{\varepsilon_{x-y}^{mech}\right\}_k = \left\{\varepsilon_o^{"}\right\} + \left((R_m + z"_k) * Cos\theta\right) * \left\{\kappa"\right\} - \left\{\alpha_{x-y}\right\}_k \Delta T - \left\{\beta_{x-y}\right\}_k \Delta C \tag{4.43}$$

Consequently, in-plane mechanical ply-stresses at any arbitrary location defining the tube circumference can be analytically computed via utilizing the previously formulated global stiffness matrix and corresponding mid-plane strains and curvatures as shown in Eqn. (4.44),

$$\left\{\sigma_{x-y}^{mech}\right\}_k = \left[\bar{Q}"_{x-y}\right]_k * \left\{\left\{\varepsilon_o^{"}\right\} + \left((R_m + z"_k) * Cos\theta\right) * \left\{\kappa"\right\} - \left\{\alpha_{x-y}\right\}_k . \Delta T - \left\{\beta_{x-y}\right\} . \Delta C\right\} \tag{4.44}$$

where, $\left\{\sigma_{x-y}^{mech}\right\}_k$ is fundamentally an implicitly defined function of fiber-orientation angle β, element rotation angle θ, structural geometry, equivalent averaged elastic stiffness parameters and the laminate's ply stacking sequence respectively. Longitudinal stresses of the composite tube for any arbitrary circumferential angle θ can be effectively acquired by re-iterating this methodology. The present work collectively analyzes the ply-per-ply longitudinal stress distribution patterns for a six-ply symmetric-balanced composite tube

configuration with a $\left[\pm 45/0\right]_{symm}$ laminate stacking sequence. Two ANSYS based FEM test-runs are conducted. First test routine involves the application of a finite longitudinal bending moment of 10 in-lbs about the neutral axis of the tube and the associated mechanical behavior is characterized without the presence of thermal loading conditions. Second test routine accommodates the addition of a uniformly distributed temperature differential upon the structure. The thin-walled composite tube cross-section is subject to a temperature difference of $\Delta T = 50^{o}F$. Stress patterns developed for the two test-run conditions are recorded and investigated.

Circumferential distribution pattern of longitudinal stresses for a tube cross-section located at 50%L_{tube} are studied. Figures 4-9 and 4-10 depict the combined in-plane longitudinal stress σ_x distribution patterns along the circumferential contours of 0^{o} and $\pm 45^{o}$ layers under the presence and absence of a pre-defined thermomechanical environment. Upon investigation of Figure 4-9, it can be observed that the magnitude of longitudinal stress σ_x estimations based on FEM and analytical formulation (Eq.4.44) encounters a state of zero stress at circumferential points located along the global neutral axes (90^{o} and 270^{o}) respectively.

Under the presence of a finite thermal loading of $\Delta T = 50^{o}F$, the composite tube mechanical response exhibits a significant increase in the 0^{o} ply longitudinal stresses across the circumference and the corresponding stress magnitudes located at circumferential (90^{o} and 270^{o}) stations indicate finite non-zero stresses. This phenomena involving elevated stress levels under the presence of a thermal loading can be attributed to the increased influence of Poisson's ratio effect within the adjoining ply boundaries.

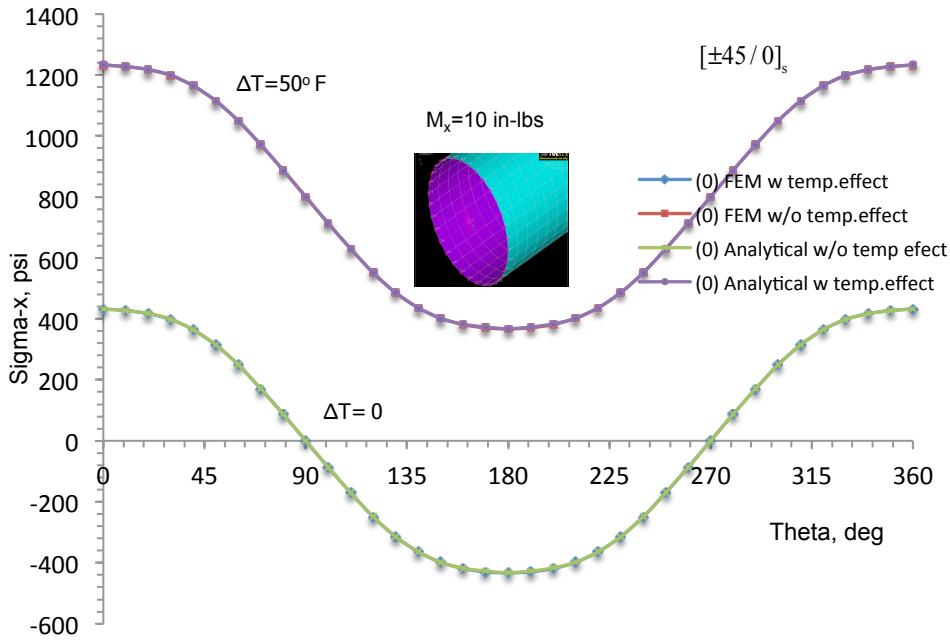

Figure 4-9 Longitudinal Stress Distribution in 0° Plies under Bending as a fn. of Circumferential Angle θ

Longitudinal stresses computed analytically utilizing the concept of Layer-Stress-Recovery are also shown in Figures 4-9 and 4-10 respectively. Interestingly enough, the 0° ply stresses determined upon the inclusion and exclusion of thermal effects collapse on top of each other, consequently indicating excellent agreement in the stress data extracted through two distinct approaches. The Stress curves for the 0° plies portray a symmetrical distribution about the global z' axis (oriented along the laminate-thickness) of the laminate. Figure 4-10 represents the longitudinal stress distributions (for $\pm 45^{0}$) predicted across the circumference of the tube as a function of circumferential arc angle respectively. Stress distribution patterns witnessed in $\pm 45^{0}$ layers indicate a decreased stress magnitude when compared to the 0° plies that are preferentially oriented along the length of the tube.

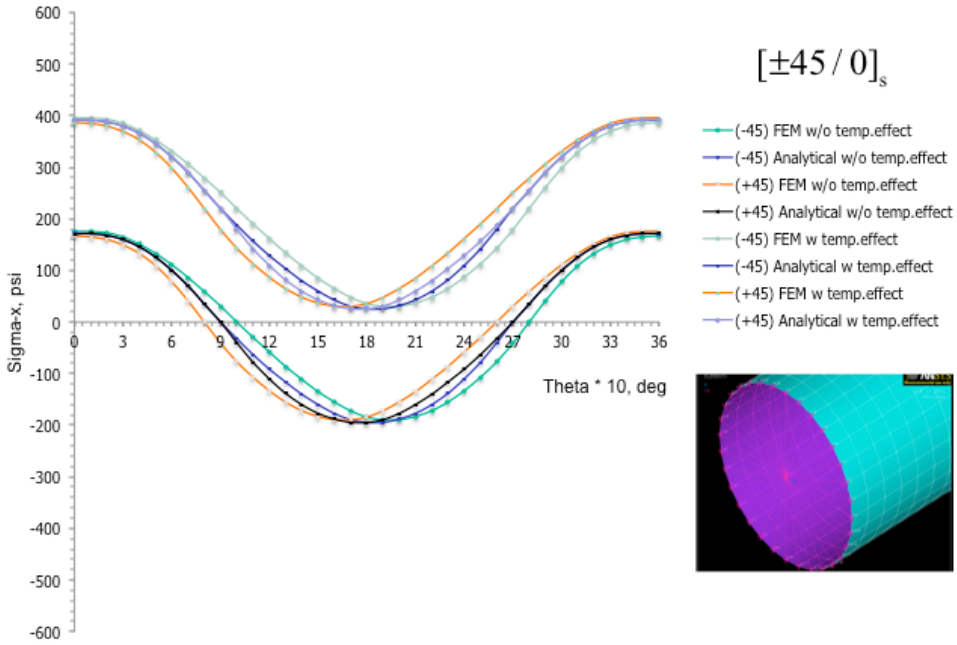

Figure 4-10 Longitudinal Stress Distribution of $\pm 45^{o}$ Plies under Bending as a fn. of Circumferential Angle θ

Analytically acquired longitudinal stress distribution curves corresponding to $\pm 45^{0}$ layers predicted across the circumference only shows good agreement in σ_x stress results in comparison to FEM data.

Furthermore, a preliminary parameteric investigation on the longitudinal σ_x stress predictions as a function of sequentially incremented tube mean-radius R_m is conducted. For this iterative study, a cross-sectional cut located at 60%L is assumed for data extraction in order to preclude the propagative influence of edge effects. Stress values are systematically recorded across two nodal coordinates of interest, represented by points 1 and 2 (Fig. 4-11) on the global coordinate system of cylindrical tube model respectively. Nodal points 1 and 2 are specifically used to analyze the longitudinal stresses in this work.

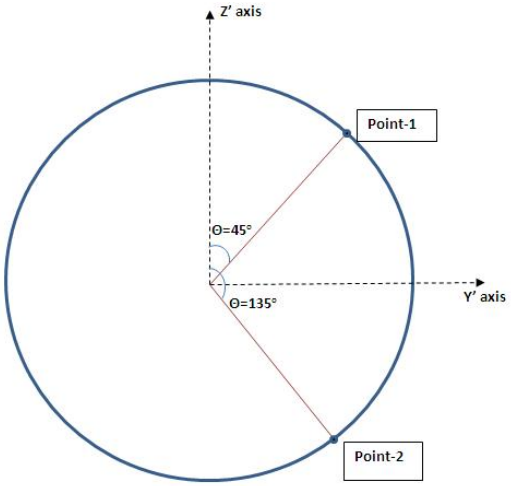

Figure 4-11 Composite Tube Node-Point Schematic at 60%L

assumed to be located at 45^0 from the vertical z' axis and node point-2 is assumed to be located at 135^o from the vertical z' axis respectively. Initially, a finite bending moment of 20 in-lbs is applied to the 6-ply symmetric-balanced cylindrical composite tube configuration and corresponding longitudinal stress values corresponding to the two nodal points are calculated (Eq. 4.1.24) respectively. Figures 4-12 through 4-14 represent the plots of longitudinal stresses σ_x distributions corresponding to 0^0 and $\pm 45^0$ as a function of tube mean-radius respectively. Although, a finite variation in stress magnitudes can be witnessed for each of the composite plies that constitutes the lay-up for the tube structure, the distribution patterns in longitudinal stresses describe an identical trend. Each of these stress plots jointly display a ply based longitudinal stress response that includes and excludes the presence of a thermal loading environment. A finite concentrated bending moment of 20 lb-in is applied on the centroidal point to acquire the stress results. Good agreement is achieved in the analytically generated stress data in comparison with the FEM predictions. 0 degree plies describe the highest longitudinal stresses σ_x for any of the specified mean-radius values.

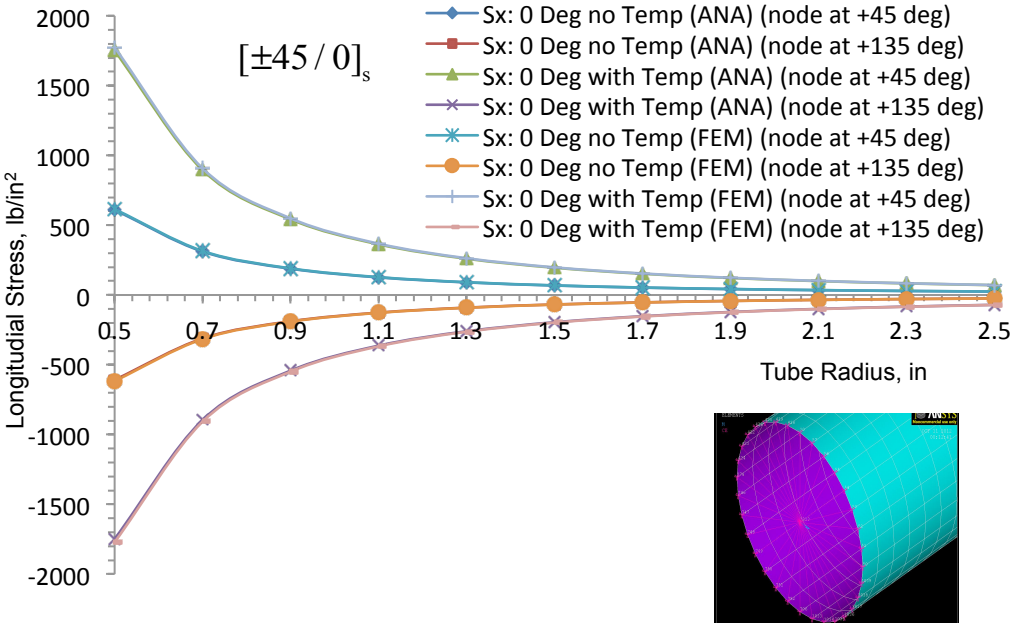

Figure 4-12 σ_x Stress Variation in 0° Plies as a fn. of Tube mean-Radius R_m

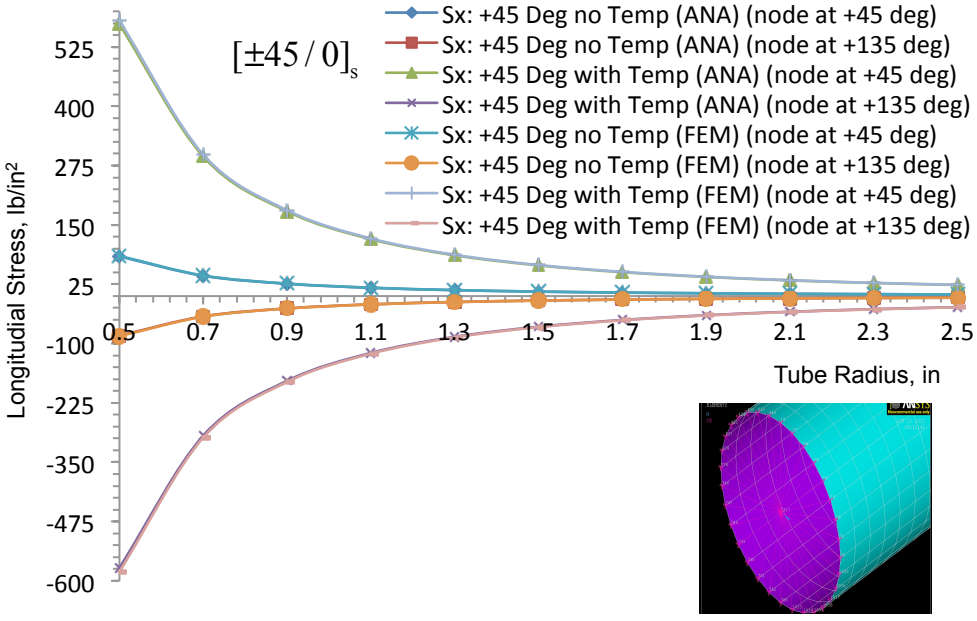

Figure 4-13 σ_x Stress Variation in $+45^\circ$ Plies as a fn. of Tube mean-Radius R_m

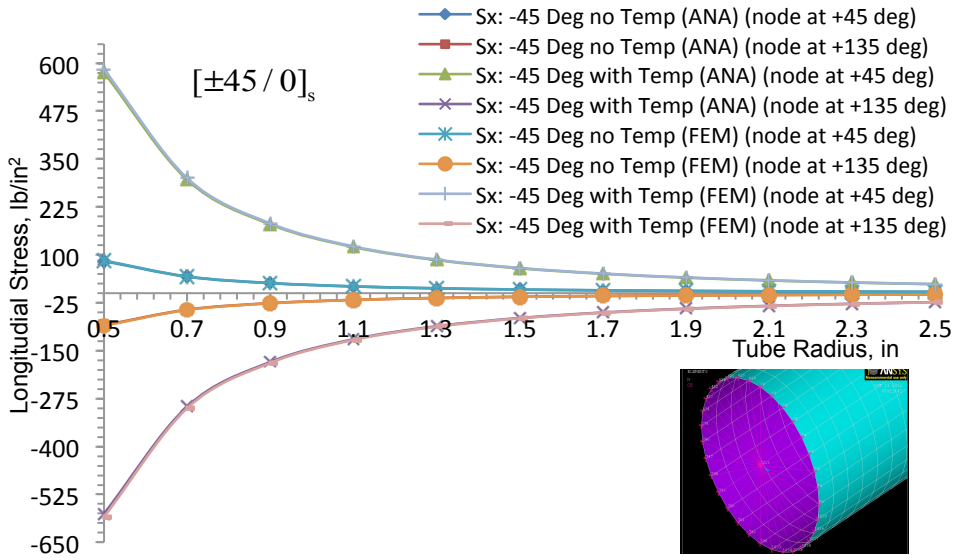

Figure 4-14 σ_x Stress Variation in -45° Plies as a fn. of Tube mean-Radius R_m

$\left[\pm 45^{0}\right]$ stress plots represent a stress distribution and magnitude that are almost identical with each other under the presence and absence of temperature environment. Essentially, each of the ply stress plots indicate a gradual reduction in longitudinal stress σ_x with increasing tube mean-radius. In essence , this chapter represents the foundation in terms of modeling, formulation and development of a simple and accurate analytical framework that demonstrates the potential to deliver closed-form (not exact) solutions that facilitate in comprehending the mechanical behavior of thin-walled closed cross-section cylindrical composite tubes. These preliminary investigative results exposes new research boundaries that warrants to formulate and develop a new analytical methodology for analyzing thin-walled composite shell configurations that are geometrically open-cross-sectioned. The following chapter is geared towards developing a novel mathematical framework that is able to accurately generate closed-form analytical solutions while charecterizing the mechanical behavior of such configurations.

Chapter 5

MECHANICAL RESPONSE INVESTIGATION OF THIN WALLED CIRCULAR OPEN CROSS-SECTIONED LAMINATED CYLINDRICAL SHELLS

The lineage of trailblazing scientific research in the field of thin-walled isotropic cylindrical shells traces back to late 20th century when an elementary understanding on the kinematics of linearly elastic homogenous shells of numerous constructions were newly formulated by Love and Kirchoff. Since the emergence of their theory, extensive literature accrued in this subject have propelled the development of a variety of mathematical models based on scientific hypotheses such as First approximations theories, Donnel's shell theories, Classical laminated plate theories, Classical laminated shell theories, thin membrane theories, higher order displacement field and moment theories, First-order and higher-order transverse shear deformation theories and "Reissner-Mindlin" based higher order shell approximation theories respectively.

Extensions and modifications on the majority of these suppositions had a restrictive stretch in their applications as their building methodology was based on some underlying modeling assumptions (Chapter 1).

Chapter-4 of this research discussed on proposing, modeling and developing a novel analytical model that adopted the conceptual mechanics of composite shell theory to deliver a broad structural understanding on thin-walled multidirectional cylindrical composite tubes. The developed analytical model is extended to formulate another new analytical methodology to charecterize the mechanical aspects of thin-walled fiber-reinforced open cylindrical shells having circular cross-sections. Therefore, the current chapter is focused on utilizing the analytical model towards conducting mechanical stiffness and ply-stress investigations on such structural elements.

5-1 Global Stiffness Model Formulation for Open-Celled Composite Cylindrical Shells

The analytical formulation for developing a simplified global stiffness estimation model (Eqns. 4.9 through 4.25), was dedicated to characterize thin-walled, closed cross-section, tubular composite configurations. Based on the extended composite shell theory approach, the scope of the model was stretched to conduct a ply-wise longitudinal stress investigation across the circumferential contour of the composite tube. Introduction of the shell-curvature factor into the governing equations played a particularly relevant role towards analyzing bending stiffness and ply-stress predictions respectively.

Notably, the uniform circular geometry as witnessed in the design of thin-walled cylindrical tubes is preserved in the design re-construction phase of open-celled composite cylindrical shells. This fundamental structural assumption facilitates in exploiting the previously formulated stress-resultant load relationships (Eqn. 4.22). A temperature-moisture based loading is still maintained for this analysis. Hygrothermal strains induce thermal loading and moments, which add upon mechanical load terms. Conceptually, for an infinitesimal composite tube element that is assumed to be subjected to a thermal and moisture environment reveal the emergence of additonal hygrothermal forces and moments ($\frac{M_x^{T"}}{R_m}, \frac{M_x^{H"}}{R_m}, \frac{M_{xy}^{T"}}{R_m}, \frac{M_{xy}^{H"}}{R_m}, L_x^{T"}, L_x^{H"}, L_{xy}^{T"}$ and $L_{xy}^{H"}$) due to an increased cross-sectional area present above the circumferential mid-plane of the composite tube. Furthermore, these additional hygrothermal load and moment terms are primarily influenced by the presence of shell curvature-factor $\left(1+\frac{z"}{R_m}\right)$. In essence, the generalized constitutive equation developed for a differential shell element (Eq. 4.24) arbitrarily oriented across the circumferential contour of circularly closed composite cross-section is still applicable for any arbitrarily oriented infinitesimal shell element

constituting a circularly open-cross-sectioned cylindrical shell configuration. Newly developed stiffnesses per unit width, hygrothermally induced longitudinal and shear stress resultants are highlighted in red respectively.

$$\begin{Bmatrix} N_x' + N_x^{T'} + N_x^{H'} + \frac{M_x^{T'}}{R_m} + \frac{M_x^{H'}}{R_m} \\ N_y' + N_y^{T'} + N_y^{H'} \\ N_{xy}' + N_{xy}^{T'} + N_{xy}^{H'} + \frac{M_{xy}^{T'}}{R_m} + \frac{M_{xy}^{H'}}{R_m} \\ M_x' + M_x^{T'} + M_x^{H'} + L_x^{T'} + L_x^{H'} \\ M_y' + M_y^{T'} + M_y^{H'} \\ M_{xy}' + M_{xy}^{T'} + M_{xy}^{H'} + L_{xy}^{T'} + L_{xy}^{H'} \\ N_{yx}' + N_{yx}^{T'} + N_{yx}^{H'} \\ M_{yx}' + M_{yx}^{T'} + M_{yx}^{H'} \end{Bmatrix} = \begin{bmatrix} A_{11} + \frac{B_{11}}{R_m} & A_{12} + \frac{B_{12}}{R_m} & A_{16} + \frac{B_{16}}{R_m} & B_{11} + \frac{D_{11}}{R_m} & B_{12} + \frac{D_{12}}{R_m} & B_{16} + \frac{D_{16}}{R_m} \\ A_{12} & A_{22} & A_{26} & B_{12} & B_{22} & B_{26} \\ A_{16} + \frac{B_{16}}{R_m} & A_{26} + \frac{B_{26}}{R_m} & A_{66} + \frac{B_{66}}{R_m} & B_{16} + \frac{D_{16}}{R_m} & B_{26} + \frac{D_{26}}{R_m} & B_{66} + \frac{D_{66}}{R_m} \\ B_{11} + \frac{D_{11}}{R_m} & B_{12} + \frac{D_{12}}{R_m} & B_{16} + \frac{D_{16}}{R_m} & D_{11} + \frac{E_{11}}{R_m} & D_{12} + \frac{E_{12}}{R_m} & D_{16} + \frac{E_{16}}{R_m} \\ B_{12} & B_{22} & B_{26} & D_{12} & D_{22} & D_{26} \\ B_{16} + \frac{D_{16}}{R_m} & B_{26} + \frac{D_{26}}{R_m} & B_{66} + \frac{D_{66}}{R_m} & D_{16} + \frac{E_{16}}{R_m} & D_{26} + \frac{E_{26}}{R_m} & D_{66} + \frac{E_{66}}{R_m} \\ A_{16} & A_{26} & A_{66} & B_{16} & B_{26} & B_{66} \\ B_{16} & B_{26} & B_{66} & D_{16} & D_{26} & D_{66} \end{bmatrix} * \begin{Bmatrix} \varepsilon_x^0 \\ \varepsilon_y^0 \\ \gamma_{xy}^0 \\ \kappa_x \\ \kappa_y \\ \kappa_{xy} \end{Bmatrix}$$

(5.1)

It must be noted that the infleunce of $\begin{Bmatrix} N_{yx}^{T'} + N_{yx}^{H'} \\ M_{yx}^{T'} + M_{yx}^{H'} \end{Bmatrix}$ cannot be neglected while investigating open-cross-sectioned composite shells. In the case of a closed composite tube configuration, charecteristic structural bi-symmetry trivializes the effects of $N_{yx}^T, M_{yx}^T, N_{yx}^H, M_{yx}^H$ loads , however for the case of a open cross-section cylindrical shell configuration such a curved composite shell, the influence of hyrothermally induced loads along the free edges cannot be ignored. Each of the highlighted load resultants are reviewed and expressed in Eqns. (5.2) through (5.9) respectively. Symmetry of the individual stiffness matrix components becomes vanished upon the introduction of curvature effect. Upon gradually increasing the value of tube mean-radius R_m towards infinity, stiffness matrix of the thin-walled laminated composite shell element gets reduced to the typical composite plate element stiffness equation.

$$\frac{M_x^{T'}}{R_m} = \frac{1}{2R_m} * \left\{ \sum_{k=1}^{n} \left(\begin{array}{ccc} \bar{Q}_{11}^{"}(z^2{}_k - z^2{}_{k-1}) & \bar{Q}_{12}^{"}(z^2{}_k - z^2{}_{k-1}) & \bar{Q}_{16}^{"}(z^2{}_k - z^2{}_{k-1}) \end{array} \right) * \left(\begin{array}{c} \alpha_x \\ \alpha_y \\ \alpha_{xy} \end{array} \right) \right\} * \Delta T$$

$$\frac{M_x^{H'}}{R} = \frac{1}{2R_m} * \left\{ \sum_{k=1}^{n} \left(\begin{array}{ccc} \bar{Q}_{11}^{"}(z^2{}_k - z^2{}_{k-1}) & \bar{Q}_{12}^{"}(z^2{}_k - z^2{}_{k-1}) & \bar{Q}_{16}^{"}(z^2{}_k - z^2{}_{k-1}) \end{array} \right) * \left(\begin{array}{c} \beta_x \\ \beta_y \\ \beta_{xy} \end{array} \right) \right\} * \Delta C$$

(5.2-5.3)

$$\frac{M_{xy}^{T'}}{R_m} = \frac{1}{2R_m} * \left\{ \sum_{k=1}^{n} \left(\begin{array}{ccc} \bar{Q}_{16}^{"}(z^2{}_k - z^2{}_{k-1}) & \bar{Q}_{26}^{"}(z^2{}_k - z^2{}_{k-1}) & \bar{Q}_{66}^{"}(z^2{}_k - z^2{}_{k-1}) \end{array} \right) * \left(\begin{array}{c} \alpha_x \\ \alpha_y \\ \alpha_{xy} \end{array} \right) \right\} * \Delta T$$

$$\frac{M_{xy}^{H'}}{R_m} = \frac{1}{2R_m} * \left\{ \sum_{k=1}^{n} \left(\begin{array}{ccc} \bar{Q}_{16}^{"}(z^2{}_k - z^2{}_{k-1}) & \bar{Q}_{26}^{"}(z^2{}_k - z^2{}_{k-1}) & \bar{Q}_{66}^{"}(z^2{}_k - z^2{}_{k-1}) \end{array} \right) * \left(\begin{array}{c} \beta_x \\ \beta_y \\ \beta_{xy} \end{array} \right) \right\} * \Delta C$$

(5.4-5.5)

$$L_x^{T'} = \frac{1}{3R_m} * \left\{ \sum_{k=1}^{n} \left(\begin{array}{ccc} \bar{Q}_{11}^{"}(z^3{}_k - z^3{}_{k-1}) & \bar{Q}_{12}^{"}(z^3{}_k - z^3{}_{k-1}) & \bar{Q}_{16}^{"}(z^3{}_k - z^3{}_{k-1}) \end{array} \right) * \left(\begin{array}{c} \alpha_x \\ \alpha_y \\ \alpha_{xy} \end{array} \right) \right\} * \Delta T$$

$$L_x^{H'} = \frac{1}{3R_m} * \left\{ \sum_{k=1}^{n} \left(\begin{array}{ccc} \bar{Q}_{11}^{"}(z^3{}_k - z^3{}_{k-1}) & \bar{Q}_{12}^{"}(z^3{}_k - z^3{}_{k-1}) & \bar{Q}_{16}^{"}(z^3{}_k - z^3{}_{k-1}) \end{array} \right) * \left(\begin{array}{c} \beta_x \\ \beta_y \\ \beta_{xy} \end{array} \right) \right\} * \Delta C$$

(5.6-5.7)

$$L_{xy}^{T'} = \frac{1}{3R_m} * \left\{ \sum_{k=1}^{n} \left(\begin{array}{ccc} \bar{Q}_{16}^{"}(z^3{}_k - z^3{}_{k-1}) & \bar{Q}_{26}^{"}(z^3{}_k - z^3{}_{k-1}) & \bar{Q}_{66}^{"}(z^3{}_k - z^3{}_{k-1}) \end{array} \right) * \left(\begin{array}{c} \alpha_x \\ \alpha_y \\ \alpha_{xy} \end{array} \right) \right\} * \Delta T$$

$$L_{xy}^{H'} = \frac{1}{3R_m} * \left\{ \sum_{k=1}^{n} \left(\begin{array}{ccc} \bar{Q}_{16}^{"}(z^3{}_k - z^3{}_{k-1}) & \bar{Q}_{26}^{"}(z^3{}_k - z^3{}_{k-1}) & \bar{Q}_{66}^{"}(z^3{}_k - z^3{}_{k-1}) \end{array} \right) * \left(\begin{array}{c} \beta_x \\ \beta_y \\ \beta_{xy} \end{array} \right) \right\} * \Delta C$$

(5.8-5.9)

5-1-1 Analytical Determination of Centroidal Point Z_c

Fundamentally, for an isotropic structural entity of uniform density, the location of centroid is purely a 2-D geometric property. The physical significance of a structure's centroid is attributed to a specific location along a cross-section that exhibits an unrestrained de-coupled extension-bend type mechanical response under the application of an isolated tensile or bending moment type loading about that point.

The following session is devoted towards developing a closed-form equation to analytically determine the location of the centroid for open cross-sectioned, thin-walled cylindrical shell configurations. For the case of a closed tubular composite configuration, the centroidal point conveniently sits on the intersection of the neutral axis. The location of mean-radius of curvature is precisely the location of cross-sectional centroid for the case of a cylindrical composite tube configuration. For the case of an open-celled, cylindrical composite tube configuration, Eqn. (5.1) is reviewed to mathematically develop the location of the centroid and further conduct a structural-response characterization study in terms of ply-stresses respectively. For a general multidirectional composite laminate, in-plane load-deformation relations involving laminate stiffnesses and reference strains can be represented in a simplified form as shown in Eqn. (4.22). The averaged elastic stiffnesses are primary functions of the structural geometry, material properties and the laminate stacking sequence respectively.

In order to acquire a closed-form solution tool that accurately predicts the location of centroid in a curved cylindrical composite shell, two hypotheses are made. The generalized laminated shell constitutive equation as described in Eqn. (5.1) is modified into a 1-D narrow cylindrical beam problem. Fundamentally, for a narrow beam (Fig 5-1), the resulting longitudinal strains under the application of a longitudinal bending moment further induces transverse cross-sectional deformations influenced by Poisson's effect.

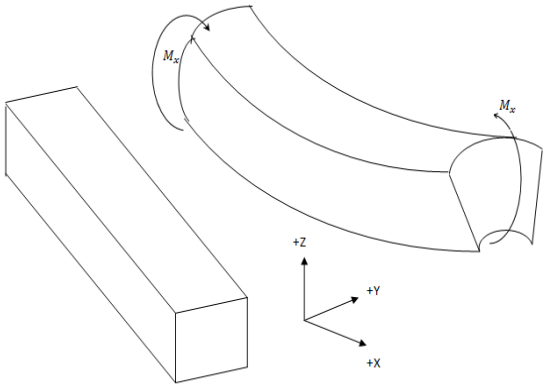

Figure 5-1 Narrow Beam Schematic: Undeformed and Deformed Configuration

Generally, only loads N_x and M_x that act along and about the designated longitudinal axis are considered for establishing the governing equations. Conceptually, beams are charecterized as a 1-D structural member that has one of its geometric dimensions (typically the beam length) significantly larger than the other two participating cross-sectional dimensions viz. width and thickness. Typically, a beam's mechanical response can be dictated crucially by its cross-sectional width to thickness $\left(\frac{w}{t}\right)$ ratio. For the case when $\left(\frac{w}{t}\right)$ ratio is approximately lesser than 6 a beam is classified as a *narrow beam* and if the $\left(\frac{w}{t}\right)$ ratio is greater than 6 it is distinguished in the *wide beam* category.

For this analysis, the infinitesimal thin-walled shell strip is fundamentally assumed to behave as a narrow beam that is subject to in-plane loads. The second vital assumption made towards this study is to assign the other applicable forces and moments such as $N_y=N_{xy}=N_{yx}=M_y=M_{xy}=M_{yx}=0$ respectively. As a consequence, resultant forces and moments (mechanical and hygrothermal) per unit width in Eqn. (5.1) can be restructured to initiate a matrix decomposition operation and can be expressed as

$$\begin{pmatrix} N_x' + N_x^T + N_x^H + \frac{M_x^T}{R_m} + \frac{M_x^H}{R_m} \\ M_x' + M_x^T + M_x^H + L_x^T + L_x^H \\ N_y' + N_y^T + N_y^H \\ N_{xy}' + N_{xy}^T + N_{xy}^H + \frac{M_{xy}^T}{R_m} + \frac{M_{xy}^H}{R_m} \\ M_y' + M_y^T + M_y^H \\ M_{xy}' + M_{xy}^T + M_{xy}^H + L_{xy}^T + L_{xy}^H \\ N_{yx}' + N_{yx}^T + N_{yx}^H \\ M_{yx}' + M_{yx}^T + M_{yx}^H \end{pmatrix} = \begin{bmatrix} A_{11} & B_{11} & A_{12} & A_{16} & B_{12} & B_{16} \\ B_{11} & D_{11} & B_{12} & B_{16} & D_{12} & D_{16} \\ A_{12} & B_{12} & A_{22} & A_{26} & B_{22} & B_{26} \\ A_{16} & B_{16} & A_{26} & A_{66} & B_{26} & B_{66} \\ B_{12} & D_{12} & B_{22} & B_{26} & D_{22} & D_{26} \\ B_{16} & D_{16} & B_{26} & B_{66} & D_{26} & D_{66} \\ A_{16} & B_{16} & A_{26} & A_{66} & B_{26} & B_{66} \\ B_{16} & D_{16} & B_{26} & B_{66} & D_{26} & D_{66} \end{bmatrix} * \begin{pmatrix} \varepsilon_x^0 \\ \kappa_x \\ \varepsilon_y^0 \\ \gamma_{xy}^0 \\ \kappa_y \\ \kappa_{xy} \end{pmatrix}$$

$$+ \frac{1}{R_m} * \begin{bmatrix} B_{11} & D_{11} & B_{12} & B_{16} & D_{12} & D_{16} \\ D_{11} & E_{11} & D_{12} & D_{16} & E_{12} & E_{16} \\ 0 & 0 & 0 & 0 & 0 & 0 \\ B_{16} & D_{16} & B_{26} & B_{66} & D_{26} & D_{66} \\ 0 & 0 & 0 & 0 & 0 & 0 \\ D_{16} & E_{16} & D_{26} & D_{66} & E_{26} & E_{66} \\ 0 & 0 & 0 & 0 & 0 & 0 \\ 0 & 0 & 0 & 0 & 0 & 0 \end{bmatrix} * \begin{pmatrix} \varepsilon_x^0 \\ \kappa_x \\ \varepsilon_y^0 \\ \gamma_{xy}^0 \\ \kappa_y \\ \kappa_{xy} \end{pmatrix} \qquad (5.10)$$

Each of these matrix components is further represented symbolically for achieving a transparent understanding. Subsequently, Eqn. (5.1.10) can be rewritten as

$$\begin{bmatrix} N_1 \\ N_2 \end{bmatrix} = \left\{ \begin{bmatrix} P_1 & P_2 \\ P_3 & P_4 \end{bmatrix} + \frac{1}{R_m} \begin{bmatrix} R_1 & R_2 \\ R_3 & R_4 \end{bmatrix} \right\} * \begin{Bmatrix} \varepsilon_1^* \\ \varepsilon_2^* \end{Bmatrix} \qquad (5.11)$$

where $[N_1]$ and $[N_2]$ matrices together represent the resultant in-plane applied mechanical and hygrothermally induced loads ,the transformed stiffness matrices per unit width are denoted by symbols $[P_1]$, $[P_2]$, $[P_3]$, $[P_4]$, $[R_1]$, $[R_2]$, $[R_3]$ and $[R_4]$ and matrices $\{\varepsilon_1^*\}$ and $\{\varepsilon_2^*\}$ jointly describe the reference in-plane strains and curvatures for a generalized curved composite cylindrical shell configuration.

Essentially, the global constitutive equation (Eqn. 5.1) is methodically decomposed into sub-matrices to establish a mathematical relation that strives to associate the extensional strain ε_x^o and curvature κ_x with the remaining 4 mid-plane strains and

curvatures $\left(\varepsilon_y^0 \quad \gamma_{xy}^0 \quad \kappa_y \quad \kappa_{xy} \right)$ respectively. For reference, each of the newly formed matrix structures are expanded to portray their stiffness constituents and are addressed in Appendix-D. Eqn.(5.13) represents fundamental hygrothermoelastic load-deformation relationship towards attaining an analytical prediction equation for calculation the centroid.

$$\begin{Bmatrix} N_x' + N_x^{T'} + N_x^{H'} + \dfrac{M_x^{T'}}{R_m} + \dfrac{M_x^{H'}}{R_m} \\ M_x' + M_x^{T'} + M_x^{H'} + L_x^{T'} + L_x^{H'} \end{Bmatrix}_{2*1} = \begin{bmatrix} A_{1,total}^* & B_{1,total}^* \\ B_{1,total}^* & D_{1,total}^* \end{bmatrix}_{2*2} * \begin{pmatrix} \varepsilon_x^0 \\ \kappa_x \end{pmatrix}_{2*1} \tag{5.13}$$

where $A_{1,total}^* = \int_{-\alpha}^{\alpha} A_1^* * R_m d\theta$, $B_{1,total}^* = \int_{-\alpha}^{\alpha} B_1^* * R_m d\theta$ and $D_{1,total}^* = \int_{-\alpha}^{\alpha} D_1^* * R_m d\theta$ respectively. $\left[A_1^*\right], \left[B_1^*\right]$ and $\left[D_1^*\right]$ are the components of the 1-D constitutive load-deformation relationship. It must be noted that $\left[A_1^*\right], \left[B_1^*\right]$ and $\left[D_1^*\right]$ are constants that are implicitly dependent on element rotation angle θ, fiber orientation angle β, material properties and tube mean-radius R_m respectively.

Figure 5-2 portrays the symbolic diagram of a thin-walled multidirectional curved cylindrical shell. The point of interest marked by point C is located at a distance Z_c from the mean-radius-of-curvature origin point O. Inherent cross-sectional symmetry demonstrated by the curved shell structure about the indicated z-axis dictates that the centroidal point exists precisely along the path of the y-plane that coincides with point O and this can be fictitiously constructed for achieving an intuitive understanding.

Given the focus of the current work on predicting and identifying the location of centroid, Eqn. (5.13) is revisited to formulate a closed-form expression, appropriate for characterizing open cross-sectioned, thin-walled curved composite shells. Based on the 1-D constitutive relationship, two mechanical cases are investigated.

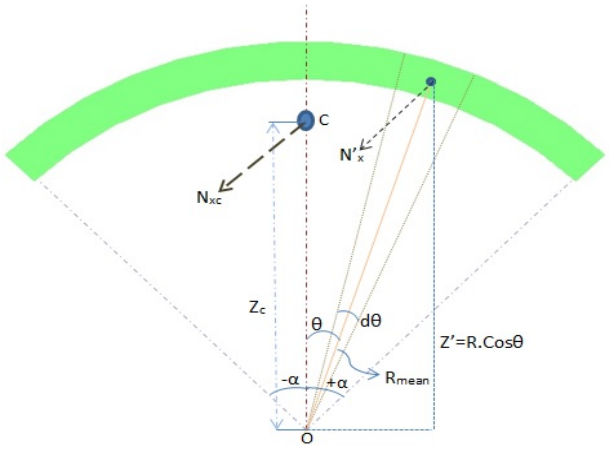

Figure 5-2 2-D Schematic of Centroid Location in a

Curved Composite Cylindrical Shell

First case deals with analytically determining the location of the centroid in the absence of a hygrothermal environment. By assuming the thin-walled curved strip as a narrow beam ($N_y=N_{xy}=N_{yx}=M_y=M_{xy}=M_{yx}=0$), the global constitutive relationship relating the resultant loads and moments with the reference mid-plane strains and curvatures reduces to

$$\begin{pmatrix} N_x' \\ N_y'=0 \\ N_{xy}'=0 \\ M_x' \\ M_y'=0 \\ M_{xy}'=0 \\ N_{yx}=0 \\ M_{yx}=0 \end{pmatrix} = \begin{bmatrix} A_{11}+\frac{B_{11}}{R_m} & A_{12}+\frac{B_{12}}{R_m} & A_{16}+\frac{B_{16}}{R_m} & B_{11}+\frac{D_{11}}{R_m} & B_{12}+\frac{D_{12}}{R_m} & B_{16}+\frac{D_{16}}{R_m} \\ A_{12} & A_{22} & A_{26} & B_{12} & B_{22} & B_{26} \\ A_{16}+\frac{B_{16}}{R_m} & A_{26}+\frac{B_{26}}{R_m} & A_{66}+\frac{B_{66}}{R_m} & B_{16}+\frac{D_{16}}{R_m} & B_{26}+\frac{D_{26}}{R_m} & B_{66}+\frac{D_{66}}{R_m} \\ B_{11}+\frac{D_{11}}{R_m} & B_{12}+\frac{D_{12}}{R_m} & B_{16}+\frac{D_{16}}{R_m} & D_{11}+\frac{E_{11}}{R_m} & D_{12}+\frac{E_{12}}{R_m} & D_{16}+\frac{E_{16}}{R_m} \\ B_{12} & B_{22} & B_{26} & D_{12} & D_{22} & D_{26} \\ B_{16}+\frac{D_{16}}{R_m} & B_{26}+\frac{D_{26}}{R_m} & B_{66}+\frac{D_{66}}{R_m} & D_{16}+\frac{E_{16}}{R_m} & D_{26}+\frac{E_{26}}{R_m} & D_{66}+\frac{E_{66}}{R_m} \\ A_{16} & A_{26} & A_{66} & B_{16} & B_{26} & B_{66} \\ B_{16} & B_{26} & B_{66} & D_{16} & D_{26} & D_{66} \end{bmatrix} * \begin{pmatrix} \varepsilon_x^0 \\ \varepsilon_y^0 \\ \gamma_{xy}^0 \\ \kappa_x \\ \kappa_y \\ \kappa_{xy} \end{pmatrix} \tag{5.14}$$

Corresponding1-D constitutive relationship reduces to

$$\begin{Bmatrix} N_x' \\ M_x' \end{Bmatrix}_{2*1} = \begin{bmatrix} A_{1,total}^* & B_{1,total}^* \\ B_{1,total}^* & D_{1,total}^* \end{bmatrix}_{2*2} * \begin{pmatrix} \varepsilon_x^0 \\ \kappa_x \end{pmatrix}_{2*1} \tag{5.15}$$

Assuming, only M_x is applied on the structure, resultant longitudinal strain ε_x computed at any arbitrary distance (within the structure) in the absence of a hygrothermal environment can be denoted in terms of extensional strain ε_x^0 and curvature κ_x and shown as,

$$\varepsilon_x^{mechanical} = \varepsilon_x^0 + Z\kappa_x \tag{5.16}$$

However of this moment is fictitiously applied on the centroid point (still unknown) the resultant longitudinal strain ε_x generated at the can be denoted in terms of extensional strain ε_x^0 and curvature κ_x is given by,

$$\varepsilon_x^{centroid} = \varepsilon_x^0 + Z_c\kappa_x = 0 \tag{5.17}$$

Imposing the assumption ($N_x = 0$ and $M_x \neq 0$ applied at apparent centroid point) into Eqn. (5.15), we get

$$\begin{pmatrix} \varepsilon_x^0 \\ \kappa_x \end{pmatrix} = \begin{bmatrix} a_1^* & b_1^* \\ b_1^* & d_1^* \end{bmatrix}_{2*1} * \begin{Bmatrix} 0 \\ M_x' \end{Bmatrix} \tag{5.18}$$

Eq.(5.18) can be expanded to to generate expressions for extensional strain ε_x^0 and curvature κ_x, which can be shown as

$$\varepsilon_x^0 = b_1^* M_x' \text{ and } \kappa_x = d_1^* M_x' \tag{5.19}$$

Comparing Eqn. (5.17) and Eqn. (5.19) , we obtain

$$Z_c = -\left(\frac{\varepsilon_x^0}{\kappa_x}\right) = -\left(\frac{b_1^*}{d_1^*}\right) \tag{5.20}$$

Eqn. (5.20) conclusively represents a simple closed-form, mathematical relationship to analytically determine the centroidal location $Z_{centroid}$ for any specified thin-walled, multidirectional, curved composite cylindrical shell configuration charecterized by total arc

angle (2α), fiber orientation angle β, material properties and structural geometry respectively. The negative sign witnessed in this expression signifies the fact that, location $Z_{centroid}$ exists outside and below the mid-reference line that essentially bisects the thin-walled curved laminate.

Case 2 involves developing a closed-form equation that predicts the geometric location of the centroid for cylindrical shell configurations in the presence of a hygrothermal environment. Previously (from Chapter-4), it was discovered from the global stiffness model (Eq. 4.24) that the presence of moisture-temperature based strains induced the emergence of additional hygrothermal load components. Eq. (5.10) is recalled and previously utilized narrow beam assumptions ($N_y=N_{xy}=N_{yx}=M_y=M_{xy}=M_{yx}=0$) are imposed for this case. However the infleunce of $\begin{Bmatrix} N_{yx}^{T'}+N_{yx}^{H'} \\ M_{yx}^{T'}+M_{yx}^{H'} \end{Bmatrix}$ cannot be neglected while investigating open-cross-sectioned composite shells in the presence of a hygrothermal environment. The final 1-D constitutive equation defining the resultant-deformation relationship in the presence of a hygrothermal environment can be shown as:

$$\begin{Bmatrix} N_x'+N_x^{T'}+N_x^{H'}+\dfrac{M_x^{T'}}{R_m}+\dfrac{M_x^{H'}}{R_m} \\ M_x'+M_x^{T'}+M_x^{H'}+L_x^{T'}+L_x^{H'} \end{Bmatrix}_{2*1} = \begin{bmatrix} A_{1,total}^{*} & B_{1,total}^{*} \\ B_{1,total}^{*} & D_{1,total}^{*} \end{bmatrix}_{2*2} * \begin{pmatrix} \varepsilon_x^0 \\ \kappa_x \end{pmatrix}_{2*1} \tag{5.21}$$

Eq. (5.21) can be rewritten as

$$\begin{Bmatrix} N_x' \\ M_x' \end{Bmatrix} + \begin{Bmatrix} J_1 \\ J_2 \end{Bmatrix} = \begin{bmatrix} A_{1,total}^{*} & B_{1,total}^{*} \\ B_{1,total}^{*} & D_{1,total}^{*} \end{bmatrix}_{2*1} * \begin{pmatrix} \varepsilon_x^0 \\ \kappa_x \end{pmatrix} \tag{5.22}$$

where J_1 and J_2 are constants comprising of the hygrothermally induced loads. These constants can be computed utlizing Eqns. (5.2-5.9) respectively. Similarly, Assuming, only M_x is applied on the structure, resultant mechanical strain ε_x computed at any

arbitrary distance (within the structure) in the presence of a hygrothermal environment can be denoted in terms of extensional strain ε_x^0 and curvature κ_x can be shown as,

$$\varepsilon_x^{\text{mechanical}} = \varepsilon_x^0 + Z\kappa_x - \varepsilon_x^{\text{thermal+moisture}} \tag{5.23}$$

However if this moment is fictitiously applied on the centroid point (still unknown) the resultant resultant mechanical strain $\varepsilon_x^{\text{centroid}}$ computed at centroid in the presence of a hygrothermal environment can be re-denoted in terms of extensional strain ε_x^0 and curvature κ_x can be shown as,

$$\varepsilon_x^{\text{centroid}} = \varepsilon_x^0 + Z_c\kappa_x - \varepsilon^{\text{thermal+moisture}} = 0 \tag{5.24}$$

where $\varepsilon^{\text{thermal+moisture}} = \varepsilon_x^{\text{thermal+moisture}} + Z_c\kappa_x^{\text{thermal+moisture}}$ .Imposing the assumption ($N_x = 0, M_x \neq 0$) at apparent centroid point into Eqn. (5.22), we get

$$\begin{pmatrix} \varepsilon_x^0 \\ \kappa_x \end{pmatrix} = \begin{bmatrix} a_1^* & b_1^* \\ b_1^* & d_1^* \end{bmatrix}_{2*1} * \begin{Bmatrix} 0 \\ M_x' \end{Bmatrix} + \begin{bmatrix} a_1^* & b_1^* \\ b_1^* & d_1^* \end{bmatrix}_{2*1} * \begin{Bmatrix} J_1 \\ J_2 \end{Bmatrix} \tag{5.25}$$

Eq.(5.25) can be expanded to to generate expressions for extensional strain ε_x^0 and curvature κ_x, which can be shown as

$$\varepsilon_x^0 = b_1^*.M_x' + \varepsilon_x^{\text{thermal+moisture}} \quad \text{and} \quad \kappa_x = d_1^*.M_x' + \kappa_x^{\text{thermal+moisture}} \tag{5.26}$$

Substituting expressions for ε_x^0 and curvature κ_x from Eq. (5.1.26) into Eq. (5.1.24) we get

$$Z_c = -\left(\frac{\varepsilon_x^0}{\kappa_x}\right) = -\left(\frac{b_1^*}{d_1^*}\right) \tag{5.27}$$

Eqn. (5.27) is discovered to be identical to Eq. (5.20). Fundamentally, from Eq. (5.26) it can be deduced that the location of centroid is not influenced by the presence of a hygrothermal loading environment and is solely geoverned by structural geometry and

material stiffness properties respectively. The negative sign witnessed in this expression signifies the fact that, location $Z_{centroid}$ exists outside and below the mid-reference line that essentially bisects the thin-walled curved laminate. It should be noted that the location of the centroid is calculated based on the undeformed curved composite shell configuration.

Fundamentally, Eq. (5.15) represents the 1-D narrow beam approach based global stiffness model for a thin-walled curved composite shell configuration. Upon observing the formulated global stiffness matrix terms, it is indicative that they primarily dependent on the material properties, element rotation angle θ, ply stacking sequence, ply lay-up and varying fiber orientation angle β respectively. The equivalent axial and bending stiffness (found by inverting the 2*2 matrix in Eqn 5.15) is given by

$$\bar{A}_x = \frac{1}{\bar{a}_{11}} \text{ and } \bar{D}_x = \frac{1}{\bar{d}_{11}} \tag{5.28}$$

Section 5-2 will discuss on investigating the variation of centroid location, as the structural geometry is sequentialy varied from an open cross-sectioned curved shell configuration to a fully closed composite tube configuration respectively.

Upon identifying the location of centroid, finite loads (axial force and bending moment) are individually applied and the structural response is characterized based on ply stresses and strains respectively. Additionally, parametric investigations are conducted (Sections 5-3 and 5-4) to gain a quick understanding on the mechanical behavior of such curved composite shell configurations. Ply stress results computed analytically are compared with FEM results.

5-2 Characteristic Axial and Bending Stiffness Parametric Study

Initial sections from Chapter-4 and Chapter-5 focused on proposing and mathematically formulating a set of novel governing equations that offer the capability to generate simple, closed-form analytical solution tools for characterizing the mechanical response of thin-walled, closed and open cross-sectioned, multi-directionally laminated, composite cylindrical shells and tubes in terms axial stiffness, bending stiffness, mid-plane reference strains and curvatures, centroid and ply-stresses respectively. Having developed a robust methodology that generates accurate estimates for the aforementioned structural variables, a parametric investigation is immediately proposed that strives to effectively capture the influence of shell curvature factor $1+\frac{z^{"}}{R_m}$ on primary structural characteristics such as axial and bending stiffness. Three classes of open-celled curved composite cylindrical shells are considered for this preliminary study. Their cross-sectional arc angles are assumed as follows;

- Case 1: arc angle spanning from $\left(-\frac{\pi}{4}\right)\text{to}\left(+\frac{\pi}{4}\right)$ radians ($2\alpha = 90^{o}$).
- Case 2: arc angle spanning from $\left(-\frac{\pi}{2}\right)\text{to}\left(+\frac{\pi}{2}\right)$ radians ($2\alpha = 180^{o}$).
- Case 3: arc angle spanning from $\left(-\frac{3\pi}{4}\right)\text{to}\left(+\frac{3\pi}{4}\right)$ radians ($2\alpha = 270^{o}$).

Based on the closed-form stiffness prediction equations (Eq. 5.24) developed utilizing the extended composite shell theory approach, case 1, case 2 and case 3 are investigated with respect to their axial and bending stiffnesses against the limiting case of a thin-walled closed composite tube construction. The four models are investigated through parametric variations in tube mean radius R_m ranging from 0.1 inch to 2.5 inches in sequential increments of 0.2 inches respectively. A six ply symmetric-balanced

configuration with a $\left[\pm 45/0\right]_{symm}$ stacking sequence is assumed to model the ply lay-up on all the aforementioned cases . Table-6 illustrates the assumed material properties of AS4/3501-6 carbon-epoxy composite material system [13] utilized for conducting this study. A constant length of 10 inches and a uniform cross-sectional thickness of the tube are assumed throughout the analysis.

Table 5-1 Material Properties for (AS4/3501-6) Carbon Epoxy

Property	Value
E_{11}	$21.3*10^6$ psi
$E_{22}= E_{33}$	$1.5*10^6$ psi
$\upsilon_{12} = \upsilon_{13}$	0.27
υ_{23}	0.54
$G_{12}= G_{13}$	$1*10^6$ psi
G_{23}	$5.4*10^5$ psi
t_{ply}	0.005 inches
α_1	$-0.5*10^{-6}$ in/in/ ^{o}F
α_2	$15*10^{-6}$ in/in/ ^{o}F

The key objective of this parametric study is to plot and examine the distribution trends in axial and bending stiffnesses for varying circumferential arc angles as a function of tube mean-radius R_m. In view of strengthening the validity of the stiffness results obtained through extended shell theory approach, axial and bending stiffness data corresponding to the case of the curved shell configuration characterized by varying mean-radius R_m, and arc angle spanning from $\left(-\frac{\pi}{4}\right)\text{to}\left(+\frac{\pi}{4}\right)$ radians ($2\alpha = 90^{o}$) are compared against FEM results as shwon in Table 7 and Table 8 respectively. Bending stiffness results computed using extended shell theory approach indicate good agreement in comparison to the FEM based approximations.

Table 5-2 Bending Stiffness Predictions for a $\left[\pm 45/0\right]_{symm}$ Curved Shell: Arc Angle $\left(-\frac{\pi}{4}\right)$ to $\left(+\frac{\pi}{4}\right)$ radians

Mean-radius R_m	FEM Results (lb/in^2)	Plate approach (lb/in^2)	Shell approach (lb/in^2)
0.1	5.36 E+00	4.76 E+00	5.28 E+00
0.3	1.04E+02	9.49 E+01	1.02 E+02
0.5	4.54 E+02	4.27 E+02	4.49 E+02
0.7	1.23 E+03	1.16 E+03	1.22 E+03
0.9	2.56 E+03	2.46 E+03	2.53 E+03
1.1	4.62 E+03	4.49 E+03	4.57 E+03
1.3	7.62 E+03	7.40 E+03	7.54 E+03
1.5	1.17 E+04	1.14 E+04	1.16 E+04
1.7	1.69 E+04	1.65 E+04	1.68 E+04
1.9	2.35 E+04	2.31 E+04	2.33 E+04
2.1	3.17 E+04	3.11 E+04	3.14 E+04
2.3	4.17 E+04	4.09 E+04	4.13 E+04
2.5	5.33 E+04	5.25 E+04	5.28 E+04

The presence of shell curvature factor $1+\frac{z^{"}}{R_m}$ does not exhibit a significant variation while comparing the axial stiffness estimations computed through three distinct approaches (FEM, shell approach and plate approach) respectively.

Table 5-3 Axial Stiffness Predictions for a $[\pm 45/0]_{symm}$ Curved Shell: Arc Angle $\left(-\frac{\pi}{4}\right)\text{to}\left(\frac{\pi}{4}\right)$ radians

Mean-radius R_m	FEM Results (lb/in^2)	Plate approach (lb/in^2)	Shell approach (lb/in^2)
0.1	5.92 E+02	5.75 E+02	5.86 E+02
0.3	1.41 E+03	1.28 E+03	1.35 E+03
0.5	2.16 E+03	2.07 E+03	2.09 E+03
0.7	3.02 E+03	2.88 E+03	2.93 E+03
0.9	3.71 E+03	3.69 E+03	3.70 E+03
1.1	4.56 E+03	4.50 E+03	4.54 E+03
1.3	5.36 E+03	5.31 E+03	5.34 E+03
1.5	6.21 E+03	6.13 E+03	6.18 E+03
1.7	6.69 E+03	6.64 E+03	6.68 E+03
1.9	7.81 E+03	7.75 E+03	7.79 E+03
2.1	8.59 E+03	8.57 E+03	8.58 E+03
2.3	9.41 E+03	9.38 E+03	9.40 E+03
2.5	1.08 E+04	1.04 E+04	1.05 E+04

Figure 5-3 and Figure 5-4 represent the combined axial stiffness plots (case-1, case-2 and case-3) as a function of mean-radius R_m of the curved composite shell. Figure 5-3 compares the variation in axial stiffness for the first two cases of interest namely: a) curved composite shell with a circumferential arc angle spanning from $\left(-\frac{\pi}{4}\right)\text{to}\left(+\frac{\pi}{4}\right)$ radians ($2\alpha = 90^o$) and b) curved composite shell with a circumferential arc angle

spanning from $\left(-\frac{\pi}{2}\right)$ to $\left(+\frac{\pi}{2}\right)$ radians ($2\alpha = 180^{\circ}$). Figure 5-4 compares the variation in axial stiffness for the last two cases of interest namely: c) curved composite shell with a circumferential arc angle spanning from $\left(-\frac{3\pi}{4}\right)$ to $\left(+\frac{3\pi}{4}\right)$ radians ($2\alpha = 270^{\circ}$) and d) completely closed cross-section cylindrical composite tube configuration.

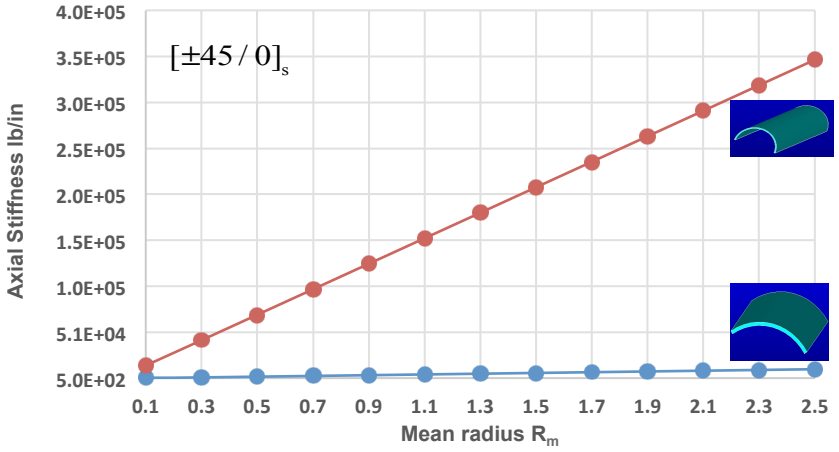

Figure 5-3 Axial Stiffness Distribution as a Function of Shell Mean Radius: Case (a) and Case (b)

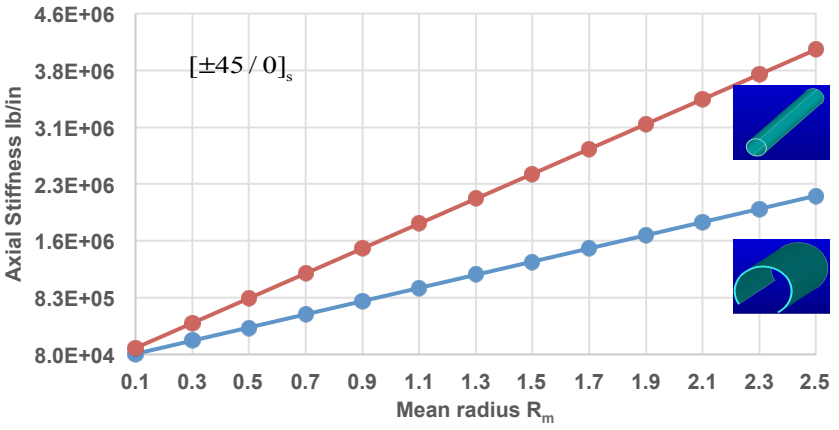

Figure 5-4 Axial Stiffness Distribution as a Function of Shell Mean Radius: Case (c) and Case (d)

In a similar fashion, Figure 5-5 and Figure 5-6 collectively represent the bending stiffness plots based on the analytical predictions utilizing the extended composite shell theory approach as a function of mean-radius R_m of the curved composite shell.

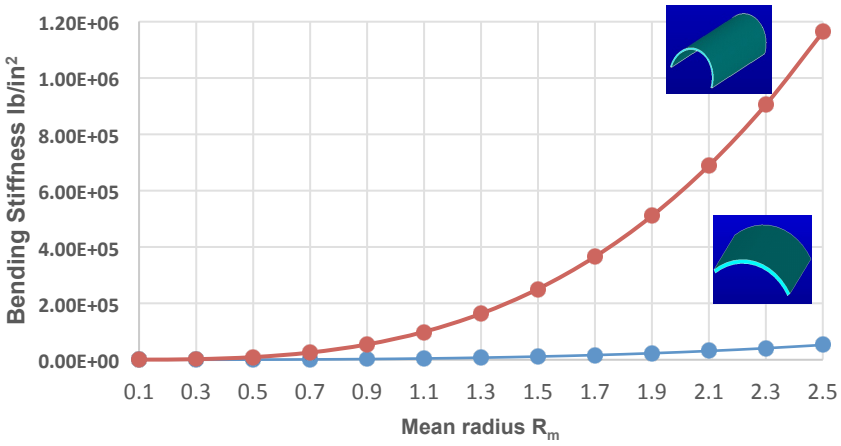

Figure 5-5 Bending Stiffness Prediction as a Function of Shell Mean Radius: Case (a) and Case (b)

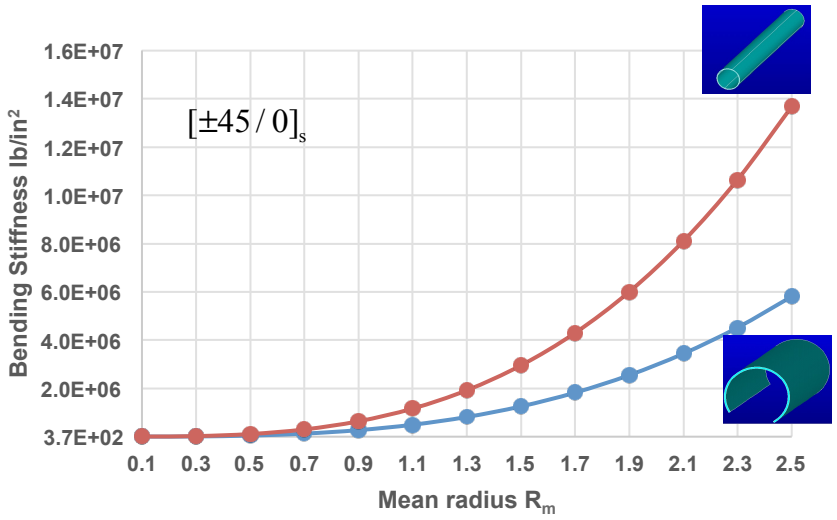

Figure 5-6 Bending Stiffness Predictions as a Function of Shell Mean Radius: Case (c) and Case (d)

Figure 5-5 compares the variation in bending stiffness for the first two cases of interest namely: a) curved composite shell with a circumferential arc angle spanning from $\left(-\frac{\pi}{4}\right)\text{to}\left(+\frac{\pi}{4}\right)$ radians ($2\alpha = 90^{o}$) and b) curved composite shell with a circumferential arc angle spanning from $\left(-\frac{\pi}{2}\right)\text{to}\left(+\frac{\pi}{2}\right)$ radians ($2\alpha = 180^{o}$). Figure 5-6 compares the variation in bending stiffness for the last two cases of interest namely: c) curved composite shell with a circumferential arc angle spanning from $\left(-\frac{3\pi}{4}\right)\text{to}\left(+\frac{3\pi}{4}\right)$ radians ($2\alpha = 270^{o}$) and d) completely closed cross-section cylindrical composite tube configuration.

Motivated from the development of a simple closed-form analytical prediction tool that accurately approximates the elementary structural stiffness characteristics such as axial stiffness and bending stiffness for slender, thin-walled, open and closed cross-section, cylindrical composite shell members, this preliminary parametric investigation provides an effective means in achieving a first understanding into the mechanical behavior of such configurations. In an effort to enhance the insight into the structural response of this class of cylindrical shell models, a ply-per-ply based in-plane mechanical stress $\left(\sigma_{x},\sigma_{y},\tau_{xy}\right)$ investigation is further conducted. The subsequent sections of this chapter is focused on constructing a FE model in the presence and absence of a temperature environment .

5.3 Finite Element Modeling of Curved Composite Cylindrical Shells

An ANSYS based geometrically linear FE analysis is established to model and computationally simulate the structural response of a thin-walled, multi-directionally laminated curved cylindrical shell configuration under centroidal tension and bending

conditions. A six ply symmetric-balanced configuration with a $\left[\pm 45/0\right]_{symm}$ stacking sequence is initially assumed. Table-6 lists the composite material properties of (AS4/3501-6) Carbon-Epoxy material system. A constant length of 10 inches and an uniform cross-sectional thickness ($t_{laminate}$=0.03 inches) of the tube are assumed throughout the analysis. Composite tube mean-radius R_m is varied incrementally in steps of 0.1 inch from 0.1 inch to 2.5 inches respectively. Initial study essentially deals with the solid modeling and finite element analysis of a thin-walled, curved, cylindrical shell configuration. As shown in (Fig. 5-7), a 3-D volume schematic of the thin-walled shell construction is initially constructed upon extruding a generated 2-D area characterized by its cross-sectional properties. The model is further categorized as a shell where the stacking arrangement is fed as a necessary input into the “sectional property” dialog box of the composite design interface [12].

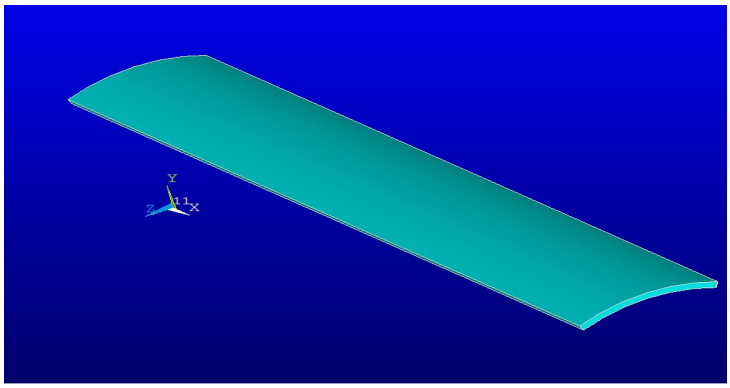

Figure 5-7 3-D Volume Schematic of a Curved Composite Cylindrical Shell

Design model tree associated with the curved shell volume generation is instructed to be discretized into 6 uniformly thick layers that consist of preferentially oriented laminas stacked in a longitudinal fashion and symmetrical about the mid-section circumferentially bisecting the shell thickness. Figure 5-8 depicts the assigned orientation pattern for each of the plies constituting the physical lay-up of the composite shell. Mesh discretization on

the curved shell structure is achieved utilizing a “volume sweep“ feature that uniformly assigns the sectional properties of the material system to the contour. A higher order 20-noded 3-DOF, 3-D, Layered-Structural-Solid Element addressed as SOLID-186 (Fig 5-9) in the ANSYS element library [13] is utilized to model the meshes for this configuration.

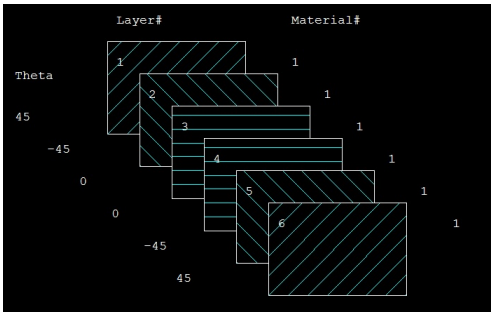

Figure 5-8 Pictorial View of Fiber Orientation in a 6-Ply Laminate Configuration

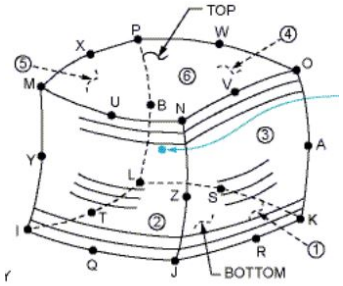

Figure 5-9 SOLID 186 Geometry Schematic and Node Structure [12]

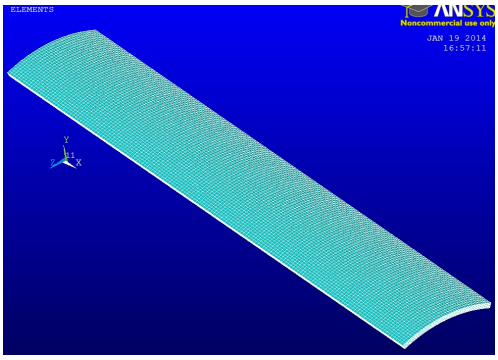

Figure 5-10 Thin-Walled Curved Composite Shell Discretization Model

This element has been fundamentally chosen to analyze the mechanical response as it exhibits a quadratic displacement behavior coupled with an inherent curvature characteristic to effectively capture various bending and twisting phenomenon associated with a multitude of loading conditions. SOLID 186 Layered Structural Solid is well suited for modeling thin-to-moderately-thick shells or solid. The element allows up to 250 different material layers. The most convenient design aspect of this element is the capability to associate SOLID-186 with a fundamental shell section. The layered composite specifications (including layer thickness, material orientation, and the number of integration points through the thickness of the layer) are specified via shell section [12]. The preliminary design phase of the curved composite shell further involved the assignment of an additional cylindrical coordinate system that primarily orients all the relevant geometric keypoints and ply lay-up associated with the contour of the curved shell structure. The total arc angle that essentially defines the circumferential arc length of the curved laminate is assumed to be 45^0. The mesh density obtained is in the order of 145800 elements. The structural boundary conditions of an ideal cantilever type shell configuration is simulated (Fig. 5-11) by essentially imposing/relaxing the following mechanical constraints:-

- Longitudinal (x-direction) degrees of freedom constrained across all nodes defining the discretized left-end of the circumferential contour.
- Lateral (y-direction) degrees of freedom constrained across the center nodes (left end) defining the thickness of the shell thus accommodating for Poisson's ratio effect induced deformation phenomenon.
- Translational and rotational degrees of freedom restricted specifically on the mid-node (left end) that traverses through the circumferential mid-plane and symmetric y-plane of the curved composite shell.

- The right-end of the curved composite shell is completely unrestrained and free to translate and rotate in all directions.

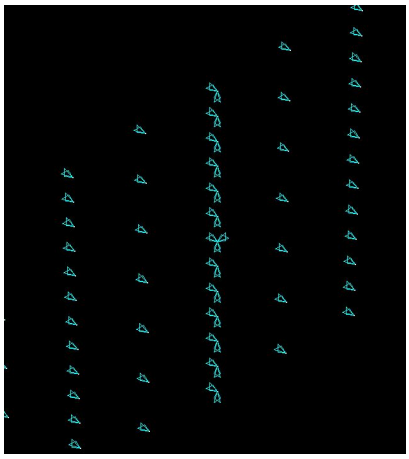

Figure 5-11 Imposed Boundary Conditions across Fixed Edge

5-3-1 Numerical Prediction of Centroid Location Z_c via FEM

Having computationally constructed a 2-D sketch of the curved composite shell and extending it to a 3-D entity upon along-the-thickness-extrusion, generated an optimal mesh density to produce a numerically converged solution, the next task deals with numerically determining the centroidal point. This is accomplished by initially applying a finite-magnitude, uniformly distributed moment that collectively amounts to 1lb-in across all the nodes characterizing the free-end of the shell structure.

In the post-processing stage, values of in-plane nodal strains are recorded at two specific locations A and B along the cross-section representing the free-end. Point A is precisely located along the circumferential path traced by the outer radius R_o of the shell and coincides with the Y=0 plane and similarly, Point B is precisely located along the circumferential path traced by the inner radius R_i of the curved composite shell and coincides with the Y=0 plane. These strains classified as ε_x^A and ε_x^B, denote the induced

axial. These strains, classified as ε_x^A and ε_x^B, denote the net induced axial strain upon the application of a finite bending moment to the shell structure. In view of the fundamental classical lamination-theory equation (Eqn. 3.13) that mathematically represents the magnitude of in-plane strains at any arbitrary point located along the cross-sectional thickness in terms of mid-plane strains $\varepsilon_{x,y}^0$ and curvature $\kappa_{x,y}^o$, Extensional strains ε_x^A and ε_x^B can be identically expressed with regards to $\varepsilon_{x,y}^0$ and curvature $\kappa_{x,y}^o$ associated with the curved composite shell.

$$\begin{aligned} \varepsilon_x^A &= \varepsilon_x^0 + Z_A \kappa_x^0 \\ \varepsilon_x^B &= \varepsilon_x^0 + Z_B \kappa_x^0 \end{aligned} \tag{5.30}$$

where Z_A and Z_B denote the precise vertical distances along the thickness of the composite shell, calculated from the mean-radius of curvature R_m respectively. From this set of linear equations, the unknown variables namely: $\varepsilon_{x,y}^0$ and curvature $\kappa_{x,y}^o$ can be computed. However, this elementary equation can be refocused from the perspective of centroidal extensional strain. Conceptually, there exists a specific point Z_c across the cross-section of the curved shell, where, the net longitudinal strain denoted by $\varepsilon_x^{centroid}$ is zero. Rewriting, $\varepsilon_x^{centroid}$ in terms of $\varepsilon_{x,y}^0$ and curvature $\kappa_{x,y}^o$ we obtain,

$$\varepsilon_x^{centroid} = \varepsilon_x^0 + Z_c \kappa_x^0 = 0 \tag{5.31}$$

Substituting, the pre-determined values of $\varepsilon_{x,y}^0$ and curvature $\kappa_{x,y}^o$ from Eqn. (5.3.1) into Eqn. (5.3.2), we can compute the numerically predicted location of Z_c via employing a FE scheme.

Fundamentally, when an axial load is applied precisely on the centroid of the structure, the resulting deformation is characterized by a uniform stretch. The structural deformation exhibits no bending. In other words, the surface strains are uniform for each layer constituting the ply-lay-up. In order to substantiate the analytically obtained centroid predictions, surface strains are evaluated analytically and compared against FEM based surface strain estimations.

In-plane surface strains are determined analytically utilizing Eq. (5.32) as follows: -

$$\left\{\varepsilon_{x-y}^{total}\right\}_k = \left\{\begin{array}{c}\varepsilon_x\\ \varepsilon_y\\ \gamma_{xy}\end{array}\right\}_{k^{th}layer} = \left\{\begin{array}{c}\varepsilon_x^o\\ \varepsilon_y^o\\ \gamma_{xy}^o\end{array}\right\} + \left((Z_c + z^{"}) * Cos\theta\right) * \left\{\begin{array}{c}\kappa_x^o\\ \kappa_y^o\\ \kappa_{xy}^o\end{array}\right\} - \left\{\begin{array}{c}\alpha_x\\ \alpha_y\\ \alpha_{xy}\end{array}\right\}_k \Delta T - \left\{\begin{array}{c}\beta_x\\ \beta_y\\ \beta_{xy}\end{array}\right\}_k \Delta C \quad (5.32)$$

The following case is investigated to validate the analytically determined centroid predictions: Assumed geometric properties of the composite strip are; length = 10 inches, ply thickness = 0.005in, number of plies = 6, total laminate thickness = 0.03 inches, laminate lay-up = $\left[\pm 45/0\right]_{symm}$, total arc length $\left(2\alpha\right)$ = 90^0, strip inner radius R_i=0485 inches and strip outer radius R_o=0.515 inches respectively. The curved composite strip is characterized by assuming the composite material properties of AS4/3501-6 carbon-epoxy composite material system as shown in Table 6 [13] respectively.

A axial load of 350 lbs is assumed to be applied to the analytically predicted centroid value (Z_c= 0.44696 inches) and the longitudinal strain ε_x variation is examined across the circumference of the 0 deg plies (3rd layer in the $\left[\pm 45/0\right]_{symm}$ lay-up). Fig 5-12 shows the combined plot of surface strain distribution detemined analytically and via FEM. Excellent agreement is achieved between the two results .

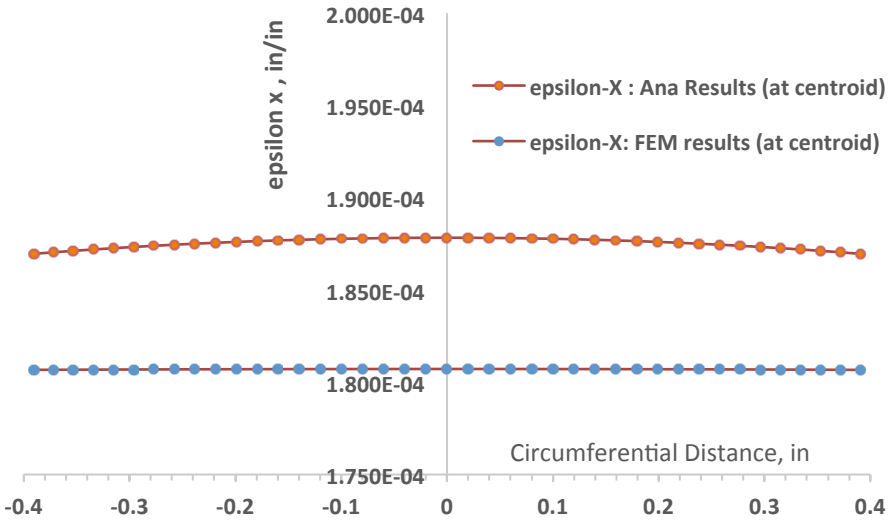

Figure 5-12 Longitudinal strain distribution as a fn. Of circumferential arc length

Surface strain bands for the 0 deg layer are extracted (using FEM) and shown in Fig 5-13. it is observed that the strain bands show a uniform coloration across the circumference except at the boundaries. Small variations in strains across the edges can be attributed to edge effects.

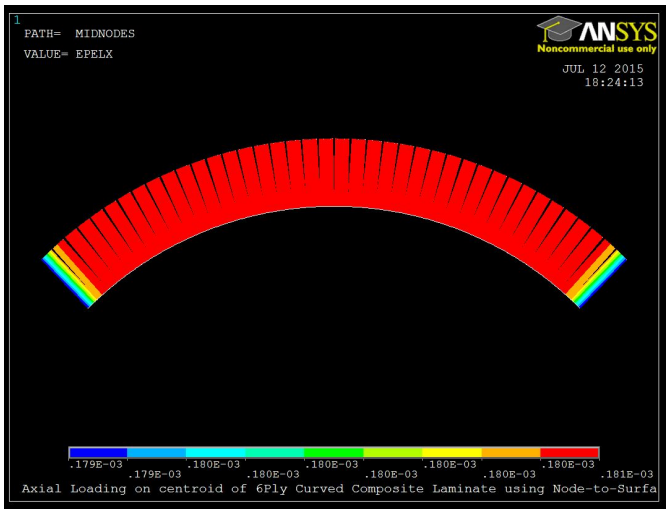

Figure 5-13 Uniform Coloration of Strain Bands across Circumference

5-3-2 Centroid Prediction Results: Substantiation & Parametric Study

Having outlined a strong analytical and FEM based solution methodology (Sections 5.1.1 & 5.3.1) that is capable of accurately evaluating the location of centroid to mechanically characterize the extension-bend type structural response in thin-walled, curved and closed cylindrical composite shells, current task indulges in methodically generating prediction data from the two aforementioned distinct schemes. The cross-sectional location of the centroid is determined along the thickness direction (global z-axis) from the point of mean-radius of curvature R_m and plotted as a function of increasing circumferential arc angles that specifically govern the classification of cylindrical shells from an open-cell configuration to a completely closed composite tube configuration.

Three classes of shell configurations are parameterized based on their geometric mean-radius of curvatures namely: R_m = 0.2, 0.5 and 0.8 and circumferential arc angles (2α) sequentially varying from 5^o to 360^o respectively. Variation in centroidal location is examined for a 6-ply symmetrical-balanced composite laminate configuration under the presence and absence of temperature environment. Extraction of data points are performed through 36 iterations on each class of composite shell configuration and a graphical comparison is made against the FEM based prediction results. Figure 5-12 represents the combined plot of analytical and FEM based centroid location estimations along the thickness direction as a function of total circumferential arc angle. Excellent concurrence has been witnessed in prediction results acquired via employing the previously generated shell theory based analytical framework and FEM technique. For example, in the case of cylindrical shell configurations defined by a constant mean-radius R_m=0.5 in and a uniform laminate thickness of 0.03 inches, it can be observed for small circumferential angles ($2\alpha \leq 50^o$) that, the predicted centroid location falls inside the

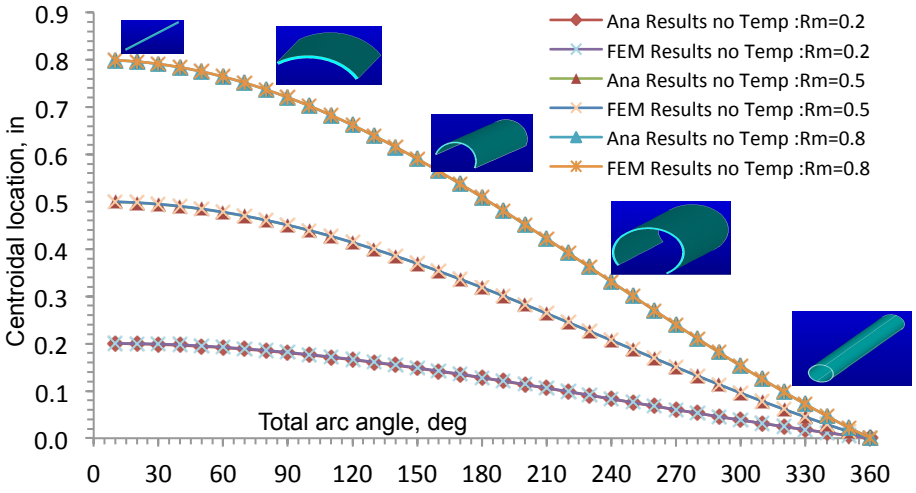

Figure 5-14 Variation in Centroidal Location Z_c as a fn. of Total Arc Angle 2α (no temperature)

Boundaries defined by the cross-sectional area of composite member as opposed to cylindrical shell configurations with larger arc angles $(2\alpha \geq 50^{\circ})$ that incrementally translate towards a fully closed composite shell construction. For thin-walled shells marked by miniscule angles $(2\alpha \leq 20^{\circ})$, the influence of shell curvature on the cross-sectional geometry significantly diminishes; as a consequence, the slender composite member can be fundamentally assumed as a thin rectangular strip that is solely characterized by its infinitesimally growing width. Under such a structural assumption, the centroid is predicted to be located on the mid-line bisecting the laminate-thickness or in very close proximity to the laminate thickness. On the contrary, for curved shell members dictated by progressively increasing, more physically realistic arc angles, predicted results reveal the centroidal location to gradually descend towards the mean-radius of curvature point and precisely for a cylindrical composite shell configuration defined by a total arc angle $2\alpha = 360^{\circ}$; centroid estimates from analytical equation and FE scheme

depict a substantially small value approaching 0; which implies that the centroid resides in extremely close proximity to the mean-radius of curvature point.

Table 5-4 Centroid Location Predictions: Analytical vs. FEM (no Temperature)

Arc Angle (deg)	R_m=0.2 in		R_m=0.5 in		R_m=0.8 in	
	ANA (in)	FEM (in)	ANA (in)	FEM (in)	ANA (in)	FEM (in)
10	0.1991	0.19894	0.49702	0.49691	0.79505	0.79479
90	0.17916	0.17908	0.44696	0.44681	0.714603	0.71448
180	0.12670	0.12622	0.31605	0.31594	0.50322	0.50319
270	0.05970	0.05968	0.14891	0.14866	0.23799	0.23719

5-3-3 Computational Modeling and Analyses of Curved Cylindrical Shell Laminates Subject to Longitudinal Tensile Force on Centroid

Figure 5-15 shows a close up view of the free edge of the strip model with an axial load applied at the centroid. The edge nodes are tied with respect to the centroidal node such that a paring in the degrees of freedom is established between the pilot node (centroidal node) and the slave nodes (edge nodes) respectively. For the tensile loading case, a finite longitudinal extension load of 10 lbs. is applied on the centroid.

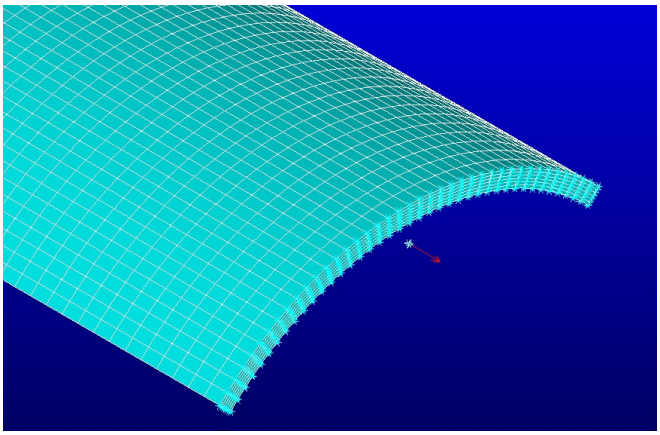

Figure 5-15 Close-up Pictorial View of Tensile Load Applied to Centroidal Point

The present work investigates the in-plane stress distributions (σ_x, σ_y and ς_{xy}) for a six-ply

symmetric-balanced curved composite laminate configuration with a $[\pm 45/0]_s$ laminate stacking sequence. A finite axial loading of 10 lbs. is applied on the PILOT node defining the centroidal location of the structure. The load is distributed uniformly among all the right-extremity nodes that are marked as TARGET nodes. In order to eliminate the influence of localized nodal deformations consistent with edge-effects, a circumferential nodal cross-section located at 50%L is assigned as the station of interest. These nodes are systematically utilized for all the following FEM based mechanical response investigations. In-plane stress distributions along the curved contour for each of the lamina constituting the ply lay-up are analyzed and compared with analytical data. Figure 5-16 depicts the discretized simulated image of the curved shell structure generated utilizing a higher order 20-noded Layered Structural Solid Element addressed as SOLID-186 in the ANSYS element library [12].

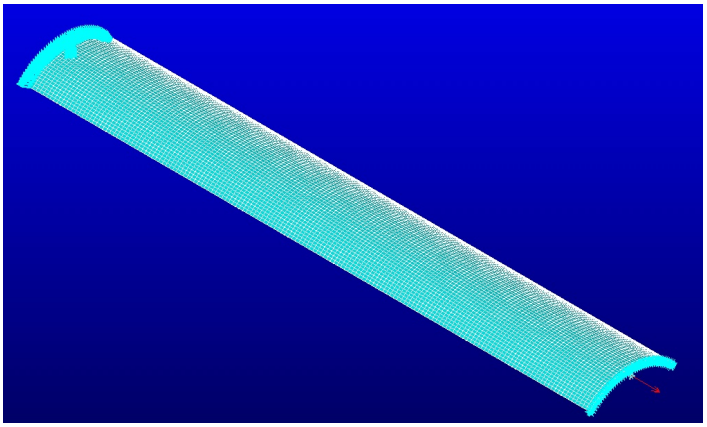

Figure 5-16 Discretized Curved Composite Shell under N_x at Centroid

The total arc angle that essentially defines the circumferential arc length of the curved laminate is assumed to be 90^0 for this loading case. The model size is in the order of 145800 elements. An ideal cantilever type configuration is simulated via implementing the structural boundary conditions as outlined in the initial commentaries of section 5.3 respectively.

5-3-4 In-plane Ply-per Ply Stress Recovery in Curved Laminate Shells

A broad mechanical investigation on the structural behavior of thin-walled, fiber-reinforced, open cross-sectioned curved shells can be obtained upon conducting a response characterization in terms of ply-stresses that are induced through centroidally applied tension and bending type loading conditions. surface strains characterizing each of the plies can be methodically evaluated and can be expressed as

$$\left\{\varepsilon_{x-y}^{total}\right\}_k = \left\{\begin{array}{c}\varepsilon_x\\ \varepsilon_y\\ \gamma_{xy}\end{array}\right\}_{k^{th}layer} = \left\{\begin{array}{c}\varepsilon_x^o\\ \varepsilon_y^o\\ \gamma_{xy}^o\end{array}\right\} + \left((Z_c + z^*) * \mathrm{Cos}\theta\right) * \left\{\begin{array}{c}\kappa_x^o\\ \kappa_y^o\\ \kappa_{xy}^o\end{array}\right\} - \left\{\begin{array}{c}\alpha_x\\ \alpha_y\\ \alpha_{xy}\end{array}\right\}_k \Delta T - \left\{\begin{array}{c}\beta_x\\ \beta_y\\ \beta_{xy}\end{array}\right\}_k \Delta C \qquad (5.33)$$

where, Z_c is the location of the centroid, $z^{"}$ is the incremental distance measured from the reference-plane bisecting the laminate thickness. The in-plane stresses can be subsequently determined utlizing Eq. (5.34) and can be shown as

$$\left\{\begin{array}{c}\sigma_x\\ \sigma_y\\ \tau_{xy}\end{array}\right\}_k^{mech} = \left[\bar{Q}"_{x-y}\right]_k * \left\{\left\{\begin{array}{c}\varepsilon_x^o\\ \varepsilon_y^o\\ \gamma_{xy}^o\end{array}\right\} + \left((Z_c + z^*) * \mathrm{Cos}\theta\right) * \left\{\begin{array}{c}\kappa_x^o\\ \kappa_y^o\\ \kappa_{xy}^o\end{array}\right\} - \left\{\begin{array}{c}\alpha_x\\ \alpha_y\\ \alpha_{xy}\end{array}\right\}_k \Delta T - \left\{\begin{array}{c}\beta_x\\ \beta_y\\ \beta_{xy}\end{array}\right\}_k \Delta C\right\} \qquad (5.34)$$

where $\left\{\sigma_{x-y}^{mech}\right\}_k$ is fundamentally an implicitly defined function of centroidal location Z_c, fiber-orientation angle β, element rotation angle θ, structural geometry, equivalent averaged elastic stiffness parameters and the laminate's ply stacking sequence. Thermal and moisture coefficients are transformed with respect to the global reference coordinate system. Since, hygrothermal loads $(\Delta T, \Delta c)$ are directly associated to inducing hygrothermal strains $(\alpha.\Delta T, \beta.\Delta c)$ on a composite structure, a strain based rotational transformation is performed to generate the appropriate thermal and moisture coefficients respectively and can be shown as

$$\left\{\alpha'_{1-2}\right\}_k = \left[T_\varepsilon(-\beta)\right]_k * \left\{\alpha_{1-2}\right\}$$
$$\left\{\alpha_{x-y}\right\}_k = \left[T_\varepsilon(\theta)\right] * \left\{\alpha'_{1-2}\right\}_k \quad (5.35)$$

Mechanical stress predictions are computed analytically and their validity is confirmed in comparison with FE-simulation based stress predictions. Figures 5-17 through Figure 5-19 represent the in-plane stress (σ_x,σ_y and τ_{xy}) distributions for +45° plies along the circumferential length of the curved shell. Similarly, Figures 5-20 through 5-25 portray the in-plane stress (σ_x,σ_y and τ_{xy}) distributions for –45° and 0° plies along the arc length of the curved shell.

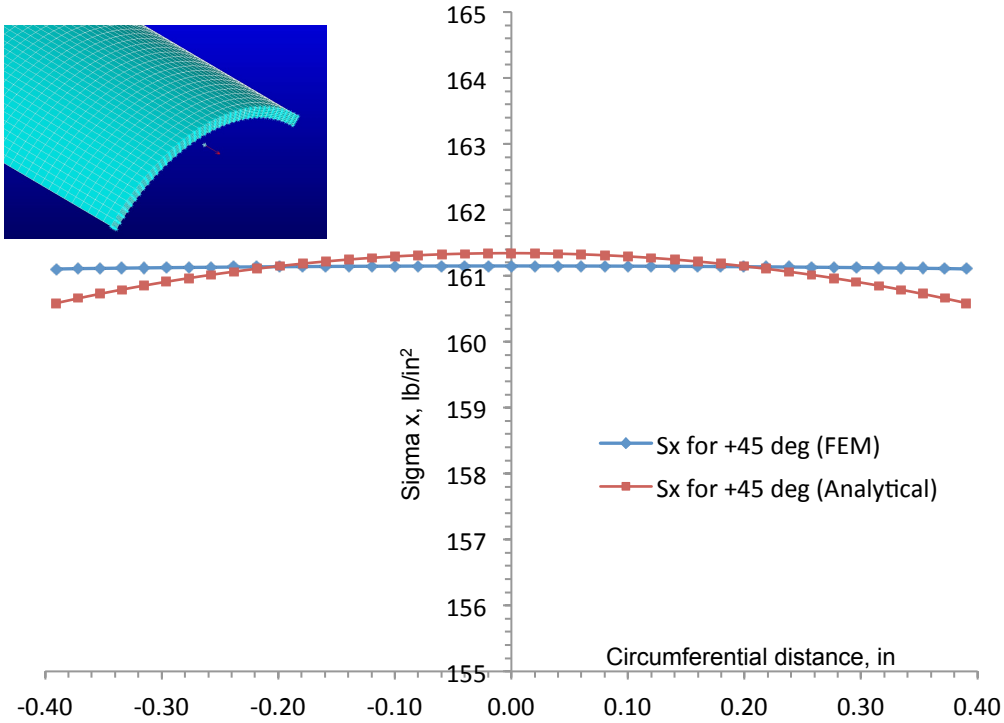

Figure 5-17 σ_x Distribution in +45 deg Plies under Axial Load as a fn. of Circumferential Arc Length $(\Delta T = 0^0 F)$

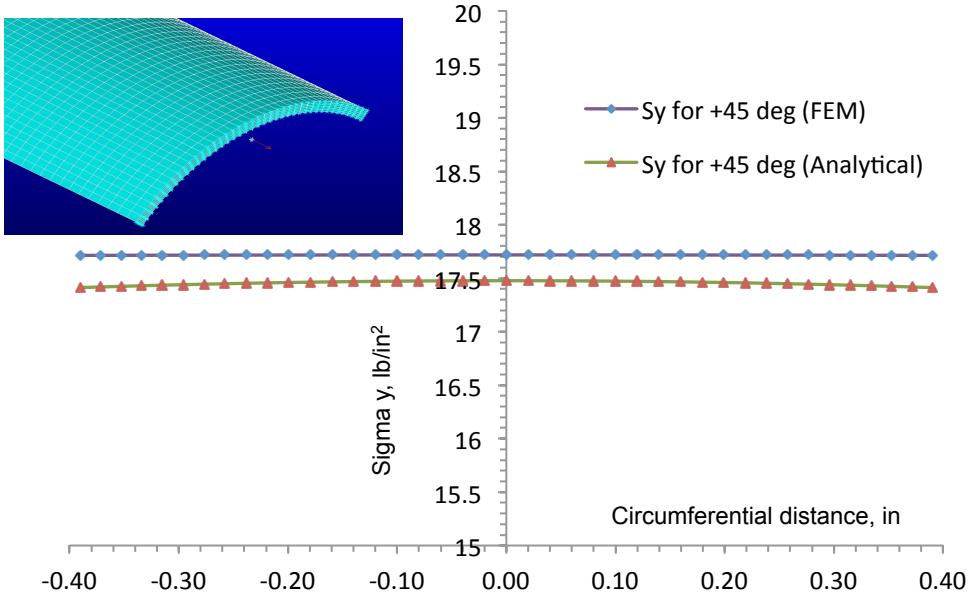

Figure 5-18 σ_y Distribution in +45 deg Plies under Axial Load as a fn. of Circumferential Arc Length $(\Delta T = 0^0 F)$

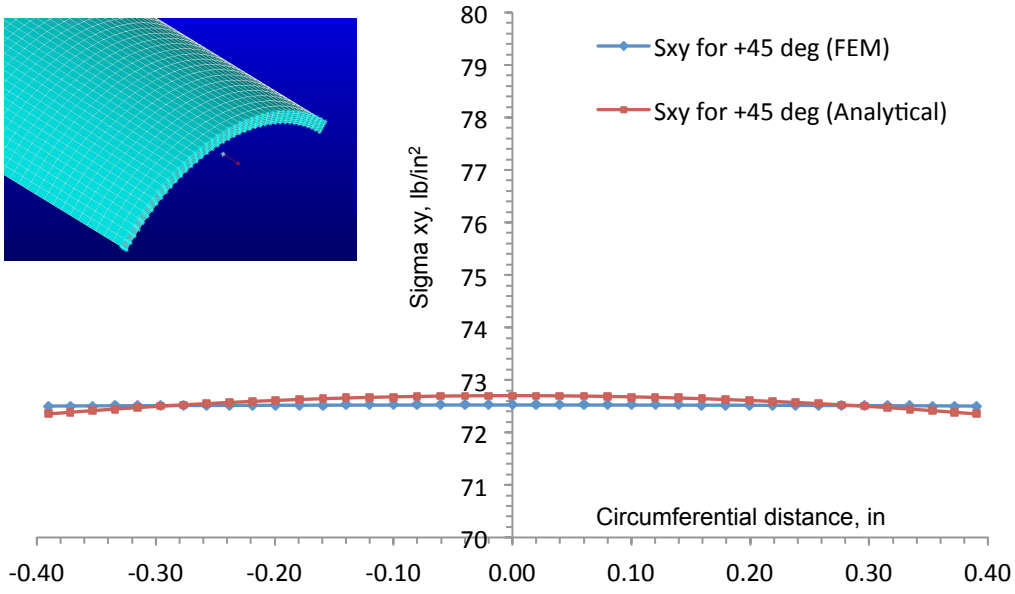

Figure 5-19 τ_{xy} Distribution in +45 deg Plies under Axial Load as a fn. of Circumferential Arc Length $(\Delta T = 0^0 F)$

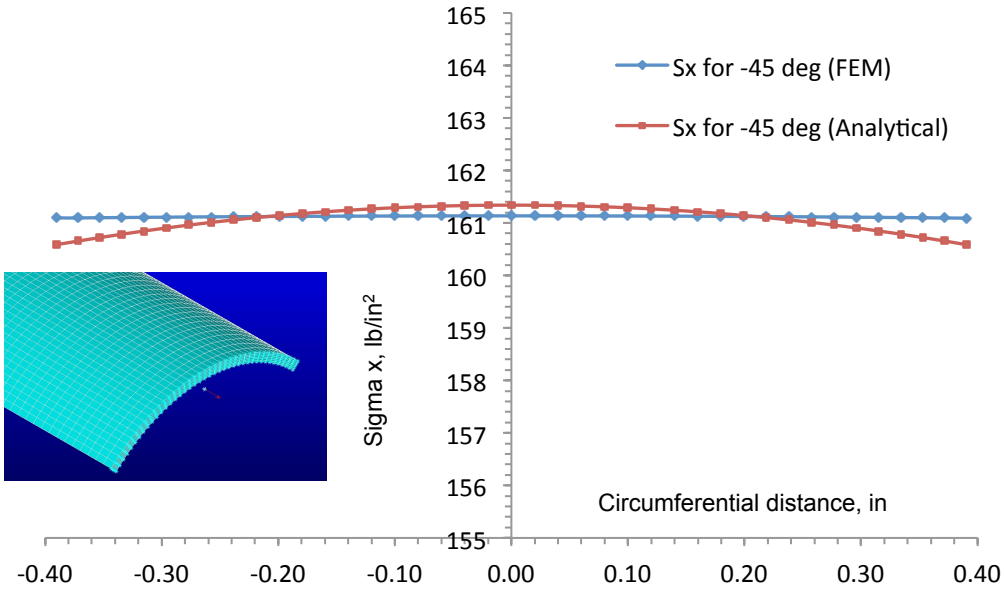

Figure 5-20 σ_x Distribution in -45 deg Plies under Axial Load as a Fn. of Circumferential Arc Length $\left(\Delta T = 0^0 F\right)$

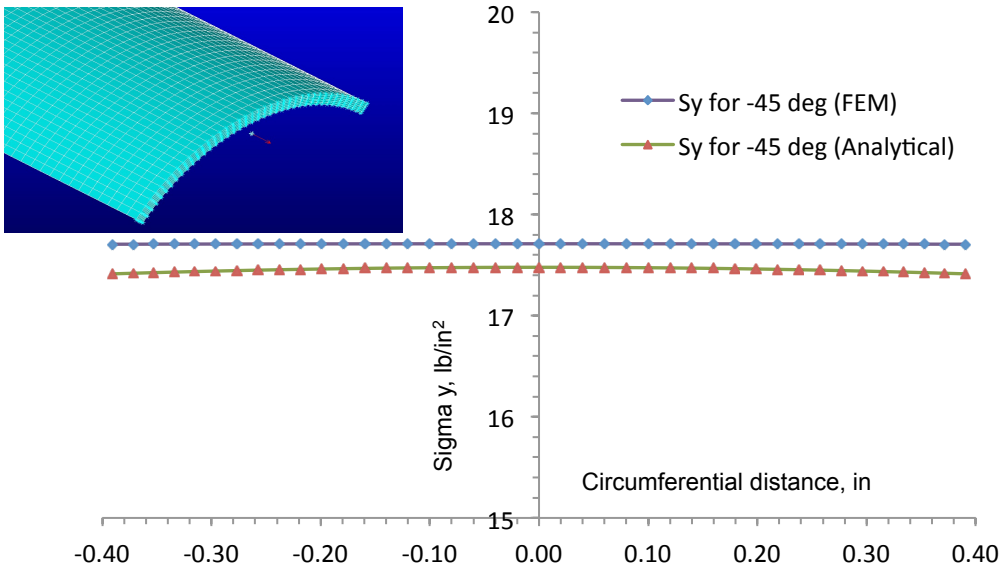

Figure 5-21 σ_y Distribution in -45 deg Plies under Axial Load as a Fn. of Circumferential Arc Length $\left(\Delta T = 0^0 F\right)$

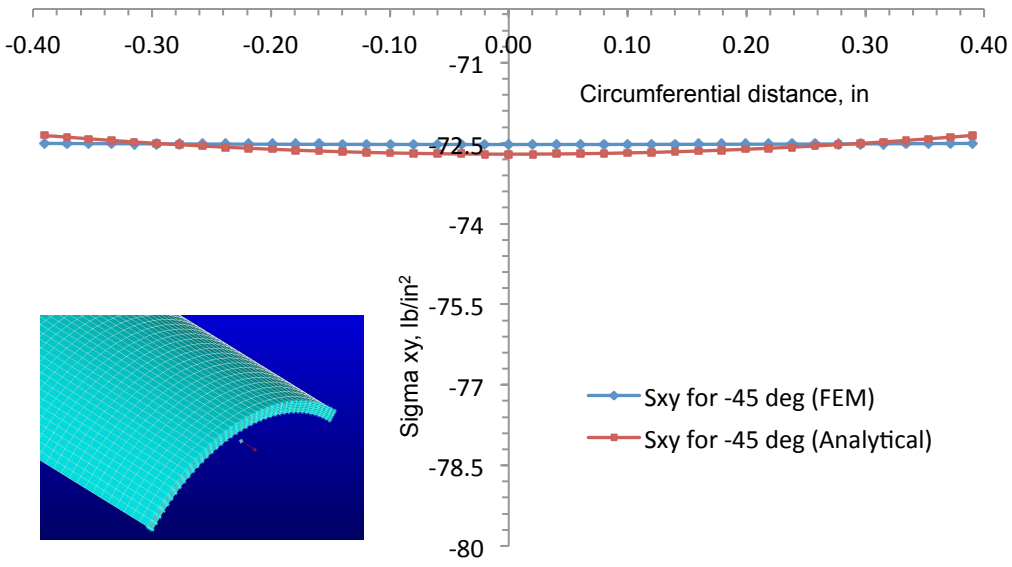

Figure 5-22 τ_{xy} Distribution in -45 deg Plies under Axial Load as a fn. of Circumferential Arc Length $\left(\Delta T = 0^0 F\right)$

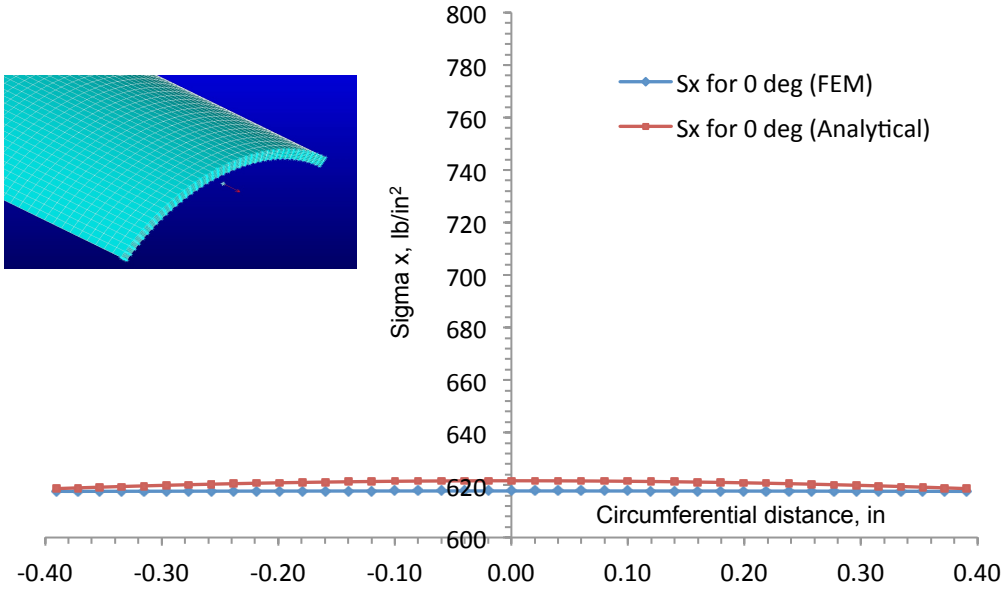

Figure 5-23 σ_x Distribution in 0 deg Plies under Axial Load as a fn. of Circumferential Arc Length $\left(\Delta T = 0^0 F\right)$

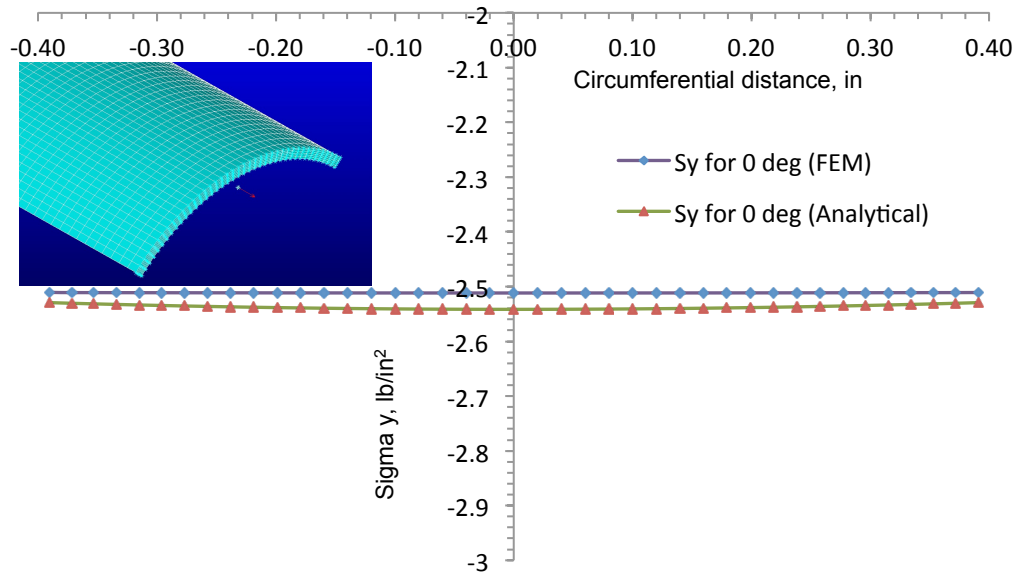

Figure 5-24 σ_y Distribution in 0 deg Plies under Axial Load as a Fn. of Circumferential Arc Length $\left(\Delta T = 0^0 F\right)$

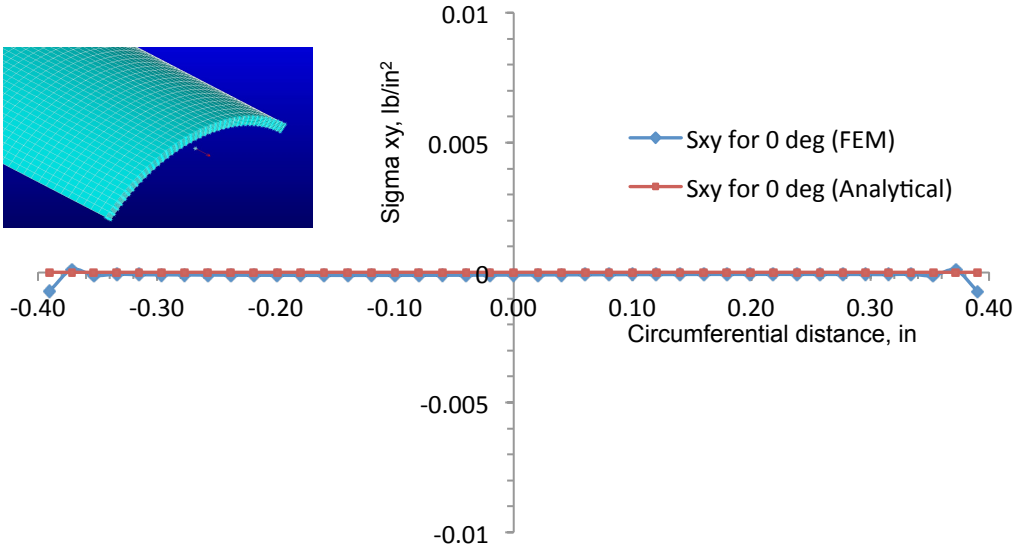

Figure 5-25 τ_{xy} Distribution in 0 deg Plies under Axial Load as a fn. of Circumferential Arc Length $\left(\Delta T = 0^0 F\right)$

The notable observations upon analyzing the stress plots for $\pm 45^{o}$ and 0^{o} plies in the absence of temperature environment include:-

a) Analytically obtained longitudinal σ_x stress predictions for $\pm 45^{o}$ layers exhibit an insignificant variation across the circumference and remain uniform.

b) FE based σ_x stress curves for $\pm 45^{o}$ layers indicate a constant distribution across the curved contour and preserves a symmetric trend; Numerical stress predictions from ANSYS show excellent consistency with the mathematically computed stress data.

c) Similarly, σ_y stresses preserve a symmetric trend and depict an uniform distribution pattern across the circumference

d) Influence of in-plane τ_{xy} stresses in $\pm 45^{o}$ plies are observed to be significantly high as opposed to the τ_{xy} stresses experienced by 0^{o} plies.

e) $\pm 45^{o}$ plies actively accommodate in-plane shear stresses τ_{xy} to occur along its contour and prove to be substantial in comparison to the role played by τ_{xy} stresses among 0^{o} plies constituting the curved laminate.

f) Additionally, the distribution trends shown by in-plane shear stresses τ_{xy} for the $\pm 45^{o}$ plies interchange while preserving the magnitudes experienced under axial loading conditions.

Figures 5-26 through Figure 5-29 represent the in-plane stress (σ_x,σ_y and τ_{xy}) distributions for $+45^{o}$ plies along the circumferential length of the curved shell upon implementing a uniformly distributed temperature differential of $\Delta T = 50^{o}F$.

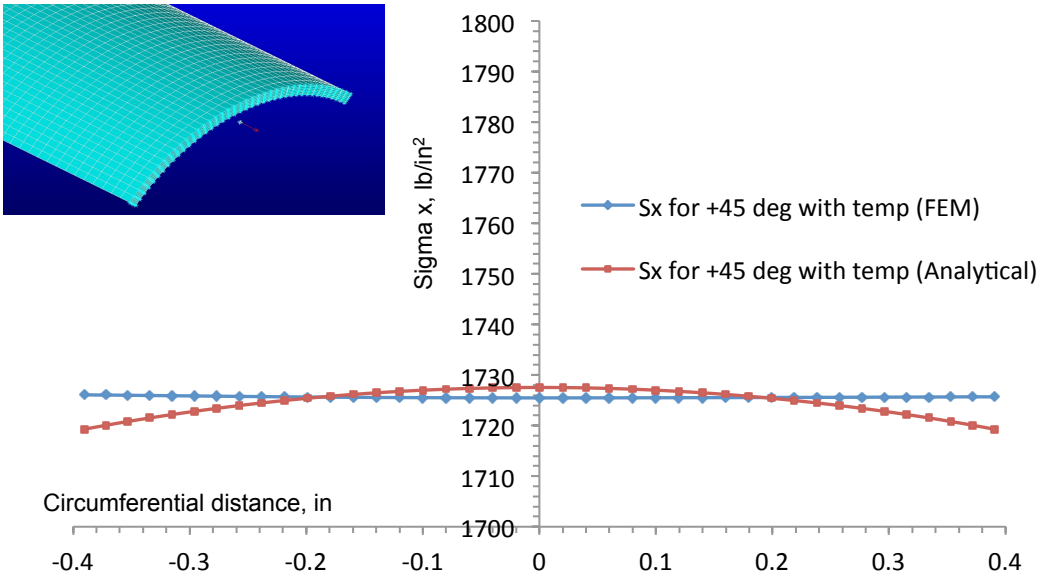

Figure 5-26 σ_x Distribution in +45 deg Plies under Axial Load as a fn. of Circumferential Arc Length $\left(\Delta T = 50^0 F\right)$

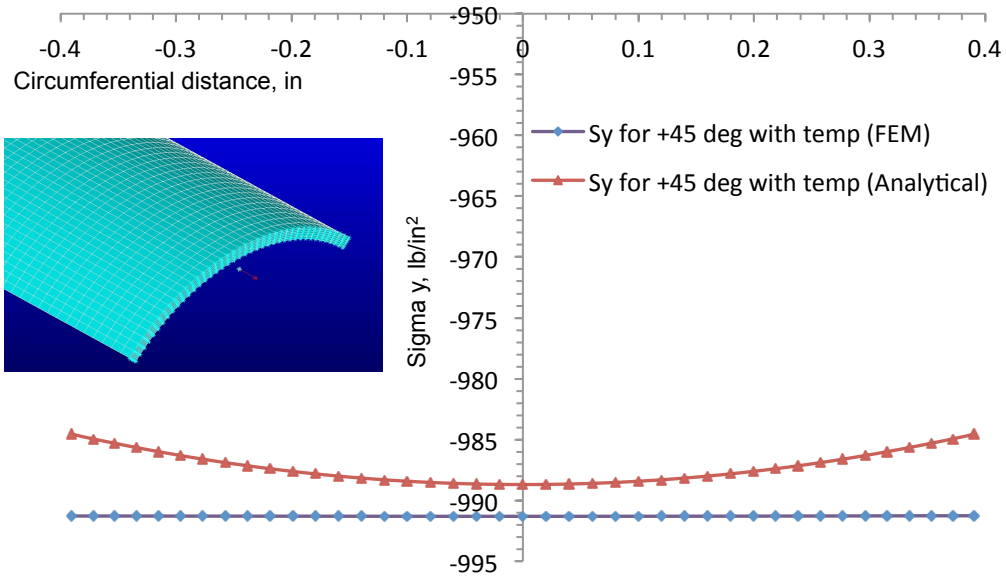

Figure 5-27 σ_y Distribution in +45 deg Plies under Axial Load as a fn. of Circumferential Arc Length $\left(\Delta T = 50^0 F\right)$

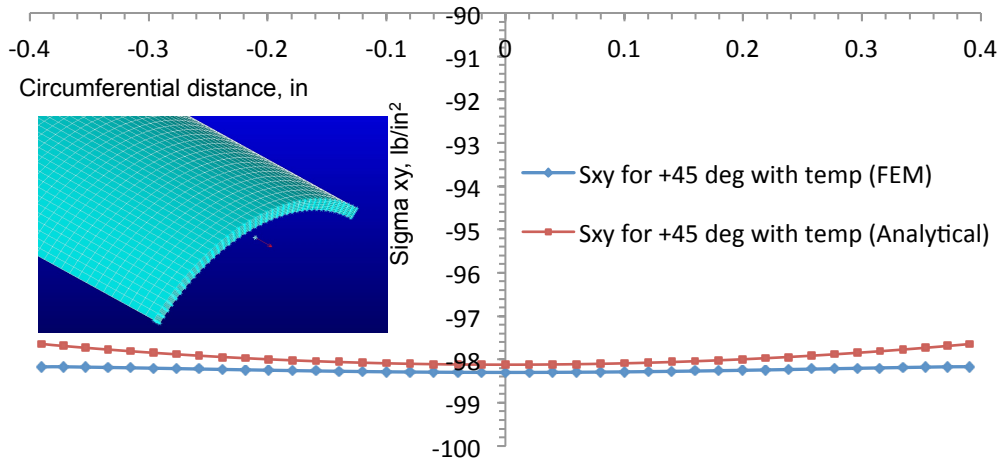

Figure 5-28 τ_{xy} Distribution in +45 deg Plies under Axial Load as a fn. of Circumferential Arc Length $\left(\Delta T = 50^0 F\right)$

Similarly, Figures 5-29 through 5-34 portray the in-plane stress $(\sigma_x, \sigma_y$ and $\tau_{xy})$ distributions for -45^0 and 0^o plies incorporating the effects of a uniformly distributed temperature differential of $\Delta T = 50^o F$ along the arc length of the curved shell.

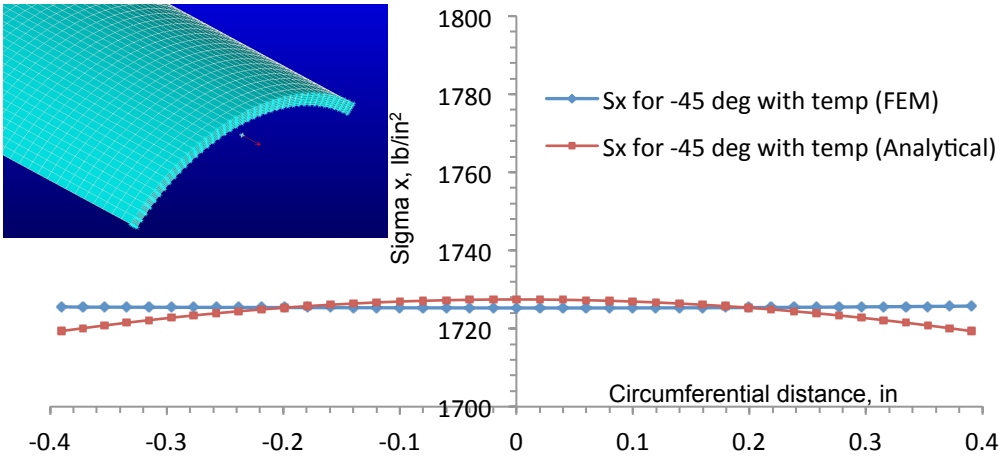

Figure 5-29 σ_x Distribution in -45 deg Plies under Axial Load as a fn. of Circumferential Arc Length $\left(\Delta T = 50^0 F\right)$

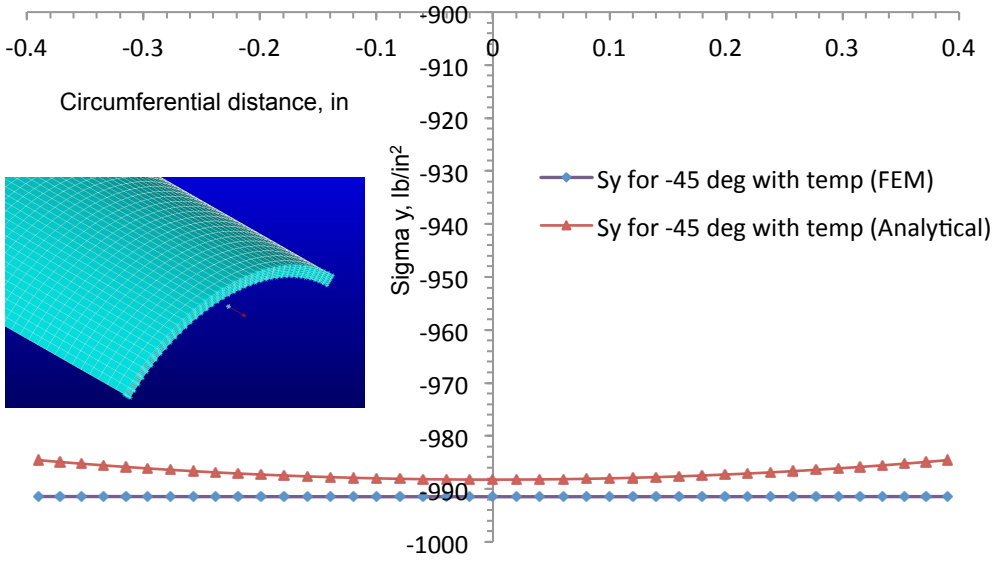

Figure 5-30 σ_y Distribution in -45 deg Plies under Axial Load as a fn. of Circumferential Arc Length $\left(\Delta T = 50^0 F\right)$

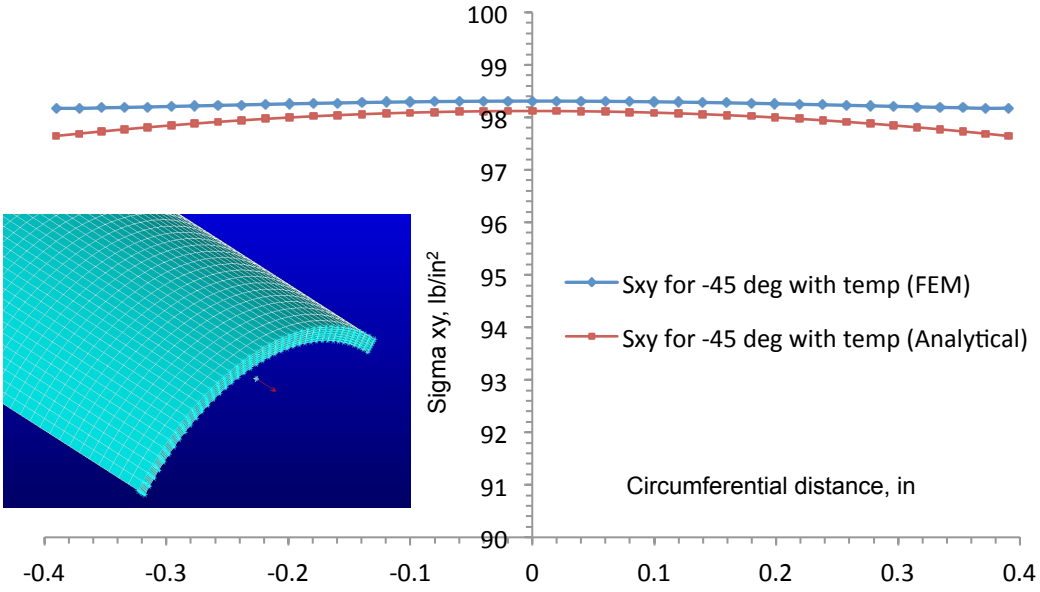

Figure 5-31 τ_{xy} Distribution in -45 deg Plies under Axial Load as a fn. of Circumferential Arc Length $\left(\Delta T = 50^0 F\right)$

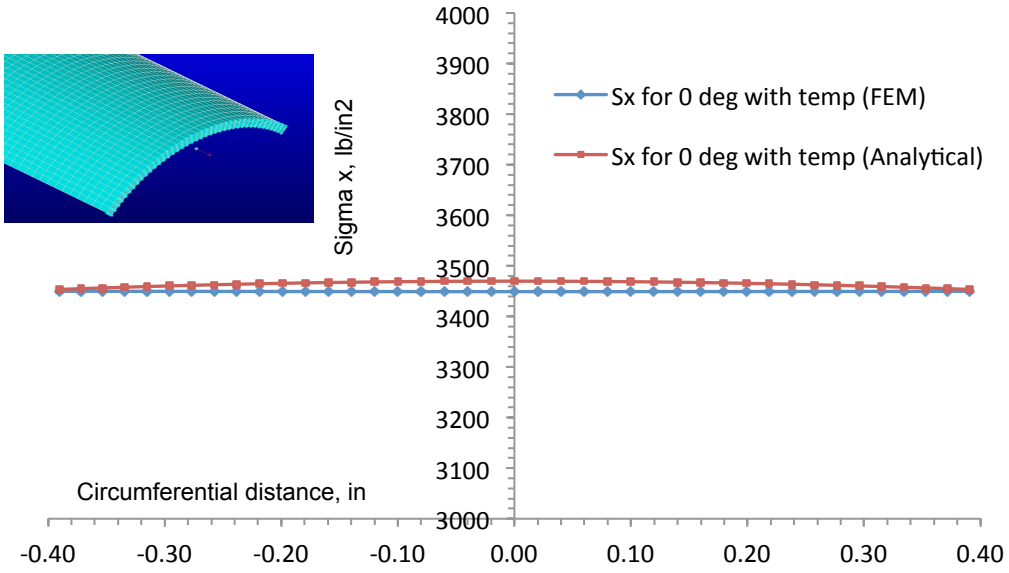

Figure 5-32 σ_x Distribution in 0 deg Plies under Axial Load as a fn. of Circumferential Arc Length $\left(\Delta T = 50^0 F\right)$

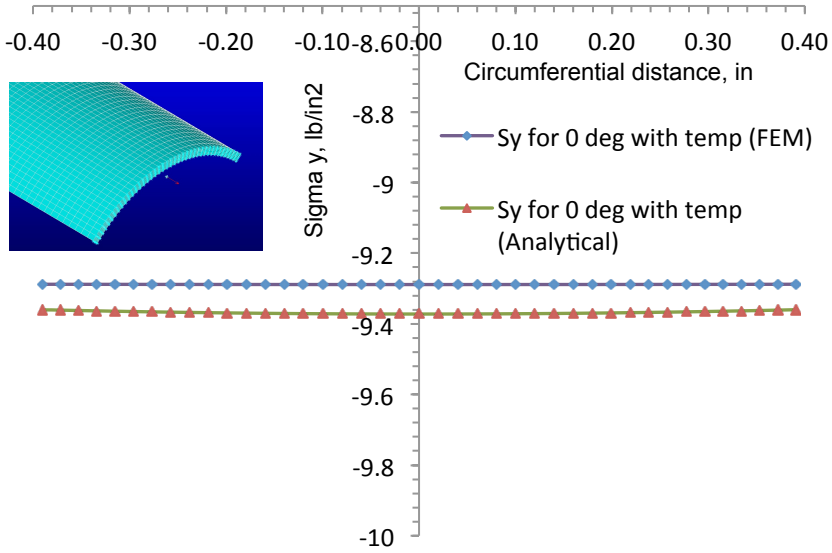

Figure 5-33 σ_y Distribution in 0 deg Plies under Axial Load as a fn. of Circumferential Arc Length $\left(\Delta T = 50^0 F\right)$

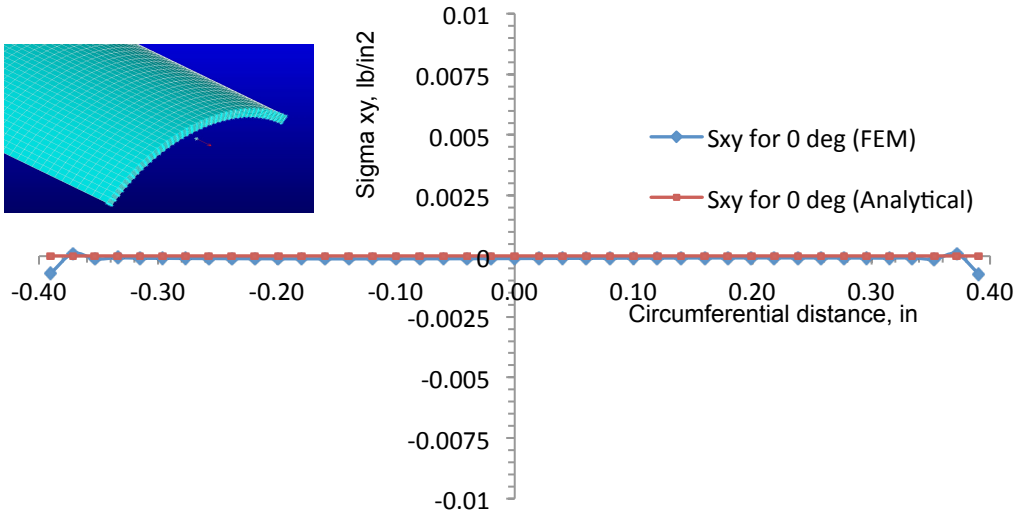

Figure 5-34 τ_{xy} Distribution in 0 deg Plies under Axial Load as a fn. of Circumferential Arc Length $\left(\Delta T = 50^0 F\right)$

The notable observations upon analyzing the stress plots for $\pm 45^{\circ}$ and 0° plies in the presence of temperature environment include:-

a) Analytically obtained longitudinal σ_x stress estimates for $\pm 45^{\circ}$ layers including the effects of a predefined and uniformly applied thermal load exhibit elevated stress data across every cross-section within the layers. This increase in stress numbers can be primarily attributed to the contribution from supplementary resultant thermal loads and moments induced as a result of the inherent shell curvature. Additionally the distribution pattern across the shell circumference remain uniform for the selected cross-section (50%L).

b) FE based σ_x stress curves for $\pm 45^{\circ}$ layers indicate a constant distribution across the curved contour and preserves a symmetric trend. Numerical stress predictions from ANSYS show excellent consistency with the mathematically computed stress data.

c) Similarly, σ_y stress distributions preserve a symmetric trend and depict an uniform pattern across the circumference.

d) Influence of in-plane τ_{xy} stresses in $\pm 45^o$ plies are observed to be substantial in comparison to the trivial τ_{xy} stresses experienced in 0^o plies circumferentially. As a consequence, thermal loads do not indicate any authority in governing the mechanical response characterized through the in-plane τ_{xy} stresses associated with 0^o plies.

e) $\pm 45^o$ plies display superior accommodation in regards to in-plane shear stresses τ_{xy} emerging along the curved shell contour and subsequently prove to be critical in comparison to the role played by τ_{xy} stresses among 0^o plies constituting the curved laminate.

f) Similarly, the distribution trend witnessed by in-plane shear stresses τ_{xy} for the $\pm 45^o$ plies interchange while preserving the magnitudes experienced under axial loading conditions.

5-3-5 Computational Modeling and Analyses of Curved Cylindrical Shell Laminates Subject to Longitudinal Bending Moment on Centroid

Current exercise further examines the in-plane stress $(\sigma_x, \sigma_y$ and $\tau_{xy})$ distributions for a six-ply symmetric-balanced curved composite laminate configuration with a $[\pm 45/0]_s$ laminate stacking sequence upon the application of a finite longitudinal bending moment of 10 lb-in on the centroidal location of the structure. In order to eliminate the influence of localized nodal deformations consistent with edge-effects, a circumferential nodal cross-section located at 50%L is designated as the station of interest. In-plane stress

distributions along the curved contour for each of the lamina constituting the ply lay-up are preferentially analyzed. Analytical stress predictions are computed via utilizing Eqns. (5.33-5.34) in the presence and absence of a uniformly distributed temperature-differential of $\Delta T = 50^{\circ}F$. Mechanical ply-per-ply stress predictions are computed analytically and their validity is confirmed in comparison with FE-simulation based stress predictions. Figure 5-35 portrays the discretized simulated image of the curved shell structure generated utilizing a higher order 20-noded Layered Structural Solid Element addressed as SOLID-186 in the ANSYS element library [12]. In this study, the centroidal node characterizing the curved cross-section of right-extremity, is subjected to a longitudinal bending moment (Fig 5-36). The total arc angle that essentially defines the circumferential arc length of the curved laminate is assumed to be 90^{0} for this loading case. The model size is in the order of 145800 elements. An ideal cantilever type configuration is simulated via implementing the structural boundary conditions as outlined in the initial commentaries of section 5.3 respectively.

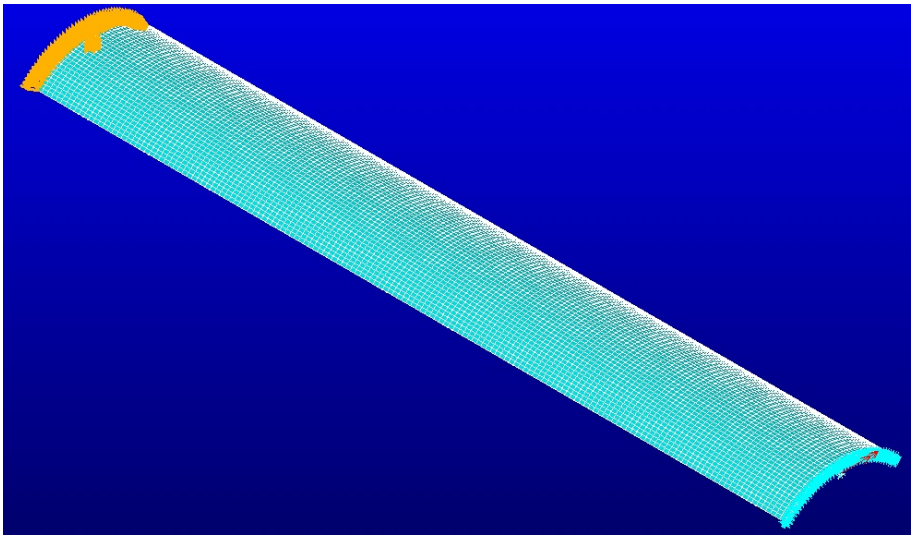

Figure 5-35 Discretized Curved Composite Shell subjected to Bending at Centroid

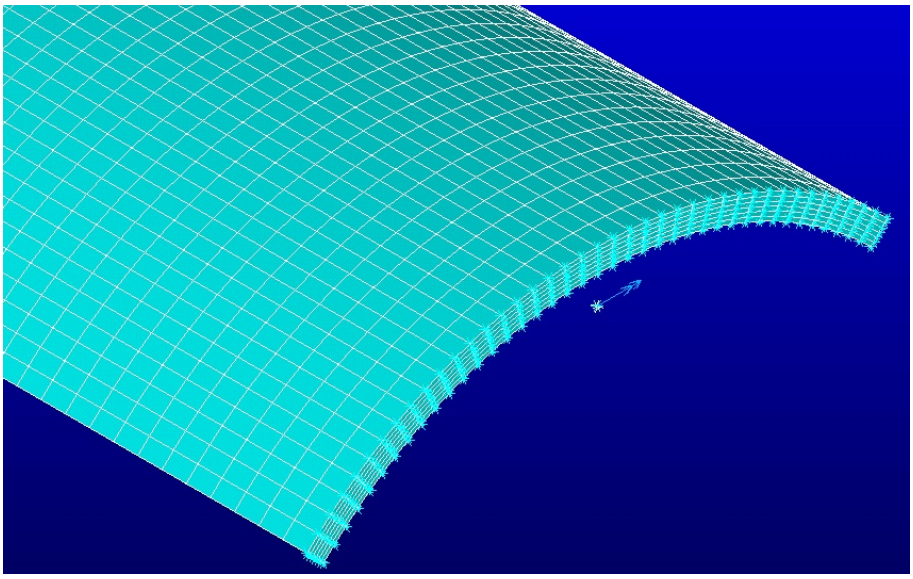

Figure 5-36 Close-up view of Bending Moment Applied at Centroid

Figures 5-37 through Figure 5-39 represent the in-plane stress distributions (σ_x,σ_y and τ_{xy}) distributions for $+45^o$ plies along the circumferential length of the curved shell.

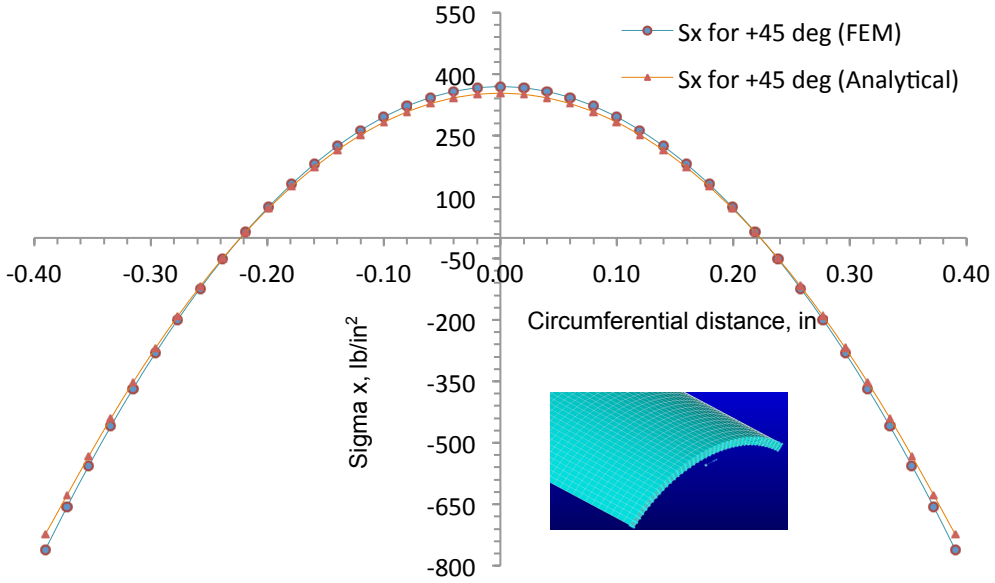

Figure 5-37 σ_x for +45 deg Plies under M_x vs. Circ. Arc Length $\left(\Delta T = 0^0 F\right)$

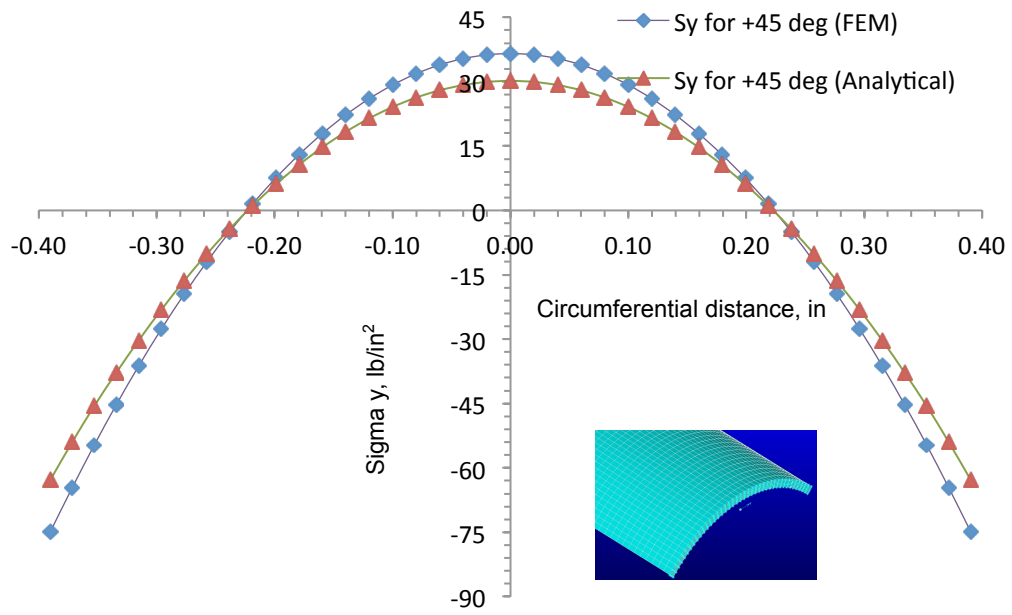

Figure 5-38 σ_y for +45 deg Plies under M_x vs. Circ. Arc Length $\left(\Delta T = 0^0 F\right)$

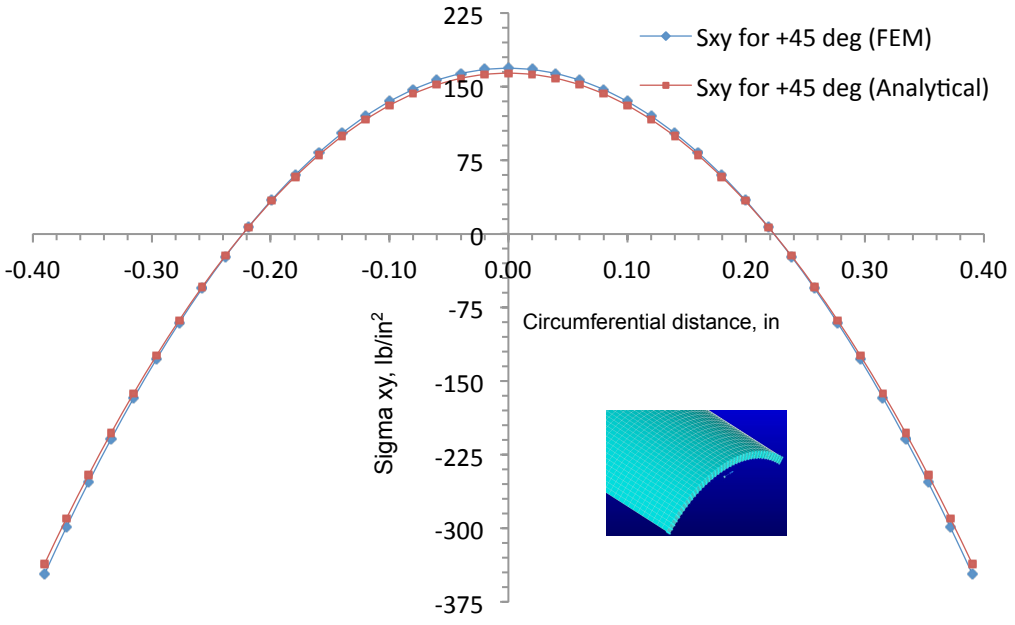

Figure 5-39 τ_{xy} for +45 deg Plies under M_x vs. Circ. Arc Length $\left(\Delta T = 0^0 F\right)$

Similarly, Figures 5-40 through 5-46 address the in-plane stress $(\sigma_x, \sigma_y \text{ and } \tau_{xy})$ distributions for -45^0 and 0^o plies along the arc length of the curved shell.

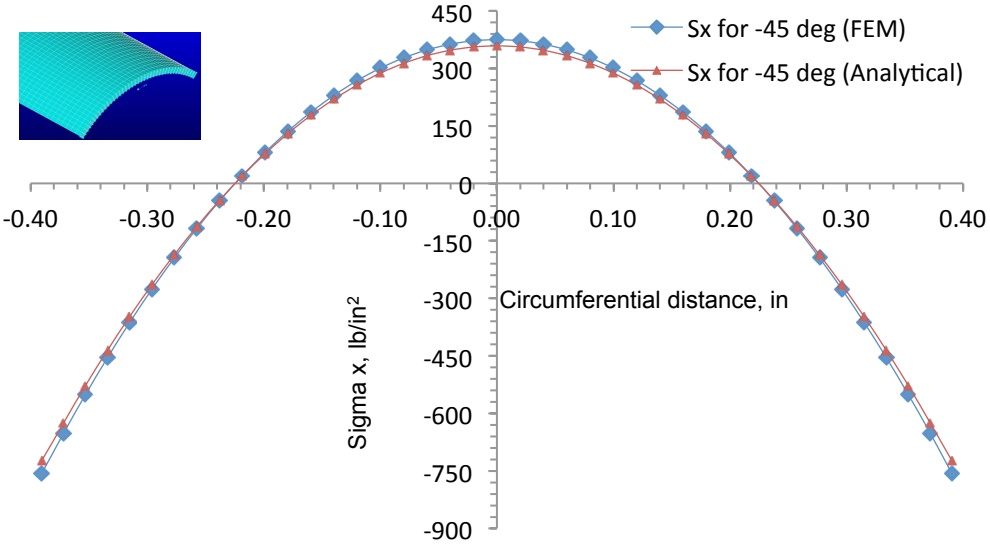

Figure 5-40 σ_x for -45 deg Plies under M_x vs. Circ. Arc Length $(\Delta T = 0^0 F)$

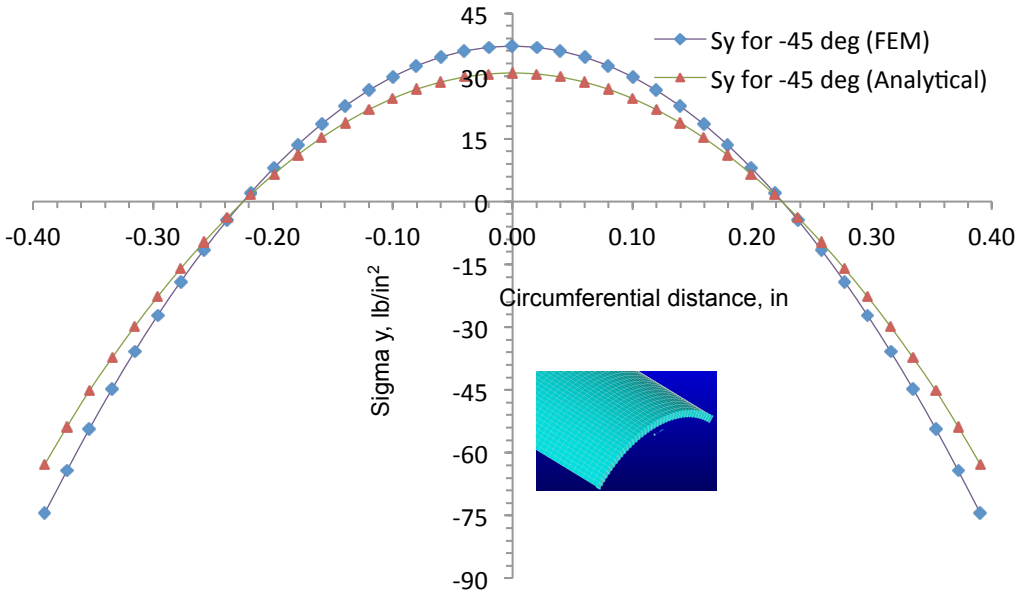

Figure 5-41 σ_y for -45 deg Plies under M_x vs. Circ. Arc Length $(\Delta T = 0^0 F)$

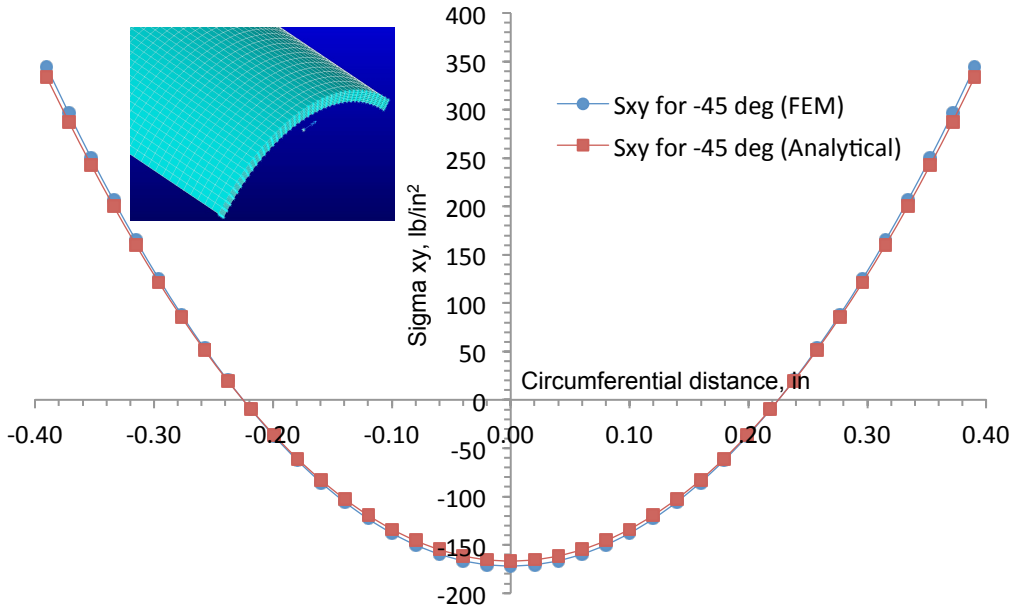

Figure 5-42 τ_{xy} for -45 deg Plies under M_x vs. Circ. Arc Length $\left(\Delta T = 0^0 F\right)$

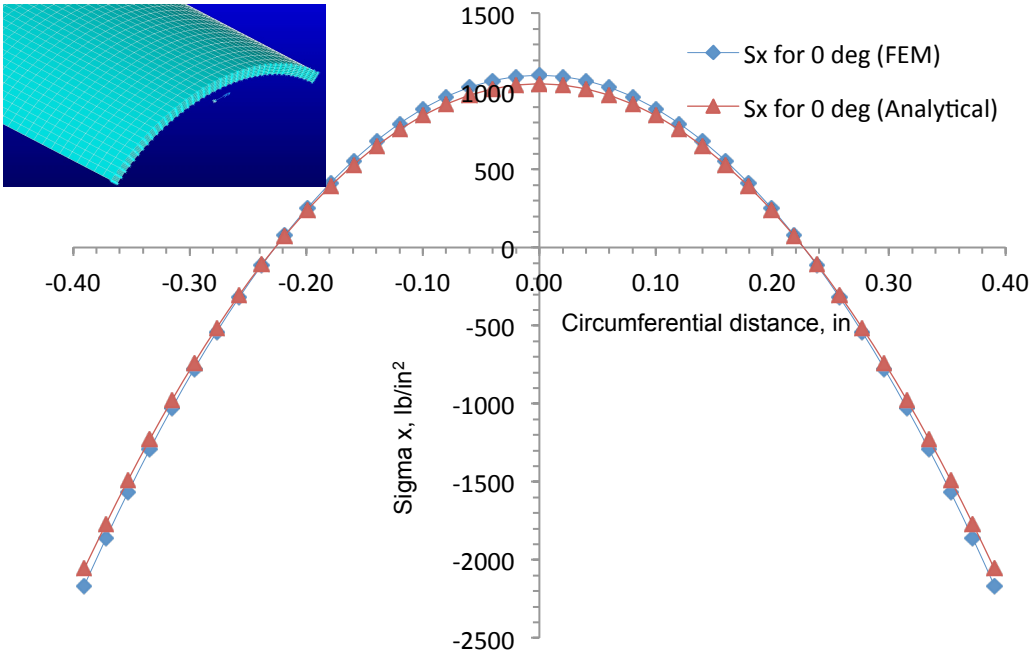

Figure 5-43 σ_x for 0 deg Plies under M_x vs. Circ. Arc Length $\left(\Delta T = 0^0 F\right)$

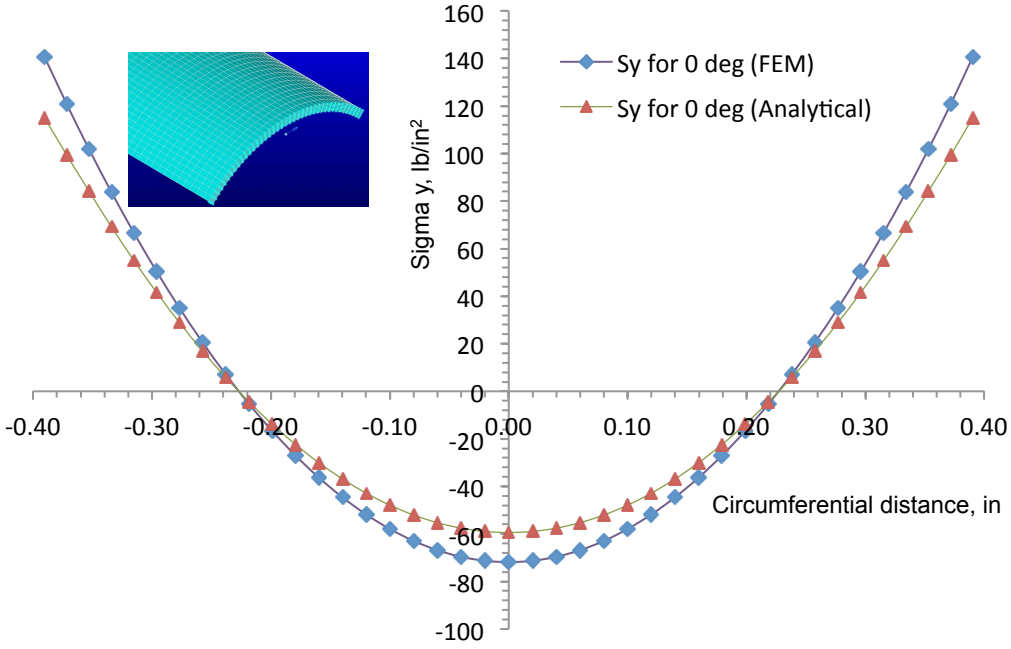

Figure 5-44 σ_y for 0 deg Plies under M_x vs. Circ. Arc Length $\left(\Delta T = 0^0 F\right)$

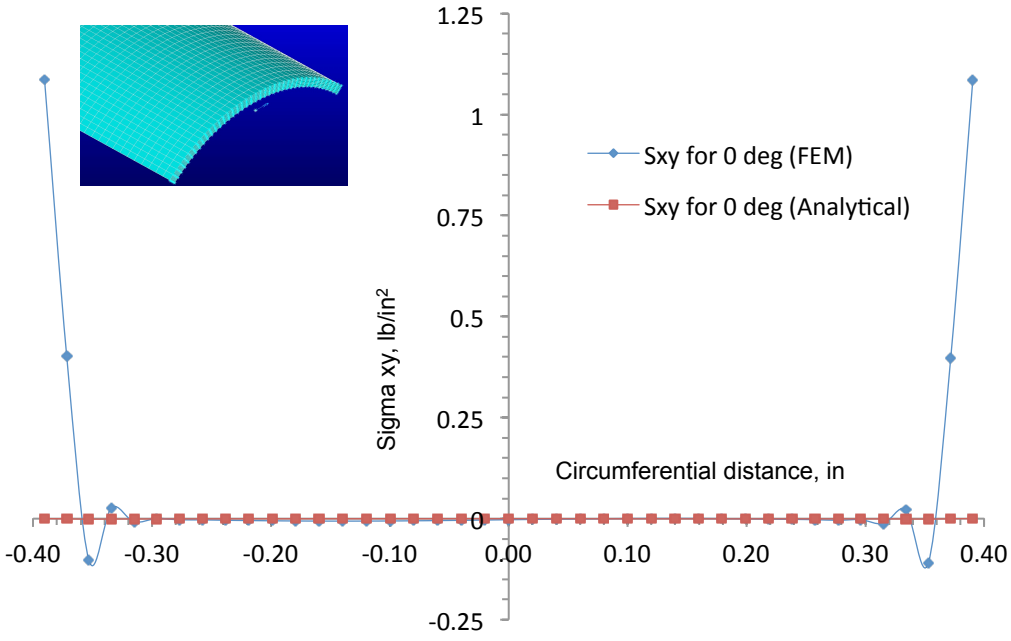

Figure 5-45 τ_{xy} for 0 deg Plies under M_x vs. Circ. Arc Length $\left(\Delta T = 0^0 F\right)$

Figures 5-46 through Figure 5-51 represent the in-plane stress (σ_x, σ_y and τ_{xy}) distributions for $+45^o$ plies and 0^o plies along the circumferential length of the curved shell upon implementing a uniformly distributed temperature differential of $\Delta T = 50^oF$.

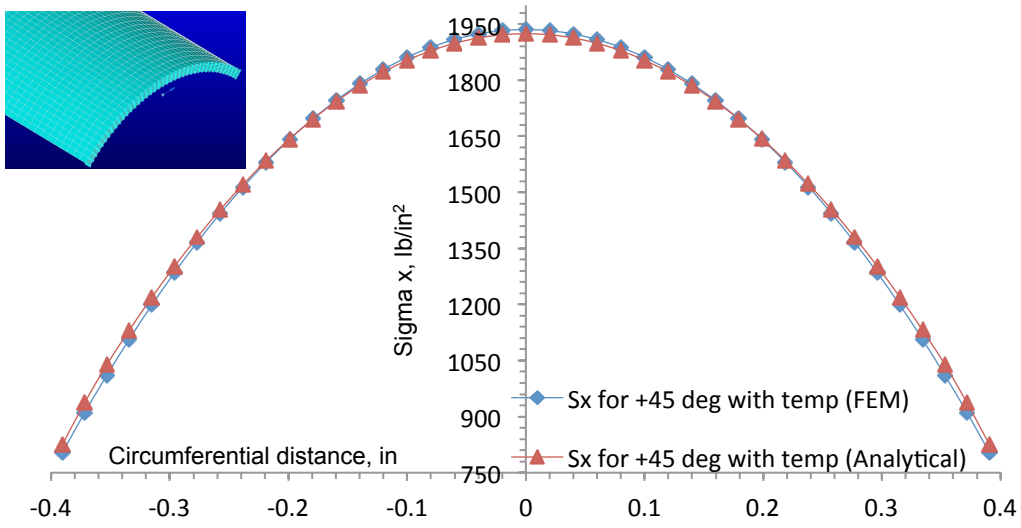

Figure 5-46 σ_x for +45 deg Plies under M_x vs. Circ. Arc Length $(\Delta T = 50^0F)$

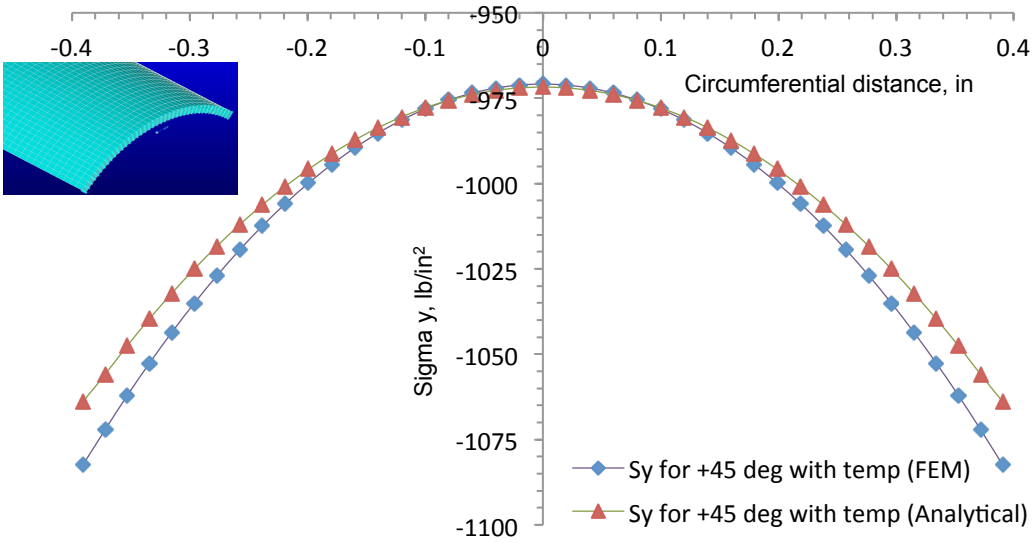

Figure 5-47 σ_y for +45 deg Plies under M_x vs. Circ. Arc Length $(\Delta T = 50^0F)$

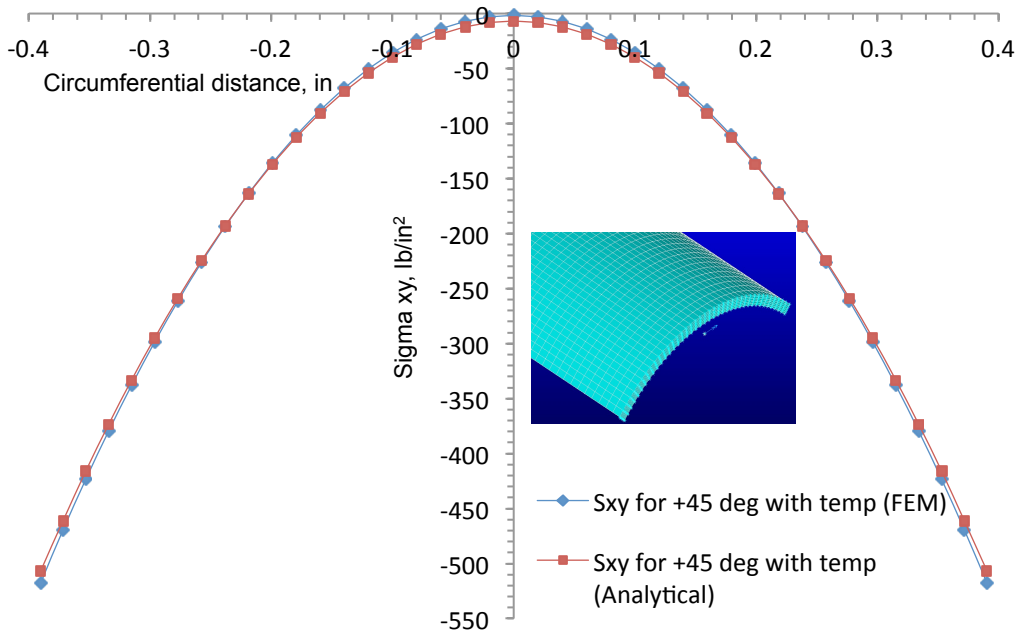

Figure 5-48 τ_{xy} for +45 deg Plies under M_x vs. Circ. Arc Length $\left(\Delta T = 50^0 F\right)$

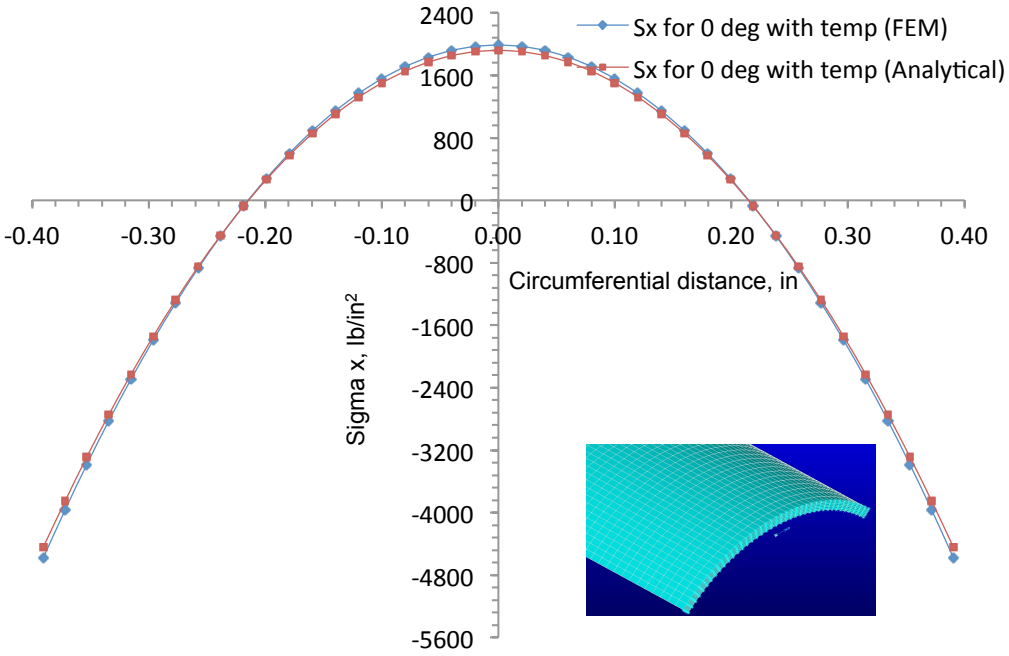

Figure 5-49 σ_x for 0 deg Plies under M_x vs. Circ. Arc Length $\left(\Delta T = 50^0 F\right)$

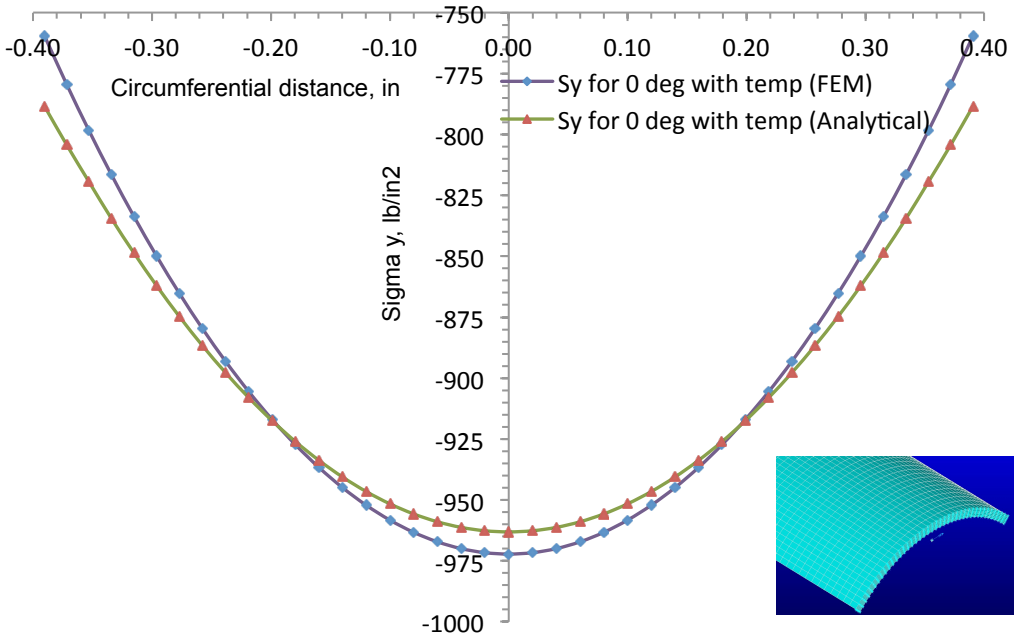

Figure 5-50 σ_y for 0 deg Plies under M_x vs. Circ. Arc Length $\left(\Delta T = 50^0 F\right)$

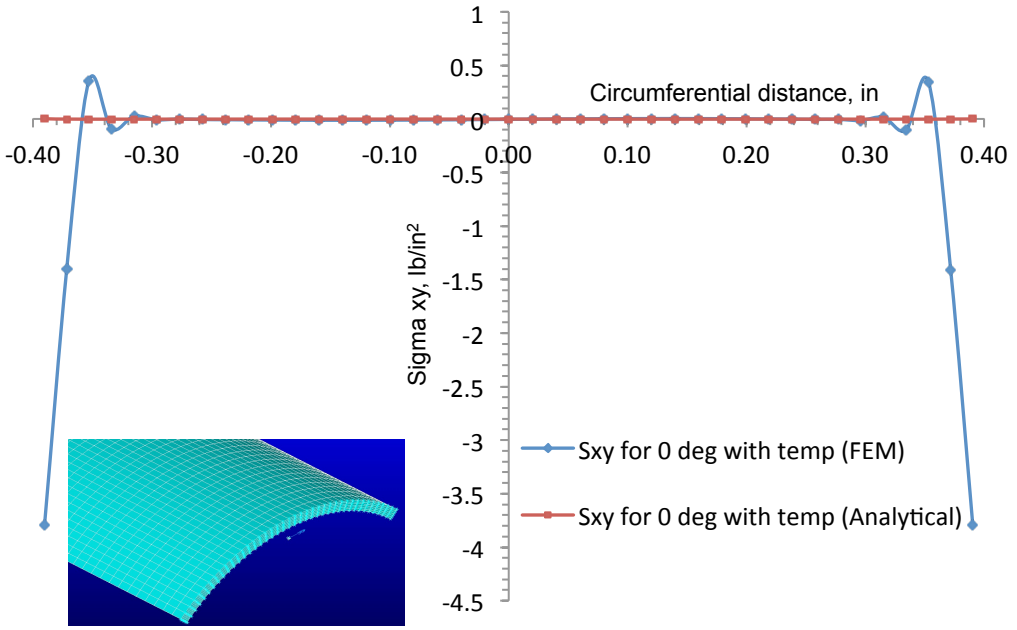

Figure 5-51 τ_{xy} for 0 deg Plies under M_x vs. Circ. Arc Length $\left(\Delta T = 50^0 F\right)$

5.4 Ply-Stress Parametric Study

5-4-1 Parametric Study based on Varying Shell Mean Radius R_m : Axial Loading case

$\left(\Delta T = 0^0 F, \Delta T = 50^0 F\right)$

Curved cylindrical shell configuration is investigated through parametric variations in ply-stresses for the axial load and bending load cases. The parameters assumed for this work are the mean radius of curvature R_m and laminate thickness-to-mean radius of curvature ratio (t/R_m) respectively. Ply-stress plots shown in previous sections show good agreement in comparison to the FE based stress predictions. Having acquired confidence in the analytical results in view of structural stiffness predictions, centroidal location predictions and ply-stress estimations the following sections will present the parametric case study results based on the formulated analytical methodology.

Figure 5-52 to Figure 5-61 portrays the combined in-plane stress $(\sigma_x, \sigma_y$ and $\tau_{xy})$ profile plots of $+45^o$ and 0^o plies constituting a thin-walled curved composite strip. Stress plots corresponding to -45^o plies are recognized to show an identical stress trend in comparison to $+45^o$ ply stresses. As a consequence, this section only illustrates the stress plots for $+45^o$ and 0^o plies. Figure 5-57 to Figure 5-61 displays the combined in-plane stress $(\sigma_x, \sigma_y$ and $\tau_{xy})$ profile plots of $+45^o$ and 0^o plies while including the presence of a uniformly distributed thermal loading environment.

The composite geometry is characterized by a $[\pm 45/0]_s$ six-ply symmetric-balanced curved composite laminate configuration while varying the shell mean radius R_m as a function of circumferential arc length. The strip is axially loaded about the centroidal point with a magnitude of 10 lbs. Axial load is maintained constant while varying the shell mean radius of curvature. The half arc angle that essentially defines the circumferential arc

length of the curved laminate is assumed to be 45^0 for this loading case. The model size is in the order of 145800 elements. An ideal cantilever type configuration is simulated via implementing the structural boundary conditions as outlined in the initial commentaries respectively.

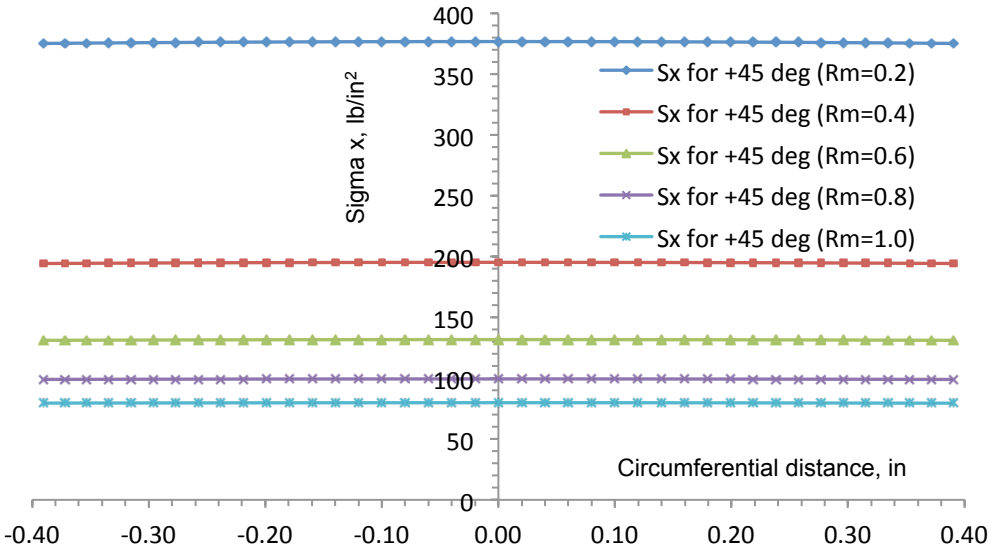

Figure 5-52 σ_x for +45 deg Plies under N_x vs. Circ. Arc Length $\left(\Delta T = 0^0 F\right)$

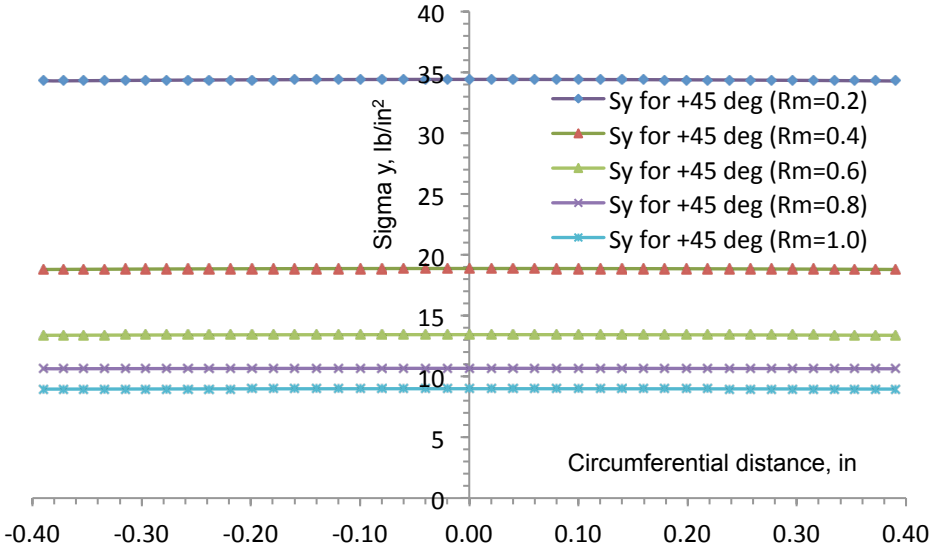

Figure 5-53 σ_y for +45 deg Plies under N_x vs. Circ. Arc Length $\left(\Delta T = 0^0 F\right)$

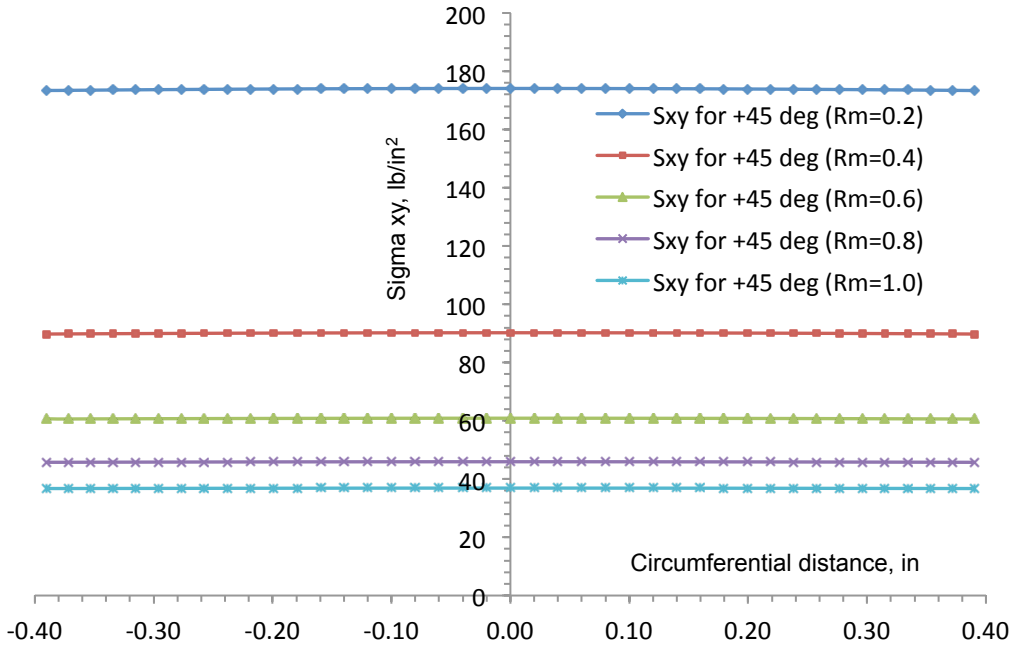

Figure 5-54 τ_{xy} for +45 deg Plies under N_x vs. Circ. Arc Length $\left(\Delta T = 0^0 F\right)$

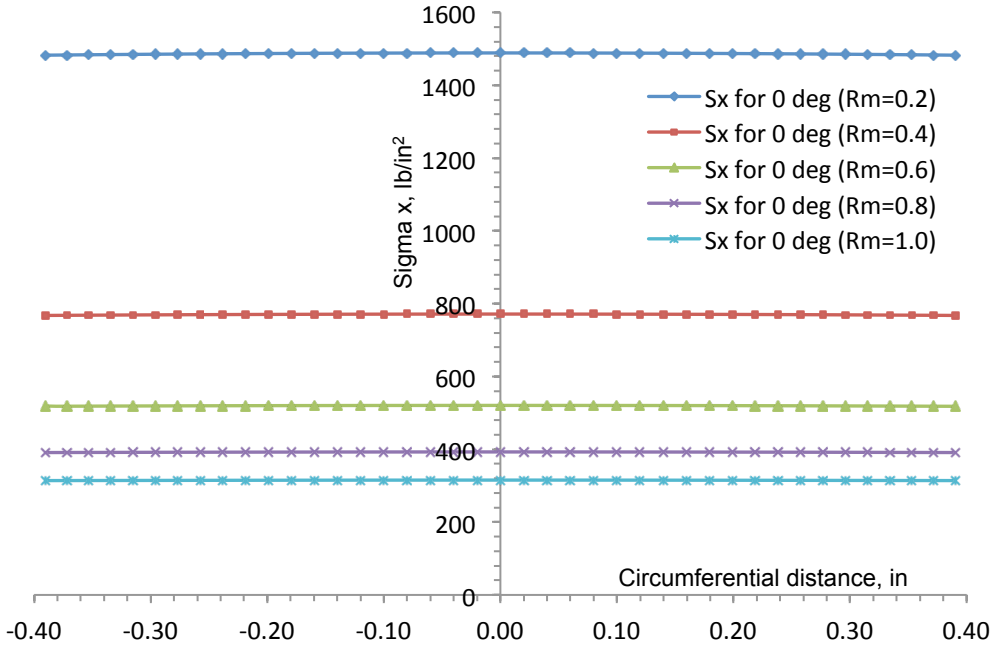

Figure 5-55 σ_x for 0 deg Plies under N_x vs. Circ. Arc Length $\left(\Delta T = 0^0 F\right)$

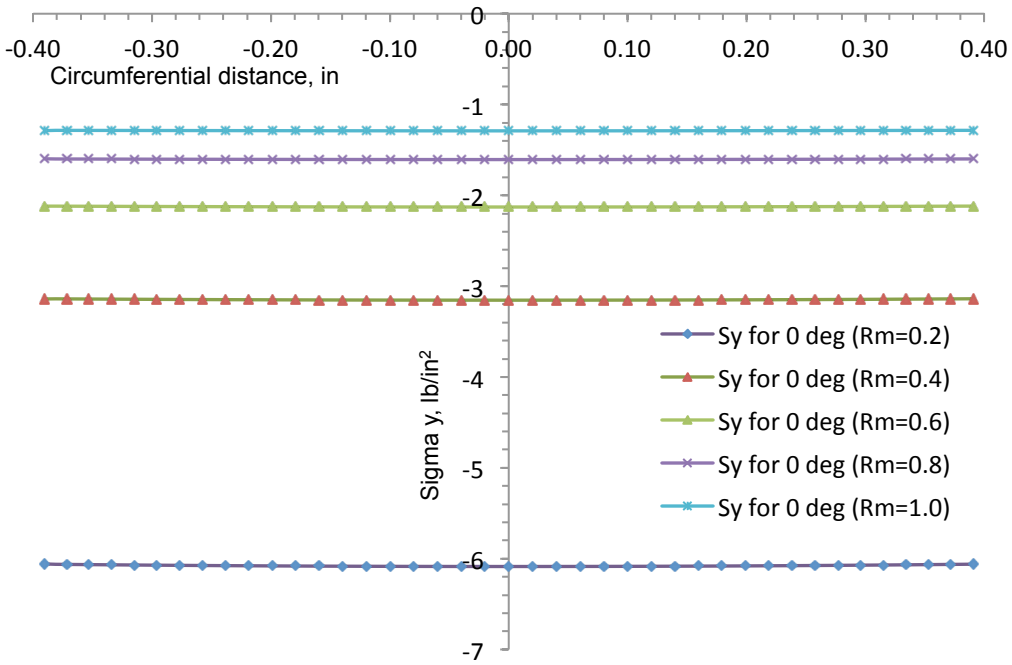

Figure 5-56 σ_y for 0 deg Plies under N_x vs. Circ. Arc Length $\left(\Delta T = 0^0 F\right)$

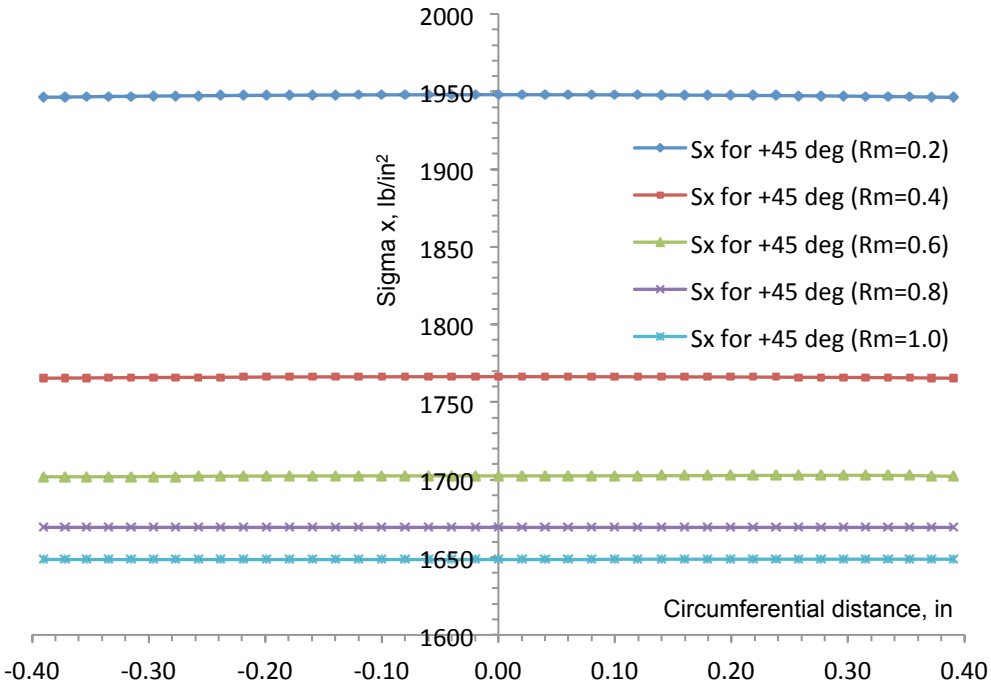

Figure 5-57 σ_x for +45 deg Plies under N_x vs. Circ. Arc Length $\left(\Delta T = 50^0 F\right)$

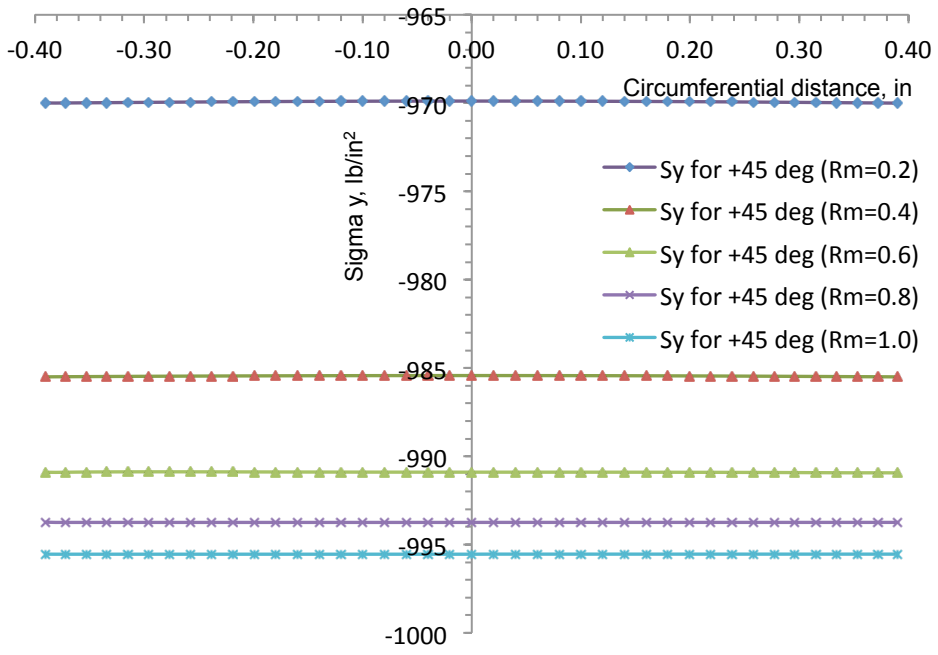

Figure 5-58 σ_y for +45 deg Plies under N_x vs. Circ. Arc Length $\left(\Delta T = 50^0 F\right)$

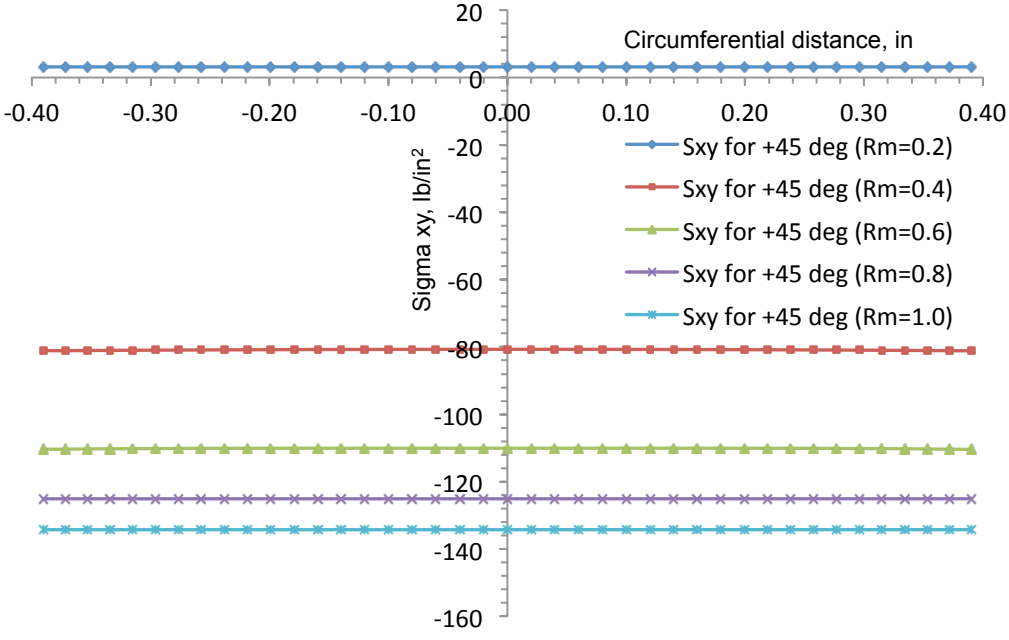

Figure 5-59 τ_{xy} for +45 deg Plies under N_x vs. Circ. Arc Length $\left(\Delta T = 50^0 F\right)$

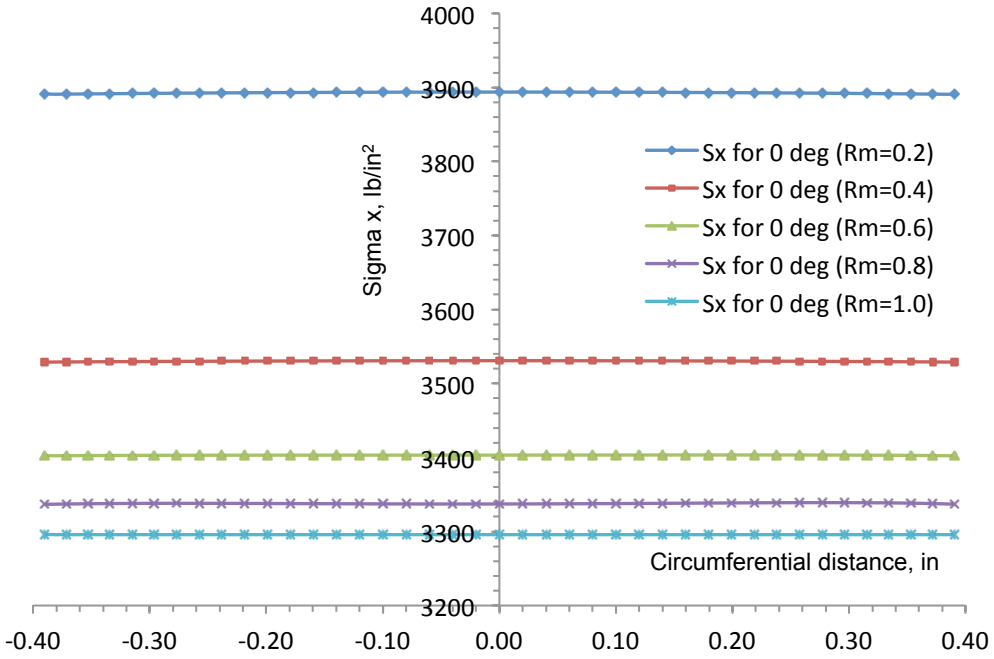

Figure 5-60 σ_x for 0 deg Plies under N_x vs. Circ. Arc Length $\left(\Delta T = 50^0 F\right)$

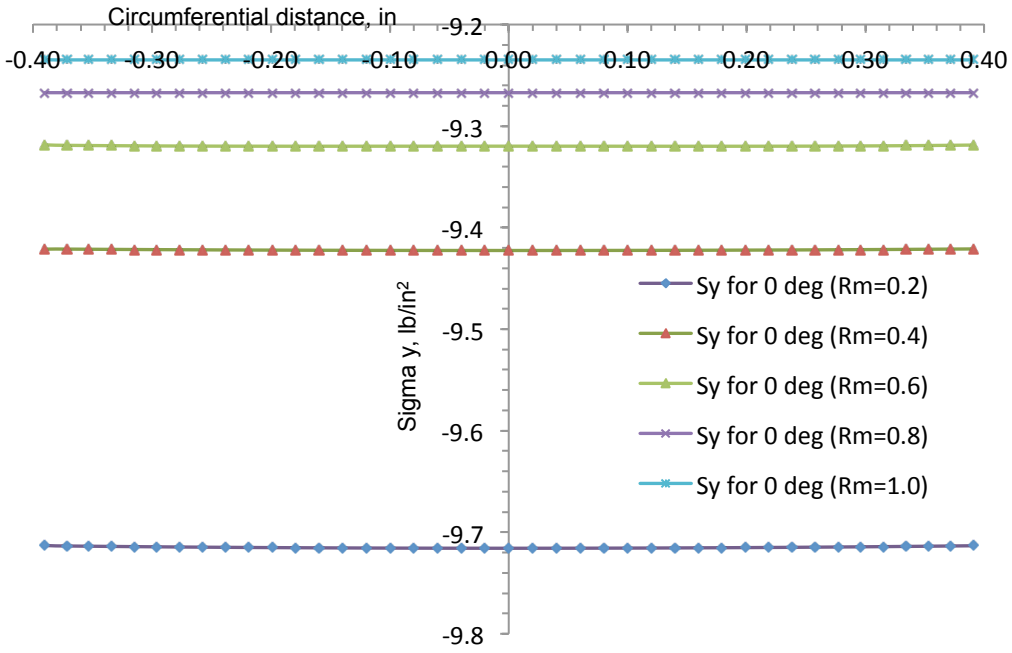

Figure 5-61 σ_y for 0 deg Plies under N_x vs. Circ. Arc Length $\left(\Delta T = 50^0 F\right)$

The notable observations upon analyzing the parametric stress plots for $+45^{o}$ and 0^{o} plies subjected to an axial load in the presence and absence of temperature environment include: -

While assuming the total arc angle (2α) to be constant and sequentially increasing the mean radius of curvature R_m, in-plane stress $(\sigma_x, \sigma_y$ and $\tau_{xy})$ predictions for $+45^{o}$ and 0^{o} layers indicate invariance while computed across the circumferential arc length of the composite strip. τ_{xy} Stress predictions encountered by $+45^{o}$ layers are shown to be significant as opposed to the zero shear stresses τ_{xy} experienced by the 0^{o} plies (trivial solution). Magnitude of in-plane longitudinal σ_x stresses in 0^{o} plies is observed to be substantial relative to the σ_x stresses experienced by the $\pm 45^{o}$ plies. Additionally, the distribution trends shown by in-plane shear stresses τ_{xy} for $\pm 45^{o}$ plies interchange while preserving the magnitudes experienced under axial loading conditions. Magnitude of in-plane transverse and shear $(\sigma_y$ and $\tau_{xy})$ stresses in 0^{o} plies are observed to be trivial (Figure 5-25 & 5-34). Under a thermal loading condition, transverse and shear $(\sigma_y$ and $\tau_{xy})$ stresses witnessed in 0^{o} plies shows no significant influence as opposed to the stresses reported for $\pm 45^{o}$ plies.

5-4-2 Parametric Study based on Varying Shell Mean Radius R_m : Bending Loading case $\left(\Delta T = 0^{0}F, \Delta T = 50^{0}F\right)$

Figure 5-62 to Figure 5-71 displays the combined in-plane stress $\left(\sigma_x, \sigma_y, \tau_{xy}\right)$ profile plots of $+45^{o}$ and 0^{o} plies while including and excluding the presence of a uniformly

distributed thermal loading environment. The composite geometry is characterized by a $[\pm 45/0]_s$ six-ply symmetric-balanced curved composite laminate configuration and a varying shell mean radius R_m as a function of circumferential arc length.

The structural response of the curved strip is influenced by a concentrated bending moment of 10 lb in applied precisely at the predicted centroid point. The loading is maintained constant while varying the shell mean radius of curvature. The half arc angle that essentially defines the circumferential arc length of the curved laminate is assumed to be 45^0 for this loading case. The mesh density is in the order of 145800 elements. An ideal cantilever type configuration is simulated via implementing the structural boundary conditions as outlined in the initial commentaries respectively.

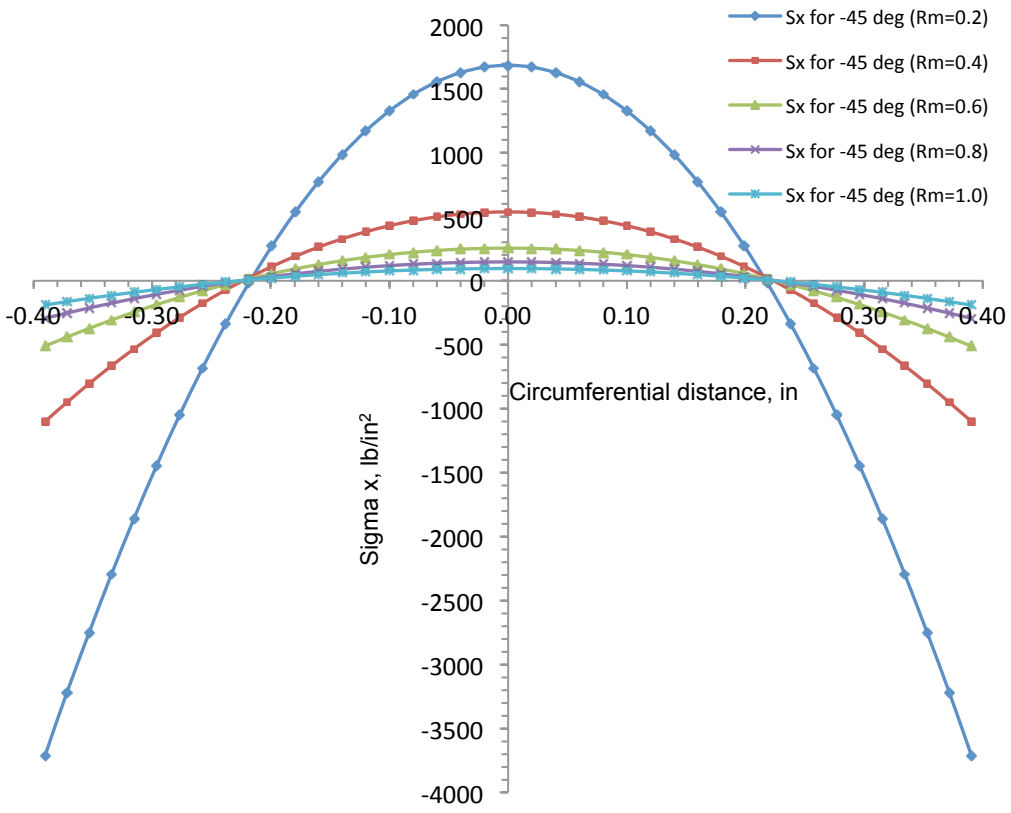

Figure 5-62 σ_x for +45 deg Plies under M_x vs. Circ. Arc Length $\left(\Delta T = 0^0 F\right)$

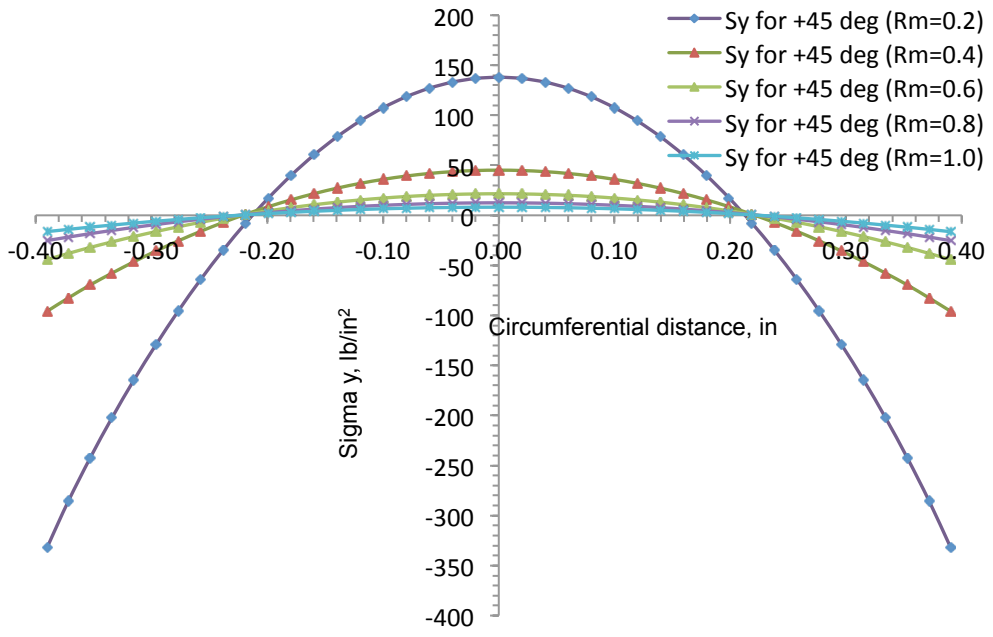

Figure 5-63 σ_y for +45 deg Plies under M_x vs. Circ. Arc Length $\left(\Delta T = 0^0 F\right)$

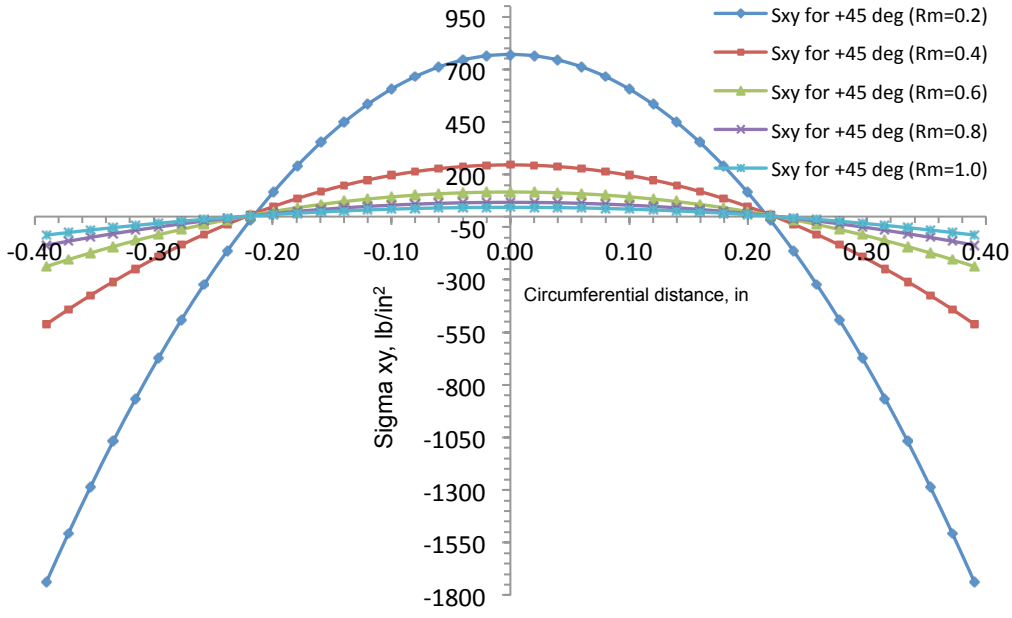

Figure 5-64 τ_{xy} for +45 deg Plies under M_x vs. Circ. Arc Length $\left(\Delta T = 0^0 F\right)$

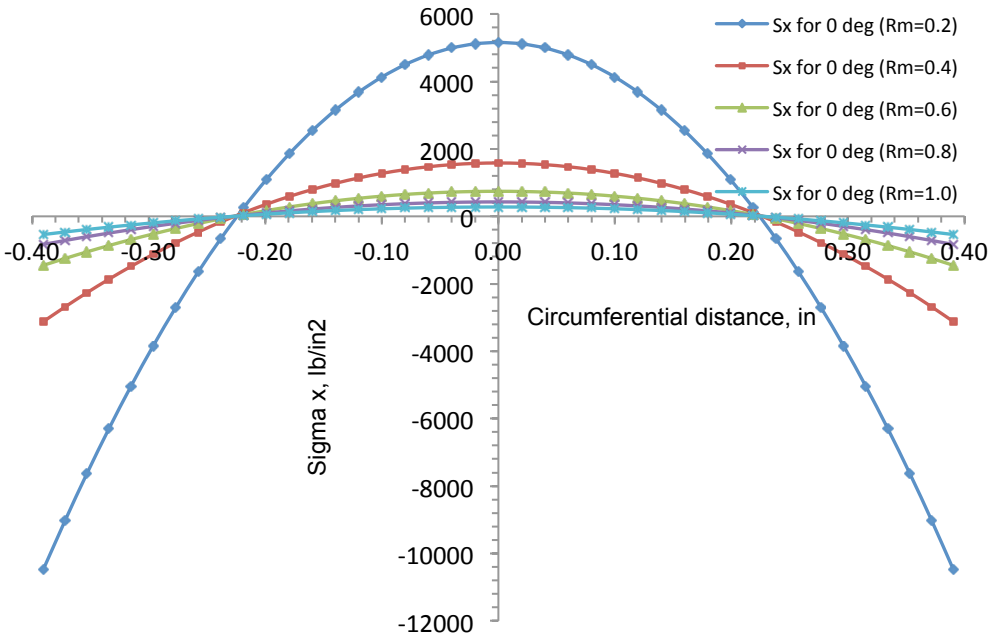

Figure 5-65 σ_x for 0 deg Plies under M_x vs. Circ. Arc Length $\left(\Delta T = 0^0 F\right)$

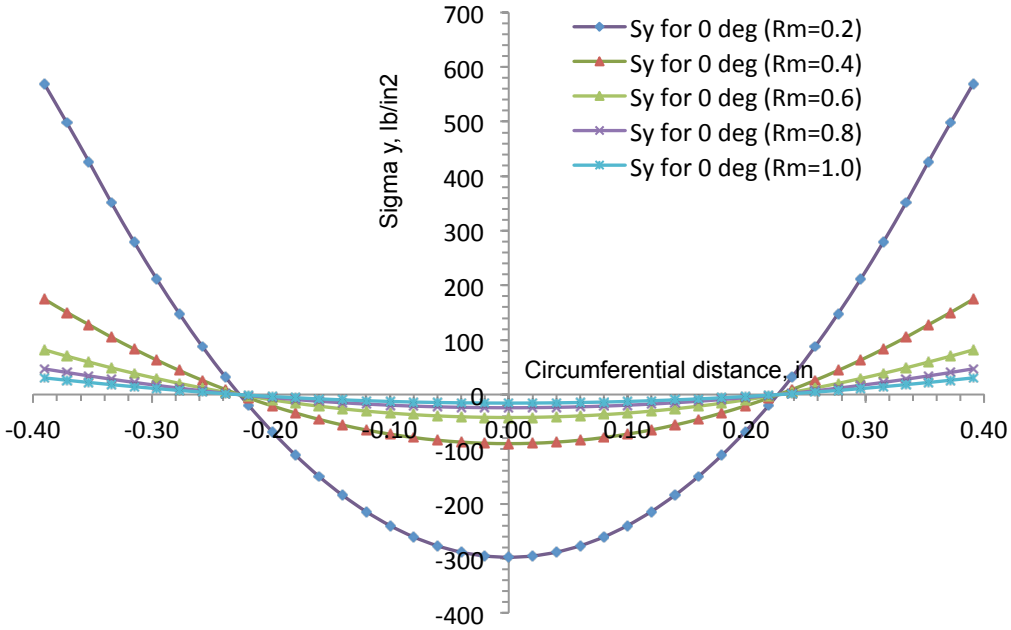

Figure 5-66 σ_y for 0 deg Plies under M_x vs. Circ. Arc Length $\left(\Delta T = 0^0 F\right)$

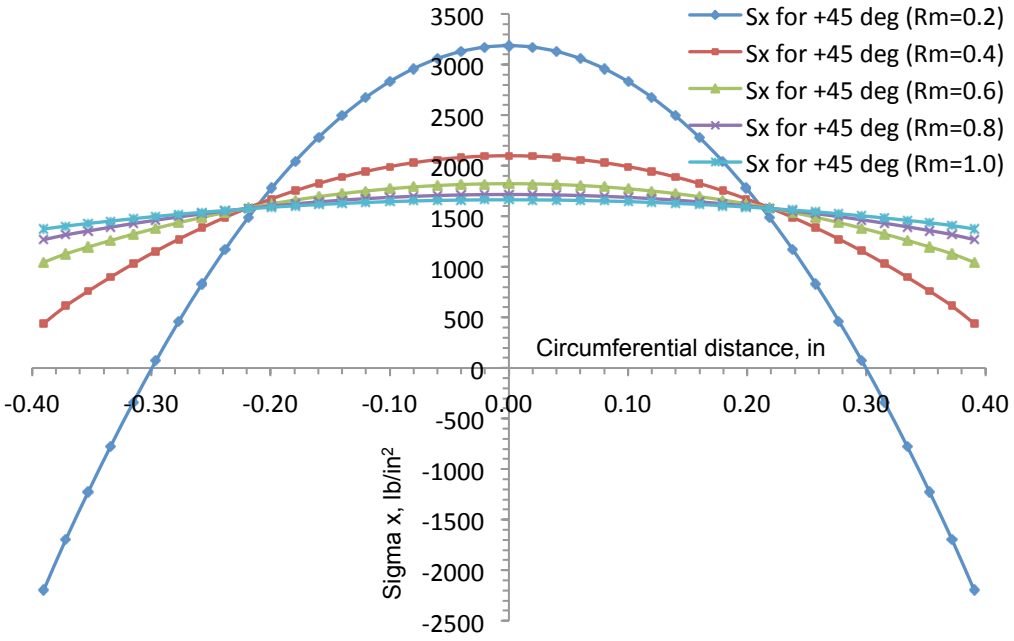

Figure 5-67 σ_x for +45 deg Plies under M_x vs. Circ. Arc Length $\left(\Delta T = 50^0 F\right)$

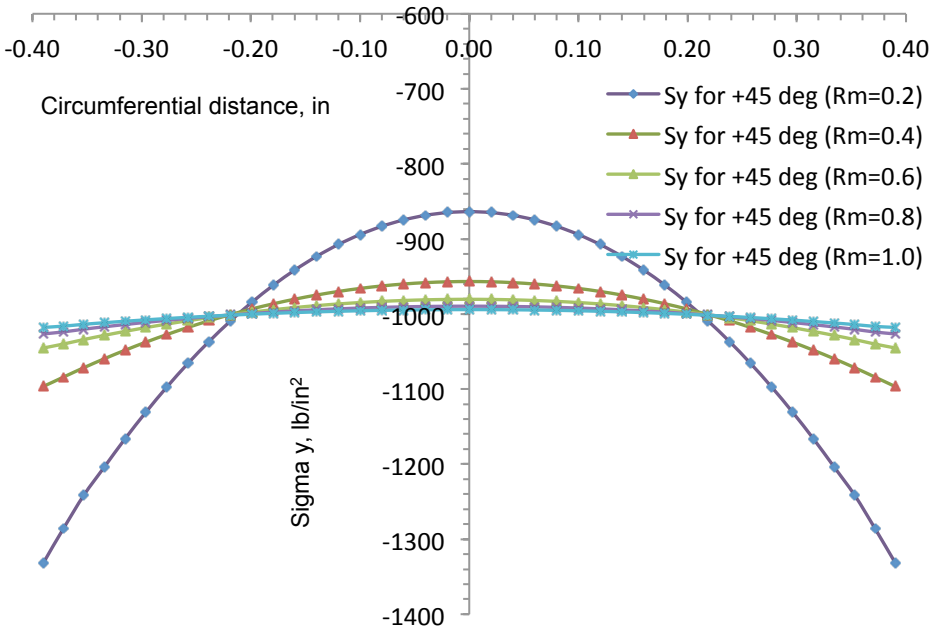

Figure 5-68 σ_y for +45 deg Plies under M_x vs. Circ. Arc Length $\left(\Delta T = 50^0 F\right)$

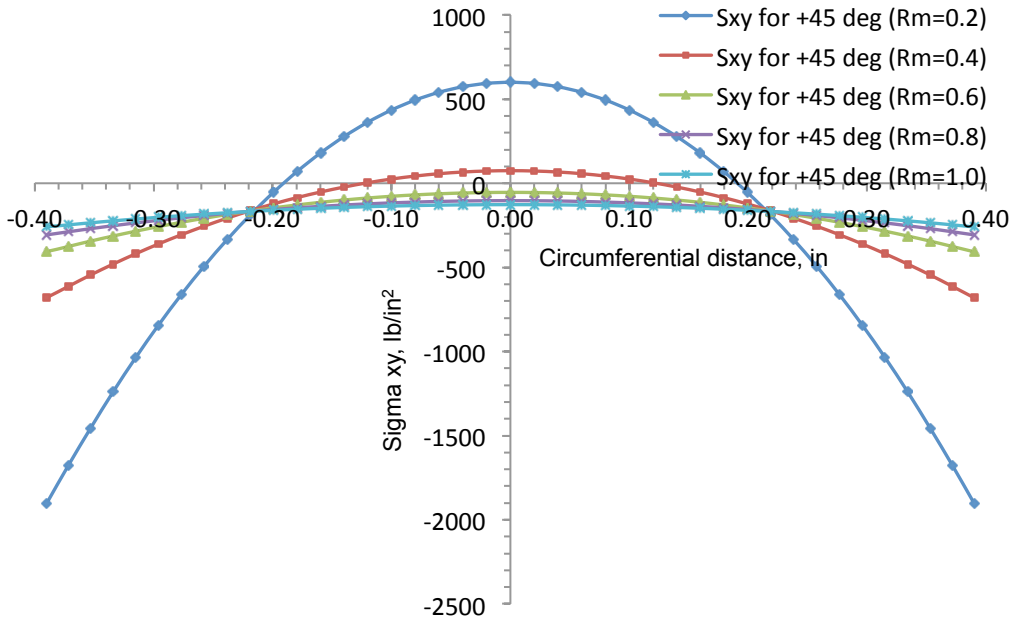

Figure 5-69 τ_{xy} for +45 deg Plies under M_x vs. Circ. Arc Length $\left(\Delta T = 50^0 F\right)$

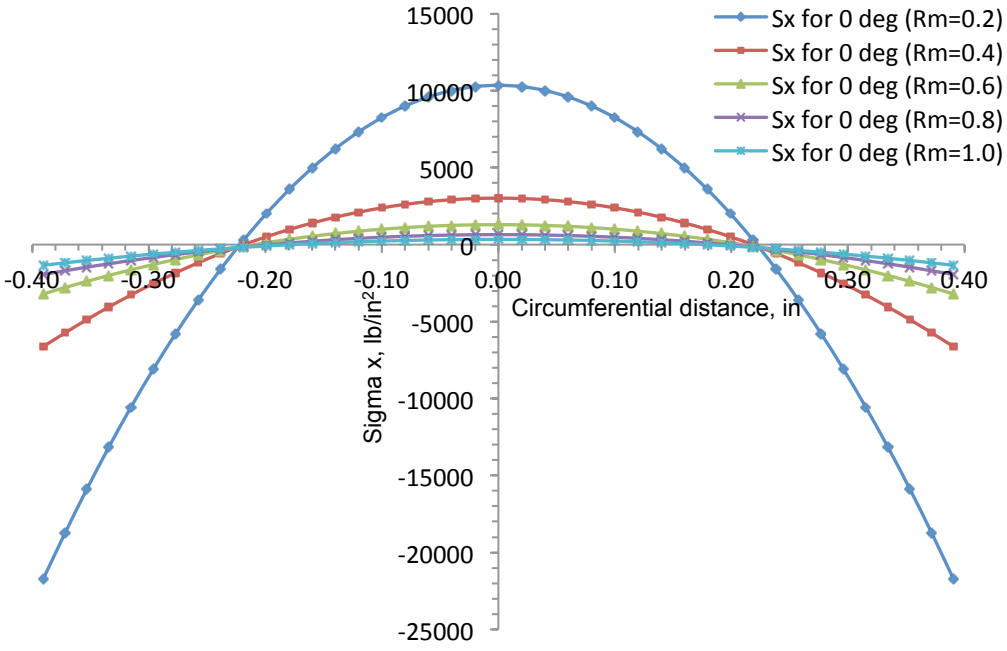

Figure 5-70 σ_x for 0 deg Plies under M_x vs. Circ. Arc Length $\left(\Delta T = 50^0 F\right)$

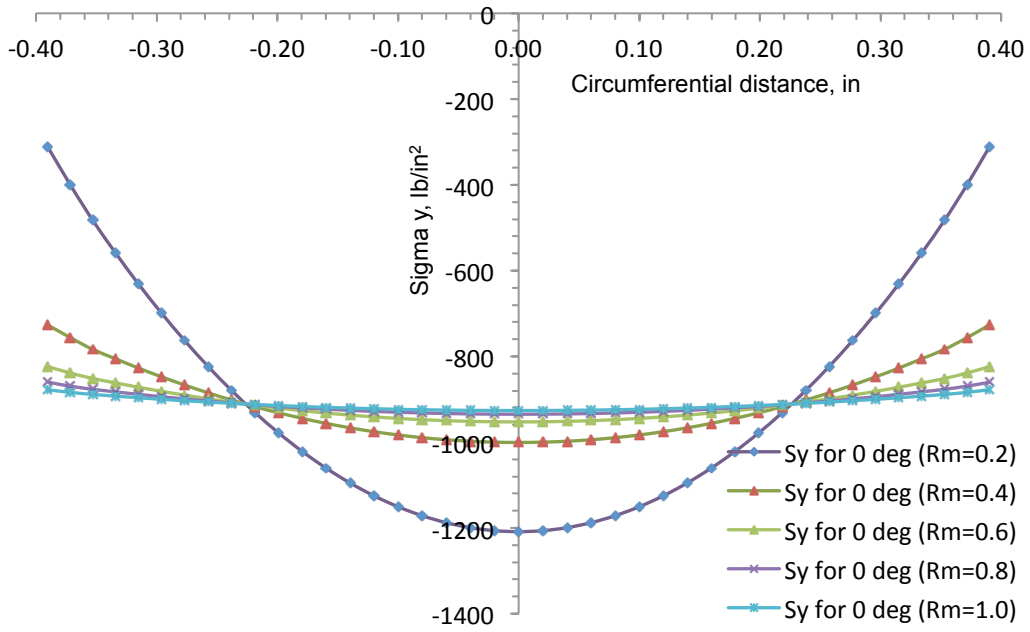

Figure 5-71 σ_y for 0 deg Plies under M_x vs. Circ. Arc Length $\left(\Delta T = 50^0 F\right)$

The notable observations upon analyzing the parametric stress plots for $+45^o$ and 0^o plies subjected to a bending load in the presence and absence of temperature environment include : -

a) While assuming the total arc angle (2α) to be constant and sequentially increasing the mean radius of curvature R_m, in-plane stress $(\sigma_x, \sigma_y$ and $\tau_{xy})$ predictions for $+45^o$ and 0^o layers indicate a parabolic distribution while computed across the circumferential arc length of the composite strip.

b) The stress bands exhibit a distinction in tension and compression across the circumference.

c) τ_{xy} Stress predictions encountered by $+45^o$ layers are shown to be significant as opposed to the zero shear stresses τ_{xy} experienced by the 0^o plies (Fig. 5-45).

d) Magnitude of in-plane longitudinal σ_x stresses in 0^o plies is observed to be substantial relative to the σ_x stresses experienced by the $\pm 45^o$ plies.

e) Additionally, the distribution trends shown by in-plane shear stresses τ_{xy} for $\pm 45^o$ plies interchange while preserving the magnitudes experienced under axial loading conditions.

f) Magnitude and distribution pattern of in-plane stresses σ_x and σ_y displayed by $\pm 45^o$ plies are identical.

h) Presence of an additional thermal loading shows no significant influence over the in-plane shear τ_{xy} stresses witnessed in 0^o plies as opposed to the elevated stress levels reported for $\pm 45^o$ plies.

5-4-2 Parametric Study based on ratio: Axial and Bending Loading case

$\left(\Delta T = 0^0 F, \Delta T = 50^0 F\right)$

The composite geometry is defined by a $[\pm 45/0]_s$ six-ply symmetric-balanced curved composite laminate configuration. Shell mean radius R_m is incrementally varied from 0.2 inch to 1 inch in steps of 0.2 inches respectively. While maintaining the total laminate thickness as a constant, $\left(\frac{t_{laminate}}{R_m}\right)$ ratio is allowed to vary. The total arc angle characterizing the circumferential length of the composite strip is assumed to possess a constant value of $(2\alpha = 90^\circ)$. Under separate circumstances, the structural response is studied in terms of variation in in-plane stress $(\sigma_x, \sigma_y$ and $\tau_{xy})$ predictions under a concentrated axial force and bending moment applied specifically to the centroid of the curved strip.

The loading is maintained constant throughout while varying the $\left(\frac{t_{laminate}}{R_m}\right)$ ratio. The mesh density is in the order of 145800 elements. An ideal cantilever type configuration is simulated via implementing the structural boundary conditions as outlined in the initial commentaries respectively. Figure 5-72 to Figure 5-77 displays the combined in-plane stress $(\sigma_x,\sigma_y$ and $\tau_{xy})$ profile plots of $\pm 45^{o}$ and 0^{o} plies subjected to a centroidal axial load while including and excluding the presence of a uniformly distributed thermal loading environment as a function of $\left(\frac{t_{laminate}}{R_m}\right)$ ratio.

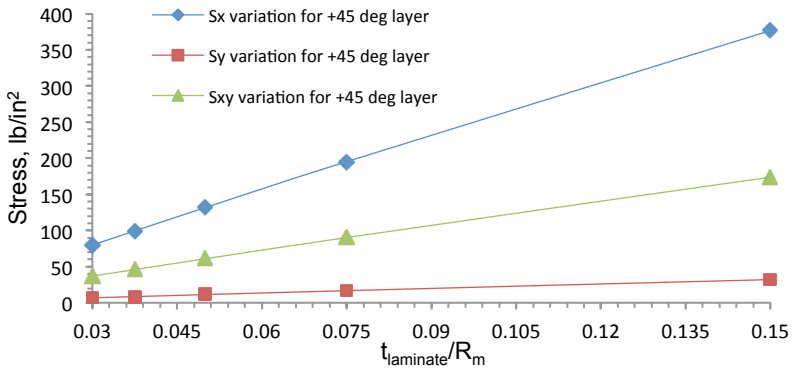

Figure 5-72 +45 deg Ply Stresses under N_x vs. vs. (t/R_m) Ratio $\left(\Delta T = 0^{0}F\right)$

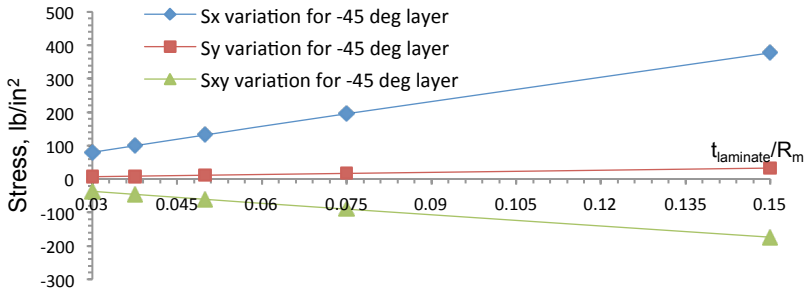

Figure 5-73 -45 deg Ply Stresses under N_x vs. vs. (t/R_m) Ratio $\left(\Delta T = 0^{0}F\right)$

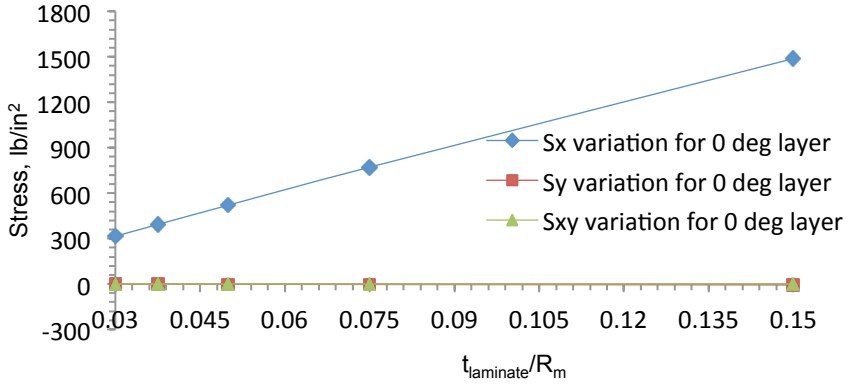

Figure 5-74 0 deg Ply Stresses under N_x vs. vs. (t/R_m) Ratio $\left(\Delta T = 0^0 F\right)$

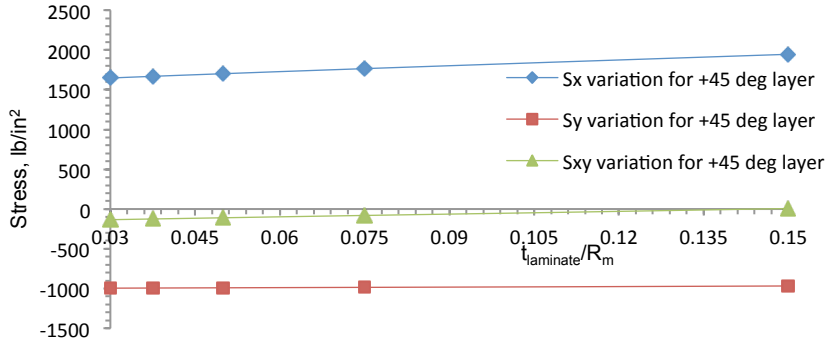

Figure 5-75 +45 deg Ply Stresses under N_x vs. vs. (t/R_m) Ratio $\left(\Delta T = 50^0 F\right)$

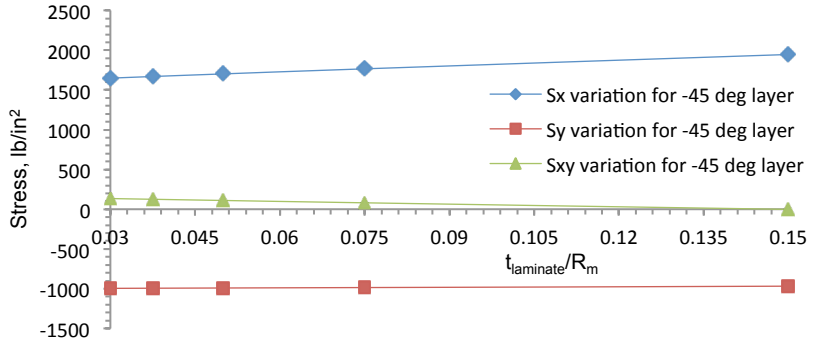

Figure 5-76 -45 deg Ply Stresses under N_x vs. vs. (t/R_m) Ratio $\left(\Delta T = 50^0 F\right)$

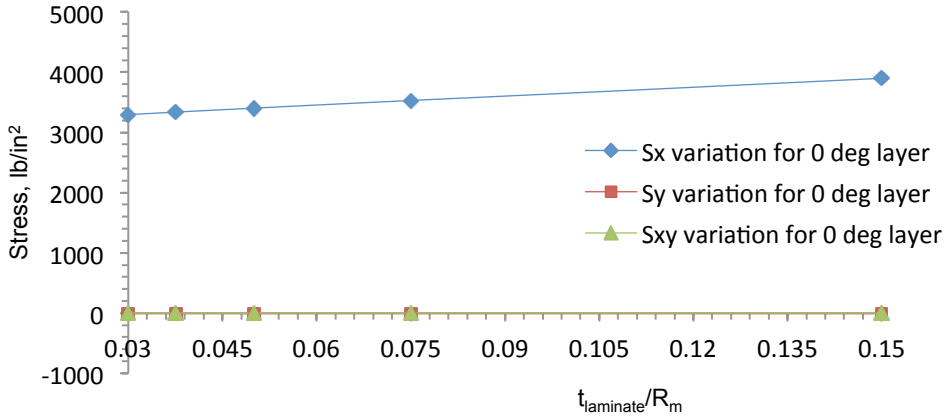

Figure 5-77 0 deg Ply Stresses under N_x vs. vs. (t/R_m) Ratio $\left(\Delta T = 50^0 F\right)$

The notable observations upon analyzing the in-plane stress distributions versus (t/R_m) ratio plots for $\pm 45^\circ$ and 0° plies subjected to a axial load in the presence and absence of temperature environment include: -

a) Decrease in R_m while assuming the laminate thickness to be constant indicates a linear increase in $(\sigma_x, \sigma_y$ and $\tau_{xy})$ stress profiles for $\pm 45^\circ$ and 0° plies respectively.

b) Magnitude of in-plane shear stresses τ_{xy} shown by angle plies are considerably large as opposed to 0° plies.

c) Influence of transverse stresses and in-plane shear stresses associated with 0° plies are negligible and show a steady invariance to changing (t/R_m) ratios.

d) A switch from positive slope to negative slope in the shear stress τ_{xy} distributions associated with $\pm 45^\circ$ plies can be witnessed as a function of varying (t/R_m) ratios.

Figure 43 to Figure 48 display the combined in-plane stress $(\sigma_x, \sigma_y$ and $\tau_{xy})$ profile plots of $+45^\circ$ and 0° plies subjected to a centroidal axial load while including and excluding

the presence of a uniformly distributed thermal loading environment as a function of $\left(\frac{t_{laminate}}{R_m}\right)$ ratio.

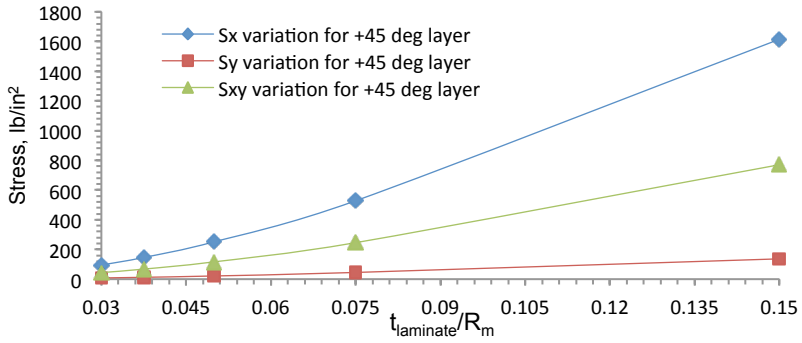

Figure 5-78 +45 deg Ply Stresses under M_x vs. vs. (t/R_m) Ratio $\left(\Delta T = 0^0 F\right)$

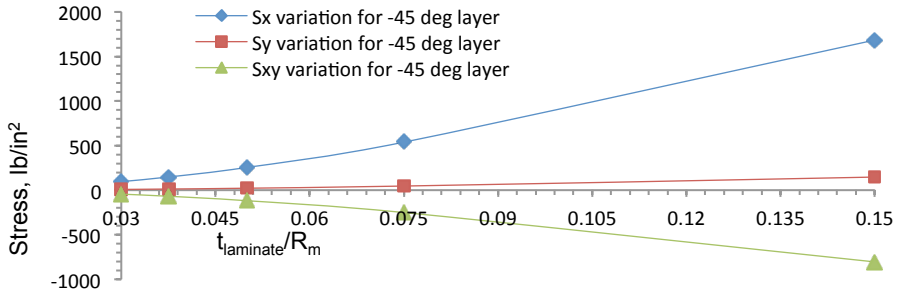

Figure 5-79 -45 deg Ply Stresses under M_x vs. vs. (t/R_m) Ratio $\left(\Delta T = 0^0 F\right)$

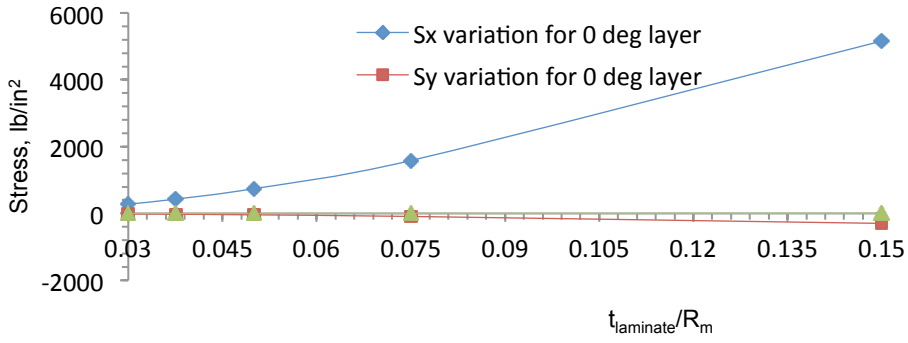

Figure 5-80 0 deg Ply Stresses under M_x vs. vs. (t/R_m) Ratio $\left(\Delta T = 0^0 F\right)$

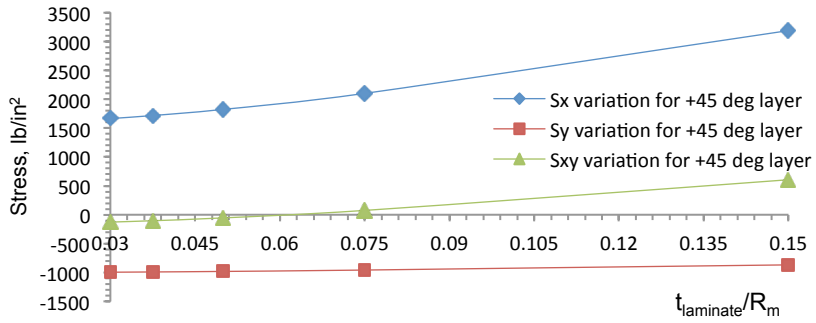

Figure 5-81 +45 deg Ply Stresses under M_x vs. vs. (t/R_m) Ratio $\left(\Delta T = 50^0 F\right)$

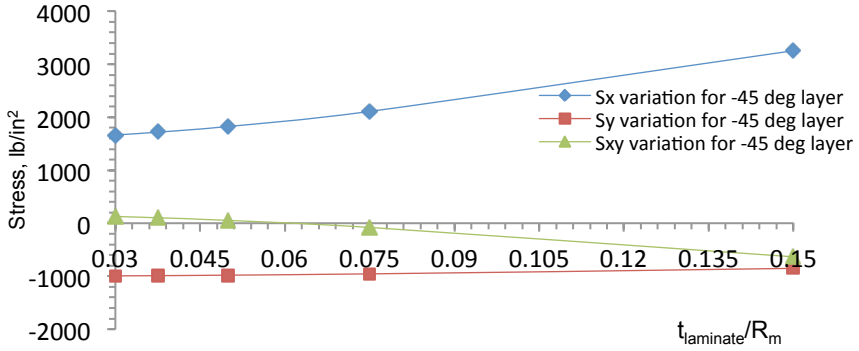

Figure 5-82 -45 deg Ply Stresses under M_x vs. vs. (t/R_m) Ratio $\left(\Delta T = 50^0 F\right)$

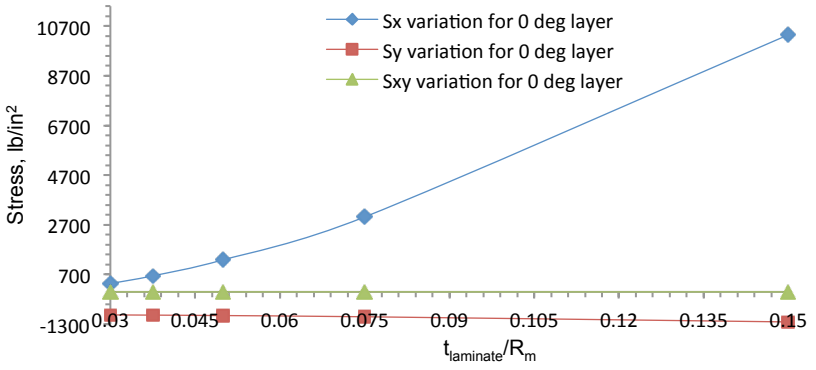

Figure 5-83 0 deg Ply Stresses under M_x vs. vs. (t/R_m) Ratio $\left(\Delta T = 50^0 F\right)$

The notable observations upon analyzing the in-plane stress distributions versus (t/R_m) ratio plots for $\pm 45^o$ and 0^o plies subjected to a bending load in the presence and absence of temperature environment include: -

a) Decrease in R_m while assuming the laminate thickness to be constant indicates a non-linear increase in $(\sigma_x, \sigma_y$ and $\tau_{xy})$ stress profiles for $\pm 45^o$ and 0^o plies respectively.

b) Magnitude of in-plane shear stresses τ_{xy} shown by angle plies is considerably large as opposed to 0^o plies (trivial solution).

c) Influence of transverse stresses and in-plane shear stresses associated with 0^o plies are negligible and show a steady decrease in stress levels to increasing (t/R_m) ratios.

d) A switch from positive slope to negative slope in the shear stress τ_{xy} distributions associated with $\pm 45^o$ plies can be witnessed as a function of varying (t/R_m) ratios.

Chapter 6

EXPERIMENTAL INVESTIGATION FOR CENTROID LOCATION DETERMINATION IN THIN-WALLED OPEN CROSS-SECTION CYLINDRICAL COMPOSITE SHELLS

This chapter presents the development of an effective experimental methodology to accurately determine the location of the centroid for a set of fabricated curved composite test specimens. The manufacturing process used to fabricate curved composite specimens is discussed. Post-fabrication steps implemented to develop the test specimens are outlined. Additionally, the design, development and manufacturing of a novel ad-hoc test set-up to provide an accurate experimental determination of the centroid is shown. Experimentally measured centroid locations are compared to analytically determined centroid results.

6-1 Fabrication of Thin-Walled Curved Composite Coupons

The plies utilized for specimen fabrication were cut from a large pre-preg tape roll (Fig 6-1). The pre-preg material utilized to manufacture the test specimens was a HexPly IM7/8552 Graphite/Epoxy [14] composite system. The HexPly IM7/8552 Graphite/Epoxy material system is highly versatile and is typically used in numerous commercial aerospace, defense and industrial applications.

Figure 6-1 IM7/8552 Graphite/Epoxy Pre-Preg Roll [14]

Key benefits and features of the IM7/8552 composite material system include:-

- Toughened epoxy matrix with excellent mechanical properties.
- Elevated temperature performance.
- Good translation of fiber properties.
- Controlled matrix flow in processing
- Appreciable drape and tack.

6.1.1 Test Coupon Fabrication Methodology

This section will present a step-by-step description of the manufacturing process for a set of 7 curved composite test coupons starting from the initial stage of pre-preg cutting to the end stage of curved shell.

- Two high grade stainless steel hollow tubes of outer radius 0.5 in and length 25 inches served as the primary mandrels for pre-preg fabric lay-up.
- Wet sanding was employed to ensure complete removal of surface impurities and oil deposits. Three gradations of sand paper were (400, 220, &140 grit sizes, respectively) were used to perform wet sanding of the steel mandrel. The mandrel was wiped thoroughly using a clean, lint-free cotton wipe cloth to make the surface free of contaminants and moisture, as shown in Figure 6-2.

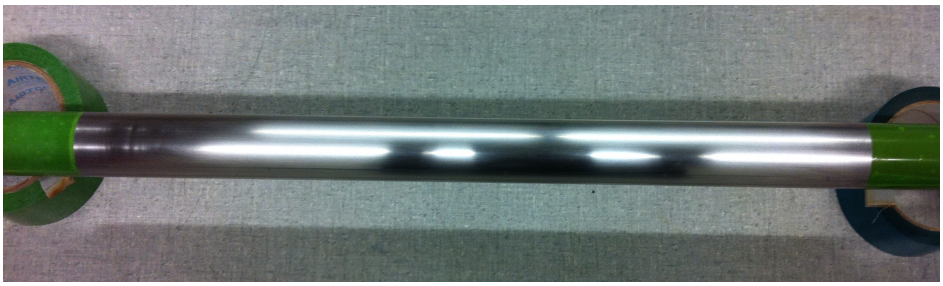

Figure 6-2 Prepped Stainless Steel Mandrel

- Industrial grade FREKOTE B15 sealer was uniformly smeared on the outer surface of the tube. B15 is formulated specifically as a sealer for composite and

metal molds with micro porosity problems, small surface scratches or imperfections. B15 is a clear, colorless solvent based polymer. A clean lint-free, cotton wiping cloth was used to effectively wipe the surface of the mandrel. Wipe cloth was uniformly run down along one direction across the length of the mandrel to avoid excessive pooling. Three coats were applied on the mandrel surface, allowing 10 minutes between successive applications.

- Generally, pre-preg rolls are stored in sub-zero temperature levels as prescribed by composite manufacturers (Hexcel product data sheet) [14]. Most pre-preg resins require a storage temperature of 0°F or lower. Pre-preg handling properties are a function of temperature. Elevated temperatures makes the material highly tacky, making it difficult to position and handle the plies. Low temperatures makes the material very stiff and difficult to work with. Typically, resins are susceptible to moisture ingress, and the absorbed water inhibits cure kinetics. Therefore, controlling the relative humidity is important for ensuring the resin will undergo an optimal cure. High humidity will also decrease the tack of the material. Pre-preg materials with high tack have been shown to trap air and moisture between the plies, resulting in porosity in laminates.
- Pre-pregs measuring 8 in x 3.1 in were precisely cut using a sharp paper knife. Plies were cut only on a glassy, impurity-free surface specifically dedicated to cutting plies. Plies were not trimmed or cut on top of the mandrel to prevent damage to the mandrel or underlying plies. Individual plies are identified by their fiber orientation and further number-marked at the time of cutting to allow for quicker layup onto the mandrel surface.. Figure 6-3 shows the precisely cut and juxtaposed 0^0, $+45^0$ and -45^0 pre-pregs.

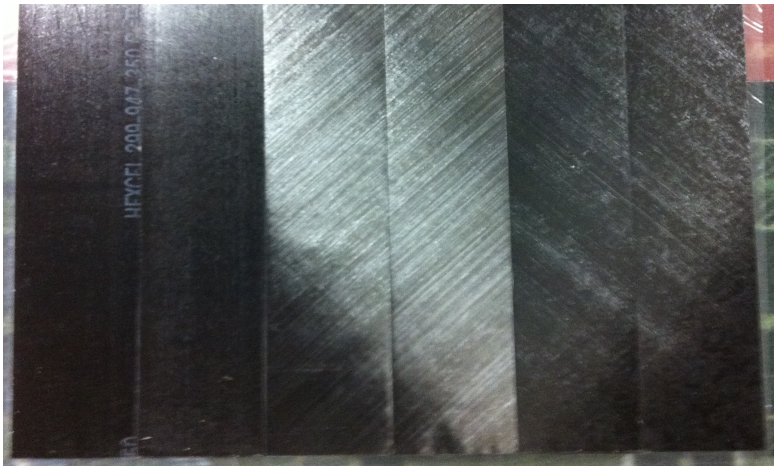

Figure 6-3 Prepped Stainless Steel Mandrel

- Individual plies were visually inspected for defects and surface impurities prior to stacking on the mandrel surface. Damaged plies were replaced as necessary. Figure 6-4 represents a stack of composite plies ready for visual inspection.

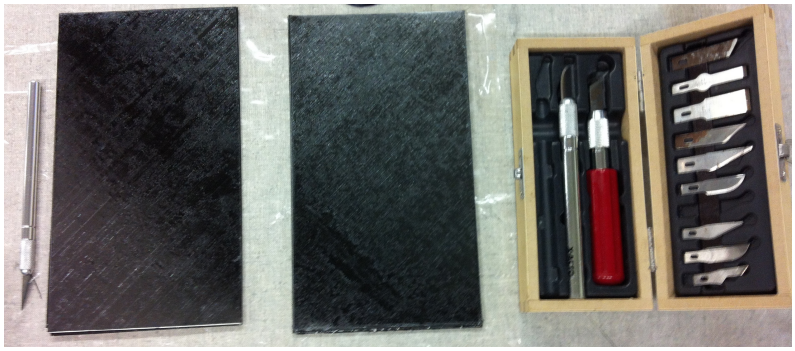

Figure 6-4 Visually Inspected Composite Ply Stack

- Pre-preg laminations required for subsequent lay-ups and cures were pre-cut and organized into kits while retaining their protective glossy coating. Such ply pre-preg kits were encapsulated in thick moisture-proof polyurethane sheets and freeze-stored until ready for lay-up.
- Upon scribing marks along the surface boundaries of the mandrel, individual plies were stacked sequentially. The objective was to fabricate a set of open-

cross sectioned composite tubes with a $[\pm 45/0]_s$ ply lay-up. The parts were characterized by a thickness of 0.03 inches, R_i=0.5 inch and R_o=0.53 inch respectively.

- In order to facilitate a uniform adherence within successively layered plies, localized heating was introduced via hot air blowing through a hair-dryer (Fig 6-5). A quick, uniform burst of hot air is blown along the length of the ply pre-preg. Slightly elevated temperature achieved across the ply surface rendered the pre-preg to be more drapable.

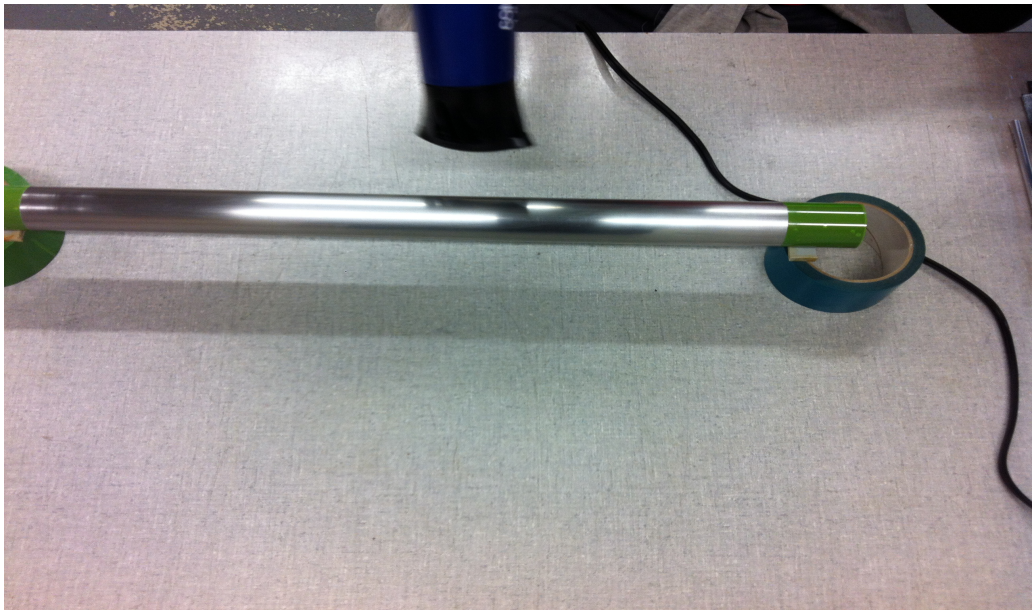

Figure 6-5 Hot Air Treatment to Aid Uniform Inter-Ply Adhesion

- The glossy protective layer was carefully peeled along the direction of fibers to maintain ply structural integrity. Quickly warmed plies were hand-laid and firmly hand-pressed along the direction of the fibers as shown in Figure 6-6. Plies were sequentially placed along the mandrel surface by hand using talc-free nitrile gloves. Caution was exercised throughout the process of ply stacking sequence to maintain inter-ply alignment.

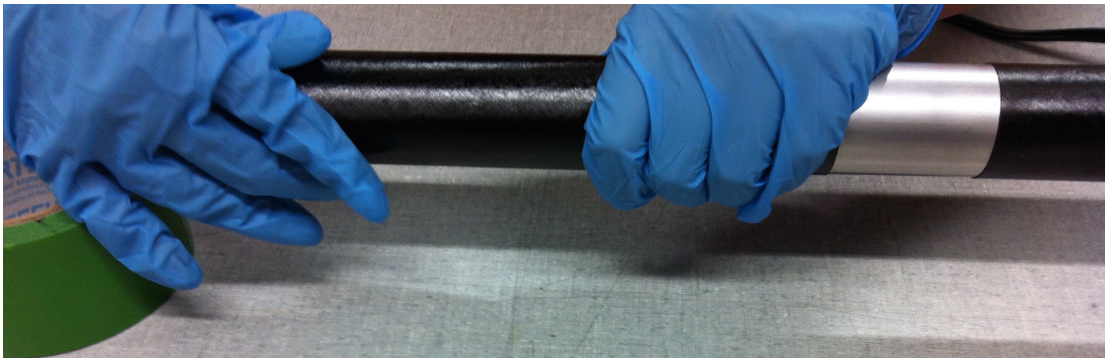

Figure 6-6 Hand-laid Ply Installment

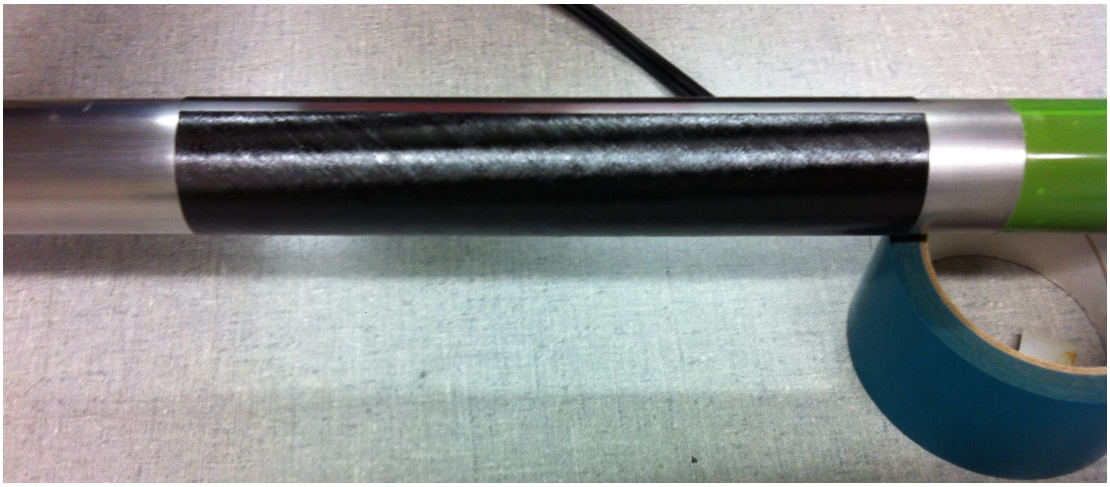

Figure 6-7 Uniform Ply Alignment and Adherence to Mandrel Surface

- Immediately following the collation of 6 plies, a debulking procedure was administered via room-temperature assisted vacuum pressure. A thin translucent nylon bagging film was laid over the laminate (Fig 6-8). This fabric aids in regulating the flow of matrix into the breather cloth fabric. Breather fabric provides the means to apply the vacuum and assists in removal of air and volatiles from the room-temperature assisted vacuum bag assembly (Fig 6-9).

Figure 6-8 Bleeder Fabric applied on Top of Ply Collations

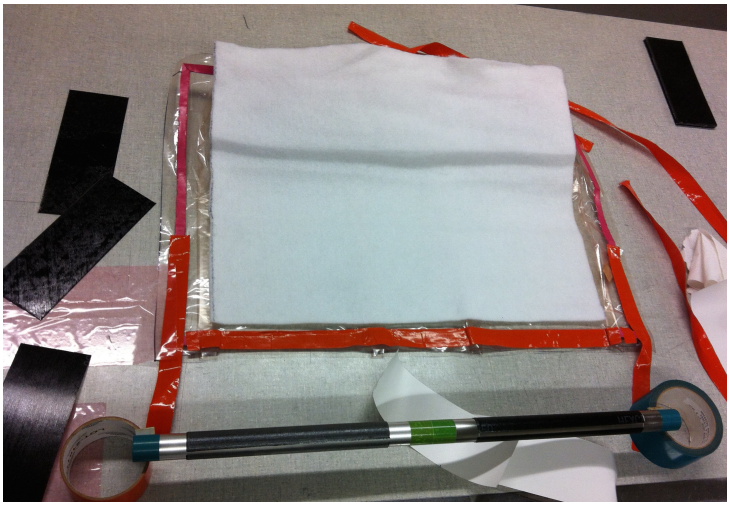

Figure 6-9 White Porous Breather Bag Application and Arrangement

- The final stage of bagging process involves the encapsulation of the mandrel-bleeder fabric-breather fabric arrangement through a translucent heat resistant vacuum bag. Double-sided sticky tape was used along all the boundaries of the vacuum bag. Vacuum valves were strategically placed outside the perimeter of the laminate and away from the corner regions of the sealed bag (Fig 6-10).
- A uniform vacuum environment was created for at least 30 minutes . A pressure gage was fitted into the lip of other vacuum valve. A uniform pressure of approximately 27.5~28 in/Hg was maintained by activating a valve operated high-speed air pump. The sealant tape was firmly pressed against the vacuum bag to generate absolute leak-proof vacuum conditions inside the bagging area. This segment of the bagging process completed the debulking procedure (Fig 6-11).

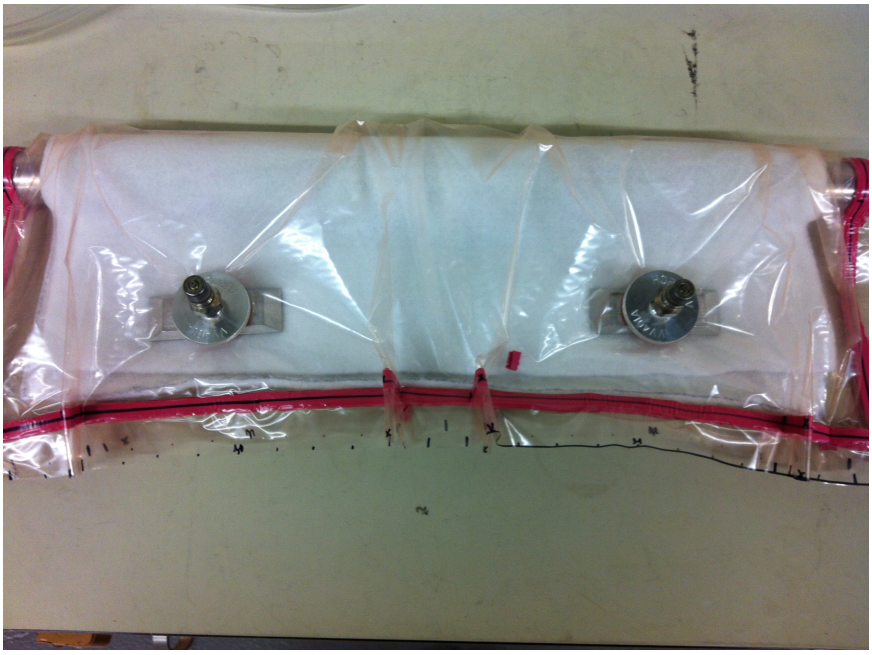

Figure 6-10 Fully Sealed Vacuum Bag Configuration

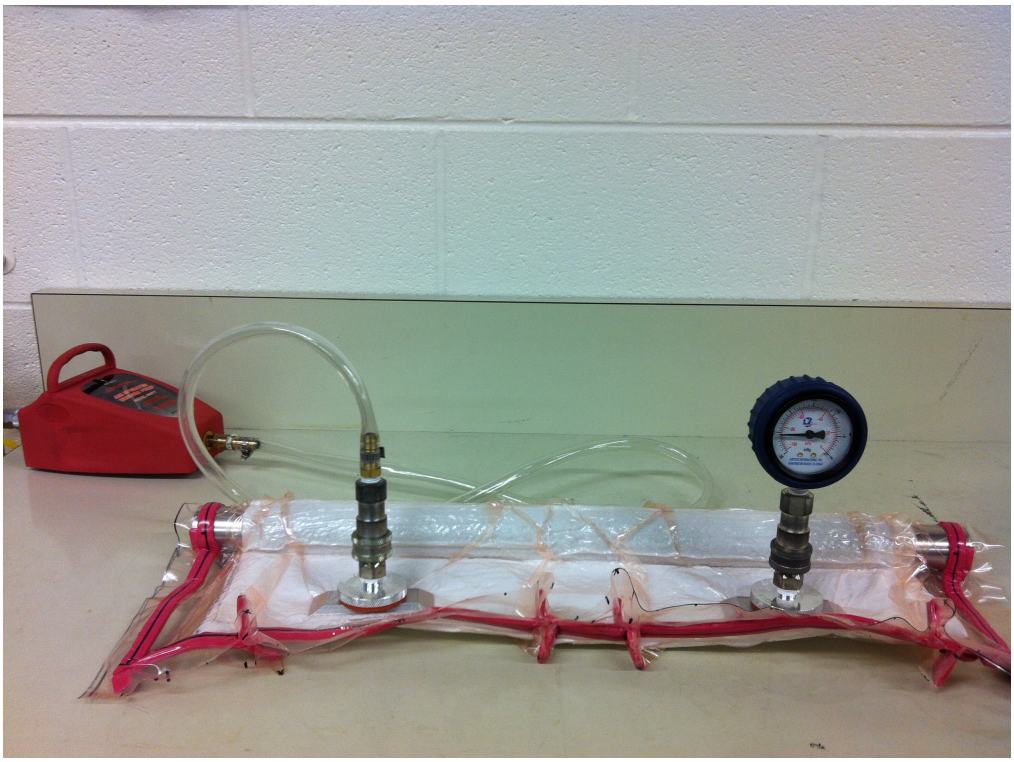

Figure 6-11 Debulking Procedure for Uniform Room-Temperature Assisted Curing

- Curing of the pre-preg ply laminates was initiated through a vacuum bag assisted, high temperature and pressure induced, autoclave molding process.
- The pressure vessel (Fig 6-12) has a rear mounted fan for forced circulation of compressed air. The rear of the vessel contains an electric heater and a cooling coil. The atmosphere circulation begins at the fan. The vessel acts as a fan housing, directing flow outward along the walls, through an annular duct. The circular outer door with 9 angularly oriented bolt heads turns the flow towards the workspace. Flow continues through the cooling coil, through the heater and returns to the fan outlet.

Figure 6-12 Autoclave Machine Set-up

- The autoclave instrumentation panel was used to set the pressure-temperature ramp cycle associated with the curing process of each specimen. Curing cycle to process the IM7/8552 material system (Fig 6-13) based composite coupons was

as prescribed by Hexcel . Manually, each stage of the curing process is programmed to sequentially execute the temperature-pressure cycle.

- Key curing characteristics that are vital to the fabrication of the open cross-sectioned cylindrical composite tubes are: a) highest curing temperature=360^{0}F (maintained for approximately 2 hrs) b) highest curing pressure= 85 psi (maintained for approximately 5 hrs) c) vacuum pressure = -27 psi d) vacuum hold time =1 hr 35 mins from the beginning of the cure cycle e) total curing cycle time = 6 hrs 55 mins. The cool-down period is gradual and is ambient air assisted to minimize residual stress build-up and prevent micro-cracking.

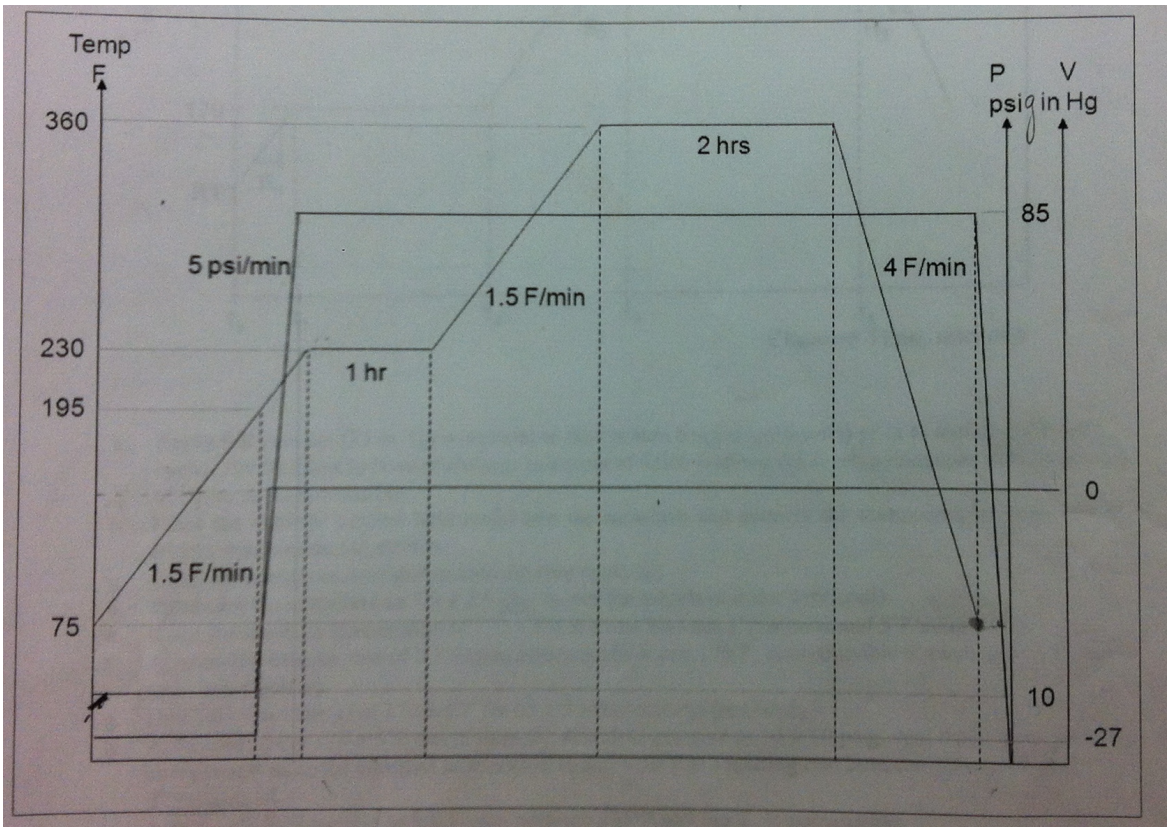

Figure 6-13 IM7/8552 Autoclave Curing Cycle

- 8 open cross-sectioned cylindrical composite tubes of inner radius R_i=0.5 in and outer radius R_o=0.53 in were fabricated. Figure 6-14 shows a set of 4 composite tube specimens along with their associated stainless steel hollow tube mandrels.

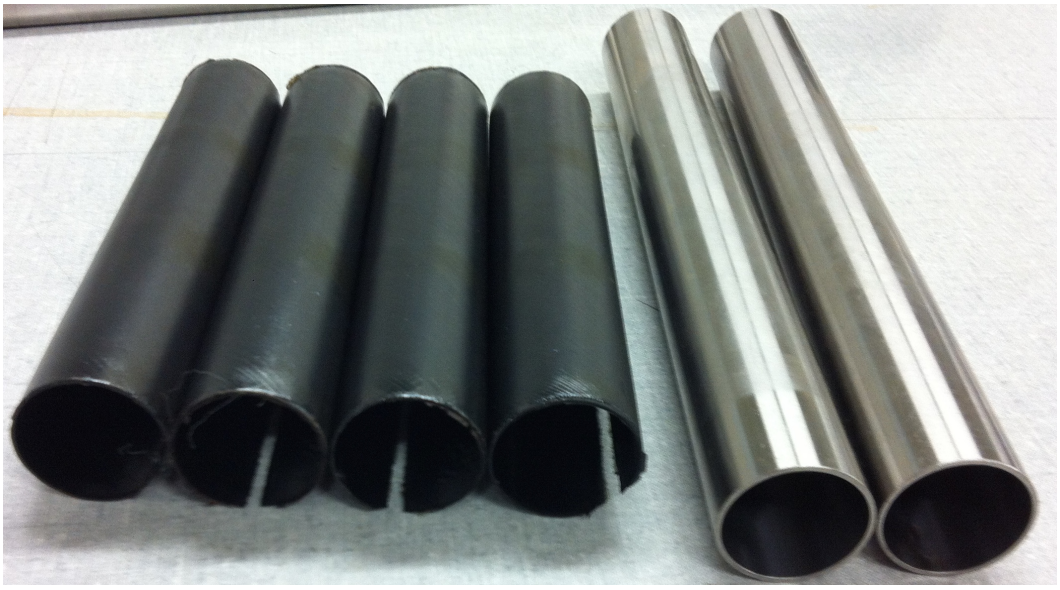

Figure 6-14 Fabricated Composite Tube Specimens

Expectations for the composite coupon fabrication process are :

1. Cured Laminate thickness is uniform across the length and circumference of the tube.
2. Variability in mechanical properties between each specimen is not substantial. The amount of resin bled out during the curing cycle is assumed to be uniform for all specimens. Conceptually, the level of resin bleed directly relates to the matrix volume fraction within the laminate. As a consequence, the ratio of fiber volume fraction to matrix volume fraction is altered. Lower FVF corresponds to a softer material and a larger FVF corresponds to stiffer material.

3. Actual curing cycle temperatures and pressures witnessed by all specimens are assumed to be identical as thermocouples were not installed to monitor the cure cycle variables.
4. Amount of void content is assumed to be minimal.
5. Amount of moisture absorbed during thawing process is assumed to be minimal .
6. Volatiles and impurities are assumed to be completely absent within the material.
7. Magnitude of residual stresses and spring-in effect is trivial.

Curved composite shells of total arc length $2\alpha = 95^{o}$ were cut from the open cross-section cylindrical composite tube specimens. The curvature imposed a challenge to perform the cuts. Initial attempts to grip and steadily translate the curved tube through an electrically operated high-speed, rotating diamond-tip steel blade were unsuccessful. Strong structural vibrations induced on the material upon contact with the rotating blade was determined to the cause of coupon motion. Consequently, gripping of the specimen imposed a challenge and led to abrupt movement of the coupon during the cutting procedure. Physical damage consistent with fiber splitting and delamination were observed.

The development of a supplementary base plate to firmly restrict the coupon motion was necessary. The aluminum mold (Fig 6-15) consists of a base plate with one edge possessing an elevated arch. The total arc angle of the arch is designed and manufactured to be consistent with the intended composite shell arc length ($2\alpha = 95^{0}$). First step involved in creating the composite strips was to level out the uneven edges. Serrated uneven tube edges were initially filed and later trimmed by the high-speed rotating diamond-tip steel blade of an electrically operated composite saw (Fig 6-16).

Secondly, the open cross-sectioned tube was sliced into two identical halves. Later, the sliced coupons were firmly seated against the elevated arch of the mold and aligned in the direction of the rotating blade. The translating base plate of the composite saw was modified to accommodate the mold structure. Excess material was precisely trimmed out in the process. The final material was visually inspected for surface delaminations and edge fiber splitting.

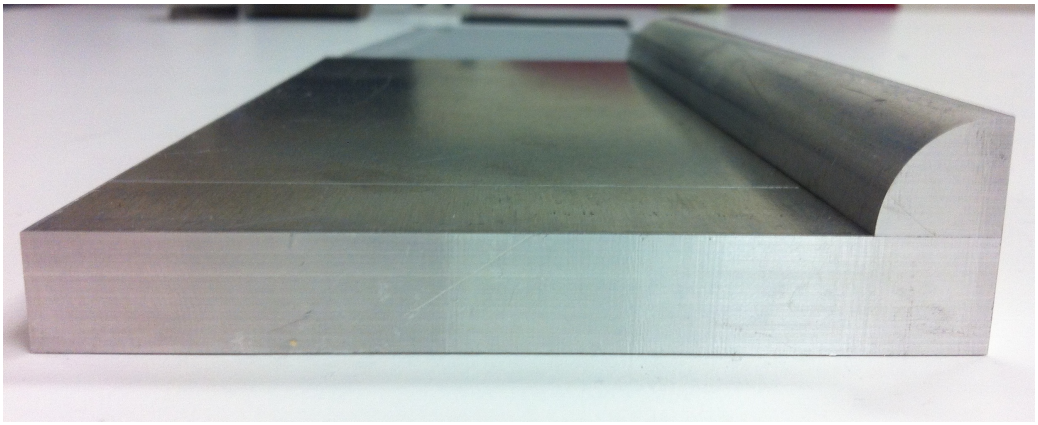

Figure 6-15 Ad-Hoc Aluminum Mold to Aid Specimen Slicing

Figure 6-16 Uniform Specimen Slicing by a Composite Saw

6-2 Test Fixture Design and Development

Design and manufacturing of a test fixture specifically suited to experimentally investigate the structural behavior of curved composite shell coupons was first undertaken. The novel fixture design fundamentally serves to accomplish three major purposes: a) to effectively provide a gripping capability for testing curved composite coupons b) to efficiently transfer the axial force from the clamp joints to the coupon c) to enable a shift in the positioning of the load application axis along the symmetry line of the specimen cross-section.

6.2.1 Structural Modeling and Design of Test Fixture

A novel ad-hoc test fixture design has been proposed to experimentally investigate the mechanical response of open cross-section , thin-walled , curved composite cylindrical shell coupons. The design of the grip is shown in Figures 6-17 through 6-20. An exploded view is represented.

In view of Figure 6-17 (top-to-bottom), the structural elements constituting the test fixture can be decomposed into 3 sub-parts namely; 1 stationary part addressed by U-channel top clamp, 1 translating part addressed by dovetail joint and a two piece translating (male-female) base clamp structure that slides along the dovetail joint. The top face of the U-channel clamping system extends into a threaded bolt that connects into the load cell. A calibrated load cell is connected to the crosshead of a uni-axial tensile testing machine. Planar side faces of the translating dovetail joint are designed to align in between the U-channel top clamp. The two components establish a pin support type structural link allowing for small angle rotations about the pin joint. The primary purpose of the dovetail joint was to very efficiently provide a new degree of freedom to the two-piece (male-female) translating base clamp structure.

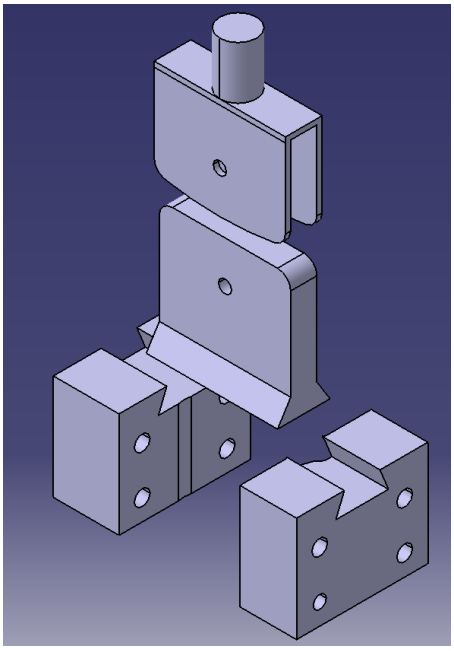

Figure 6-17 Test Fixture Structural Elements: Exploded View

The top face of the base clamp structure is designed to consist of a “dovetail” shaped groove (Fig 6-18).

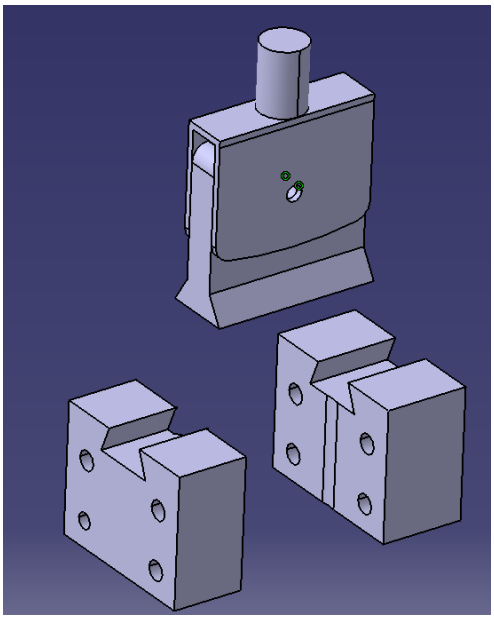

Figure 6-18 Dovetail Shaped Groove Design in Base Clamp Structure

This physical characteristic allows the two-piece base clamp structure to slide along the dovetail joint (Fig 6-19, Fig 6-20). The dovetail design allows to locally shift the tensile loading axis, thus enabling the cylindrical shell coupon to exhibits a characteristic extension-bend type coupled mechanical deformation response.

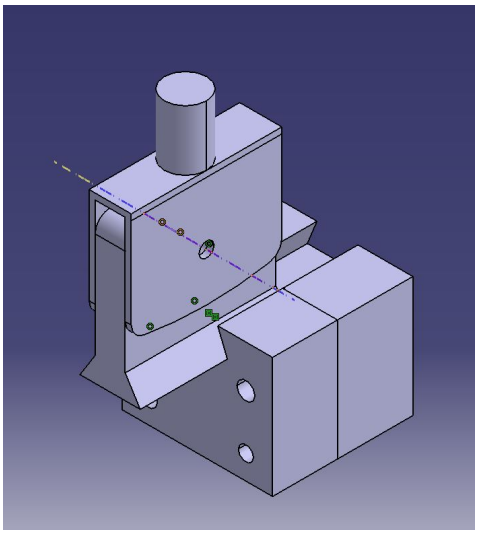

Figure 6-19 Off-axis Loading Scenario: Dovetail ahead of Base Clamp

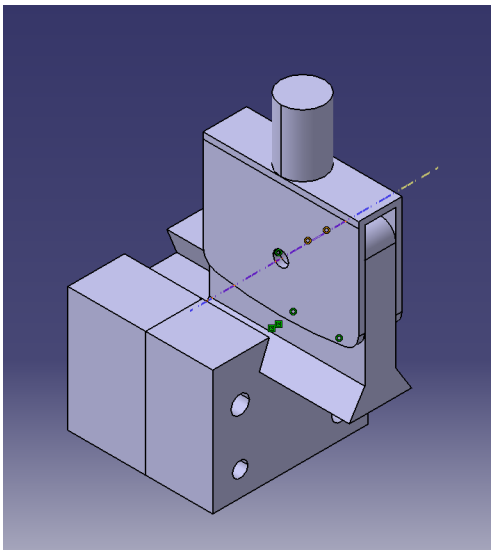

Figure 6-20 Off-axis Loading Scenario: Dovetail aft of Base Clamp

For loading scenarios when the tensile loading axis is offset from the unknown neutral axis of the cylindrical shell coupon , extension-bending deformation occurs. When the position of the translating two-piece base clamp structure is such that the mechanical extension-bend behavior is decoupled, the location of the neutral axis associated with the composite coupon is experimentally identified.

Figure 6-21 represents the manufactured structural components of the test fixture. The test fixture set-up consists of two pairs of base clamp structures, 2 dovetail sliding joints and 2 U-Channel top clamp units respectively. Figure 6-22 shows the assembled configuration of the test-set-up.

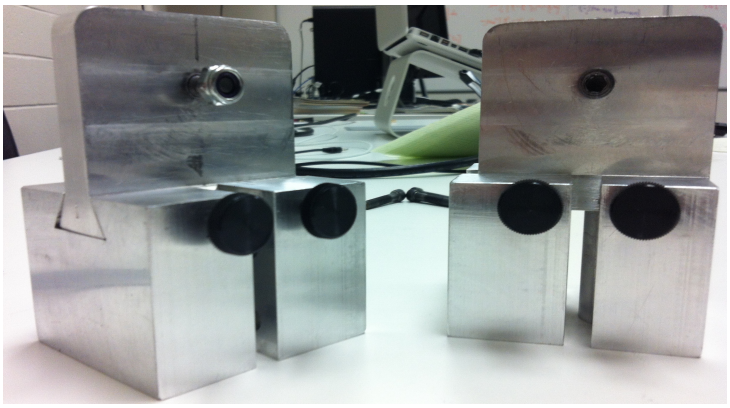

Figure 6-21 Manufactured Structural Components of Test Fixture Set-up

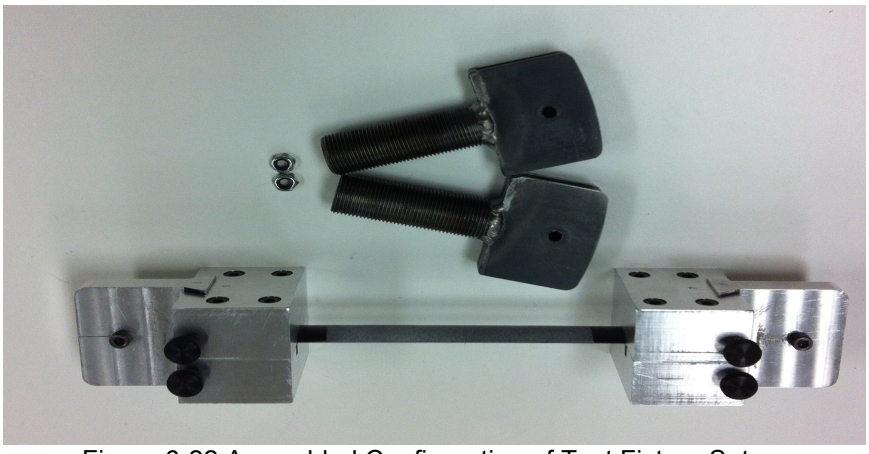

Figure 6-22 Assembled Configuration of Test Fixture Set-up

6-3 Experimental Set-up and Centroid Location Determination

The prime objective of this effort is to experimentally determine the location of the centroid for a set of open cross-section curved cylindrical shell coupons characterized by the following assumed geometric and mechanical properties:

Assumed mechanical and geometric characteristics

- Coupon Length = 8 inches.
- Total arc angle (2α) = 95 deg.
- Coupon outer radius R_o= 0.53 inches.
- Coupon inner radius R_i= 0.5 inches.
- Effective gage length for analysis = 6 inches.
- Specimen height = 0.2 inches.
- Material system utilized for coupon fabrication = Hexcel IM7/8552 .

6.3.1 Experimental Methodology for Centroid Determination

The previous section addressed the design and development of the novel test fixture to characterize the structural response in terms of surface strain fields and the location of centroid for curved cylindrical composite shell strips. The main idea built around identifying the location of neutral axis is to effectively investigate the surface strain response for such coupons under predefined offset load conditions. Strains induced in a structure are a measure of structural deformation. Cylindrical shell coupons subjected to off-neutral axis tensile loading conditions exhibit a strain response $\varepsilon_{measured}$ that is a combination of extension strains produced by contribution due to axial force component ε_N and extensional strains produced by contribution due to bending moment ε_M respectively.

$$\varepsilon_{measured} = \varepsilon_N + \varepsilon_M \tag{6.1}$$

Figure 6-23 illustrates the schematic of a curved cylindrical shell configuration assumed to be characterized by the geometric and mechanical characteristics discussed above. The specimen is indicated to be subject to two offset tensile loading scenarios.

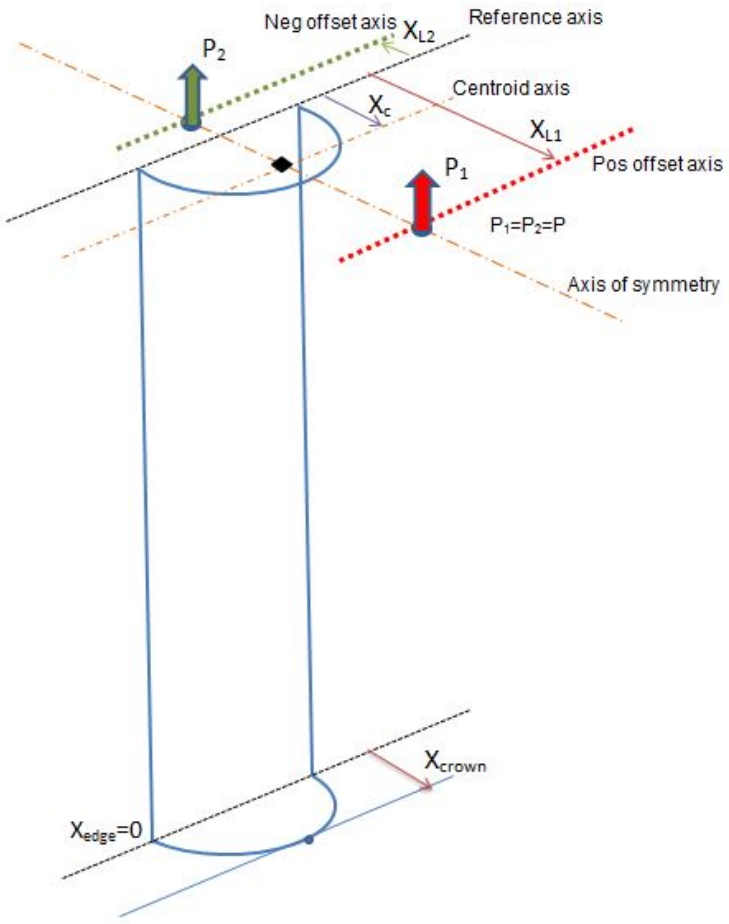

Figure 6-23 Schematic of Curved Cylindrical Shell

under Offset Loading Conditions

In case-1, the mid-axis of the dovetail joint (always coinciding with the primary loading axis of the tensile testing machine) is translated forward across the dovetail groove of the base clamp structure gripping the specimen and positioned at a distance X_{L1} (Fig 6-24). A predefined quasi-static, uni-axial load P_1 is applied to the test coupon.

The averaged strain response measured along the crown and the edge of the composite coupon is given by

$$\varepsilon_{measured}^{crown} = \varepsilon_N + \varepsilon_{moment}^{crown}$$
$$\varepsilon_{measured}^{edge} = \varepsilon_N + \varepsilon_{moment}^{edge} \quad (6.2)$$

Figure 6-24 Loading Axis Shifted to a Positive Offset from Specimen Edge

For a given load P_1, the extensional strain contribution due to ε_N is constant along the entire cross-section and extensional strain contribution due to the presence of an induced moment M_1 is assumed to vary linearly along the height of the specimen.

$$N_1 = P_1 \rightarrow \varepsilon_N$$
$$M_1 = P_1.(X_{L1} - X_c) \rightarrow \varepsilon_{M1} \quad (6.3)$$

where $\varepsilon_{M1} = \alpha.(X_{L1} - X_c)$, α is the curvature induced by the specimen by the bending moment M, X_c is the distance measured from reference axis (Fig 6-23) to the unknown

centroid location, and X_{L1} is the known distance measured from reference axis of the specimen to the loading axis.

In case-2, the mid-axis of the dovetail joint (always coinciding with the primary loading axis of the tensile testing machine) is translated backward across the dovetail groove of the base clamp structure gripping the specimen and positioned at a distance X_{L2} (Fig 6-25). A predefined quasi-static, uni-axial load $P_2=P_1=P$ is applied to the test coupon.

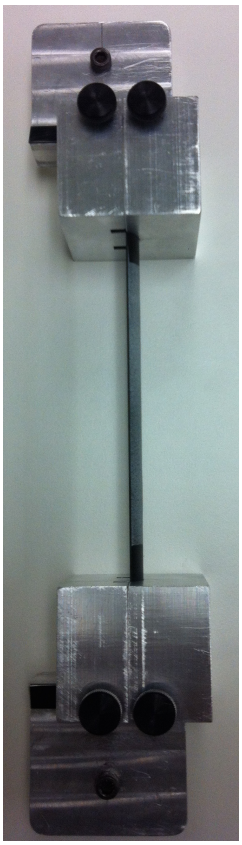

Figure 6-25 Loading Axis Shifted to a Negative Offset from Specimen Edge

The averaged strain response measured along the crown and the edge of the composite coupon is given by

$$\varepsilon_{measured}^{crown} = \varepsilon_N + \varepsilon_{moment}^{crown}$$
$$\varepsilon_{measured}^{edge} = \varepsilon_N + \varepsilon_{moment}^{edge} \quad (6.2)$$

fundamentally, for a given load P_2, extensional strain contribution due to ε_N is constant along the entire cross-section and extensional strain contribution due to the presence of an induced moment M_2 is assumed to vary linearly along the height of the specimen.

$$N_2 = P_2 \rightarrow \varepsilon_N$$
$$M_2 = P_2.(X_{L2} - X_c) \rightarrow \varepsilon_{M2} \quad (6.3)$$

where $\varepsilon_{M2} = \alpha.(X_{L2} - X_c)$, α is the curvature induced by the specimen by the bending moment M, X_c is the distance measured from reference axis (Fig 6-23) to the unknown centroid location, and X_{L2} is the known distance measured from reference axis of the specimen to the loading axis.

The determination of a suitable positive offset location (X_{L1}) and negative offset location (X_{L2}) is primarily dependent of several key mechanical and structural factors namely;

- when the magnitude of $(X_{L1} - X_c) = (X_{L2} - X_c)$, the moment arm becomes equal in magnitude and opposite in sign for the two offset loading conditions. This condition generates the same bending moment magnitude but with opposite sign.
- The offset distances must be far enough such that the contribution of extensional strains experienced by the coupon due to the induced bending moment is significantly higher as opposed to the extensional strains contributed by axial force component.
- Choosing the offset loading distances to be too far from the specimen edge can induce additional structural phenomena such a localized kinking and instabilities associated with in-plane warping of the shell cross-section.

For developing an experimental methodology to accurately predict the location of centroid for a particular set of curved cylindrical shell coupons, attention is warranted on several key factors that govern the determination of accurately measurable strain results and eventually compute the location of centroid. Since the structural configuration is characterized by a thin-walled cross section possessing anisotropic material properties and a circular curvature, the deformational response demonstrated by such composite coupons when loaded axially at predefined strip offsets can exhibit various form of non-linearities.

In order to gain a preliminary understanding by analyzing the mechanical behavior and capture the underlying phenomena exhibited by such curved composite coupons, an effective quantitative tool is necessary. A preliminary FEM based structural simulation of the testing conditions is necessary to predict the allowable operational range in terms of strip offsets and axial load ranges. The computer simulation served as a guide towards determining a combination of strip offsets and applied load ranges over which the structural response can be approximated as linear.

An ABAQUS based non-linear FE analysis is employed to study the structural behavior of open cross-sectioned thin-walled composite coupons. The study deals with the application of a transverse shell-edge load across the tip of a thin-walled curved composite strip (Fig 6-26) modeled utilizing S4R quadrilateral reduced integration shell elements [15]. Assumed geometric properties of the composite strip are; length = 8 inches, ply thickness = 0.005in, number of plies = 6, total laminate thickness = 0.03 inches, laminate lay-up = $\left[\pm 45/0\right]_{symm}$ total arc length 2α = 95^0 and mean radius of curvature R_m=0.515 inches respectively. The curved composite strip is modeled by assuming the composite material properties of Hexcel IM7/8552 Graphite/Epoxy as given in Table 6-1 [16] respectively.

Table 6-1 Material Properties for (Hexcel IM7/8552) Graphite-Epoxy

Property	Value
E_{11}	$23.3510*10^6$ psi
$E_{22}= E_{33}$	$1.6505*10^6$ psi
$\upsilon_{12} = \upsilon_{13}$	0.32
$G_{12} = G_{13}$	$0.749*10^6$ psi
G_{23}	$0.568547*10^6$ psi
υ_{23}	0.45
t_{ply}	0.0050 inches

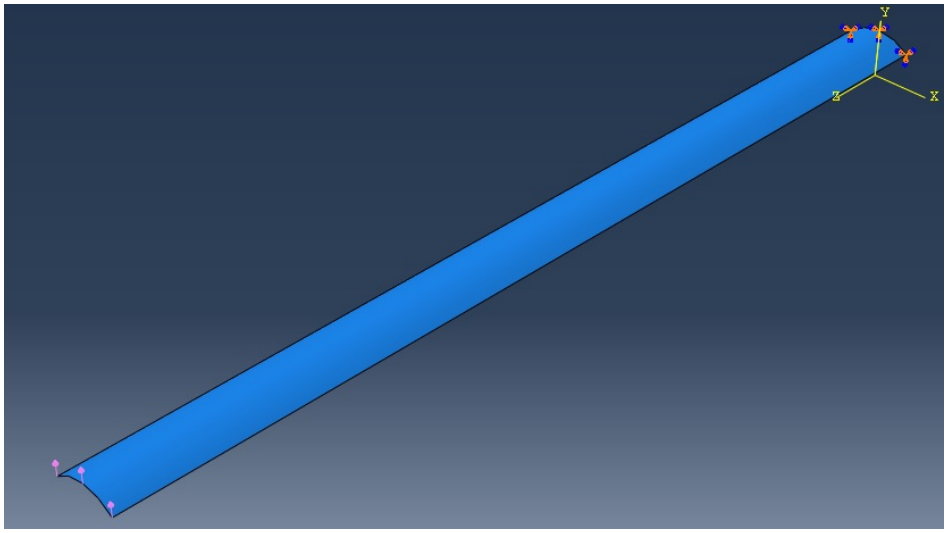

Figure 6-26 Thin-Walled Curved Composite Strip Subject to Shell Edge Load

It is assumed that the entire cross section is of uniform thickness. A geometrically non-linear analysis is conducted to fully capture non-linear phenomena. The discretized model size is in the order of 8900 elements as shown in Figure 6-27. Boundary conditions for the model correspond to a built-in cantilever type edge at one end and the other edge (front edge) is free to deform.

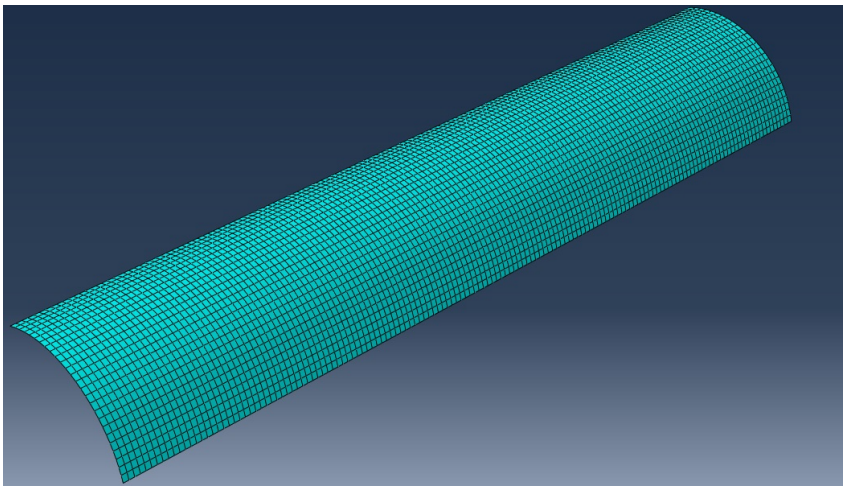

Figure 6-27 Discretized Curved Composite Strip Model

All the nodes across the cantilevered edge are encastered with all six degrees of freedom restricted. An ABAQUS based FE routine is utilized to initially investigate the mechanical response of a thin-walled curved isotropic member via activating the NLGEOM analysis feature.

The Riks method [15] is used to predict and capture the unstable, geometrically nonlinear response of the structure. This method is proven to be very effective when a) the analysis can include nonlinear materials and boundary conditions b) often follows an eigenvalue buckling analysis to provide complete information about a structure's collapse and c) can be used to speed convergence of ill-conditioned or snap-through problems that do not exhibit instability. The Riks method uses the load magnitude as an additional unknown. It solves simultaneously for loads and displacements. Therefore, another quantity must be used to measure the progress of the solution. Therefore Abaqus/Standard [15] uses the "arc length," *l*, along the static equilibrium path in load-displacement space. This approach provides solutions regardless of whether the response is stable or unstable. Tip rotation angles are computed and shown for increasing transverse shell edge loads. In order to distinguish the non-linear deformation response, a linear structural response

approximation is obtained based on the initial three data points corresponding to actual tip rotations. A linear regression curve fit is produced that aligns with the first three data points. Additionally, an extended linear approximation is generated by extrapolating the assumed data points to a broader load domain as shown in Figure 6-28.

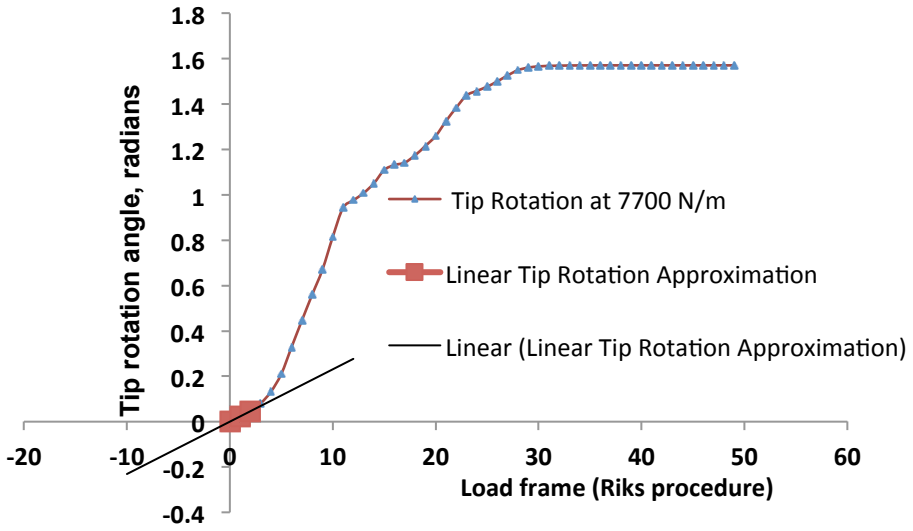

Figure 6-28 Tip Rotation Angle as a function of Load Frame Events (Riks Procedure)

Subsequently, upon increasing the applied shell edge load, the magnitude of induced bending moment grows and the resulting structural response begins to deviate from the linearly approximated behavior. The open cross-sectioned system exhibits a geometrically non-linear structural response. The structural response of a curved circular arc cross-section is governed by two fundamental phenomena.

For infinitesimal bending moments acting on the structure, the system response can be assumed to be linear. With progressively increasing bending moment, very quickly a non-linearity is observed. To resist the deformation developed by the induced bending moment, the tendency for the cross-section is to exhibit a closing (inward curl) along the length of the strip (warping) (Fig 6-29). A majority of the specimen length (highlighted in

blue) demonstrates a structural stiffening effect that is directly attributed to the geometric non-linearity associated with in-plane warping.

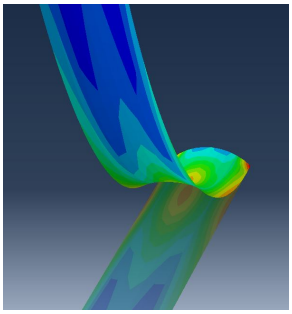

Figure 6-29 Structural Stiffening due to Cross-sectional Inward Curl

Beyond a certain level of increasing bending moments applied to the structure, a new form of additional non-linearity is triggered locally in close proximity to the fully restrained edge of the structure. Locally, the cross-section starts to deform outward, resulting in a decreased curvature (Fig 6-30). A significantly high compressive stress region emerges on the crown of the cross section that quickly leads to a buckling type instability terminating in a sudden structural collapse.

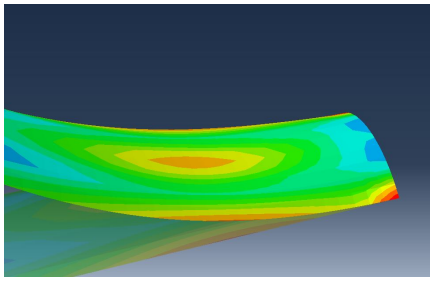

Figure 6-30 Compressive Stress Region Concentrated in Crown Area close to Fixed Edge

The physical response is consistent with a sudden jump in tip rotation angle and is indicative of a new form of non-linear behavior that is associated with sudden localized kinking observed in close proximity to the built-in edge of the structure (Fig 6-31).

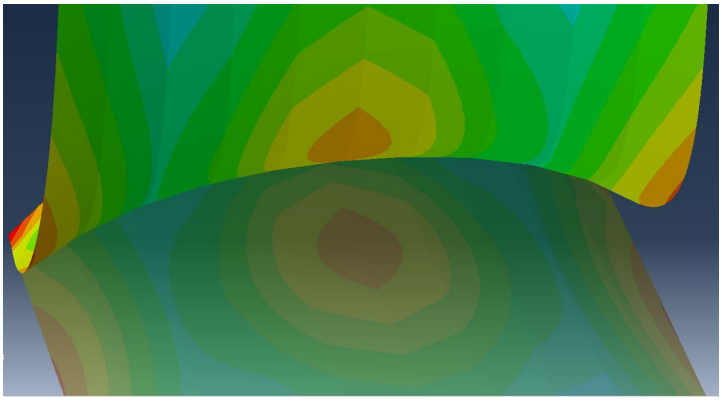

Figure 6-31 Rapid Localized Kinking in the Crown Area:

Precursor to Collapse

At this stage, the system requires only small amounts of tip force to initiate large displacements and rotations. The system response becomes unstable and presents a precursor to collapse.

On the other hand, by increasing the applied shell edge load to larger magnitudes in the downward direction, the cross-section of the structure starts to exhibit an opening (uncurl) along the length of the strip (in-plane warping) (Fig 6-32).

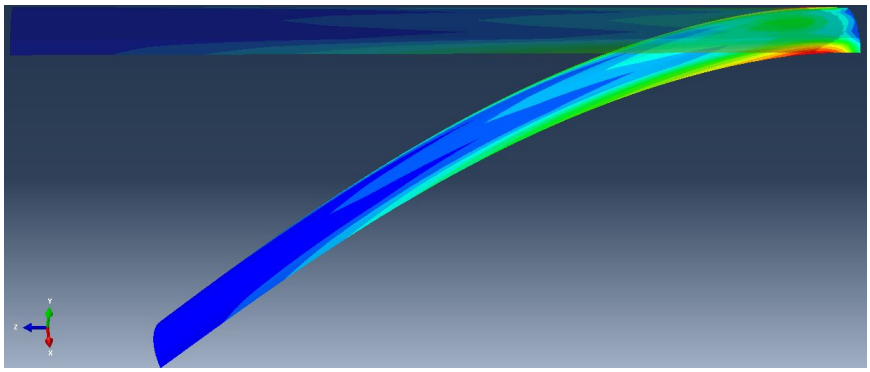

Figure 6-32 Structural Softening due to Cross-sectional Opening (Uncurl)

Initially, A softening occurs along the structure to prevent the structure from a sudden collapse. As discussed earlier, beyond a finite load carrying ability of the system, an identically new form of non-linearity is evolved in close proximity to the fully restrained

edge of the structure. Locally, the cross-section starts to deform outward, resulting in a decreased curvature. A significantly high compression region emerges on the internal face of the structure that quickly escalates into a buckling type instability terminating in a sudden structural collapse. The tip rotational response becomes significantly large in the downward direction for a specified force (Fig. 6-33).

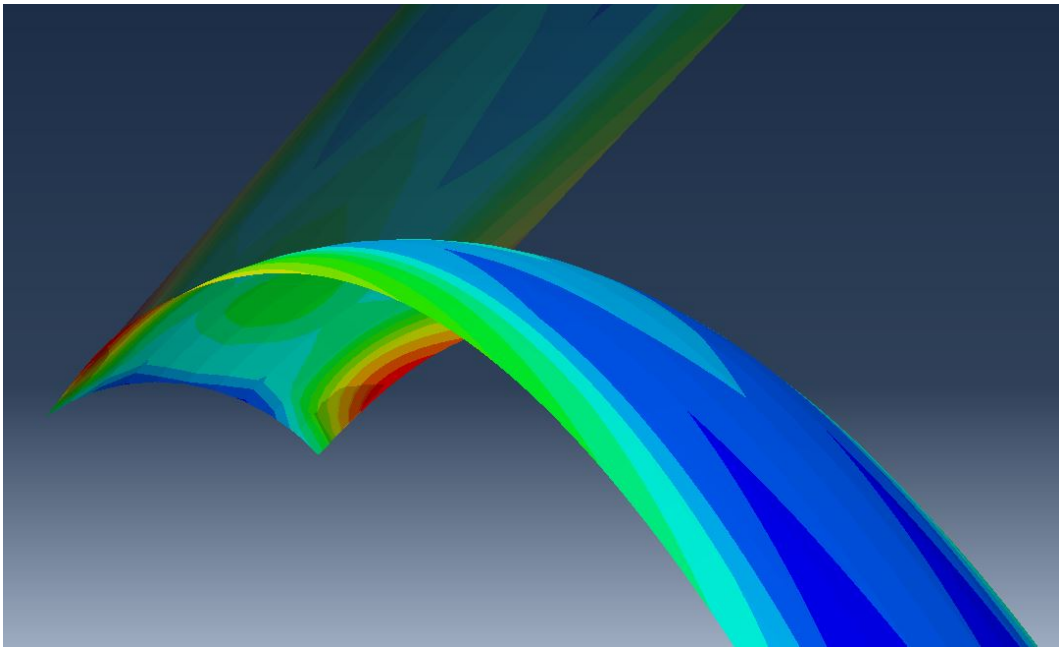

Figure 6-33 Compressive Stress Region Concentrated towards the Edge:

(Across the Width Close to Fixed Edge)

In essence, the structure demonstrates two types of non-linear responses; both due to in-plane warping followed by sudden collapse. For a curved strip subjected to an increasing upward bending moment, as warping progresses into a structure, a localized buckling is developed. Similarly, for a curved strip subjected to an increasing downward bending moment, warping continuously develops along the structure that is consistent with a cross-sectional opening followed by a sudden collapse. The structural geometry of the

cylindrical shell constructions allows for such non-linear effects to grow with the structure upon moment-induced deformations.

The onset and development of geometric non-linearities associated with warping can be outlined into two separate mechanisms:

- The presence of localized kinking characterized by a localized structural instability (buckling) that is predominant during large positive bending moments.
- The occurrence of a localized kinking preceded by structural softening that is predominant during large negative bending moments.

The second FEM exercise deals with simulating the actual test conditions of a thin-walled curved composite strip. This study attempts to gain a preliminary understanding into the structural response of such open cross-section curved composite coupons that are exposed to several combinations of strip offset and tensile loading conditions. More importantly, since a non-contact based full field strains measurement technique (Digital Image Correlation-DIC) will be primarily utilized to experimentally investigate the structural response by ultimately computing the location of centroid for such coupons, key characteristic elements pertaining to DIC such as system noise, admissible system noise-to-load ratio etc. must additionally be devoted attention while determining the combination of strip offsets and range of axial loads. As a consequence, the FEM model presents itself as an accurate quantitative tool to guide the experimental investigation.

Assuming the effective gauge length of the specimen to be 6 inches (1 inch from either side is clamped firmly), the only admissible degrees of freedom (assumed) for the test coupon are longitudinal stretching and cross-sectional bending (outward and inward) depending on the location of the applied strip offsets.

A thin-walled curved composite strip (Fig 6-34) is modeled utilizing S4R quadrilateral reduced integration shell elements [15]. Due to the symmetry associated with the test set-

up, loading conditions and structural geometry; symmetric boundary conditions are imposed by constructing a half-model of the test arrangement. Assumed geometric properties of the composite strip are; length = 3 inches, ply thickness = 0.005in, number of plies = 6, total laminate thickness = 0.03 inches, laminate lay-up = $\left[\pm 45/0\right]_{symm}$, total arc length (2α) = 95^0 and mean radius of curvature R_m=0.515 inches respectively. The curved composite strip is characterized by assuming the composite material properties of Hexcel IM7/8552 Graphite/Epoxy as previously shown in Table 10 [16] respectively.

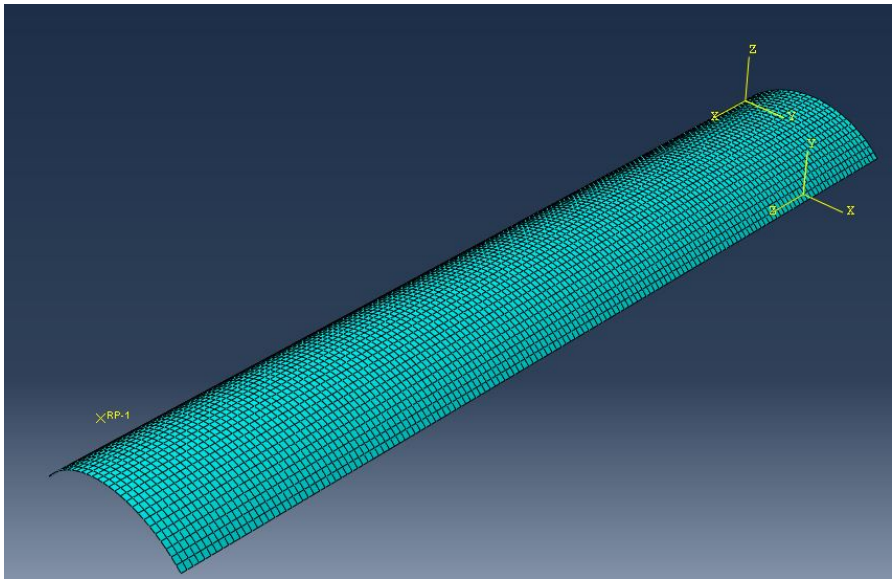

Figure 6-34 Discretized Symmetric Half-Model of Curved Composite Strip

It is assumed that the entire cross section is of uniform thickness. A geometrically non-linear analysis is conducted in this work to capture the geometrically non-linear phenomena. The discretized model size is in the order of 12200 elements as shown in Figure 6-34. Two separate reference coordinate systems are generated to characterize the geometry and fiber orientations within the structure. Global X-Y-Z coordinate system is used to construct the model and another local x-y-z coordinate system is constructed

with its origin to be located at the corner keypoints defining the bac-end edge. The local z-axis is designated along the height of the specimen, local x-axis is assigned along the length of the specimen and the local y-axis is oriented along the width of the specimen respectively (Fig 6-34). Figure 6-35 represents the schematic diagram illustrating all the boundary conditions have been imposed to fundamentally simulate the test set-up conditions. Figure 6-36 and Figure 6-37 shows the development of a reference point corresponding to a positive strip offset condition and a negative strip offset condition. The reference point represents the tensile load application point on both cases. The assumed boundary conditions on the front end of the strip model is collectively imposed specifically on the reference point Rp. A rigid body constraint [15] type interaction feature is generated that enables to mutually share the degrees of freedom imposed (Fig 6-35) to the reference point with the front-end edge respectively.

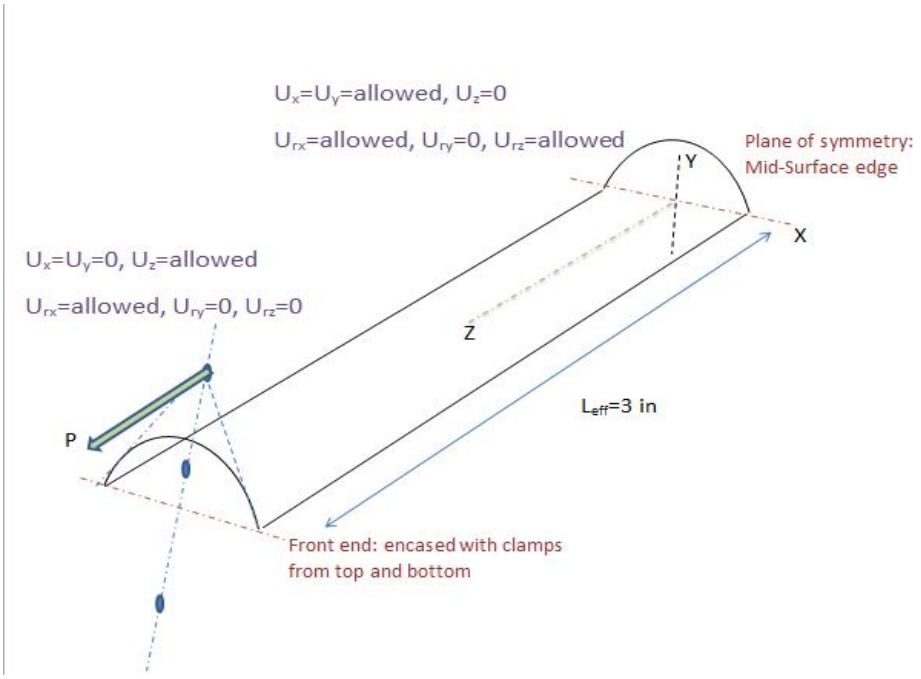

Figure 6-35 Imposed Boundary Conditions to

Simulate Experiment: Schematic

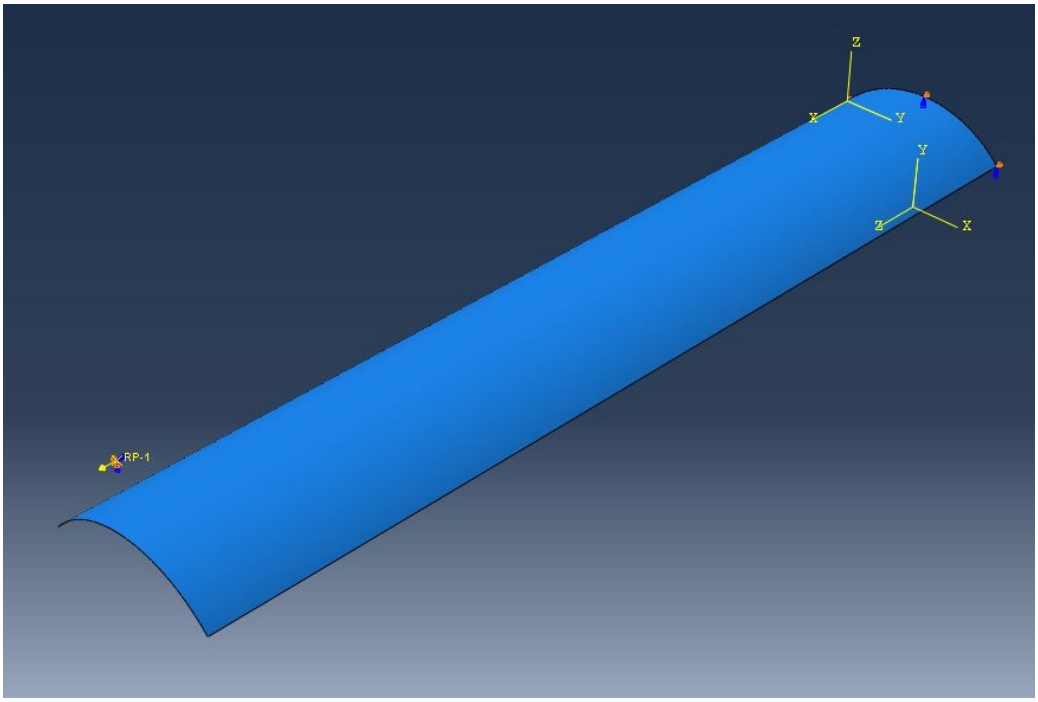

Figure 6-36 Axial Load Applied at a Positive Load Offset

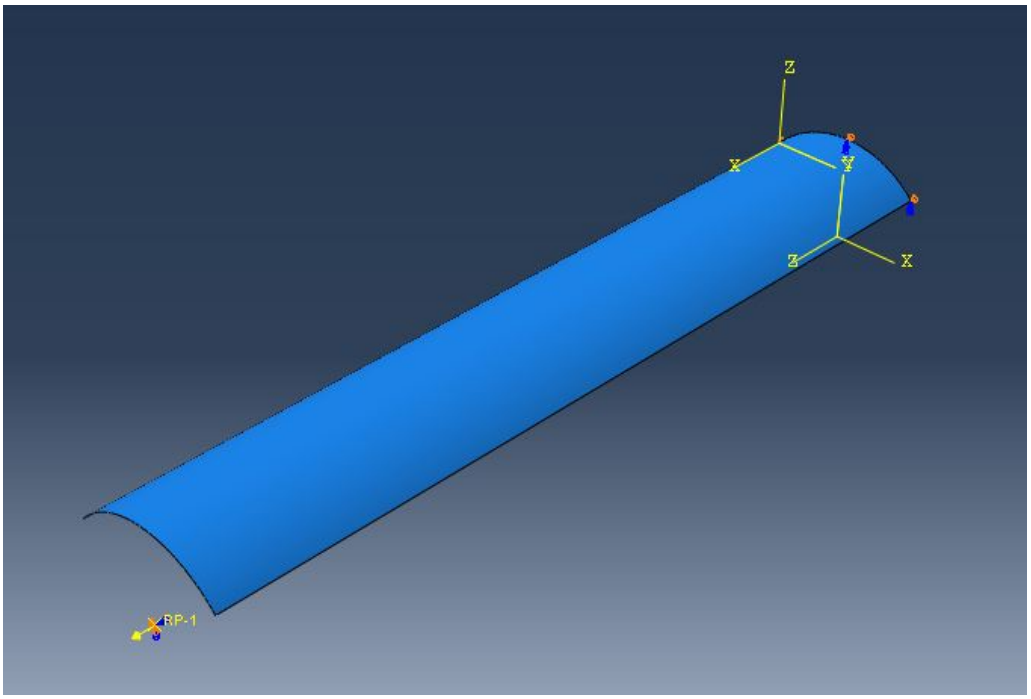

Figure 6-37 Axial Load Applied at a Negative Load Offset

Based on the preliminary FEM studies, for thin-walled open cross-sectioned curved composite strips, the application of an axial load at a specified offset from the centroidal point results in bending. In light of the bending induced non-linear response produced by the structure, the acceptable range of bending moments is of primary concern in order to obviate the occurrence of a potential structural collapse. In the presence of bending loads, two effects are observed. The first effect is the presence of a geometric non-linearity associated with warping. The second effect is a potential sudden structural collapse.

For the case when bending loads (induced from the applied strip offset (moment arm) multiplied to the applied axial load) act on the strip in addition to the originally applied axial loads, interestingly enough, the applied longitudinal load always attempts to stabilize the structure in an effort to alleviate the effects of an instantaneous structural collapse. However, the system is still predominantly influenced by the effects of non-linearity associated with warping. For the first case, when such open cross-sectioned curved strips were subjected to increasing transverse shell edge-loads, primary structural deformations were governed by induced bending loads and all fundamental geometric non-linearities were warp-driven.

A limited combination of bending moments (product of offsets and applied load) is observed to be considered applicable for the case of a thin-walled curved strip. Firstly, only for a small set of strip offsets and limited range of applied loads, the structural response can be approximated as linear. Under this assumption, applied axial loads can offer the potential to develop large measurable strain fields that can be effectively observed using DIC. Fundamentally low loads applied at small offsets produce small surface strains across the specimen. Low levels of observable strains via DIC are affected by system noise. Secondly, assuming the loading axis to be precisely aligned

with the centroidal axis of the thin-walled open cross-sectioned composite strip, all bending loads are eliminated. As a consequence, non-linearities associated with warping are absent, structural response is linear and measured surface strains are witnessed to be uniform.

Thirdly, application of low loads result in low strains and the accuracy of DIC based strain measurement technique are poor for low strain measurements. Hence, the proposed experiment is necessary to be operated under small strip offsets, allowing for the application of large loads, subsequently enabling the extraction of large strains, where DIC presents a good signal to noise ratio.

6-4 Analytical Formulation for Experimental Centroid Measurement

In order to experimentally determine the location of centroid, two tests are conducted on a specimen. The first test scenario is associated with axially loading the curved cylindrical shell at a positive offset. The test measurands are namely the averaged longitudinal strains across the edge of the specimen denoted as ε_{edge-1} and across the crown of the specimen shown as $\varepsilon_{crown-1}$ respectively. Mathematically a set of linear equations can be formulated and can be shown as

$$\begin{aligned} \varepsilon_{crown-1} &= \varepsilon_N + \alpha_1.(X_{crown} - X_c) \\ \varepsilon_{edge-1} &= \varepsilon_N + \alpha_1.(X_{edge} - X_c) \end{aligned} \tag{6.4}$$

assuming X_{crown}= 0.2 inches and X_{edge} = 0, Eq. 6.4 can be rewritten as

$$\begin{aligned} \varepsilon_{crown-1} &= \varepsilon_N + \alpha_1.(0.2 - X_c) \\ \varepsilon_{edge-1} &= \varepsilon_N + \alpha_1.(-X_c) \end{aligned} \tag{6.5}$$

Similarly, the second test is associated with axially loading the curved cylindrical shell at a predefined negative offset. The test measurands are namely the averaged longitudinal strains across the edge of the specimen denoted as ε_{edge-2} and across the crown of the

specimen shown as $\varepsilon_{crown-2}$ respectively. Mathematically a set of linear equations can be formulated and can be shown as

$$\begin{aligned}\varepsilon_{crown-2} &= \varepsilon_N + \alpha_2.(X_{crown} - X_c)\\ \varepsilon_{edge-2} &= \varepsilon_N + \alpha_2.(X_{edge} - X_c)\end{aligned} \tag{6.6}$$

assuming X_{crown}= 0.2 inches and X_{edge} = 0, Eq. 6.4 can be rewritten as

$$\begin{aligned}\varepsilon_{crown-2} &= \varepsilon_N + \alpha_2.(0.2 - X_c)\\ \varepsilon_{edge-2} &= \varepsilon_N + \alpha_2.(-X_c)\end{aligned} \tag{6.7}$$

For a generalized case, $\varepsilon_{crown} = \varepsilon_N + \alpha.(X_{crown} - X_c)$ and $\varepsilon_{edge} = \varepsilon_N + \alpha.(X_{crown} - X_c)$. Solving for curvature α, we get $\alpha = \dfrac{\varepsilon_{crown} - \varepsilon_{edge}}{X_{crown}}$. In view of Eqns 6.4 through 6.7, the unknown variables are ε_N and X_c (centroid location), whereas, the known variables that are experimentally measured are expressed as $\varepsilon_{crown-1}, \varepsilon_{edge-1}, \varepsilon_{crown-2}$ and ε_{edge-2} respectively. Curvatures α_1 and α_2 are computed based on measured strain values across the edge and crown of the curved shell specimen.

Considering the expressions for $\varepsilon_{crown-1}$ and $\varepsilon_{crown-2}$ from Eq. 6-6 and Eq. 6.7 and solving for X_c, we obtain the following expression

$$\begin{aligned}\varepsilon_{crown-1} - \varepsilon_{crown-2} &= \alpha_1.(0.2 - X_c) - \alpha_1.(0.2 - X_c)\\ \varepsilon_{crown-1} - \varepsilon_{crown-2} &= 0.2(\alpha_1 - \alpha_2) + X_c.(\alpha_2 - \alpha_1)\\ X_c &= \frac{(\varepsilon_{crown-1} - \varepsilon_{crown-2}) - 0.2(\alpha_1 - \alpha_2)}{(\alpha_2 - \alpha_1)}\end{aligned} \tag{6.8}$$

Considering the expressions for ε_{edge-1} and ε_{edge-2} from Eq. 6-6 and Eq. 6.7 and solving for X_c, we obtain the following expression

$$\varepsilon_{edge-1} - \varepsilon_{edge-2} = -\alpha_1.X_c + \alpha_1.X_c$$
$$\varepsilon_{edge-1} - \varepsilon_{edge-2} = X_c.(\alpha_2 - \alpha_1) \quad (6.9)$$
$$X_c = \frac{\varepsilon_{edge-1} - \varepsilon_{edge-2}}{(\alpha_2 - \alpha_1)}$$

Therefore, final expressions of Eq. 6.8 and Eq. 6.9 can be effectively utilized to experimentally determine the location of centroid for thin-walled, open cross-sectioned curved cylindrical composite coupons respectively. The value for X_c determined by using Eq. 6.8 and Eq. 6.9 provide identical results.

Alternatively, the location of centroid can also be graphically obtained by first experimentally measuring the averaged strain values for $\varepsilon_{crown-1}, \varepsilon_{edge-1}, \varepsilon_{crown-2}$ and ε_{edge-2} respectively. Linear equations involving the four measurands can be developed in the form of $\varepsilon_{edge-1} + X_c.\left(\frac{\varepsilon_{crown-1} - \varepsilon_{edge-1}}{0.2}\right) == \varepsilon_{edge-2} + X_c.\left(\frac{\varepsilon_{crown-2} - \varepsilon_{edge-2}}{0.2}\right)$ and solve for X_c respectively. The intersection of two line equations will be considered the location of neutral axis prediction (Fig 6-38) and the corresponding strain magnitude ε_N will be extensional strain component that is wholly due to the contribution of a normal tensile force.

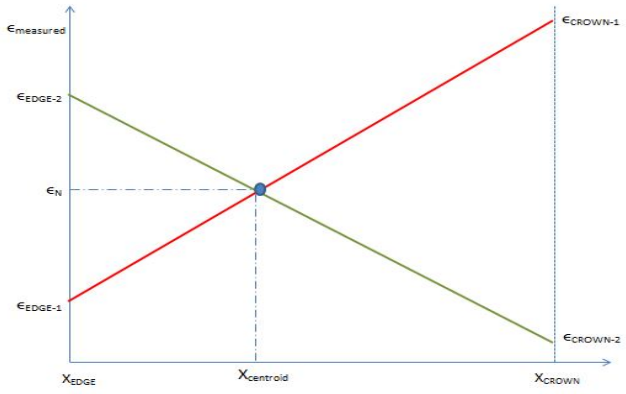

Figure 6-38 Graphical Prediction for Centroidal Location Schematic

6-5 Digital Image Correlation (DIC) Based Structural Response Characterization of Open Cross Section Composite Strips

The key characteristics of a Digital image correlation (DIC) based strain measurement technique are: a) provides excellent capability to measure full-field strains in a deformable body b) Complete non-contact measurement technique c) Strain quantification driven by principles of optics d) proven potential to investigate quasi-static and dynamic load induced structural elements e) Significantly higher ease in determining 2-D and 3-D surface strains. DIC has constantly proven to be accurate [17].

The commercially available VIC-2D and VIC-3D systems from Correlated Solutions [18] implement this advanced optical measurement technology. The fundamental working principle of this technique in measuring surface strains from a deformable structural body is by making use of a stereoscopic sensor setup (Fig. 6-39) that maps each object point with an associated pixel in the image plane of the respective sensor.

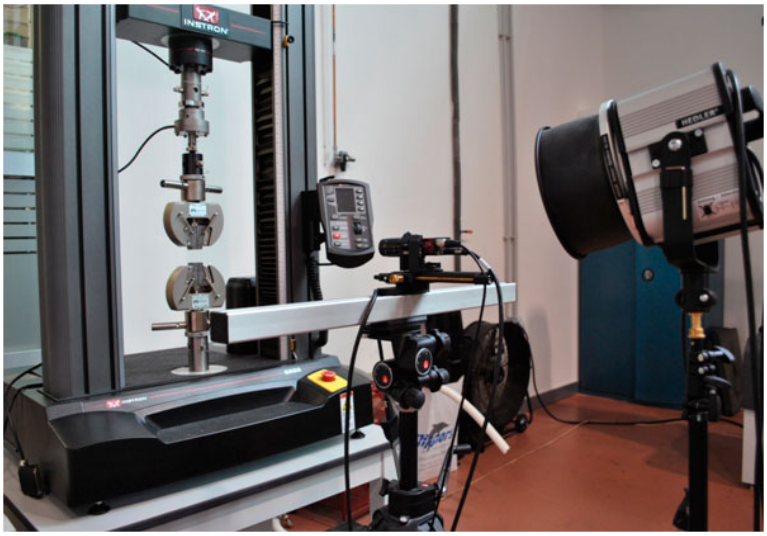

Figure 6-39 Typical DIC based Experiment Set-up [19]

With knowledge of the imaging parameter for each sensor (intrinsic parameter) and the orientation of the sensors with respect to each other (extrinsic parameter), the position of

each object point in three dimensions can be calculated using a stochastic intensity pattern [17] on the object surface, the position of each object point in the two images can be identified by applying a correlation algorithm. Figure 6-39 shows a DIC based testing set-up for investigating structural bodies under typical quasi-static loading conditions. Figure 6-40 represents a snapshot of the sequence of a deformation events and strain distribution pattern for a typical isotropic dog-bone specimen under uniaxial tension . This example shows the potential of DIC to effectively capture the various underlying geometric phenomena such as longitudinal stretching, lateral shrinking due to Poisson's effect and localized necking (precursor to failure by shear). Detailed description on the working principles, theory and applications of DIC can be found in Ref. [17].

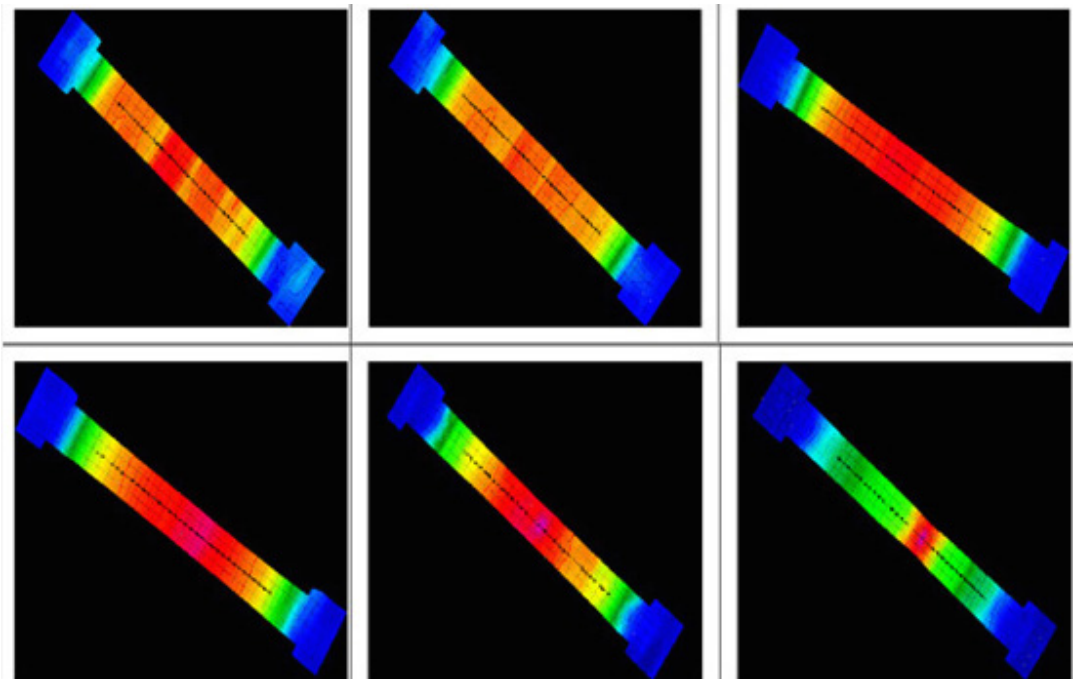

Figure 6-40 Deformation Pattern Investigation via DIC [20]

6-5-1 Experimental Methodology for Curved Composite Strips Investigation

The focus of current work is to conduct a response characterization for a set of seven open cross-sectioned, thin-walled curved composite strips in terms of surface strain

examination in the longitudinal direction and to determine the location of the centroid. This section describes the experimental procedure to estimate the mechanical characteristics for such coupons that are primarily assisted by a DIC based strain measurement technique. Seven composite articles characterized by the following geometric and material characteristics are experimentally investigated: Specimen length = 8 inches, effective gauge length = 6 inches, ply thickness = 0.005in, number of plies = 6, total laminate thickness = 0.03 inches, specimen height = 0.2 inches, laminate lay-up = $\left[\pm 45/0\right]_{symm}$, total arc length $(2\alpha) = 95^0$ and specimen inner radius (cut from a tube fabricated using a steel tube mandrel) = 0.5 inches and specimen outer radius (cut from a tube fabricated using a steel tube mandrel) = 0.5 inches respectively.

The effective gauge length (6 in) of all composite specimens are initially identified by color-taping 1 inch from either edges of the specimen (Fig 6-41). The primary purpose in performing this procedure is to generate a color contrast pattern across the effective gauge length while analyzing against the dark background (Fig 6-42). This procedure involved spraying of three coatings of a primer (lead based white paint) followed by one coating of black paint uniformly over the effective gauge length of the specimen. Three coatings of lead based white paint were sprayed with a five minute interval within the enclosures of a high-intensity exhaust chamber (Fig 6-43).

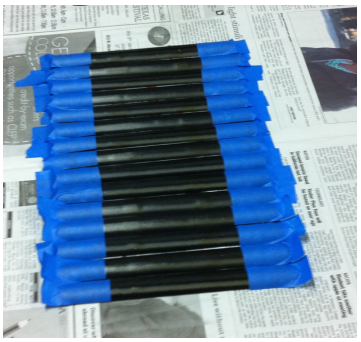

Figure 6-41 Gauge Area Isolated for Paint Spray

Figure 6-42 Spray Gun Utilized to Generate Uniform Paint Smear

Figure 6-43 Spray Process Conducted inside an Exhaust Chamber

6-5-2 Test Set-up Equipment and Quantification Instruments

A uni-axial, quasi-static tension testing was conducted in a MTS electromechanical universal testing machine (33700 lbs. capacity). MTS Test Works [21] was used to execute the tensile tests through a computer interface. The tests are displacement-controlled and the cross-head displacement rate was set at 0.05 in/min. Either ends of the test fixture set up consists of an $1\frac{1}{16}$ inch diameter threaded bolt . The top end of the fixture is installed the threaded groove of the load cell. The load cell is attached to a translating column (cross-head) that displaces at a rate of 0.05 in/min.

Figure 6-44 represents the test set-up arrangement consisting of the test fixture with the specimen attached to the load cell. A stereo-vision arrangement comprising of a pair of 5MP CCD cameras mounted over a multi-degree of freedom tri-pod stand is installed to snap pictures of the composite specimens during the loading history (Fig 6-44). The dye coated surface of the specimen is oriented to directly face the camera system arrangement. A pair of high intensity LED light emitting flexible fiber optic guides offer enhanced lighting and assist in improving the brightness around the gage area of interest (Fig 6-45). CCD cameras are caliberated separately for the two test conditions. To briefly describe, the calibration exercise consists of initially allowing all light to enter into eye-piece by tuning the aperture dial in a fully-open configuration. At this point , the lens dial are simultaneously fine-tuned and caliberated to focus the dye-smeared part of the specimen while manipulating the magnification slider on the VIC-Snap software window. Upon achieving a highly focused image of the area of interest, the aperture dial is locked and set on 8.

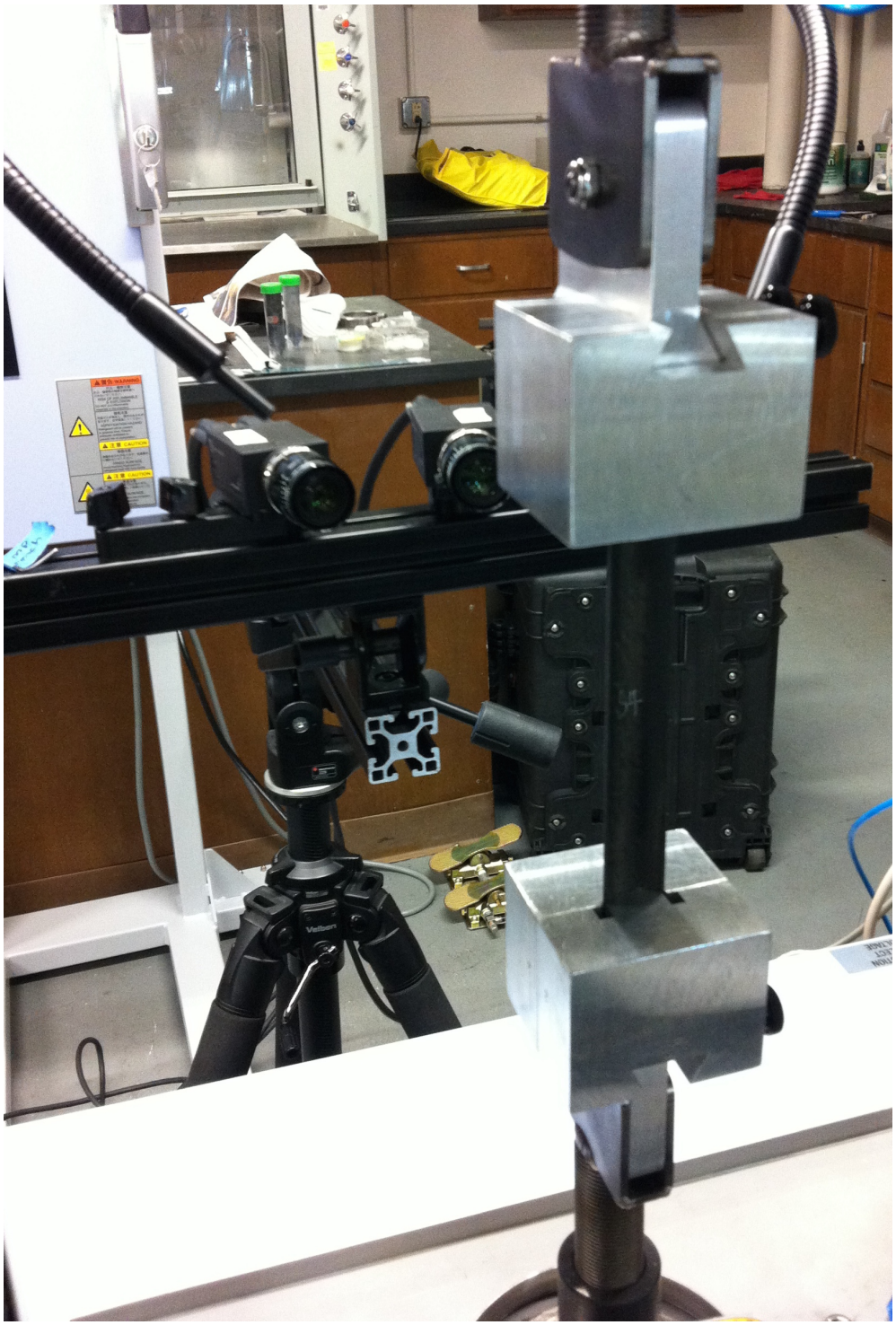

Figure 6-44 Uni-Axial Tensile Test Set-up

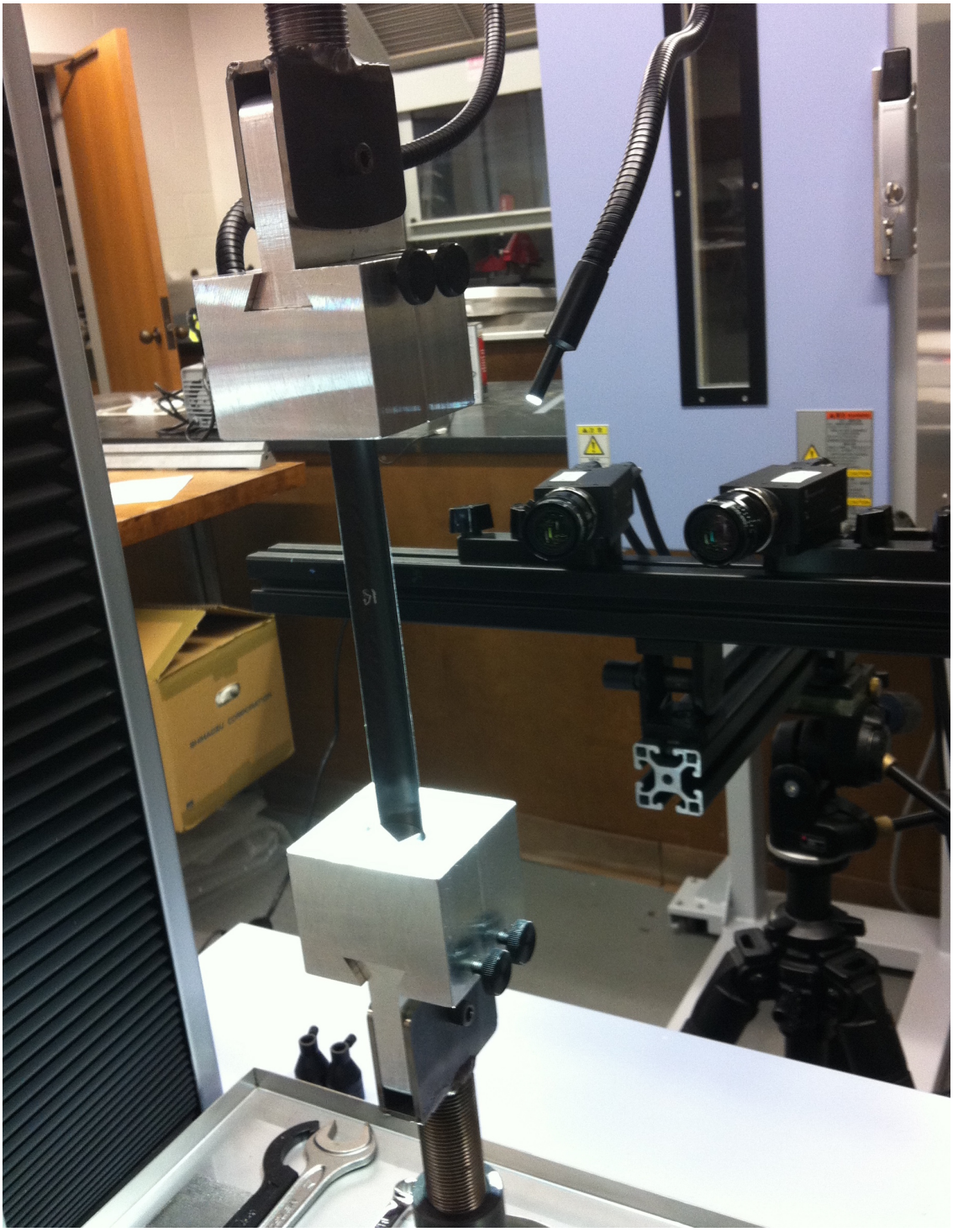

Figure 6-45 Stereo-vision Camera Mount System with LED Light Enhancement

VIC-Snap primarily assists in interfacing the stereo-vision camera system with the test machine. Furthermore, VIS-Snap is utilized for conducting initial camera calibration procedures and for capturing live images of the composite specimen through the course of the tension loading cycle. Prior to conducting the test, a reference image consisting of the undeformed specimen configuration is taken. To analyze the reference image, approximately 50 calibration images were generated by holding a 12mm*9mm calibration grid plate in front of the specimen facing the camera system as shown in Figure 6-46. The calibration plate is locally translated and rotated by small amounts and images are captured for each arbitrary orientation simultaneously. VIC 3D is utilized to process the calibration images and assists in computing the standard deviation of the camera system. A standard deviation below 5% is considered to be excellent for DIC analysis [18]. The standard deviation reported for this camera system set-up amounted to 3.6%. The reference image is later analyzed against the caliberated images to investigate the projection error of the image. The projection error was reported to be below 4%.

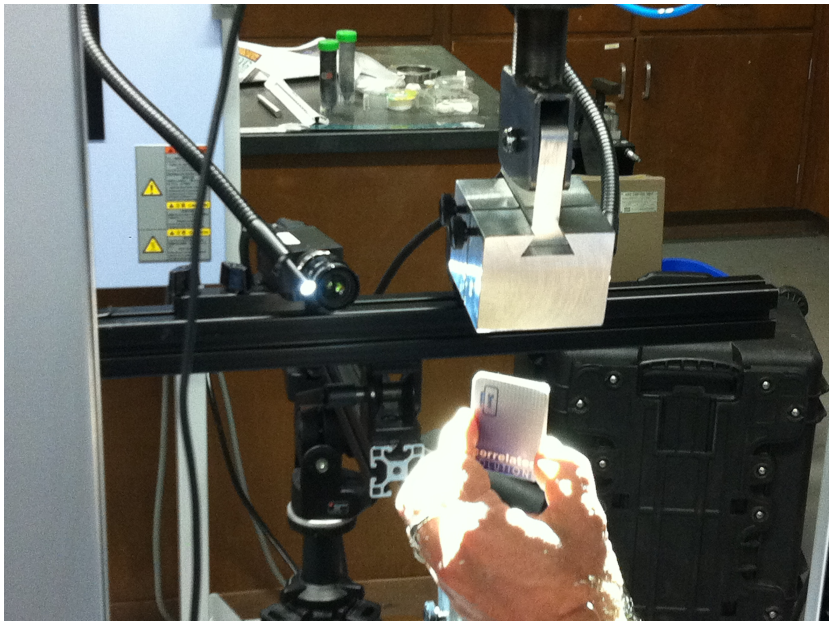

Figure 6-46 Camera System Calibration Using Calibration Grid Plates

Seven composite coupons are labeled SP-1, SP-2, SP-3,SP-4, SP-5, SP-6 and SP-7 respectively. In loading test scenario-1, the cross-head displacement rate is set at 0.05 in/min. All specimens are separately loaded at an axis offset by +0.5 in from the base of the specimen edge (marked as reference in Fig. (6-23)). For this loading case, each of the seven test specimens are uni-axially loaded five times up to 250 lbs and unloaded back to their respective undeformed configurations. Images are captured at the end of every load cycle (250 lbs). Deformed images for each test run (5 tests per specimen) are analyzed with respect to the initial reference image associated with the undeform test configuration set-up. Longitudinal surface strains are investigated at two regions along the specimen. A small rectangular construction area is created along the edge and crown of 2-D DIC generated strain image. Averaged surface strains measured within the two rectangular construction areas are recorded five times for each specimen and the strains are further averaged among themselves. In this test scenario, since the loading axis is offset at a predefined positive distance (0.5 in) from the base of the composite strip, coupled to the axial load component , the induced bending moment tends to deform the specimen such that larger extensional strains (tensile for this case) are observed along the crown region as opposed to the smaller extensional strains observed in close proximity to the edge of the specimen. As an example, Figure 6-47 through Figure 6-50 show the corresponding 2-D and 3-D strain images for SP1 respectively. Figure 6-47 and Figure 6-48 represents the strain field and strain intensity associated with test run-1 whereas, Figure 6-49 and Figure 6-50 represents the strain field and strain intensity associated with test run-5 for the same specimen (SP-1) respectively. It is observed that , there is a consistency in the strain data measured (between test run-1 and test run-5) across the crown region and edge region (Table 11). The 3-D DIC image can be used to visually inspect the strain distribution fields and areas of larger magnitude in terms of

color gradients. The 2-D DIC image associated with each 3-D image is utilized to quantify surface strains along the edge and crown region of the composite strips.

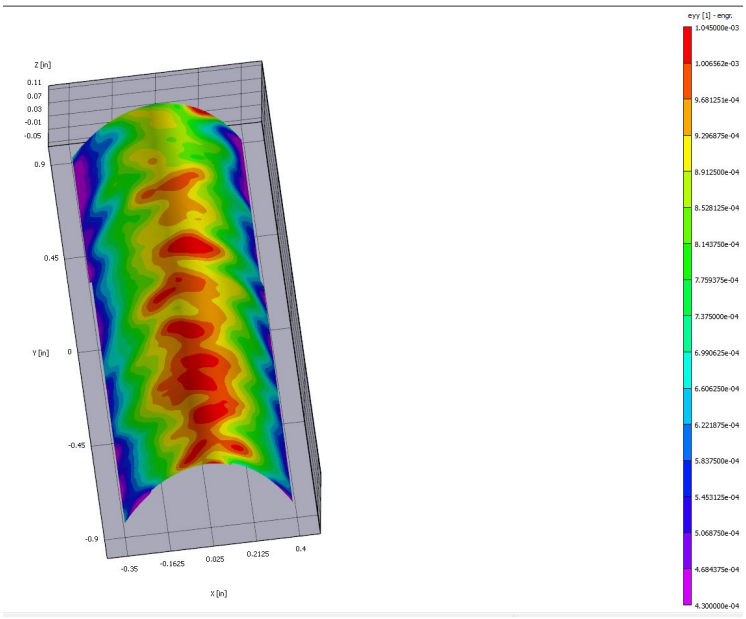

Figure 6-47 3-D DIC Image for SP-1 (+ 0.5 in load offset; test run-1)

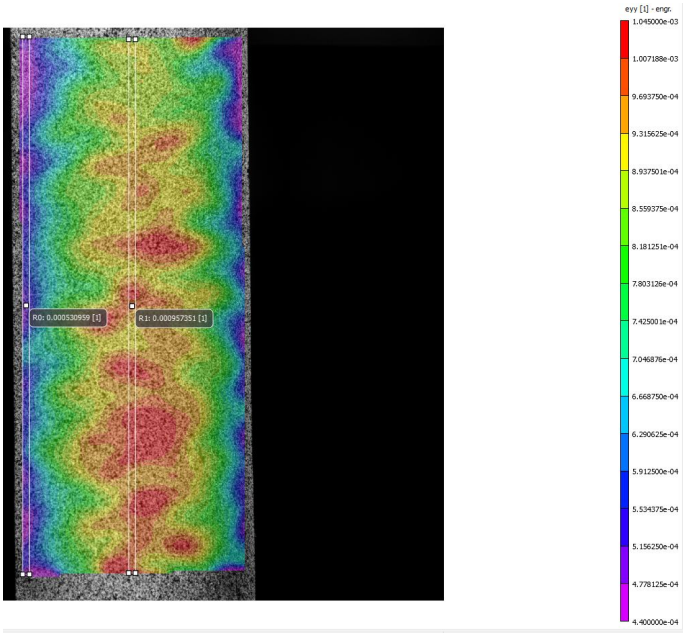

Figure 6-48 2-D DIC Image for SP-1 (+ 0.5 in load offset; test run-1)

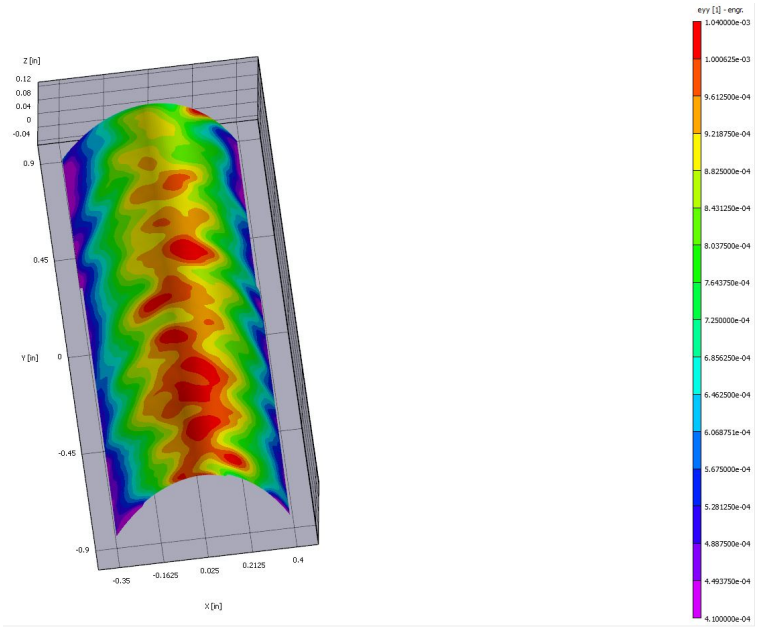

Figure 6-49 3-D DIC Image for SP-1 (+ 0.5 in load offset; test run-5)

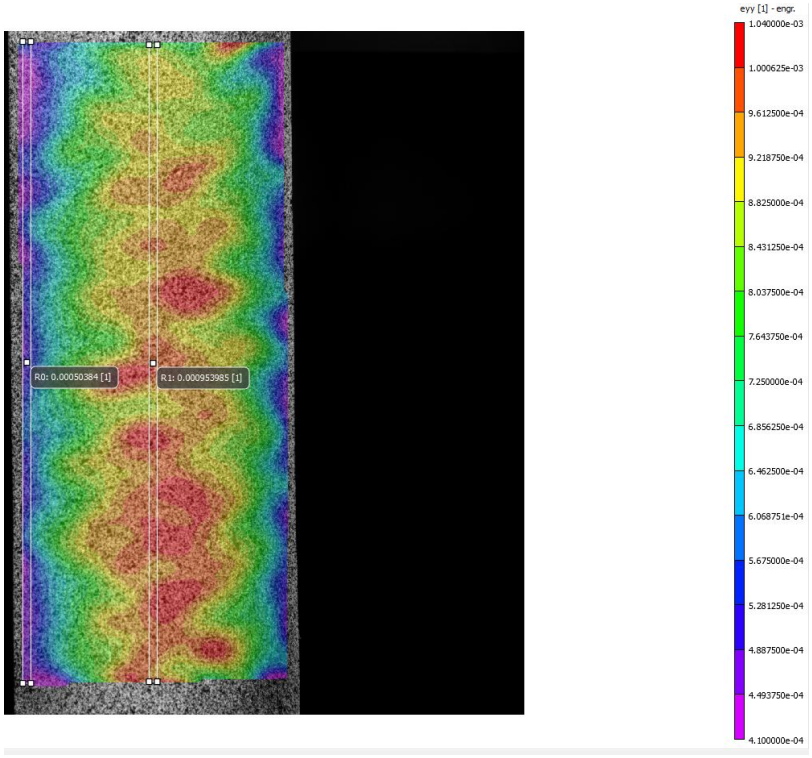

Figure 6-50 2-D DIC Image for SP-1 (+ 0.5 in load offset; test run-5)

In loading test scenario-2, the cross-head displacement rate is set at 0.05 in/min. All specimens are separately loaded at an axis offset by -0.268 in from the base of the specimen edge (marked as reference in Fig. (6-23)). For this loading case, each of the seven test specimens are uni-axially loaded up to 250 lbs and unloaded back to their respective undeformed configurations five times. Images are captured at the end of every load cycle (250 lbs). Deformed images for each test run (5 tests per specimen) are analyzed with respect to the initial reference image associated with the undeformed test configuration set-up. Longitudinal surface strains are investigated at two regions along the specimen. Similarly, a small rectangular construction area is created along the edge and crown of 2-D DIC generated strain image. Averaged surface strains measured within the two rectangular construction areas are recorded five times for each specimen and the strains are further averaged among themselves. The same procedure is conducted five times for all seven specimens. In this test scenario, since the loading axis is offset at a predefined negative distance (-0.268 in) from the base of the composite strip, coupled to the axial load component , the induced bending moment tends to deform the specimen such that smaller extensional strains (tensile for this case) are observed along the crown region as opposed to the larger extensional strains strains observed in close proximity to the edge of the specimen. As an example, Figure 6-51 through Figure 6-54 show the corresponding 2-D and 3-D strain images for SP1 respectively. Figure 6-51 and Figure 6-52 represents the strain field and strain intensity associated with test run-1 (SP-1) whereas, Figure 6-53 and Figure 6-54 represents the strain field and strain intensity associated with test run-5 for the same specimen (SP-1) respectively. It is observed that , there is a consistency in the strain data measured (between test run-1 and test run-5) across the crown region and edge region (Table 6-2). The 3-D DIC image can be used to visually inspect the strain distribution fields and areas of larger magnitude

in terms of color gradients. The 2-D DIC image associated with each 3-D image is utilized to quantify surface strains along the edge and crown region of the composite strips.

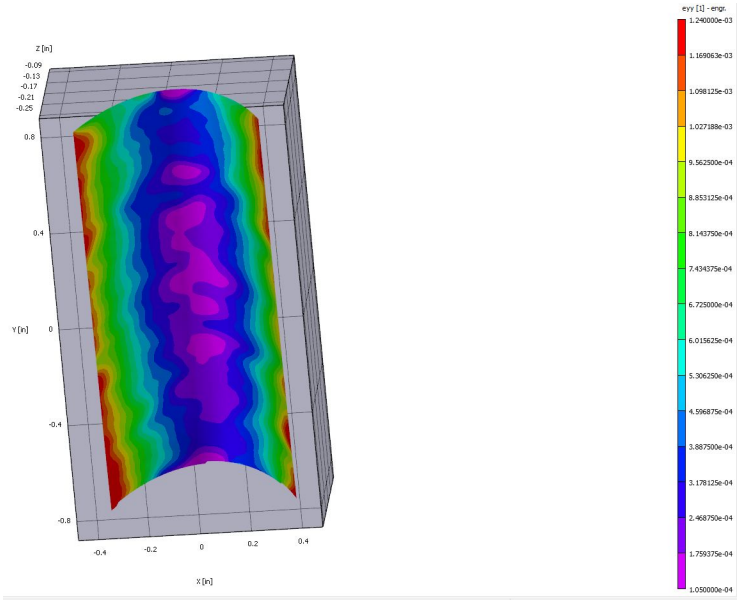

Figure 6-51 3-D DIC Image for SP-1 (-0.268 in load offset case, test run-1)

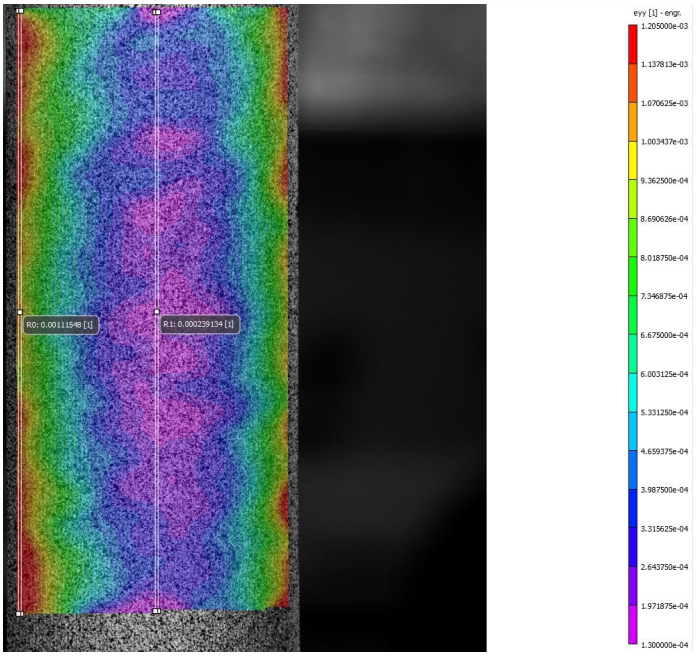

Figure 6-52 2-D DIC Image for SP-1 (-0.268 in load offset case, test run-1)

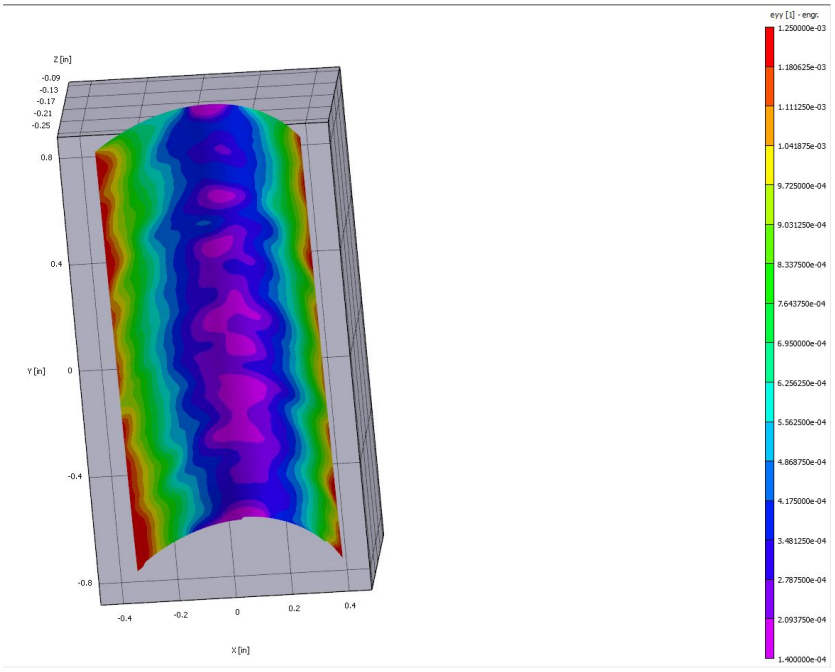

Figure 6-53 3-D DIC Image for SP-1 (-0.268 in load offset case, test run-5)

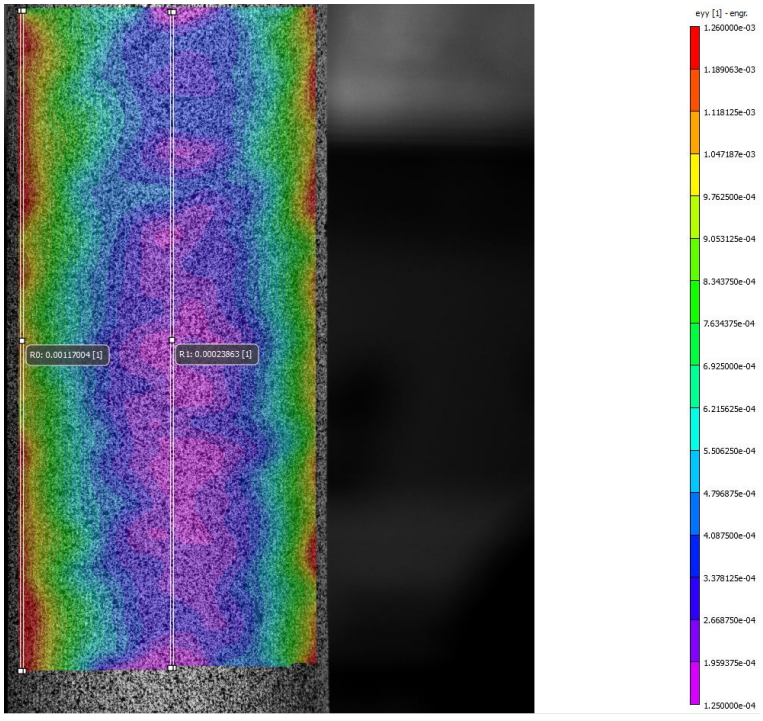

Figure 6-54 2-D DIC Image for SP-1 (-0.268 in load offset case, test run-5)

Table 6-2 Strain Data Measured across Crown and Edge of Specimen (SP-1)

Test run no:	X-crown (in)	ε_{edge} (0.5 in offset) ($\mu\varepsilon$)	ε_{crown} (0.5 in offset) $(\mu\varepsilon)$	ε_{edge} (-0.268 in offset) $(\mu\varepsilon)$	ε_{crown} (-0.268 in offset) $(\mu\varepsilon)$
Run-1	0.2	530	957	1111	240
Run-2	0.2	524	958	1137	252
Run-3	0.2	532	963	1148	255
Run-4	0.2	509	954	1172	244
Run-5	0.2	503	953	1117	238

Appendix F consists of DIC images and strain measurement data for remaining six specimens (SP-2 through SP-7) respectively. Utilizing the strain measurement data for each specimen, Eq. 6.8 and Eq. 6.9 are used to experimentally predict the location of the centroid. Table 6-3 illustrates the location of measured centroid value corresponding to each specimen and compares against the analytically calculated centroid value (Using Eqs. 5-15 through 5-27) with the reference assumed to be the base of each specimen.

Table 6-3 Centroid Comparisons with Ref. as Base of Specimen

(Analytical vs. Experiment)

Sp no:	Assumed Specimen height (in)	Analytical Cent estimate (in)	Experimental Cent measurement (in)	% error diff
SP-1	0.2	0.115	0.094	18.62
SP-2	0.2	0.115	0.102	11.12
SP-3	0.2	0.115	0.083	27.63
SP-4	0.2	0.115	0.091	20.83
SP-5	0.2	0.115	0.111	3.49
SP-6	0.2	0.115	0.104	10.05
SP-7	0.2	0.115	0.107	6.87

Table 6-4 illustrates the location of measured centroid value corresponding to each specimen and compares against the analytically calculated centroid value by assuming the reference as the origin of mean radius of curvature (Using Eqs. 5-15 through 5-27).

Table 6-4 Centroid Comparisons with Ref. as Geometric Origin of R_m

(Analytical vs. Experiment)

Sp no:	Assumed Specimen height (in)	Analytical Cent prediction (in)	Experimental Cent measurement (in)	% error diff
SP-1	0.2	0.44565	0.424109	4.83
SP-2	0.2	0.44565	0.432785	2.88
SP-3	0.2	0.44565	0.413690	7.17
SP-4	0.2	0.44565	0.421553	5.40
SP-5	0.2	0.44565	0.441611	0.91
SP-6	0.2	0.44565	0.434029	2.61
SP-7	0.2	0.44565	0.437708	1.78

6-5-3 Centroid Evaluation (Analytical vs. FEM)

Based on the assumed mechanical properties of Hexcel IM7/8552 Graphite/Epoxy [16] (Table 6-1), a non-linear FEM analysis is conducted in ABAQUS for the two strip offset conditions (+0.3 in from base of strip and -0.08 in from base of strip). The resulting strains along crown and edge of the strip are recorded and used for determining the location of centroid. A thin-walled curved composite strip (Fig 6-55) is modeled utilizing S4R quadrilateral reduced integration shell elements [15]. Due to the symmetry associated with the test set-up, loading conditions and structural geometry; symmetric boundary conditions are imposed by constructing a half-model of the test arrangement. Assumed geometric properties of the composite strip are; length = 3 inches, ply thickness = 0.005in, number of plies = 6, total laminate thickness = 0.03 inches, laminate lay-up =

$[\pm 45/0]_{symm}$, total arc length (2α) = 95^0, strip inner radius R_i=0.5 inches and strip outer radius R_o=0.53 inches respectively. The curved composite strip is characterized by assuming the composite material properties of Hexcel IM7/8552 Graphite/Epoxy as previously shown in Table 10 respectively.

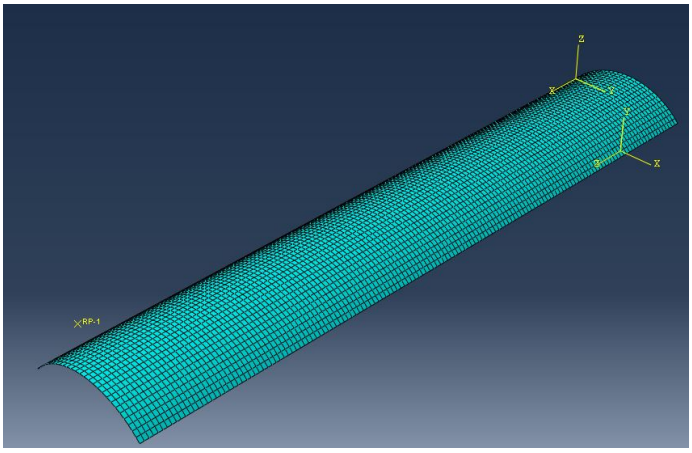

Figure 6-55 Discretized Symmetric Half-Model of Curved Composite Strip

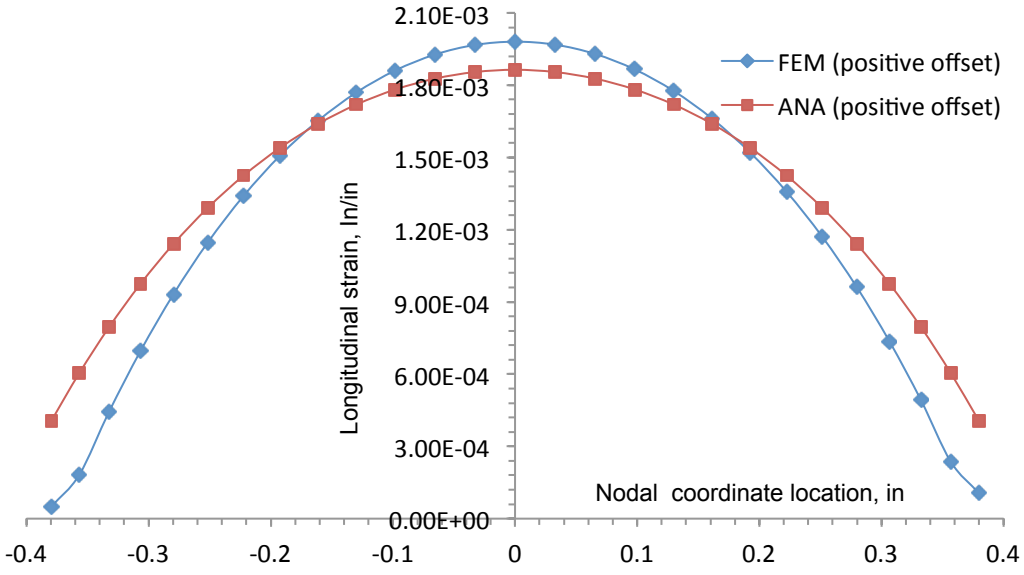

Figure 6-56 Longitudinal Strain ε_x Distribution across Circumference vs. Circumferential distance (positive strip offset case)

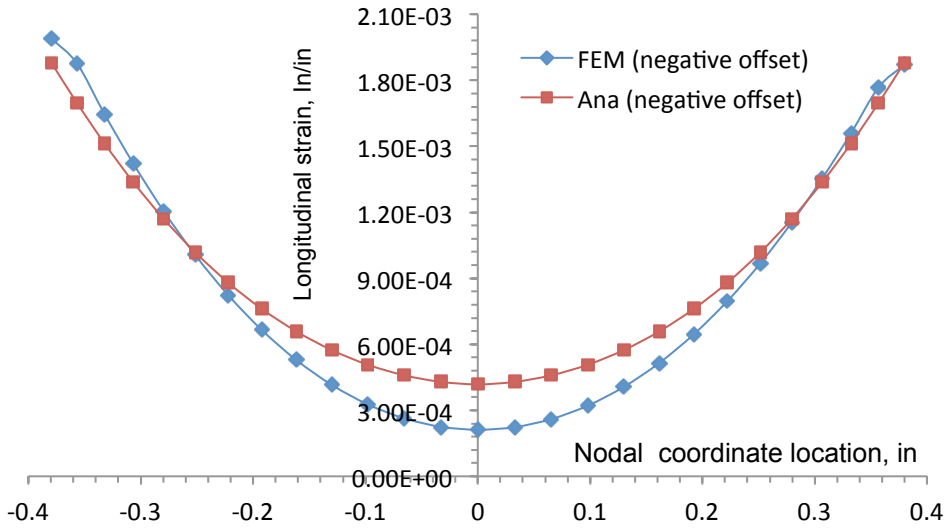

Figure 6-57 Longitudinal Strain ε_x Distribution across Circumference vs. Circumferential distance (negative strip offset case)

Figure 6-56 and Figure 6-57 indicates the distribution of surface strains computed analytically (Eqs 5.15 through 5-27) and based on FEM (ABAQUS) on the topmost layer (+45 deg layer located at z= 0.53 inches from the mean radius of curvature point) of the curved composite strip. In order to compute the FEM based surface strains associated with the global coordinate system, the layered strains (expressed in material coordinate system by default in ABAQUS needs to undergo a strain transformation procedure;

$$\begin{Bmatrix} \varepsilon_x \\ \varepsilon_y \\ \gamma_{xy} \end{Bmatrix} = \left[T_\varepsilon\left(\theta_{45^0}\right)\right]^{-1} * \begin{Bmatrix} \varepsilon_1 \\ \varepsilon_2 \\ \gamma_{12} \end{Bmatrix}$$ where the strain transformation matrix $\left[T_\varepsilon(\theta)\right]$ is given

by in (Eq. 3.2) respectively. Higher longitudinal strain (combination of axial load and bending loads) magnitudes are witnessed at the crown of the specimen and lower strains are recorded in the edge of curved strip (Fig 6-56).

On the contrary, when an axial load of 250lbs is applied along an axis offset at -0.08 in from the base of the specimen, the curved strip undergoes a extension-bending type structural response associated with a combination of axial load and induced bending loads. Higher longitudinal strains (tensile) are witnessed in the edge of the specimen and lesser strain magnitudes are observed in the crown of the composite strip model (Fig 6-58). Based on the strain data computed (analytical and FEM) ; longitudinal strains precisely located on the crown and edge of the specimen are identified (Table 6-5) and substituted into Eqn. 6.10 respectively to solve for the location of centroid (X_{FEM} and X_{ANA}).

$$\left[\varepsilon_{edge-1(FEA)} + X_{FEM} * \left(\frac{\varepsilon_{crown-1(FEA)} - \varepsilon_{edge-1(FEA)}}{0.167071043}\right)\right]_{for+0.5inoffset} = \left[\varepsilon_{edge-2(FEA)} + X_{FEM} * \left(\frac{\varepsilon_{crown-2(FEA)} - \varepsilon_{edge-2(FEA)}}{0.167071043}\right)\right]_{for-0.268inoffset}$$

$$\left[\varepsilon_{edge-1(ANA)} + X_{ANA} * \left(\frac{\varepsilon_{crown-1(ANA)} - \varepsilon_{edge-1(ANA)}}{0.167071043}\right)\right]_{for+0.5inoffset} = \left[\varepsilon_{edge-2(ANA)} + X_{ANA} * \left(\frac{\varepsilon_{crown-2(ANA)} - \varepsilon_{edge-2(ANA)}}{0.167071043}\right)\right]_{for-0.268inoffset}$$

(6.10)

Table 6-5 Strain Estimates at Crown and Edge (Analytical vs FEM)

Strip offset from base of strip	FEM based ε_x strains $(\mu\varepsilon)$	Analytical based ε_x strains $(\mu\varepsilon)$
positive strip offset	edge: 49.765	edge: 406.675
	crown: 1980.5	crown: 1863.8
Negative strip offset	edge: 1990.89	edge: 1880.78
	crown: 211.97	crown: 418.015

Substituting the predicted strain values in Eq. 6.10 we get $X_{cent} = 0.44565in$ and from FEM we get $X_{cent(FEM)} = 0.4425in$ respectively. Excellent agreement is observed in

centroid estimations based on the two methods. Additionally, the applied load (250 lbs) is precisely applied along the predicted FEM based centroid location in order to verify the presence of uniform strains across the circumference (at the top surface of uppermost layer: +45 deg) of the curved composite strip model.

Based on the strain estimates shown in Table 16 and solving for $X_{centroid}$ using Eq. 6.10, corresponding values of $X_{centroid(FEM)}$ and $X_{centroid(ANA)}$ can be resubstituted back into Eq. 6.10 and solved to an estimate ($\varepsilon_{FEM} = 1061\mu\varepsilon$ and $\varepsilon_{ANA} = 1142\mu\varepsilon$) on longitudinal surface strains observed across the circumference of the curved composite strip corresponding to a centroidally applied axial load of 250 lbs. Surface strain distributions (for topmost layer: +45 deg) for the case of centroidally applied axial loading (250 lbs) are computed analytically (Eqns in chapter 5) and compared with FEM strain data. Fig 6-58 shows the longitudinal strain distribution as a function of circumferential arc length for a centroidally applied axial load of 250 lbs.

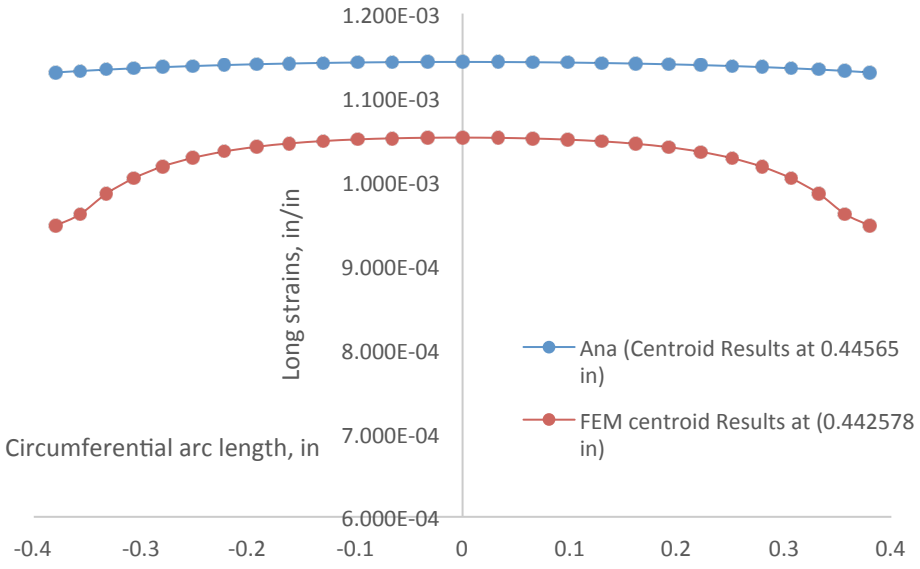

Figure 6-58 Longitudinal Strain ε_x Distribution across Circumference vs. Arc Length (Centroidally Applied Load)

Figure 6-59 indicates a uniform strain distribution pattern (FEM) for the 0 deg layer (layer-3 of the $[\pm 45/0]_{symm}$ lay-up), when the loading axis is aligned at the analytically predicted centroid value and the strip model is loaded at 250 lbs.

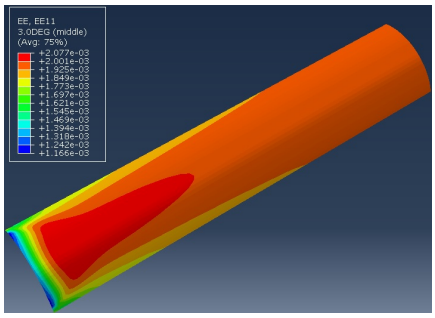

Figure 6-59 Uniform Strain Distribution Pattern (250 lbs at Centroid)

Based on the values of experimentally measured centroid values (Table 6-3 & Table 6-4), each of the composite strip coupons are axially loaded by translating the loading axis to their respective measured centroid locations. As an example, Figure 6-60 through Fig 6-64 represent the 2-D strain field images obtained from DIC for SP-1 respectively. Each of the specimens are loaded five times up to 250 lbs and analyzed for the longitudinal distribution of surface strains respectively. It is observed that , there is an uniformity in the strain values measured across the width of the specimen (between test run-1 and test run-5).

Table 6-6 Surface Strains (centroidal) across Width of Specimen (SP-1)

Run-1 (με)	Run-2 (με)	Run-3 (με)	Run-4 (με)	Run-5 (με)
791	800	786	804	792
733	743	733	747	736
701	711	699	717	705
704	715	702	720	708
738	749	73	755	741
753	744	736	748	737

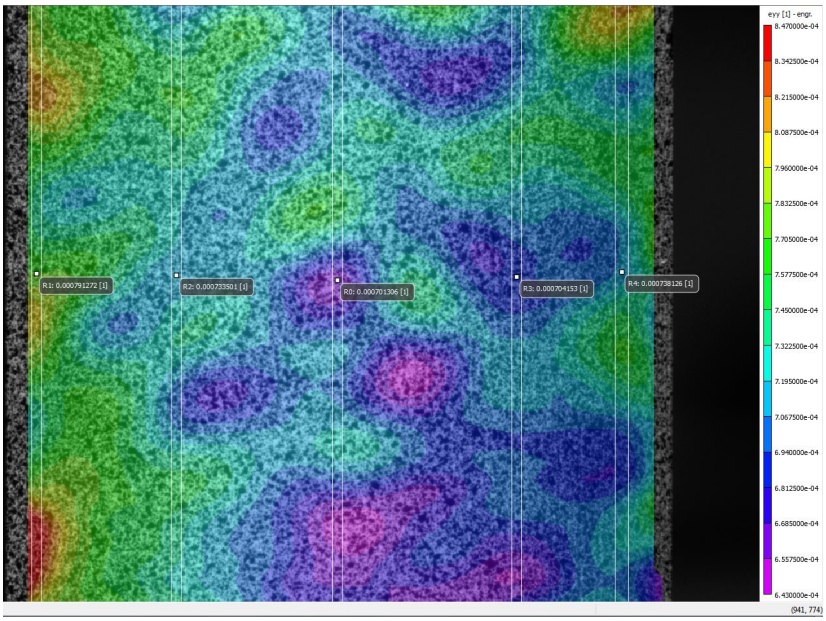

Figure 6-60 Strain Distribution Field across

Width of Specimen (SP-1 Run-1 loaded at 250 lbs)

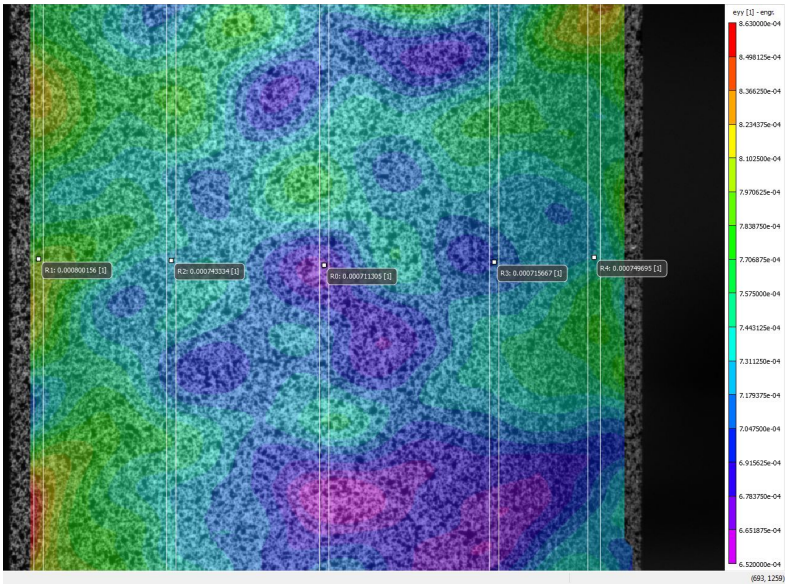

Figure 6-61 Strain Distribution Field across

Width of Specimen (SP-1 Run-2 loaded at 250 lbs)

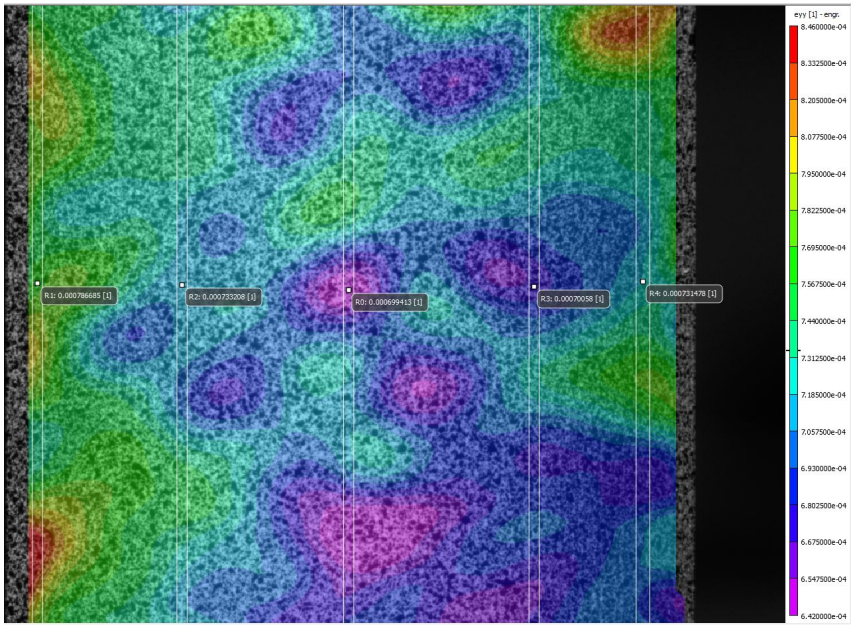

Figure 6-62 Strain Distribution Field across

Width of Specimen (SP-1 Run-3 loaded at 250 lbs)

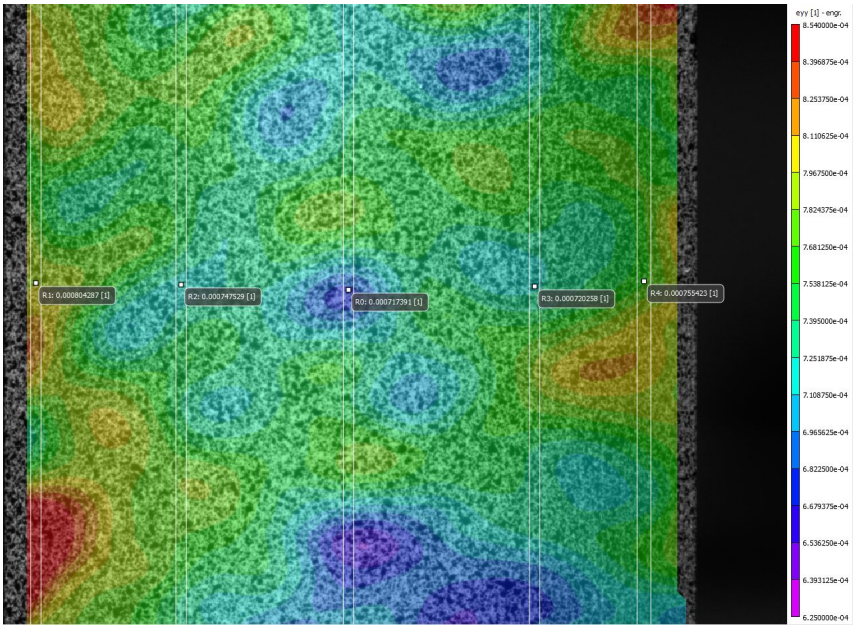

Figure 6-63 Strain Distribution Field across

Width of Specimen (SP-1 Run-4 loaded at 250 lbs)

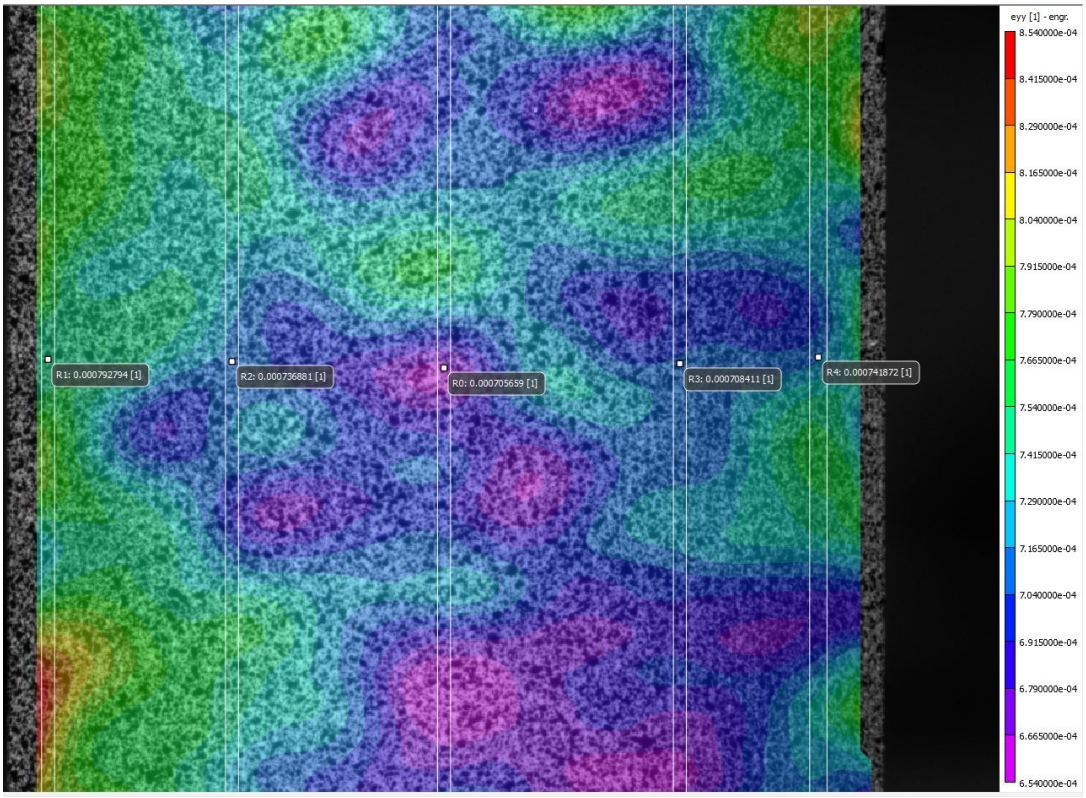

Figure 6-64 Strain Distribution Field across

Width of Specimen (SP-1 Run-5 loaded at 250 lbs)

Table 6-6 indicates the measured averaged strain values across 5 regions spread across the width of specimen SP-1 respectively. Location and size of the rectangular construction areas generated while observing the averaged strains remains constant within each enclosed region for all the 5 test runs. The sixth row in Table 6-6 represents the average of all the measured longitudinal strains (across the width corresponding to each test run). Another average of all the averaged longitudinal strains provides the magnitude of longitudinal strains measured across the surface of the topmost layer of each specimen respectively. Table 16 lists the averaged axial strains measured across the top surface of each specimen that are subjected to an tensile load of 250lbs respectively.

Table 6-7 Measured Surface Strains Averaged across width of each Specimen (250 lbs at centroid)

Specimen no:	Measured averaged axial strains ($\mu\varepsilon$)
SP-1	739
SP-2	748
SP-3	772
SP-4	774
SP-5	785
SP-6	736
SP-7	724

Based on the results observed in Table 6-3 & Table 6-4, it is indicative that the percentage error diff made between the experimental centroid predictions and analytical predictions vary between a lower bound of approximately 3% and an upper bound of 27%. Each of the specimens tested, indicate a different predicted centroid value in comparison to the analytical predictions. Such differences can be attributed to a material property variability among the specimens. Fundamentally, in order to acquire a better comparison accuracy between the experimentally obtained centroid predictions and the analytical predictions, a material property characterization is warranted to better determine the actual mechanical properties of the material used for coupon fabrication. In this section, the FEM predictions and analytical predictions utilize the assumed material characteristics of IM7-8552 Carbon/Epoxy system (Table 6-1) whereas the actual mechanical properties characterizing the physical response of each fabricated coupon were not characterized for the purpose of this research. Additionally, Table 18 is indicative of the range of strains (approximately between $735\mu\varepsilon$ (lower bound) and $785\mu\varepsilon$

(upper bound)) encountered between each test coupon when loaded under 250 lbs at their respective experimentally measured centroid locations. Measured tensile strain values for each test specimen (loaded at 250 lbs) reveal a clear uniformity in the range of extensional strains experienced when compared against each other. The results from Table 18 are optimistic for each test specimen from the standpoint of designing, developing and implementing a novel test-fixture set-up and methodology that has proven to very accurately determine, physically the location of their centroid (initially assumed to be unknown prior to testing).

A large amount of resin-bleed was witnessed on the breather fabric utilized in each coupon fabrication process. This factor is highly suggestive of the resulting manufactured parts to very stiff that possess an highly varying physical properties that can be substantially different from the assumed material properties utilized for analytical and FEM calculations. Furthermore, the material used for coupon fabrication was generously donated (expired shelf-life; year of manufacture: 2010) by external sources for academic research work. In order to obtain an improved strain and centroid comparison trend between the analytical calculations and experiments, an elaborate material characterization routine (evaluation of all in-plane (2-D) and through thickness (3-D) physical properties by adopting standardized ASME prescribed manufacturing and testing procedures on at least 30 test specimens) is necessary. By doing so, a broad initial understanding on the structural response of the test material can be achieved. Experimentally obtained material properties can then be used in conducting a wide range of parametric studies by adopting developed analytical models and FEM analyses. Additionally, a non-linear FEM analyses can be very effectively implemented in tandem to serve as a guide to visually examine and capture any observable structural phenomena

(in terms of geometric non-linearities) that are associated with structural geometry and material characteristics.

Chapter 7

CONCLUSION AND FUTURE WORK

This research discourse fundamentally provides the analytical development of simple closed-form mathematical formulations for accurately predicting key structural characteristics such as axial stiffness, bending stiffness, centroid location and ply-stress variations that govern the extension-bend type mechnical response in thin-walled composite cylindrical tubes and open cross-sectioned curved composite strip configurations respectively. A novel closed form constitutive relationship for closed and open laminated shell structures subjected to mechanical and hygrothermal load environments are formulated. The global stiffness model (associated with relating resultant load matrices to mind-plane strains and curvatures) is initlally constructed by utilising extended Lamination theory principles (incorporating the mechanics of Classical Lamination Theory, transformation matrices and concepts of parallel-axes theorem) for describing the mechanical characteristics of a cylindrical composite tube system distinguishable by varying key parameters such as mean radius of curvature, circumferential arc length, ply-lay-up, laminate stracking sequence etc. The model has proven to show significant advancement in terms of result accuracy and substantiation of charectersitic stiffness predictions as opposed to smear property and plate theory based results. The constitutive relationship recognizes the emergence of additional hygrothermal loads (forces and moments) that are induced as a result of non-symmetric cross-sectional area (above and below the mid-reference line). The stiffness model captures the influence and effects of geometric curvature while charecterizing cylindrical composite constructions of small radii. While comparing stiffness data results utilizing the

present analytical model against other existing approaches (smear property approach and plate theory approach), bending stiffness properties in particular was found to be sensitive after incorporating the effects of shell curvature as opposed to the variation in axial stiffness response exhibited by cylindrical composite shells. Excellent agreement is achieved while substantiating shell approach based stiffness and ply-stress results as opposed to FEM (ANSYS) results.

The identification of centroid location is pivotal for characterizing the structural response in thin-walled, open cross-section cylindrical composite shell constructions that are subjected to concentrated tensile loads. Generally, decoupled extension-bending deformation response is demonstrated by a tensile loaded composite structure upon the identification of centroid properties. The novel constitutive relationship developed earlier in this research for studying composite tube configurations is extended to analyze the mechanical behavior of curved cylindrical shell structures. The model is more comprehensive by incorporating the effects due to resultant load terms such as N_{yx} and M_{yx} respectively. In the process, an accurate mathematical framework for analytically predicting the location of centroid is formulated. A detailed closed-form derivation is further developed to mathematically prove that for a curved composite shell configuration, the location of centroid is not governed and remains invariant under the influence of a hygrothermal environment. Excellent agreement is shown in analytical centroid predictions in comparison to FEM based results (ANSYS & ABAQUS). Parametric studies are conducted to observe the shift in centroid location by progressively altering the cross-sectional area distributed across the circumference.

It is shown that for composite strips characterized by very small arc angles, the location of centroid fundamentally resided within the cross-sectional area. In other words, for composite strips dominated by small arc angles, the strip can be largely assumed as a

rectangular strip with a centroid located in close proximity to the mid-thickness. Upon gradual increase in total arc angle, the location of the centroid starts to translate outside the cross-section. In thin walled curved strips dominated by large circumferential arc lengths, the centroid point translates closer to the origin of its mean–radius. Consequently, for a fully closed, thin-walled cylindrical composite tube, the centroid point precisely matches with the geometric center of the tube. Under the influence and absence of a hygrothermal environment, ply-per-ply stress distribution patterns are parametrically investigated and cross-validated against FEM results. Analytical estimations for structural stiffness and in-plane stress distributions via Layer Stress Recovery indicated very good agreement with a percentage error difference of less than 3% as opposed to finite element predictions. Based on the analytical equations developed for curved composite strips, the centroid is observed to be characteristically associated with the arc angle defining the circumference, fiber orientation angle describing the ply lay-up, composite stacking sequence, core material properties and has no influence due to hygrothermal forces and moments acting on the structure.

Current research work also included an experimental study to investigate the structural response of thin-walled open cross-sectioned cylindrical shell structures in terms of identifying the location of centroid and longitudinal surface strain fields. This work encompassed the fabrication of a set of curved cylindrical shell coupons, the design and development of a novel test-fixture design and an effective experimental methodology that demonstrated the capability to very accurately predict the location of centroid in such curved composite cylindrical strips via employing a DIC based strain measurement technique. Error percentage difference between experimental centroid measurements and analytical centroid estimates is shown and disparity between the two data is observed. It is observed that the tubular laminate lost significant amounts of resin

material during the fabrication process. This loss in matrix material can be associated with material property variability as opposed to the assumed material constants (from materials handbook). As a result, the coupons appeared to exhibit increased stiffness charecteristics (via comparing longitudinal surface strains) while subject to tensile and bending loading conditions. Results can be improved by conducting detailed material characterization studies to determine the actual mechanical properties of material under investigation.

Although such cylindrical composite shell configurations carry limited usefulness as stand-alone structural elements, they can be incorporated as reinforcement elements for a larger composite structure. The developed linear analytical theory offers the capability to understand the fundamental behavior of thin-walled cylindrical shells and can generate novel avenues to understand the physics of such structures at a laminate level. Structural design engineers can develop quick, back-of-the-envelope results studies to analyze the mechanical behavior of such structural elements by conducting preliminary parametric and structural optimization prior to conducting detailed FEM based structural analyses.

The research initiated in this thesis provides further motivation to develop a more rigorous mathematical model that can facilitate in examining the structural behavior of such curved shell configurations. Building on this model enables to focus towards investigating several other new and equally interesting areas of inquiry. The recommended research areas for future work are:

1. The development of an analytical model that effectively incorporates the effects due to geometric non-liearities associated with in-plane warping. This research shed some light on the actual physical phenomena exhibited by curved composite shell structures when large finite tensile loads are applied at an offset from their centroidal axis. This linear analytical model can be extended to capture

the effets due to geometric non-linearities by formulating new higher-order dispacement functions.

2. Investigation of torsional and warping stiffness charectersitics to fully understand the bend –twist response exhibited by such structures.
3. A mechanical response examination of curved composite shells in terms of center of shear
4. A first-ply failure analyses by parameterizing ply-lay up, composite stacking sequence and associated material properties.
5. Development of a more comprehensive model that investigates delamination and crack-growth phenomena in curved cylindrical shell configurations.
6. Structural response characterization of cylindrical shell coupons under fatigue loading.

Appendix A

DETERMINATION OF BENDING CURVATURE FROM FEM UTILIZING ANSYS

A brief methodology that describes the computation of cross-sectional bending curvature is presented in this segment. The concept of the "Bending Curvature" κ_{ij} is central towards gaining a fundamental understanding on beam bending. Essentially, curvature is a structural phenomenon that is associated with the rate of change of slope angle ψ witnessed with respect to the initial arc length S along the contour of a structural member subjected to bending. The initial step involved towards determining the amount of bending induced curvature induced in a composite tube subjected to a concentrated finite bending moment M_x is to calculate the slope angle that is defined by any arbitrarily chosen element strip along the length of the composite tube.

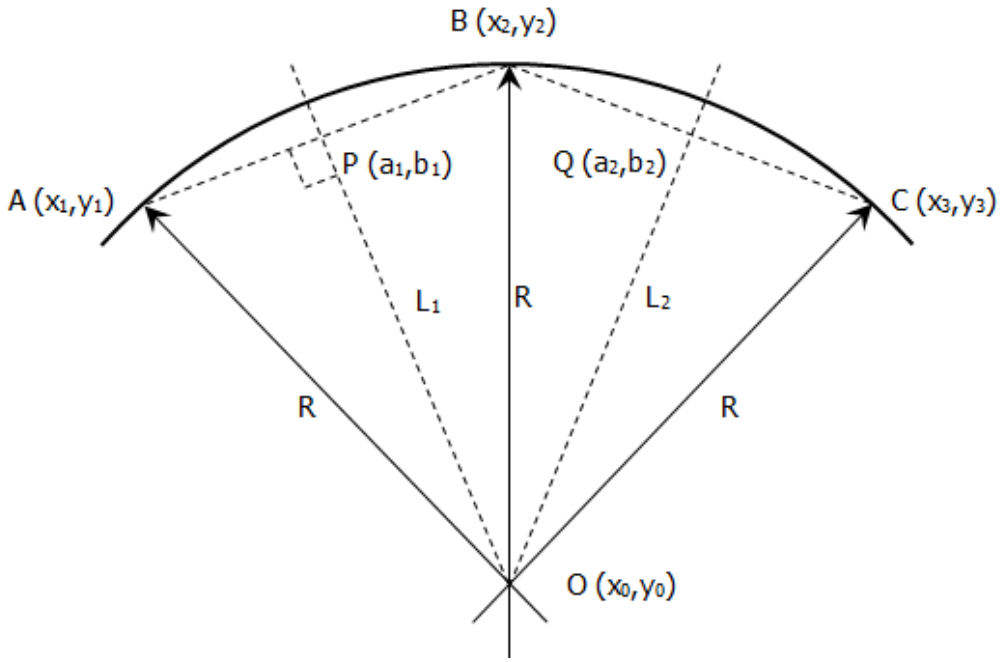

Figure A.1 Generalized Schematic of a Deformed Tube Strip

Three fictitious points represented by A, B and C are arbitrarily chosen along the deformed length of the composite tube. These points are spatially oriented and identified with their designated coordinates as A (x_1,y_1) , B (x_2,y_2) and C (x_3,y_3) respectively. Figure A.1 portrays a 2-d side-view schematic of the deformed tube strip along the length of the composite member.

Point O signifies the effective mean radius-of curvature that geometrically relates the three points. Points P and Q denote the center-points for each of the imaginary lines that describe a straight line across points A to B and between points B and C respectively. Fundamentally, utilizing the cartesian coordinates (x and y) associated with points A and B , their relative slope and center–point can be determined and is shown as:

Slope of Line AB: $$S_{AB} = \frac{y_2 - y_1}{x_2 - x_1} \quad \text{(A.1)}$$

Center point, P: $$P(a_1, b_1) = \left(\frac{x_1 + x_2}{2}, \frac{y_1 + y_2}{2}\right) \quad \text{(A.2)}$$

Geometric slope of line segment L1 that is orthogonal and precisely bisects line AB about point P can be expressed as $y = S_{L1}(x - a_1) + b_1$:

$$S_{L1} = -\frac{1}{Slope\ of\ line\ AB} = -\frac{1}{S_{AB}} \quad \text{(A.3)}$$

Similarly, expressions for center-point Q and slope that characterizes line BC can be denoted by;

Slope of Line BC: $$S_{BC} = \frac{y_3 - y_2}{x_3 - x_2} \quad \text{(A.4)}$$

Center point, Q: $$Q(a_2, b_2) = \left(\frac{x_2 + x_3}{2}, \frac{y_2 + y_3}{2}\right) \quad \text{(A.5)}$$

Geometric slope of line segment L1 that is orthogonal and precisely bisects line AB about point P can be expressed as $y = S_{L2}(x - a_2) + b_2$

$$S_{L2} = -\frac{1}{Slope\ of\ line\ BC} = -\frac{1}{S_{BC}} \quad \text{(A.6)}$$

Next course of action is to analytically determine the spatial coordinates of the true intersection point O that represents the point of convergence for line segments L1 and L2 associated with the assumed curve A-B-C. The expressions utilized to calculate the coordinates (x_o,y_o) distinguishing the location of point O can be shown as

$$x_0 = \frac{S_{L1}a_1 - S_{L2}a_2 - b_1 + b_2}{S_{L1} - S_{L2}} \quad \text{(A.7)}$$

$$y_0 = \frac{S_{L1}S_{L2}(a_1 - a_2) - S_{L1}b_1 - S_{L2}b_2}{S_{L1} - S_{L2}} \quad \text{(A.8)}$$

As a consequence, the effective radius of curvature R and its associated curvature κ that is produced along the curve ABC can be denoted by

$$R = \sqrt{(x_0 - x_1)^2 + (y_0 - y_1)^2} = \sqrt{(x_0 - x_2)^2 + (y_0 - y_2)^2} = \sqrt{(x_0 - x_3)^2 + (y_0 - y_3)^2} \tag{A.9}$$

whereas the resulting $\kappa = \frac{1}{R}$.

Curvature calculations are basically generated on a general MICROSOFT EXCEL 2013 spreadsheet upon recording the nodal spatial coordinates for the assumed points A, B and C respectively. Following results are recorded in a tabular format for straightforward inspection.

Appendix B

ANSYS 15.0 WORKBENCH BATCH CODE FOR COMPOSITE TUBE AND CYLINDRICAL SHELL

```
TITLE, Composite Tube
/UNITS,BIN
/PREP7

LOCAL,11,CYLIN,0,0,0,0,90,90

Rm=1
force=1
length_elements=2000
angular_elements=41
tply=0.005
r=Rm+tply*6
length=10


MP,EX,1,21.3E6
MP,EY,1,1.5E6
MP,EZ,1,1.5E6
MP,PRXY,1,0.27
MP,PRXZ,1,0.27
MP,PRYZ,1,0.54
MP,GXY,1,1.0E6
MP,GXZ,1,1.0E6
MP,GYZ,1,0.54E6
MP,ALPX,1,-0.5E-6
MP,ALPY,1,15E-6
MP,ALPZ,1,15E-6

KEYOPT,1,2,2
KEYOPT,1,3,1
KEYOPT,1,6,0
KEYOPT,1,8,1
KEYOPT,1,10,0

sect,1,shell,,
secdata, 0.005,1,45,3
secdata, 0.005,1,-45,3
secdata, 0.005,1,0,3
secdata, 0.005,1,0,3
secdata, 0.005,1,-45,3
secdata, 0.005,1,45,3
secoffset,MID
seccontrol,,,, , , ,

SECPLOT,   1,,,
CYL4,0,0,1.0
VOFFST,1,10, ,
/VIEW,1,1,1,1
/ANG,1
/REP,FAST
VDELE,      1
APLOT

FLST,2,2,5,ORDE,2
FITEM,2,1
FITEM,2,-2
ADELE,P51X
APLOT
/REPLOT,RESIZE
```

```
R,1
RMODIF,1,1,1,0,0,0,0
RMODIF,1,7,0
RMODIF,1,13,1,45,tply

R,2
RMODIF,2,1,1,0,0,0,0
RMODIF,2,7,0
RMODIF,2,13,1,-45,tply

R,3
RMODIF,3,1,1,0,0,0,0
RMODIF,3,7,0
RMODIF,3,13,1,90,tply

R,4
RMODIF,6,1,1,0,0,0,0
RMODIF,6,7,0
RMODIF,6,13,1,0,tply

R,5
RMODIF,9,1,1,0,0,0,0
RMODIF,9,7,0
RMODIF,9,13,1,-45,tply

R,6
RMODIF,10,1,1,0,0,0,0
RMODIF,10,7,0
RMODIF,10,13,1,45,tply

CSYS,11
*DO,I,1,6,1

K,1+4*(I-1),r-tply*(I-1),0,0
K,2+4*(I-1),r-tply*(I-1),90,0
K,3+4*(I-1),r-tply*(I-1),180,0
K,4+4*(I-1),r-tply*(I-1),270,0
K,69+4*(I-1),r-tply*(I-1),0,length
K,70+4*(I-1),r-tply*(I-1),90,length
K,71+4*(I-1),r-tply*(I-1),180,length
K,72+4*(I-1),r-tply*(I-1),270,length

L,1+4*(I-1),2+4*(I-1)
L,2+4*(I-1),3+4*(I-1)
L,3+4*(I-1),4+4*(I-1)
L,4+4*(I-1),1+4*(I-1)
L,69+4*(I-1),70+4*(I-1)
L,70+4*(I-1),71+4*(I-1)
L,71+4*(I-1),72+4*(I-1)
L,72+4*(I-1),69+4*(I-1)
L,1+4*(I-1),69+4*(I-1)
L,2+4*(I-1),70+4*(I-1)
L,3+4*(I-1),71+4*(I-1)
L,4+4*(I-1),72+4*(I-1)
*ENDDO


*DO,J,1,6,1
AL,1+12*(J-1),9+12*(J-1),5+12*(J-1),10+12*(J-1)
AL,2+12*(J-1),10+12*(J-1),6+12*(J-1),11+12*(J-1)
AL,3+12*(J-1),11+12*(J-1),7+12*(J-1),12+12*(J-1)
```

```
AL,4+12*(J-1),12+12*(J-1),8+12*(J-1),9+12*(J-1)
ENDDO

CSYS,0
LSEL,S,LOC,Z,0
LSEL,R,LOC,X,0
LPLOT
LESIZE,ALL,,,1

LSEL,S,LOC,Y,0
LSEL,R,LOC,X,0
LPLOT
LESIZE,ALL,,,1

LSEL,S,LOC,Z,0
LSEL,R,LOC,X,length
LPLOT
LESIZE,ALL,,,1

LSEL,S,LOC,Y,0
LSEL,R,LOC,X,length
LPLOT
LESIZE,ALL,,,1

ALLSEL
*DO,N,1,16,1
TYPE,1,
ESYS,0
MAT,1,

REAL,N
VMESH,1+4*(N-1),4+4*(N-1),1
*ENDDO
EPLOT

FLST,5,4,6,ORDE,3
FITEM,5,1
FITEM,5,5
FITEM,5,-7
CM,_Y,VOLU
VSEL, , , ,P51X
CM,_Y1,VOLU
CHKMSH,'VOLU'
CMSEL,S,_Y

MSHAPE,0,3d
MSHKEY,1
VMESH,_Y1
MSHKEY,0
CMDELE,_Y
CMDELE,_Y1
CMDELE,_Y2
CSYS,0
EPLOT
NSEL,S,LOC,Z,0
NPLOT
NSEL,S,LOC,Z,0

ALLSEL
NSEL,S,LOC,Z,0
D,ALL,ALL,0
```

```
NSEL,S,LOC,Z,10
NPLOT
NSEL,S,LOC,Z,10

ALLSEL
NUMMRG,NODE,1.0e-4
NUMMRG,ELEMENT,1.0e-4
NUMMRG,KP,1.0e-4
EPLOT
NSEL,S,LOC,X,0
D,ALL,ALL,0
NSEL,S,LOC,X,length
CP,1,UZ,ALL
F,1,FZ,-10
NSORT,S,X,0,0, ,SELECT
PRNSOL,S,COMP

AVPRIN,0, ,
PDEF, ,S,X,AVG
/PBC,PATH, ,0
AVPRIN,0, ,
PDEF, ,S,Y,AVG
/PBC,PATH, ,0
AVPRIN,0, ,
PDEF, ,S,Z,AVG
/PBC,PATH, ,0
AVPRIN,0, ,
PDEF, ,S,XY,AVG
/PBC,PATH, ,0
AVPRIN,0, ,
PDEF, ,S,YZ,AVG
/PBC,PATH, ,0
AVPRIN,0, ,

PDEF, ,S,XZ,AVG
/PBC,PATH, ,0
AVPRIN,0, ,
PDEF, ,EPTO,X,AVG
PBC,PATH, ,0
PLPATH,SX

DO,K,1,64,1
VOFFST,K,-tply
ENDDO
NUMMRG,KP,1.0e-4

LSEL,S,,,1,8,1
*DO,L,1,15,1
LSEL,A,,,1+12*L,8+12*L,1
*ENDDO
LPLOT
LESIZE,ALL,,,angular_elements

LSEL,S,,,9,12,1
*DO,M,1,15,1
LSEL,A,,,9+12*M,12+12*M,1

*ENDDO
LPLOT
LESIZE,ALL,,,length_elements

CSYS,0
```

```
LSEL,S,LOC,Z,0
LSEL,R,LOC,X,0
LPLOT
LESIZE,ALL,,,1

LSEL,S,LOC,Y,0
LSEL,R,LOC,X,0
LPLOT
LESIZE,ALL,,,1

LSEL,S,LOC,Z,0
LSEL,R,LOC,X,length
LPLOT
LESIZE,ALL,,,1

LSEL,S,LOC,Y,0
LSEL,R,LOC,X,length
LPLOT
LESIZE,ALL,,,1

ALLSEL
*DO,N,1,16,1
TYPE,1,
ESYS,0
MAT,1,

REAL,N
VMESH,1+4*(N-1),4+4*(N-1),1
*ENDDO
EPLOT

VOFFST,3,0.04, ,
VOFFST,4,0.04, ,
VOFFST,5,0.04, ,
VOFFST,6,0.04, ,
VPLOT
/VIEW,1,1,1,1
/ANG,1
/REP,FAST

FLST,2,4,6,ORDE,2
FITEM,2,1
FITEM,2,-4
VGLUE,P51X

FLST,5,8,4,ORDE,6
FITEM,5,9
FITEM,5,-12
FITEM,5,14
FITEM,5,16
FITEM,5,22
FITEM,5,30
CM,_Y,LINE
LSEL, , , ,P51X
CM,_Y1,LINE
CMSEL,,_Y


LESIZE,_Y1, , ,80, , , , ,1
FLST,5,16,4,ORDE,6
FITEM,5,1
FITEM,5,-8
```

```
FITEM,5,13
FITEM,5,15
FITEM,5,45
FITEM,5,-50

CM,_Y,LINE
LSEL, , , ,P51X
CM,_Y1,LINE
CMSEL,,_Y
LESIZE,_Y1, , ,18, , , , ,1

FLST,5,1,4,ORDE,1
FITEM,5,26
CM,_Y,LINE
LSEL, , , ,P51X
CM,_Y1,LINE
CMSEL,,_Y
LESIZE,_Y1, , ,8, , , , ,1

FLST,5,1,4,ORDE,1
FITEM,5,34
CM,_Y,LINE
LSEL, , , ,P51X
CM,_Y1,LINE
CMSEL,,_Y
LESIZE,_Y1, , ,8, , , , ,1
FLST,5,1,4,ORDE,1
FITEM,5,17
CM,_Y,LINE
LSEL, , , ,P51X
CM,_Y1,LINE
CMSEL,,_Y
LESIZE,_Y1, , ,8, , , , ,1
FLST,5,1,4,ORDE,1
FITEM,5,18
CM,_Y,LINE
LSEL, , , ,P51X
CM,_Y1,LINE
CMSEL,,_Y
LESIZE,_Y1, , ,8, , , , ,1

FLST,5,3,4,ORDE,3
FITEM,5,20
FITEM,5,27
FITEM,5,35
CM,_Y,LINE
LSEL, , , ,P51X
CM,_Y1,LINE
CMSEL,,_Y
LESIZE,_Y1, , ,8, , , , ,1
FLST,5,1,4,ORDE,1
FITEM,5,19
CM,_Y,LINE
LSEL, , , ,P51X
CM,_Y1,LINE
CMSEL,,_Y
LESIZE,_Y1, , ,8, , , , ,1
FLST,5,4,6,ORDE,3
FITEM,5,1
FITEM,5,5
FITEM,5,-7
CM,_Y,VOLU
```

```
VSEL, , , ,P51X
CM,_Y1,VOLU
CHKMSH,'VOLU'
CMSEL,S,_Y

MSHAPE,0,3d
MSHKEY,1
VMESH,_Y1
MSHKEY,0
CMDELE,_Y
CMDELE,_Y1
CMDELE,_Y2
CSYS,0
EPLOT
NSEL,S,LOC,Z,0
NPLOT
NSEL,S,LOC,Z,0

ALLSEL
NSEL,S,LOC,Z,0
D,ALL,ALL,0

NSEL,S,LOC,Z,10
NPLOT
NSEL,S,LOC,Z,10

ALLSEL
NUMMRG,NODE,1.0e-4
NUMMRG,ELEMENT,1.0e-4
NUMMRG,KP,1.0e-4
EPLOT
NSEL,S,LOC,X,0
D,ALL,ALL,0
NSEL,S,LOC,X,length
CP,1,UZ,ALL
F,1,FZ,-10
NSORT,S,X,0,0, ,SELECT
PRNSOL,S,COMP

AVPRIN,0, ,
PDEF, ,S,X,AVG
/PBC,PATH, ,0
AVPRIN,0, ,
PDEF, ,S,Y,AVG
/PBC,PATH, ,0
AVPRIN,0, ,
PDEF, ,S,Z,AVG
/PBC,PATH, ,0
AVPRIN,0, ,
PDEF, ,S,XY,AVG
/PBC,PATH, ,0
AVPRIN,0, ,
PDEF, ,S,YZ,AVG
/PBC,PATH, ,0
AVPRIN,0, ,

PDEF, ,S,XZ,AVG
/PBC,PATH, ,0
AVPRIN,0, ,
PDEF, ,EPTO,X,AVG
PBC,PATH, ,0
PL
```

Appendix C

NUMERICAL CODE FOR COMPOSITE TUBE

```
Clear["Global`*"]
E1/(1-(v12*v21))==Q11;
E2/(1-(v12*v21))==Q22;
(v12*E2)/(1-(v12*v21))==Q12;
Q21=Q12;
G12==Q66;
Qreduced=({{Q11, Q12, 0},{Q21, Q22, 0},{0, 0, Q66}})
m1=Cos[β];n1=Sin[β];
Simplify[MatrixForm[Tσβ=({{m1^2, n1^2, 2*m1*n1}, {n1^2, m1^2, -2*m1*n1},
{-m1*n1, m1*n1, m1^2-n1^2}})]]

Simplify[MatrixForm[Tεβ=({{m1^2, n1^2, m1*n1},{n1^2, m1^2, -m1*n1},
 {-2*m1*n1, 2*m1*n1, m1^2-n1^2}})]]

Simplify[MatrixForm[Tσβinverse=Inverse[Tσβ]]]
Simplify[MatrixForm[Tεβinverse=Inverse[Tεβ]]]
QBAR=Tσβinverse.Qreduced.Tεβ; {{Q11,Q12,0},{Q12,Q22,0},{0,0,Q66}}
({{Cos[β]^2, Sin[β]^2, Sin[2 β]},{Sin[β]^2, Cos[β]^2, -2 Cos[β] Sin[β]},
{-Cos[β] Sin[β], Cos[β] Sin[β], Cos[2 β]}})
({{Cos[β]^2, Sin[β]^2, Cos[β] Sin[β]},Sin[β]^2, Cos[β]^2, -Cos[β] Sin[β]},
{-2 Cos[β] Sin[β], Sin[2 β], Cos[2 β]}})
({{Cos[β]^2, Sin[β]^2, -2 Cos[β] Sin[β]},{Sin[β]^2, Cos[β]^2, Sin[2 β]},
{Cos[β] Sin[β], -Cos[β] Sin[β], Cos[2 β]}}) ({{Cos[β]^2, Sin[β]^2, -Cos[β] Sin[β]},
{Sin[β]^2, Cos[β]^2, Cos[β] Sin[β]},{Sin[2 β], -2 Cos[β] Sin[β], Cos[2 β]}})

Q11BAR=FullSimplify[QBAR[[1,1]],Trig→False]
Q12BAR=FullSimplify[QBAR[[1,2]],Trig→False]
Q16BAR=FullSimplify[QBAR[[1,3]],Trig→False]
Q21BAR=FullSimplify[QBAR[[2,1]],Trig→False]
Q22BAR=FullSimplify[QBAR[[2,2]],Trig→False]
Q26BAR=FullSimplify[QBAR[[2,3]],Trig→False]
Q61BAR=FullSimplify[QBAR[[3,1]],Trig→False]
Q62BAR=FullSimplify[QBAR[[3,2]],Trig→False]
Q66BAR=FullSimplify[QBAR[[3,3]],Trig→False]
```

Acquiring the components of [Q] Matrix

$Q11 \cos[\beta]^4+2 (Q12+2 Q66) \cos[\beta]^2 \sin[\beta]^2+Q22 \sin[\beta]^4$
$Q12 \cos[\beta]^4+(Q11+Q22-4 Q66) \cos[\beta]^2 \sin[\beta]^2+Q12 \sin[\beta]^4$
$(Q11-Q12-2 Q66) \cos[\beta]^3 \sin[\beta]+(Q12-Q22+2 Q66) \cos[\beta] \sin[\beta]^3$
$Q12 \cos[\beta]^4+(Q11+Q22-4 Q66) \cos[\beta]^2 \sin[\beta]^2+Q12 \sin[\beta]^4$
$Q22 \cos[\beta]^4+2 (Q12+2 Q66) \cos[\beta]^2 \sin[\beta]^2+Q11 \sin[\beta]^4$
$(Q12-Q22+2 Q66) \cos[\beta]^3 \sin[\beta]+(Q11-Q12-2 Q66) \cos[\beta] \sin[\beta]^3$
$(Q11-Q12-2 Q66) \cos[\beta]^3 \sin[\beta]+(Q12-Q22+2 Q66) \cos[\beta] \sin[\beta]^3$
$(Q12-Q22+2 Q66) \cos[\beta]^3 \sin[\beta]+(Q11-Q12-2 Q66) \cos[\beta] \sin[\beta]^3$
$Q66 \cos[\beta]^4+(Q11-2 Q12+Q22-2 Q66) \cos[\beta]^2 \sin[\beta]^2+Q66 \sin[\beta]^4$

```
m2=Cos[θ];n2=Sin[θ];
N[MatrixForm[Tσθ=({1, 0, 0},{0, m2^2, 0},{0, 0, m2})]]
N[MatrixForm[Tεθ=({{1, 0, 0},{0, m2^2, 0}, {0, 0, m2} })]]
N[MatrixForm[Tσθinverse=Inverse[Tσθ]]]
```

N[MatrixForm[Tεθinverse=Inverse[Tεθ]]]

({{1., 0., 0.},{0., $\cos[\theta]^2$, 0.} {0., 0., Cos[θ]}})
({{1., 0., 0.}, {0., $\cos[\theta]^2$, 0.},{0., 0., Cos[θ]} })
({{1., 0., 0.},{0., $\sec[\theta]^2$, 0.},{0., 0., Sec[θ]}})
({{1., 0., 0.},{0., $\sec[\theta]^2$, 0.},0., 0., Sec[θ]}})
FullSimplify[MatrixForm[QBARdash=Tσθ.QBAR.Tεθ],Trig→False];
Q11hat=FullSimplify[QbarDash[[1,1]],Trig→False]
Q12hat=FullSimplify[QbarDash[[1,2]],Trig→False]
Q16hat=FullSimplify[QbarDash[[1,3]],Trig→False]
Q21hat=FullSimplify[QbarDash[[2,1]],Trig→False]
Q22hat=FullSimplify[QbarDash[[2,2]],Trig→False]
Q26hat=FullSimplify[QbarDash[[2,3]],Trig→False]
Q61hat=FullSimplify[QbarDash[[3,1]],Trig→False]
Q62hat=FullSimplify[QbarDash[[3,2]],Trig→False]
Q66hat=FullSimplify[QbarDash[[3,3]],Trig→False]
Q11 $\cos[\beta]^4$+2 (Q12+2 Q66) $\cos[\beta]^2$ $\cos[\theta]^2$ $\sin[\beta]^2$+Q22 $\cos[\theta]^4$ $\sin[\beta]^4$
Q12 $\cos[\beta]^4$ $\cos[\theta]^2$+$\cos[\beta]^2$ (Q11-4 Q66 $\cos[\theta]^2$+Q22 $\cos[\theta]^4$)$\sin[\beta]^2$+Q12 $\cos[\theta]^2$ $\sin[\beta]^4$
$\cos[\beta]^3$ (Q11-(Q12+2 Q66) $\cos[\theta]^2$) Sin[β]+Cos[β] $\cos[\theta]^2$(Q12+2 Q66-Q22 $\cos[\theta]^2$) $\sin[\beta]^3$
Q12 $\cos[\beta]^4$ $\cos[\theta]^2$+$\cos[\beta]^2$ (Q11-4 Q66 $\cos[\theta]^2$+Q22 $\cos[\theta]^4$)$\sin[\beta]^2$+Q12 $\cos[\theta]^2$ $\sin[\beta]^4$
Q22 $\cos[\beta]^4$ $\cos[\theta]^4$+2 (Q12+2 Q66) $\cos[\beta]^2$ $\cos[\theta]^2$ $\sin[\beta]^2$+Q11 $\sin[\beta]^4$
$\cos[\beta]^3$ $\cos[\theta]^2$ (Q12+2 Q66-Q22 $\cos[\theta]^2$) Sin[β]+Cos[β]
(Q11-(Q12+2 Q66) $\cos[\theta]^2$) $\sin[\beta]^3$

$\cos[\beta]^3$ (Q11-(Q12+2 Q66) $\cos[\theta]^2$) Sin[β]+Cos[β] $\cos[\theta]^2$(Q12+2 Q66-Q22 $\cos[\theta]^2$) $\sin[\beta]^3$
$\cos[\beta]^3$ $\cos[\theta]^2$ (Q12+2 Q66-Q22 $\cos[\theta]^2$) Sin[β]+Cos[β](Q11-(Q12+2 Q66) $\cos[\theta]^2$) $\sin[\beta]^3$
Q66 $\cos[\beta]^4$ $\cos[\theta]^2$+$\cos[\beta]^2$ (Q11-2 (Q12+Q66) $\cos[\theta]^2$+Q22 $\cos[\theta]^4$) $\sin[\beta]^2$+Q66 $\cos[\theta]^2$ $\sin[\beta]^4$

Acquiring the components of [A] Matrix

-(1/4) π R (8 Q11 $\cos[\beta]^4$+3 Q22 $\sin[\beta]^4$+2 (Q12+2 Q66) $\sin[2\beta]^2$) (z_{-1+k}-z_k)
-(1/16) π R (4 Q12 (3+Cos[4 β])+(8 Q11+3 Q22-16 Q66) $\sin[2\beta]^2$) (z_{-1+k}-z_k)
-(1/16) π R (8 Q11-3 Q22+(8 Q11-8 Q12+3 Q22-16 Q66) Cos[2 β]) Sin[2 β] (z_{-1+k}-z_k)
-(1/16) π R (4 Q12 (3+Cos[4 β])+(8 Q11+3 Q22-16 Q66) $\sin[2\beta]^2$) (z_{-1+k}-z_k)
-(1/4) π R (3 Q22 $\cos[\beta]^4$+8 Q11 $\sin[\beta]^4$+2 (Q12+2 Q66) $\sin[2\beta]^2$) (z_{-1+k}-z_k)
1/16 π R (-8 Q11+3 Q22+(8 Q11-8 Q12+3 Q22-16 Q66) Cos[2 β]) Sin[2 β] (z_{-1+k}-z_k)
-(1/16) π R (8 Q11-3 Q22+(8 Q11-8 Q12+3 Q22-16 Q66) Cos[2 β]) Sin[2 β] (z_{-1+k}-z_k)
1/16 π R (-8 Q11+3 Q22+(8 Q11-8 Q12+3 Q22-16 Q66) Cos[2 β]) Sin[2 β] (z_{-1+k}-z_k)
1/16 π R (4 Q66 (3+Cos[4 β])+(8 Q11-8 Q12+3 Q22-8 Q66) $\sin[2\beta]^2$) ($-z_{-1+k}$+z_k)

Acquiring the components of [B] Matrix

-(1/8) π R (8 Q11 $\cos[\beta]^4$+3 Q22 $\sin[\beta]^4$+2 (Q12+2 Q66) $\sin[2\beta]^2$) (-)
-(1/32) π R (4 Q12 (3+Cos[4 β])+(8 Q11+3 Q22-16 Q66) $\sin[2\beta]^2$) (-)
-(1/32) π R (8 Q11-3 Q22+(8 Q11-8 Q12+3 Q22-16 Q66) Cos[2 β]) Sin[2 β] (-)

$-(1/32)\ \pi\ R\ (4\ Q12\ (3+\cos[4\ \beta])+(8\ Q11+3\ Q22-16\ Q66)\ \sin[2\ \beta]^2)\ (-)$
$-(1/8)\ \pi\ R\ (3\ Q22\ \cos[\beta]^4+8\ Q11\ \sin[\beta]^4+2\ (Q12+2\ Q66)\ \sin[2\ \beta]^2)\ (-)$
$1/32\ \pi\ R\ (-8\ Q11+3\ Q22+(8\ Q11-8\ Q12+3\ Q22-16\ Q66)\ \cos[2\ \beta])\ \sin[2\ \beta]\ (-)$
$-(1/32)\ \pi\ R\ (8\ Q11-3\ Q22+(8\ Q11-8\ Q12+3\ Q22-16\ Q66)\ \cos[2\ \beta])\ \sin[2\ \beta]\ (-)$

$1/32\ \pi\ R\ (-8\ Q11+3\ Q22+(8\ Q11-8\ Q12+3\ Q22-16\ Q66)\ \cos[2\ \beta])\ \sin[2\ \beta]\ (-)$
$-(1/64)\ \pi\ R\ (8\ Q11-8\ Q12+3\ Q22+16\ Q66+(-8\ Q11+8\ Q12-3\ Q22+16\ Q66)\ \cos[4\ \beta])\ ()$
$1/8\ \pi\ R^3\ (8\ Q11\ \cos[\beta]^4+5\ Q22\ \sin[\beta]^4+3\ (Q12+2\ Q66)\ \sin[2\ \beta]^2)\ (-z_{-1+k}+z_k)$

$-1/12\ \pi\ R\ (8\ Q11\ \cos[\beta]^4+3\ Q22\ \sin[\beta]^4+2\ (Q12+2\ Q66)\ \sin[2\ \beta]^2)\ (-)$
$-(1/32)\ \pi\ R^3\ (6\ Q12\ (3+\cos[4\ \beta])+(8\ Q11+5\ Q22-24\ Q66)\ \sin[2\ \beta]^2)\ (z_{-1+k}-z_k)$

$-1/48\ \pi\ R\ (4\ Q12\ (3+\cos[4\ \beta])+(8\ Q11+3\ Q22-16\ Q66)\ \sin[2\ \beta]^2)\ (-)$
$1/32\ \pi\ R^3\ (8\ Q11-5\ Q22+(8\ Q11-12\ Q12+5\ Q22-24\ Q66)\ \cos[2\ \beta])\ \sin[2\ \beta]\ (-z_{-1+k}+z_k)$

$-1/48\ \pi\ R\ (8\ Q11-3\ Q22+(8\ Q11-8\ Q12+3\ Q22-16\ Q66)\ \cos[2\ \beta])\ \sin[2\ \beta]\ (-)$
$-(1/32)\ \pi\ R^3\ (6\ Q12\ (3+\cos[4\ \beta])+(8\ Q11+5\ Q22-24\ Q66)\ \sin[2\ \beta]^2)\ (z_{-1+k}-z_k)$

$-1/48\ \pi\ R\ (4\ Q12\ (3+\cos[4\ \beta])+(8\ Q11+3\ Q22-16\ Q66)\ \sin[2\ \beta]^2)\ (-)$
$1/8\ \pi\ R^3\ (5\ Q22\ \cos[\beta]^4+8\ Q11\ \sin[\beta]^4+3\ (Q12+2\ Q66)\ \sin[2\ \beta]^2)\ (-z_{-1+k}+z_k)$

$-1/12\ \pi\ R\ (3\ Q22\ \cos[\beta]^4+8\ Q11\ \sin[\beta]^4+2\ (Q12+2\ Q66)\ \sin[2\ \beta]^2)\ (-)$
$1/32\ \pi\ R^3\ (8\ Q11-5\ Q22+(-8\ Q11+12\ Q12-5\ Q22+24\ Q66)\ \cos[2\ \beta])\ \sin[2\ \beta]\ (-z_{-1+k}+z_k)$
$+1/48\ \pi\ R\ (-8\ Q11+3\ Q22+(8\ Q11-8\ Q12+3\ Q22-16\ Q66)\ \cos[2\ \beta])\ \sin[2\ \beta]\ (-)$
$1/32\ \pi\ R^3\ (8\ Q11-5\ Q22+(8\ Q11-12\ Q12+5\ Q22-24\ Q66)\ \cos[2\ \beta])\ \sin[2\ \beta]\ (-z_{-1+k}+z_k)$

$-1/48\ \pi\ R\ (8\ Q11-3\ Q22+(8\ Q11-8\ Q12+3\ Q22-16\ Q66)\ \cos[2\ \beta])\ \sin[2\ \beta]\ (-)$
$1/32\ \pi\ R^3\ (8\ Q11-5\ Q22+(-8\ Q11+12\ Q12-5\ Q22+24\ Q66)\ \cos[2\ \beta])\ \sin[2\ \beta]\ (-z_{-1+k}+z_k)$

$+1/48\ \pi\ R\ (-8\ Q11+3\ Q22+(8\ Q11-8\ Q12+3\ Q22-16\ Q66)\ \cos[2\ \beta])\ \sin[2\ \beta]\ (-)$
$1/64\ \pi\ R^3\ (8\ Q11-12\ Q12+5\ Q22+24\ Q66+(-8\ Q11+12\ Q12-5\ Q22+24\ Q66)\ \cos[4\ \beta])$
$(-z_{-1+k}+z_k)$

Acquiring the components of [D] and [E] Matrix

$-1/96\ \pi\ R\ (8\ Q11-8\ Q12+3\ Q22+16\ Q66+(-8\ Q11+8\ Q12-3\ Q22+16\ Q66)\ \cos[4\ \beta])\ (-)$
$3/16\ \pi\ R^3\ (8\ Q11\ \cos[\beta]^4+5\ Q22\ \sin[\beta]^4+3\ (Q12+2\ Q66)\ \sin[2\ \beta]^2)\ (-+)$
$-1/16\ \pi\ R\ (8\ Q11\ \cos[\beta]^4+3\ Q22\ \sin[\beta]^4+2\ (Q12+2\ Q66)\ \sin[2\ \beta]^2)\ (-)$
$-(3/64)\ \pi\ R^3\ (6\ Q12\ (3+\cos[4\ \beta])+(8\ Q11+5\ Q22-24\ Q66)\ \sin[2\ \beta]^2)$

$(-)-1/64\ \pi\ R\ (4\ Q12\ (3+\cos[4\ \beta])+(8\ Q11+3\ Q22-16\ Q66)\ \sin[2\ \beta]^2)\ (-)$
$3/64\ \pi\ R^3\ (8\ Q11-5\ Q22+(8\ Q11-12\ Q12+5\ Q22-24\ Q66)\ \cos[2\ \beta])\ \sin[2\ \beta]\ (-+)-$
$1/64\ R\ (8\ Q11-3\ Q22+(8\ Q11-8\ Q12+3\ Q22-16\ Q66)\ \cos[2\ \beta])\ \sin[2\ \beta]\ (-)$
$-(3/64)\ \pi\ R^3\ (6\ Q12\ (3+\cos[4\ \beta])+(8\ Q11+5\ Q22-24\ Q66)\ \sin[2\ \beta]^2)\ ($
$-)-1/64\ \pi\ R\ (4\ Q12\ (3+\cos[4\ \beta])+(8\ Q11+3\ Q22-16\ Q66)\ \sin[2\ \beta]^2)\ (-)$

$3/16\ \pi\ R^3\ (5\ Q22\ \cos[\beta]^4+8\ Q11\ \sin[\beta]^4+3\ (Q12+2\ Q66)\ \sin[2\ \beta]^2)\ (-+)$
$-1/16\ \pi\ R\ (3\ Q22\ \cos[\beta]^4+8\ Q11\ \sin[\beta]^4+2\ (Q12+2\ Q66)\ \sin[2\ \beta]^2)\ (-)$
$3/64\ \pi\ R^3\ (8\ Q11-5\ Q22+(-8\ Q11+12\ Q12-5\ Q22+24\ Q66)\ \cos[2\ \beta])$
$\sin[2\ \beta]\ (-+)+1/64\ \pi\ R\ (-8\ Q11+3\ Q22+(8\ Q11-8\ Q12+3\ Q22-16\ Q66)$

Cos[2 β]) Sin[2 β] (-)

3/64 π R^3 (8 Q11-5 Q22+(8 Q11-12 Q12+5 Q22-24 Q66) Cos[2 β]) Sin[2 β]
(-+)-1/64 π R (8 Q11-3 Q22+(8 Q11-8 Q12+3 Q22-16 Q66) Cos[2 β]) Sin[2 β] (-)
3/64 π R^3 (8 Q11-5 Q22+(-8 Q11+12 Q12-5 Q22+24 Q66) Cos[2 β])
Sin[2 β] (-+)+1/64 π R (-8 Q11+3 Q22+(8 Q11-8 Q12+3 Q22-16 Q66)
Cos[2 β]) Sin[2 β] (-)

3/128 π R^3 (8 Q11-12 Q12+5 Q22+24 Q66+(-8 Q11+12 Q12-5 Q22+24 Q66)
Cos[4 β]) (-+)-1/128 π R (8 Q11-8 Q12+3 Q22+16 Q66+
(-8 Q11+8 Q12-3 Q22+16 Q66) Cos[4 β])

Appendix D

EXPANDED SUB-MATRICES FOR DEVELOPING CLOSED-FORM CENTROID EXPRESSION:GENERALIZED CASE

This section expands on developing a closed-form analytical expression that offers the potential to accurately predict the location of centroid in thin-walled composite structural elements characterized by an open cylindrical cross-section, uniform cross-sectional thickness and one axis of cross-sectional symmetry. The generalized hygrothermoelastic load-deformation relation (constitutive relationship) characterizing a curved composite cylindrical shell can be represented as

$$\begin{pmatrix} N_x' + N_x^{T'} + N_x^{H'} + \frac{M_x^{T'}}{R_m} + \frac{M_x^{H'}}{R_m} \\ N_y' + N_y^{T'} + N_y^{H'} \\ N_{xy}' + N_{xy}^{T'} + N_{xy}^{H'} + \frac{M_{xy}^{T'}}{R_m} + \frac{M_{xy}^{H'}}{R_m} \\ M_x' + M_x^{T'} + M_x^{H'} + L_x^{T'} + L_x^{H'} \\ M_y' + M_y^{T'} + M_y^{H'} \\ M_{xy}' + M_{xy}^{T'} + M_{xy}^{H'} + L_{xy}^{T'} + L_{xy}^{H'} \\ N_{yx}' + N_{yx}^{T'} + N_{yx}^{H'} \\ M_{yx}' + M_{yx}^{T'} + M_{yx}^{H'} \end{pmatrix} = \begin{bmatrix} A_{11} + \frac{B_{11}}{R_m} & A_{12} + \frac{B_{12}}{R_m} & A_{16} + \frac{B_{16}}{R_m} & B_{11} + \frac{D_{11}}{R_m} & B_{12} + \frac{D_{12}}{R_m} & B_{16} + \frac{D_{16}}{R_m} \\ A_{12} & A_{22} & A_{26} & B_{12} & B_{22} & B_{26} \\ A_{16} + \frac{B_{16}}{R_m} & A_{26} + \frac{B_{26}}{R_m} & A_{66} + \frac{B_{66}}{R_m} & B_{16} + \frac{D_{16}}{R_m} & B_{26} + \frac{D_{26}}{R_m} & B_{66} + \frac{D_{66}}{R_m} \\ B_{11} + \frac{D_{11}}{R_m} & B_{12} + \frac{D_{12}}{R_m} & B_{16} + \frac{D_{16}}{R_m} & D_{11} + \frac{E_{11}}{R_m} & D_{12} + \frac{E_{12}}{R_m} & D_{16} + \frac{E_{16}}{R_m} \\ B_{12} & B_{22} & B_{26} & D_{12} & D_{22} & D_{26} \\ B_{16} + \frac{D_{16}}{R_m} & B_{26} + \frac{D_{26}}{R_m} & B_{66} + \frac{D_{66}}{R_m} & D_{16} + \frac{E_{16}}{R_m} & D_{26} + \frac{E_{26}}{R_m} & D_{66} + \frac{E_{66}}{R_m} \\ A_{16} & A_{26} & A_{66} & B_{16} & B_{26} & B_{66} \\ B_{16} & B_{26} & B_{66} & D_{16} & D_{26} & D_{66} \end{bmatrix} * \begin{pmatrix} \varepsilon_x^0 \\ \varepsilon_y^0 \\ \gamma_{xy}^0 \\ \kappa_x \\ \kappa_y \\ \kappa_{xy} \end{pmatrix} \quad \text{(D-1)}$$

Underlying assumptions towards formualting an analytical methodology are :

- Mechanical characteristics of a typical composite narrow beam ($N_y = N_{xy} = N_{yx} = M_y = M_{xy} = M_{yx} = 0$) is adopted to analyze the behavior of the curved composite shell.
- Effects of any transverse shear deformations are negligible.
- Linear static analysis (ignores effects of geometric non-linearities)
- Bernouilli's hypothesis is considered
- Plane stress conditions

Utilizing a 1-D narrow beam approach, this formulation empahsizes on developing a closed-form centroid based on the constitutive relationship along the x-direction. As a consequence, the thermo-hydro-mechanical load components $M_x' + M_x^{T'} + M_x^{H'} + L_x^{T'} + L_x^{H'}$ is moved up to the second row of the resultant load matrix. This procedure triggers a row-

column manipulation of the associated stiffnes matrix terms respectively. Eq. (D-1) can therefore be regrouped and expressed as a two-part constitutive relationship system(Eq. D-2).

$$\begin{Bmatrix} N_x' + N_x^T + N_x^H + \frac{M_x^T}{R_m} + \frac{M_x^H}{R_m} \\ M_x' + M_x^T + M_x^H + L_x^T + L_x^H \\ N_y' + N_y^T + N_y^H \\ N_{xy}' + N_{xy}^T + N_{xy}^H + \frac{M_{xy}^T}{R_m} + \frac{M_{xy}^H}{R_m} \\ M_y' + M_y^T + M_y^H \\ M_{xy}' + M_{xy}^T + M_{xy}^H + L_{xy}^T + L_{xy}^H \\ N_{yx}' + N_{yx}^T + N_{yx}^H \\ M_{yx}' + M_{yx}^T + M_{yx}^H \end{Bmatrix} = \begin{bmatrix} A_{11} & B_{11} & A_{12} & A_{16} & B_{12} & B_{16} \\ B_{11} & D_{11} & B_{12} & B_{16} & D_{12} & D_{16} \\ A_{12} & B_{12} & A_{22} & A_{26} & B_{22} & B_{26} \\ A_{16} & B_{16} & A_{26} & A_{66} & B_{26} & B_{66} \\ B_{12} & D_{12} & B_{22} & B_{26} & D_{22} & D_{26} \\ B_{16} & D_{16} & B_{26} & B_{66} & D_{26} & D_{66} \\ A_{16} & B_{16} & A_{26} & A_{66} & B_{26} & B_{66} \\ B_{16} & D_{16} & B_{26} & B_{66} & D_{26} & D_{66} \end{bmatrix} * \begin{Bmatrix} \varepsilon_x^0 \\ \kappa_x \\ \varepsilon_y^0 \\ \gamma_{xy}^0 \\ \kappa_y \\ \kappa_{xy} \end{Bmatrix} + \frac{1}{R_m} * \begin{bmatrix} B_{11} & D_{11} & B_{12} & B_{16} & D_{12} & D_{16} \\ D_{11} & E_{11} & D_{12} & D_{16} & E_{12} & E_{16} \\ 0 & 0 & 0 & 0 & 0 & 0 \\ B_{16} & D_{16} & B_{26} & B_{66} & D_{26} & D_{66} \\ 0 & 0 & 0 & 0 & 0 & 0 \\ D_{16} & E_{16} & D_{26} & D_{66} & E_{26} & E_{66} \\ 0 & 0 & 0 & 0 & 0 & 0 \\ 0 & 0 & 0 & 0 & 0 & 0 \end{bmatrix} * \begin{Bmatrix} \varepsilon_x^0 \\ \kappa_x \\ \varepsilon_y^0 \\ \gamma_{xy}^0 \\ \kappa_y \\ \kappa_{xy} \end{Bmatrix} \tag{D-2}$$

Governing stiffness parameters are efficiently decomposed into 4 sub-matrix system and can be denoted as

$$\begin{Bmatrix} N_x' + N_x^T + N_x^H + \frac{M_x^T}{R_m} + \frac{M_x^H}{R_m} \\ M_x' + M_x^T + M_x^H + L_x^T + L_x^H \\ N_y' + N_y^T + N_y^H \\ N_{xy}' + N_{xy}^T + N_{xy}^H + \frac{M_{xy}^T}{R_m} + \frac{M_{xy}^H}{R_m} \\ M_y' + M_y^T + M_y^H \\ M_{xy}' + M_{xy}^T + M_{xy}^H + L_{xy}^T + L_{xy}^H \\ N_{yx}' + N_{yx}^T + N_{yx}^H \\ M_{yx}' + M_{yx}^T + M_{yx}^H \end{Bmatrix} = \left\{ \begin{bmatrix} P_1 & P_2 \\ P_3 & P_4 \end{bmatrix} + \frac{1}{R_m} \begin{bmatrix} T_1 & T_2 \\ T_3 & T_4 \end{bmatrix} \right\} * \begin{Bmatrix} \varepsilon_x^0 \\ \kappa_x \\ \varepsilon_y^0 \\ \gamma_{xy}^0 \\ \kappa_y \\ \kappa_{xy} \end{Bmatrix} \tag{D.3}$$

$$\begin{bmatrix} N_1 \\ N_2 \end{bmatrix} = \left\{ \begin{bmatrix} P_1 & P_2 \\ P_3 & P_4 \end{bmatrix} + \frac{1}{R_m} \begin{bmatrix} T_1 & T_2 \\ T_3 & T_4 \end{bmatrix} \right\} * \begin{Bmatrix} \varepsilon_1^* \\ \varepsilon_2^* \end{Bmatrix} \tag{D-4}$$

where $[N_1]$ and $[N_2]$ matrices encompass the resultant in-plane applied mechanical and hygrothermally induced loads whereas the stiffness matrices denoted by symbols $[P_1]$,

$[P_2]$, $[P_3]$, $[P_4]$, $[T_1]$, $[T_2]$, $[T_3]$ and $[T_4]$ are the sub-matrix structures representing each of the doubly-rotated average stiffness parameters per unit width (Chapter-4) and matrices $\left\{\varepsilon_1^*\right\}_{2*1}$ and $\left\{\varepsilon_2^*\right\}_{4*1}$ jointly describe the reference in-plane strains and curvatures for a generalized curved composite cylindrical shell configuration.

$$N_1 = \left\{ \begin{array}{c} N_x^{'} + N_x^{T'} + N_x^{H'} + \frac{M_x^{T'}}{R_m} + \frac{M_x^{H'}}{R_m} \\ M_x^{'} + M_x^{T'} + M_x^{H'} + L_x^{T'} + L_x^{H'} \end{array} \right\}_{2*1} \qquad N_2 = \left\{ \begin{array}{c} N_y^{'} + N_y^{T'} + N_y^{H'} \\ N_{xy}^{'} + N_{xy}^{T'} + N_{xy}^{H'} + \frac{M_{xy}^{T'}}{R_m} + \frac{M_{xy}^{H'}}{R_m} \\ M_y^{'} + M_y^{T'} + M_y^{H'} \\ M_{xy}^{'} + M_{xy}^{T'} + M_{xy}^{H'} + L_{xy}^{T'} + L_{xy}^{H'} \\ N_{yx}^{'} + N_{yx}^{T'} + N_{yx}^{H'} \\ M_{yx}^{'} + M_{yx}^{T'} + M_{yx}^{H'} \end{array} \right\}_{6*1}$$

$$P_1 = \begin{bmatrix} A_{11} & B_{11} \\ B_{11} & D_{11} \end{bmatrix}_{2*2} \qquad P_2 = \begin{bmatrix} A_{12} & A_{16} & B_{12} & B_{16} \\ B_{12} & B_{16} & D_{12} & D_{16} \end{bmatrix}_{2*4} \qquad P_3 = \begin{bmatrix} A_{12} & B_{12} \\ A_{16} & B_{16} \\ B_{12} & D_{12} \\ B_{16} & D_{16} \\ A_{16} & B_{16} \\ B_{16} & D_{16} \end{bmatrix}_{6*2}$$

$$P_4 = \begin{bmatrix} A_{22} & A_{26} & B_{22} & B_{26} \\ A_{26} & A_{66} & B_{26} & B_{66} \\ B_{22} & B_{26} & D_{22} & D_{26} \\ B_{26} & B_{66} & D_{26} & D_{66} \\ A_{26} & A_{66} & B_{26} & B_{66} \\ B_{26} & B_{66} & D_{26} & D_{66} \end{bmatrix}_{6*4} \qquad \text{(D.5)}$$

$$T_1 = \begin{bmatrix} B_{11} & D_{11} \\ D_{11} & E_{11} \end{bmatrix}_{2*2} \quad T_2 = \begin{bmatrix} B_{12} & B_{16} & D_{12} & D_{16} \\ D_{12} & D_{16} & E_{12} & E_{16} \end{bmatrix}_{2*4} \quad T_3 = \frac{1}{R_m} \begin{bmatrix} 0 & 0 \\ B_{16} & D_{16} \\ 0 & 0 \\ D_{16} & E_{16} \\ 0 & 0 \\ 0 & 0 \end{bmatrix}_{6*2} \quad T_4 = \frac{1}{R_m} \begin{bmatrix} 0 & 0 & 0 & 0 \\ B_{26} & B_{66} & D_{26} & D_{66} \\ 0 & 0 & 0 & 0 \\ D_{26} & D_{66} & E_{26} & E_{66} \\ 0 & 0 & 0 & 0 \\ 0 & 0 & 0 & 0 \end{bmatrix}_{6*4}$$

$$\varepsilon_1^* = \begin{pmatrix} \varepsilon_x^0 \\ \kappa_x \end{pmatrix} \quad \varepsilon_2^* = \begin{pmatrix} \varepsilon_y^0 \\ \gamma_{xy}^0 \\ \kappa_y \\ \kappa_{xy} \end{pmatrix}$$

or, in brief,

$$\begin{bmatrix} (N_1)_{2*1} \\ (N_2)_{6*1} \end{bmatrix} = \left\{ \begin{bmatrix} \left(P_1 + \frac{T_1}{R_m}\right)_{2*2} & \left(P_2 + \frac{T_2}{R_m}\right)_{2*4} \\ \left(P_3 + \frac{T_3}{R_m}\right)_{6*2} & \left(P_4 + \frac{T_4}{R_m}\right)_{6*4} \end{bmatrix} \right\} * \begin{Bmatrix} (\varepsilon_1^*)_{2*1} \\ (\varepsilon_2^*)_{4*1} \end{Bmatrix} \quad \text{(D.6)}$$

In view of Eqn. (D.5), all the terms associated with matrix $(N_2)_{4*1}$ are isolated to generate a relationship between reference extensional strain ε_x^o and curvature κ_x and the remaining 4 mid-plane strains and curvatures $\begin{pmatrix} \varepsilon_y^0 & \gamma_{xy}^0 & \kappa_y & \kappa_{xy} \end{pmatrix}$ respectively. This can be shown as follows: $\left[(N_2)_{6*1}\right] = \left(P_3 + \frac{T_3}{R_m}\right)_{6*2} * (\varepsilon_1^*)_{2*1} + \left(P_4 + \frac{T_4}{R_m}\right)_{6*4} * (\varepsilon_2^*)_{4*1}$. With the objective on expressing the strain components of $\{\varepsilon_2^*\}_{4*1}$ matrix in terms $\{\varepsilon_1^*\}_{2*1}$ of expression involving $\left[(N_2)_{6*1}\right] = \left(P_3 + \frac{T_3}{R_m}\right)_{6*2} * (\varepsilon_1^*)_{2*1} + \left(P_4 + \frac{T_4}{R_m}\right)_{6*4} * (\varepsilon_2^*)_{4*1}$ can be efficiently manipulated and rewritten (while assuming ($N_y = N_{xy} = N_{yx} = M_y = M_{xy} = M_{yx} = 0$) as follows:

It should be noted that $[T_4]$ is singular matrix that cannot be inversed mathematically. However, $\left(P_4 + \frac{T_4}{R_m}\right)_{6*4}$ is a non-singular matrix and an inverse matrix operation is achievable. Assuming $\left(P_3 + \frac{T_3}{R_m}\right)_{6*2} = \left[G_1\right]_{6*2}$ and $\left(P_4 + \frac{T_4}{R_m}\right)_{6*4} = \left[G_2\right]_{6*4}$, expression involving $[N_2]$ can be simplified by taking the transpose of $\left[G_2\right]_{6*4}$ and multiply on both sides of $\left[(N_2)_{6*1}\right] = \left(P_3 + \frac{T_3}{R_m}\right)_{6*2} * (\varepsilon_1^*)_{2*1} + \left(P_4 + \frac{T_4}{R_m}\right)_{6*4} * (\varepsilon_2^*)_{4*1}$ respectively.

Since $\left[G_2\right]_{6*4}$ is not a square matrix , the inverse of $\left[G_2\right]_{6*4}$ can be eventually calculated by performing the operation $\left[G_2\right]^{-1}=\left[\left[G_2\right]^T*\left[G_2\right]\right]^{-1}*\left[G_2\right]^T$.

$$\left[G_2\right]^T_{4*6}\left[\left\{N_2\right\}_{6*1}\right]=\left[G_2\right]^T*\left[\left[G_1\right]*\left\{\varepsilon_1^*\right\}\right]+\left[G_2\right]^T_{4*6}*\left[G_2\right]_{6*4}\left(\varepsilon_2^*\right)_{4*1} \qquad \text{(D-7)}$$

$$\left(\varepsilon_2^*\right)_{4*1}=\left[G_2\right]^{-1}*\left\{N_2\right\}_{6*1}-\left(\left[G_2\right]^{-1}*\left[G_1\right]_{6*2}\left(\varepsilon_1^*\right)_{2*1}\right)$$

as the matrices $\left[G_2\right]^{-1}$ and $[N]_2$ are composed of constants we can assume $\left[G_2\right]^{-1}*\left\{N_2\right\}_{6*1}=\left[G_3\right]$ and $-\left(\left[G_2\right]^{-1}*\left[G_1\right]_{6*2}\right)=\left[G_4\right]$, we can express $\left\{\varepsilon_2^*\right\}_{4*1}$ as

$$\left(\varepsilon_2^*\right)_{4*1}=\left[G_3\right]_{4*1}+\left[G_4\right]_{4*2}.\left(\varepsilon_1^*\right)_{2*1} \qquad \text{(D-8)}$$

Since multidirectional laminates in general are characterized by stress discontinuities from ply-per-ply, it is more suitable to work with strains, which are continuous through the thickness. Based on this fundamental argument, determination of the centroidal location can be formulated by expressing strain and curvatures as a function of applied loads and moments.

Substituting $\begin{pmatrix}\varepsilon_y^0\\ \gamma_{xy}^0\\ \kappa_y\\ \kappa_{xy}\end{pmatrix}_{4*1}=\left[G_3\right]_{4*1}+\left[G_4\right]_{4*2}.\left(\varepsilon_1^*\right)_{2*1}$ into the first part of Eqn. (D.5), we obtain

$$\begin{Bmatrix}N_x^{'}+N_x^{T'}+N_x^{H'}+\dfrac{M_x^{T'}}{R_m}+\dfrac{M_x^{H'}}{R_m}\\ M_x^{'}+M_x^{T'}+M_x^{H'}+L_x^{T'}+L_x^{H'}\end{Bmatrix}=\left[\left(P_1+\frac{T_1}{R_m}\right)_{2*2}*\left(\varepsilon_1^*\right)_{2*1}+\left(P_2+\frac{T_2}{R_m}\right)_{2*4}*\left(\left[G_3\right]_{4*1}+\left[G_4\right]_{4*2}.\left(\varepsilon_1^*\right)_{2*1}\right)\right]_{2*1} \qquad \text{(D-9)}$$

The hygrothermally induced loads (force and moment) from the (N_1) matrix are essentially constants and can therefore be denoted as $\begin{Bmatrix} N_x^{T'} + N_x^{H'} + \frac{M_x^{T'}}{R_m} + \frac{M_x^{H'}}{R_m} \\ M_x^{T'} + M_x^{H'} + L_x^{T'} + L_x^{H'} \end{Bmatrix} = \begin{Bmatrix} J_1 \\ J_2 \end{Bmatrix}$.

Eq. D-8 can be rewritten as follows:

$$\begin{Bmatrix} N_x' + J_1 \\ M_x' + J_2 \end{Bmatrix} = \left[\left(P_1 + \frac{T_1}{R_m} \right)_{2*2} * \begin{pmatrix} \varepsilon_x^0 \\ \kappa_x \end{pmatrix} + \left(P_2 + \frac{T_2}{R_m} \right)_{2*4} * \left(\left[G_3 \right]_{4*1} + \left[G_4 \right]_{4*2} . \left(\varepsilon_1^* \right)_{2*1} \right) \right]_{2*1} \quad \text{(D10)}$$

Eq. (D-9) can further be reduced and shown as

$$\begin{Bmatrix} N_x' \\ M_x' \end{Bmatrix} + \begin{Bmatrix} J_1 \\ J_2 \end{Bmatrix} = \begin{bmatrix} A_{1,total}^* & B_{1,total}^* \\ B_{1,total}^* & D_{1,total}^* \end{bmatrix}_{2*1} * \begin{pmatrix} \varepsilon_x^0 \\ \kappa_x \end{pmatrix} \quad \text{(D-11)}$$

where $A_{1,total}^* = \int_{-\alpha}^{\alpha} A_1^* * R_m d\theta$, $B_{1,total}^* = \int_{-\alpha}^{\alpha} B_1^* * R_m d\theta$ and $D_{1,total}^* = \int_{-\alpha}^{\alpha} D_1^* * R_m d\theta$ respectively. Assuming N_x=0 and a pure bending moment M_x is applied to the centroid (still unknown) of the curved shell structure, Eq. (D-10) reduces as follows:

$$\begin{pmatrix} \varepsilon_x^0 \\ \kappa_x \end{pmatrix} = \begin{bmatrix} a_1^* & b_1^* \\ b_1^* & d_1^* \end{bmatrix}_{2*1} * \begin{Bmatrix} 0 \\ M_x' \end{Bmatrix} + \begin{bmatrix} a_1^* & b_1^* \\ b_1^* & d_1^* \end{bmatrix}_{2*1} * \begin{Bmatrix} J_1 \\ J_2 \end{Bmatrix} \quad \text{(D-12)}$$

where $\begin{bmatrix} a_1^* & b_1^* \\ b_1^* & d_1^* \end{bmatrix}_{2*1} * \begin{Bmatrix} J_1 \\ J_2 \end{Bmatrix} = \begin{Bmatrix} \varepsilon_x^{thermal+moisture} \\ \kappa_x^{thermal+moisture} \end{Bmatrix}$ By definition, the centroidal mechanical strains witnessed by the structure subjected to a pure bending moment M_x in the presence of a hygrothermal environment is given by

$$\varepsilon_x^{centroid} = \varepsilon_x^0 + Z_c \kappa_x - \varepsilon^{thermal+moisture} = 0 \quad \text{(D-13)}$$

where $\varepsilon^{thermal+moisture} = \varepsilon_x^{thermal+moisture} + Z_c \kappa_x^{thermal+moisture}$. Expanding Eq. (D-11) we can generate expressions for ε_x^0 and κ_x as shown in Eq. (D-13).

$$\varepsilon_x^0 = b_1^* M_x' + \varepsilon_x^{\text{thermal+moisture}}$$

$$\kappa_x = d_1^* M_x' + \kappa_x^{\text{thermal+moisture}} \qquad \text{(D-14)}$$

Substituting Eq. (D-13) in to Eq. D-12 and solving for Z_c we get

$$Z_c = -\left(\frac{\varepsilon_x^0}{\kappa_x}\right) = -\left(\frac{b_1^*}{d_1^*}\right) \qquad \text{(D-15)}$$

Fundamentally Eq. (D-14) represents an analytical verification that hygrothermal loads acting on a composite structural configuration do not influence the location of centroid. The location of centroid in a composite structural configuration is primarily governed by the structural geometry, material properties, ply lay-up and stacking sequence respectively.

Appendix E

TEST FIXTURE DESIGN DRAWINGS :CATIA V5 R21

This section details on the 2-D drawings designed towards the development of a novel ad-hoc test fixture utilizing CATIA V5-R21. Each part constituting the test fixture is computationally designed and dimensionalized for convenience. CAD drawings portray the part designs in various views for reader's understanding and part recreation.

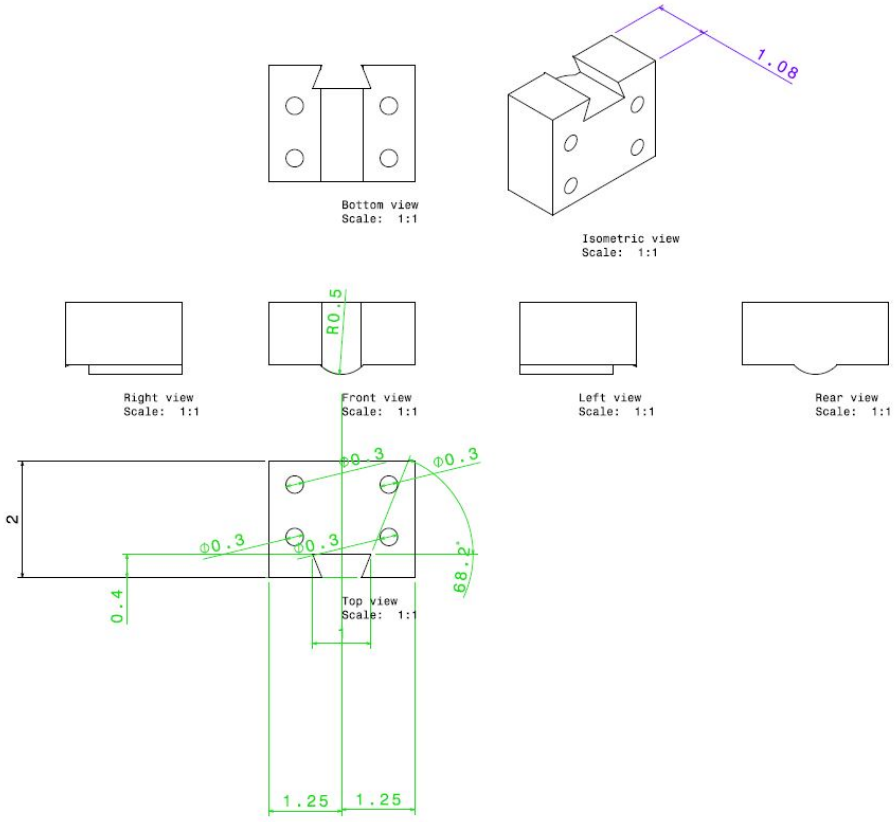

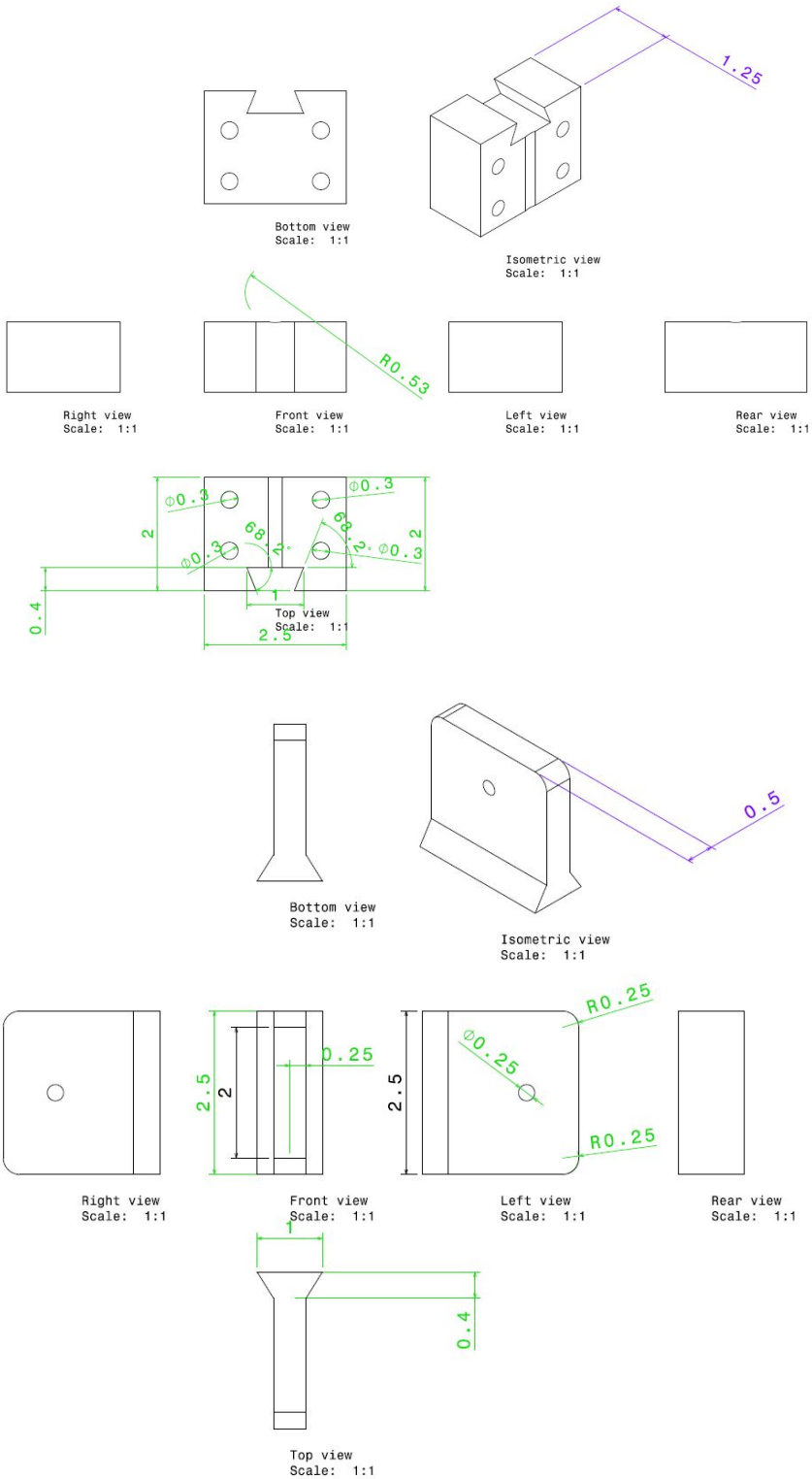
1.25
Bottom view
Scale: 1:1
Isometric view
Scale: 1:1
R0.53
Right view
Scale: 1:1
Front view
Scale: 1:1
Left view
Scale: 1:1
Rear view
Scale: 1:1
Φ0.3
Φ0.3
Φ0.3
Φ0.3
68.2°
68.2°
2
2
0.4
1
2.5
Top view
Scale: 1:1
0.5
Bottom view
Scale: 1:1
Isometric view
Scale: 1:1
R0.25
R0.25
Φ0.25
0.25
2.5
2
2.5
Right view
Scale: 1:1
Front view
Scale: 1:1
Left view
Scale: 1:1
Rear view
Scale: 1:1
1
0.4
Top view
Scale: 1:1

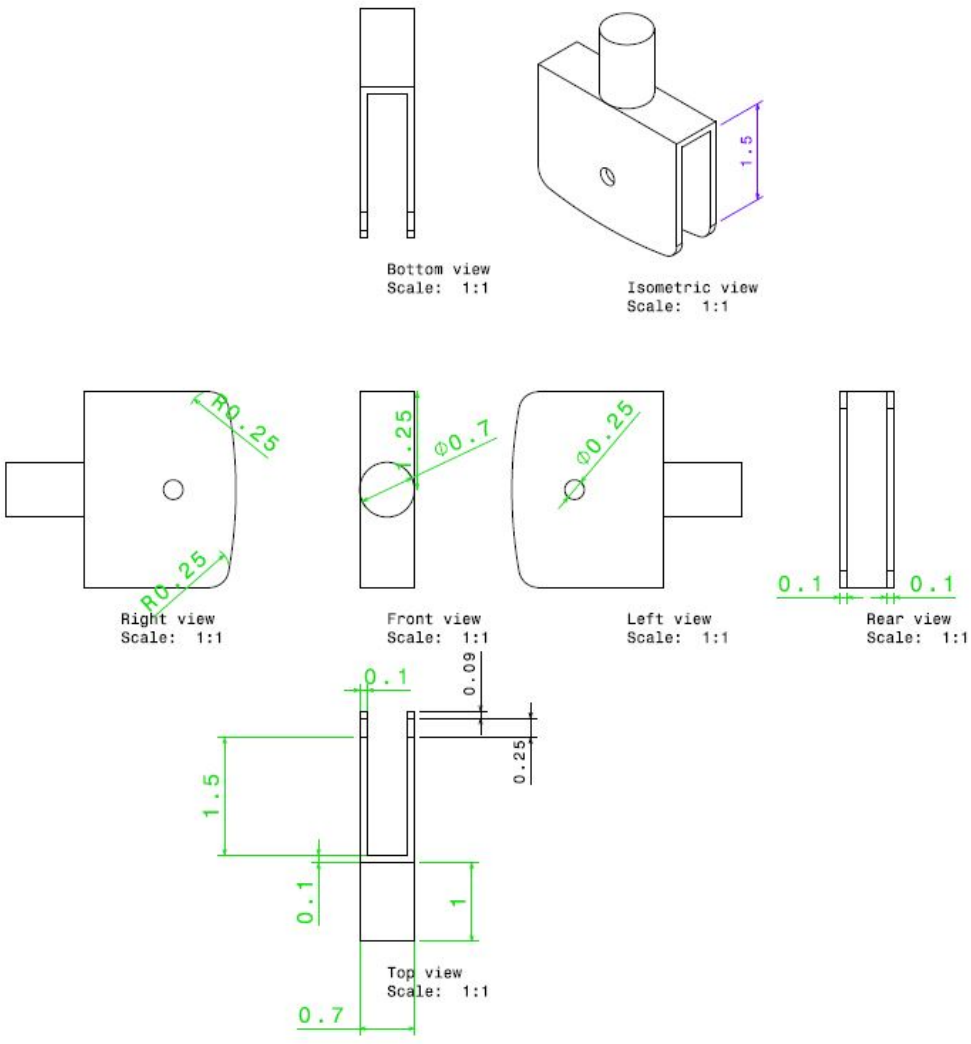
Bottom view
Scale: 1:1
1.5
Isometric view
Scale: 1:1
R0.25
R0.25
Right view
Scale: 1:1
1.25
Ø0.7
Front view
Scale: 1:1
Ø0.25
Left view
Scale: 1:1
0.1
0.1
Rear view
Scale: 1:1
0.1
0.09
0.25
1.5
0.1
1
Top view
Scale: 1:1
0.7

Appendix F

DIGITAL IMAGE CORRELATION (DIC) STRAIN FIELD IMAGES AND STRAIN MEASUREMENT DATA (SP2-SP7)

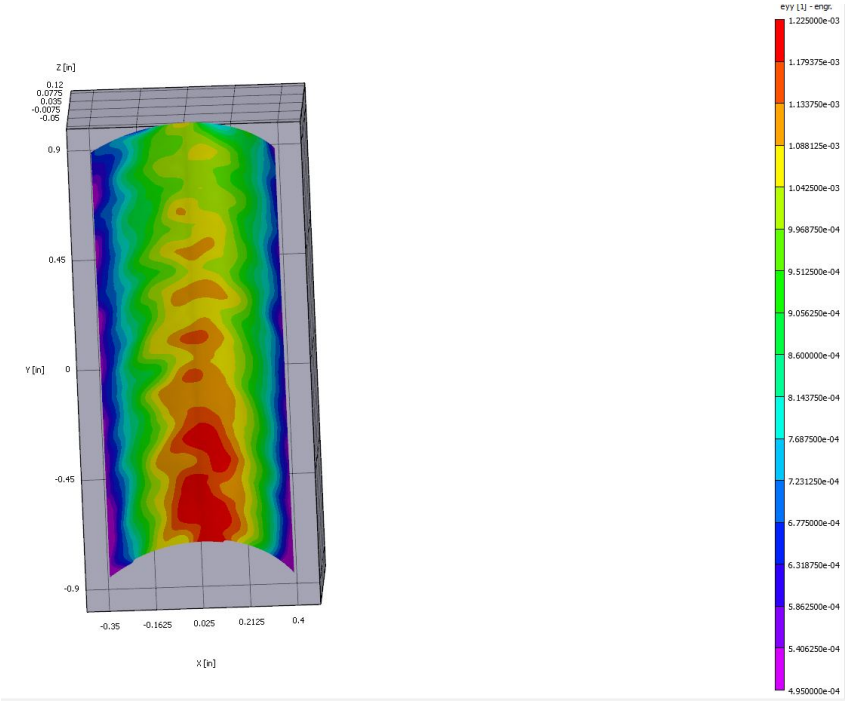

SP-2 Run-1 (+0.5 in offset)

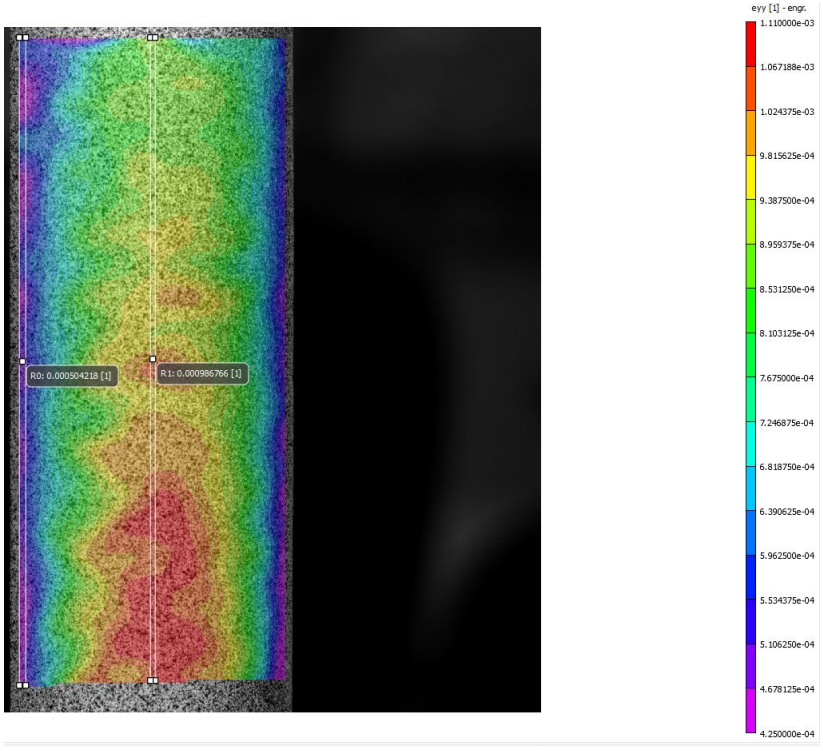

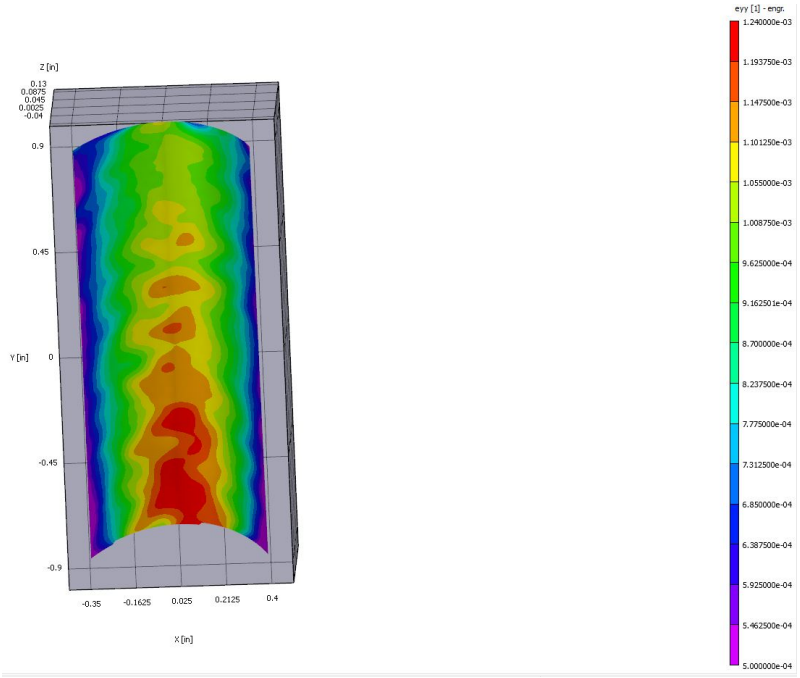

SP-2 Run-5 (+ 0.5 in Offset)

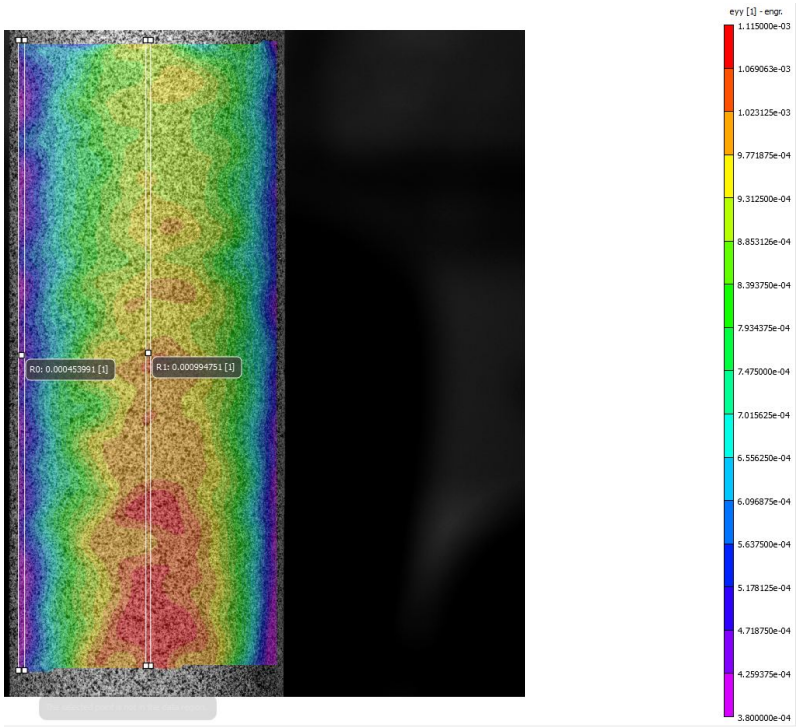

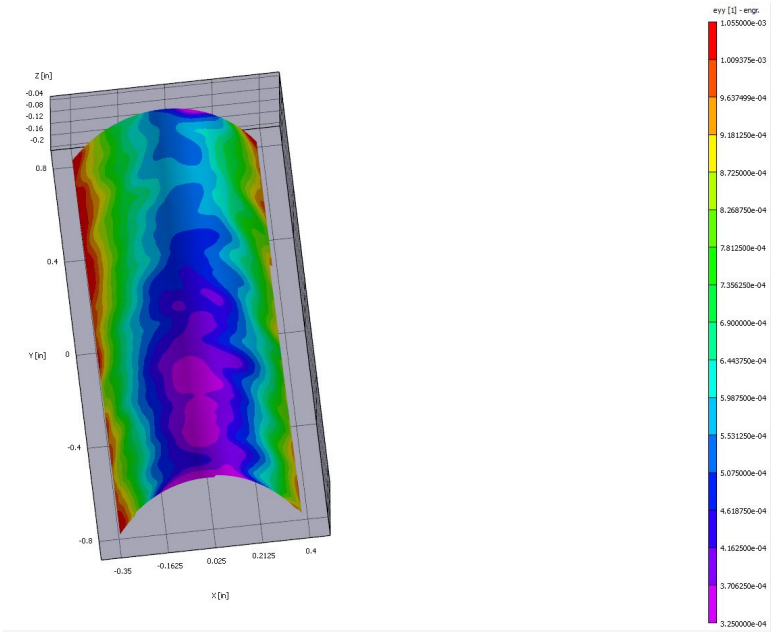

SP-2 Run-1 (-0.268 in Offset)

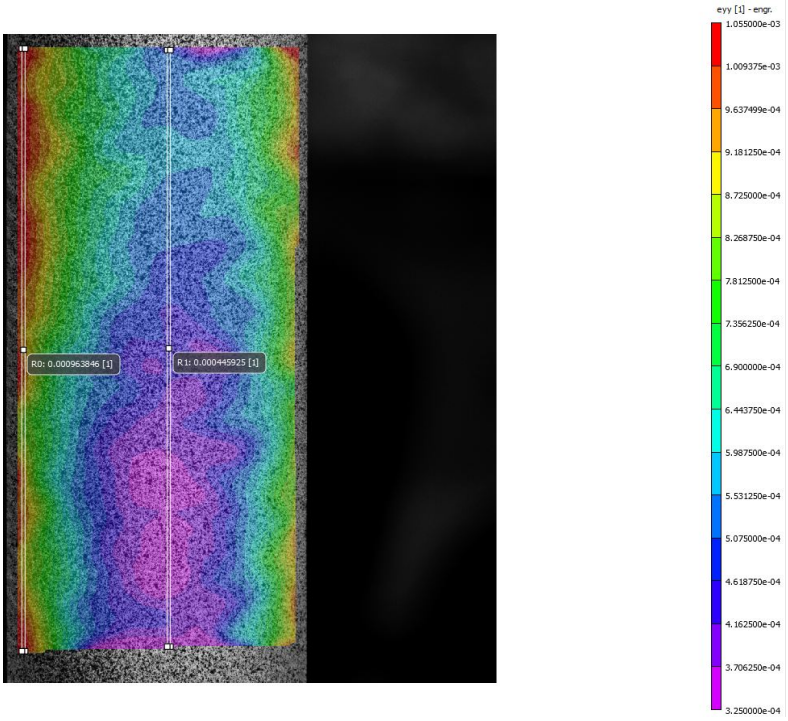

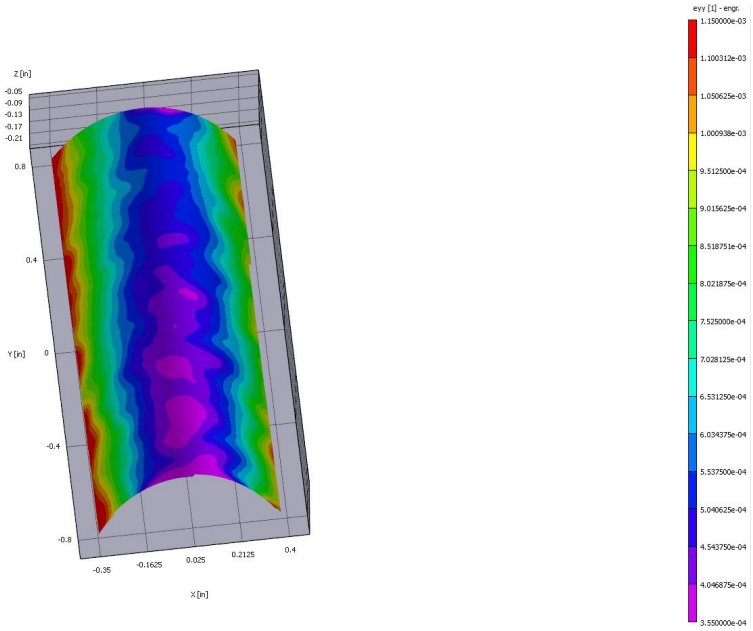

SP-2 Run-5 (-0.268 in offset)

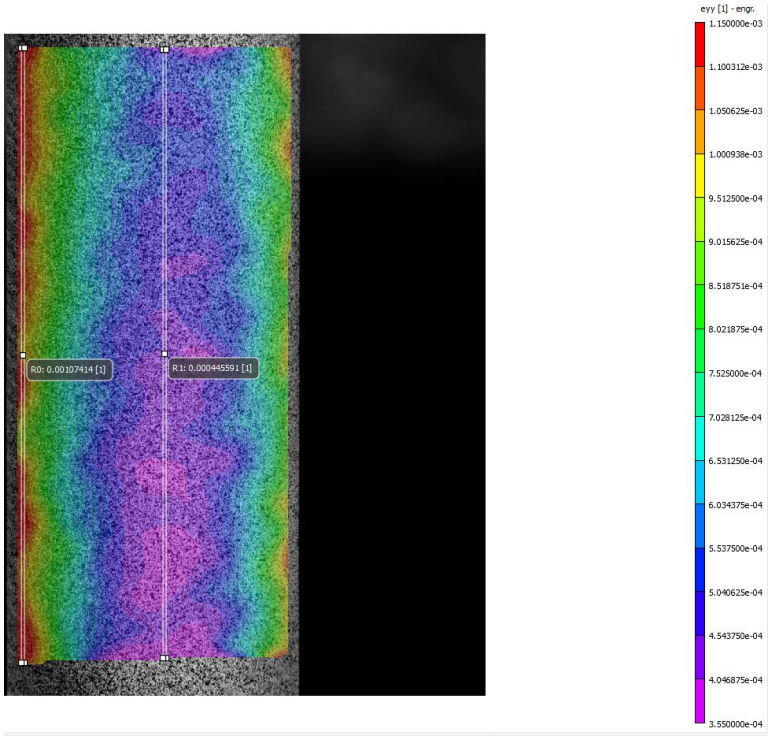

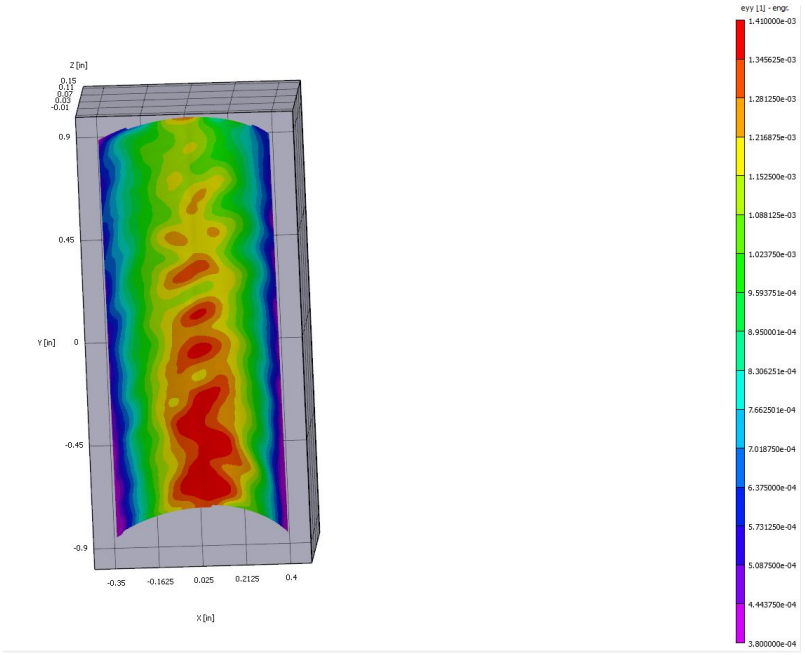

SP-3 Run-1 (+0.5 in offset)

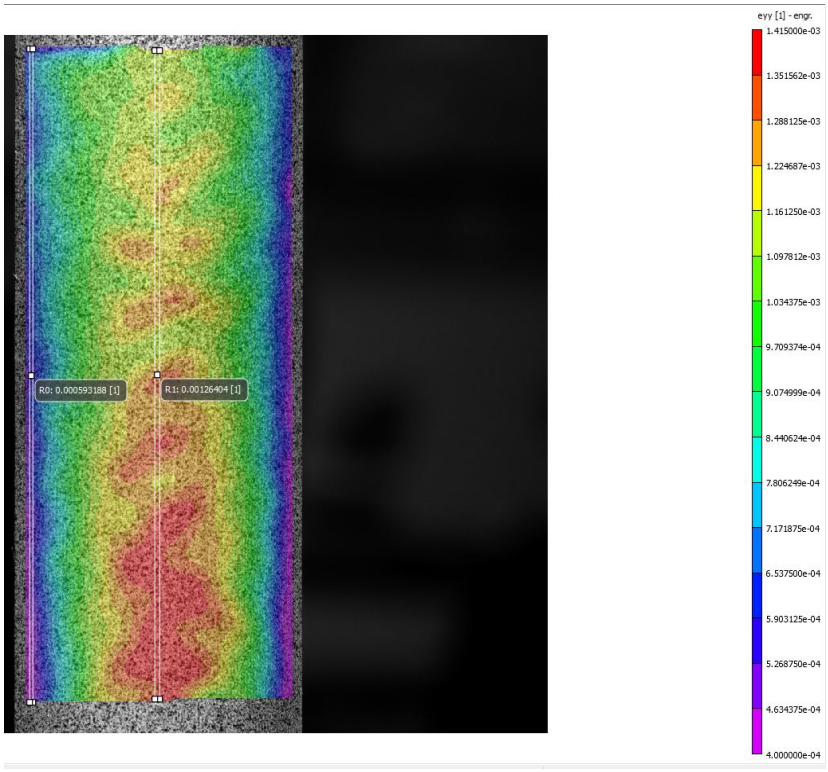

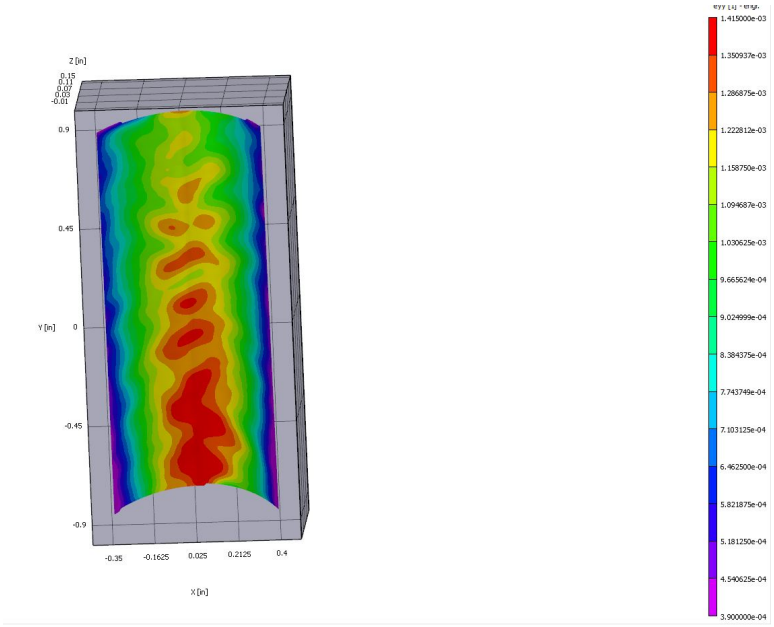

SP-3 Run-5 (+0.5 in offset)

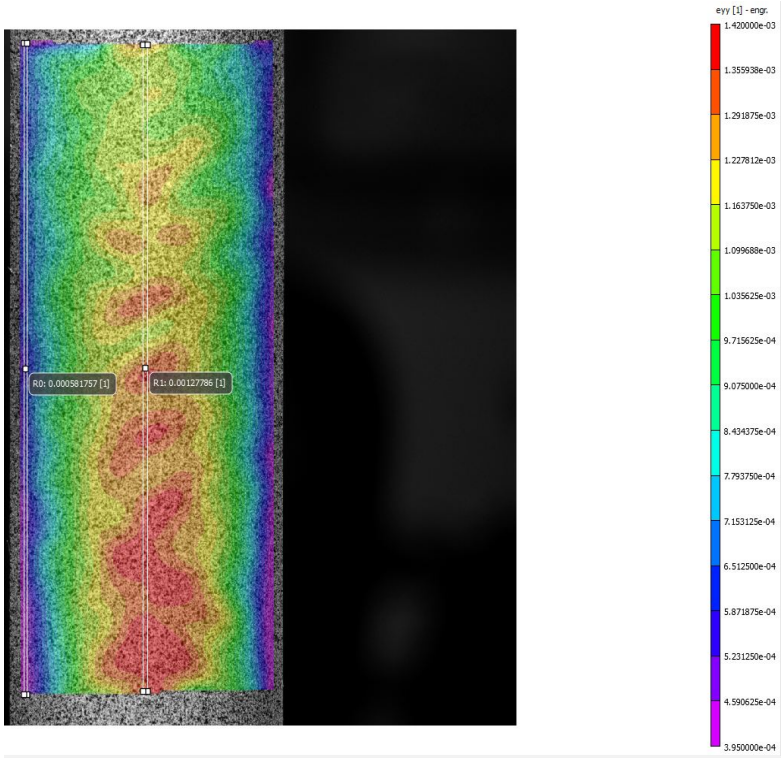

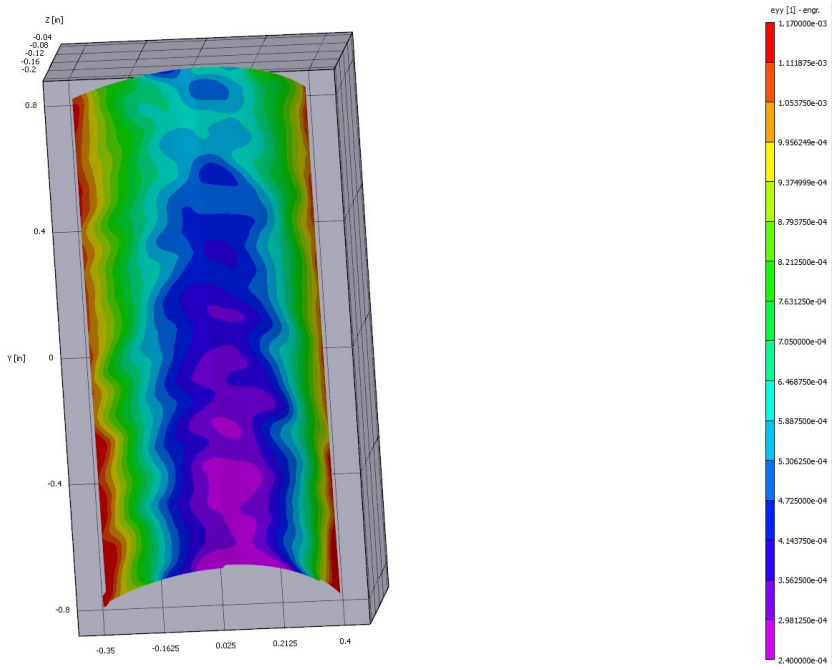

SP-3 Run-1 (-0.268 in offset)

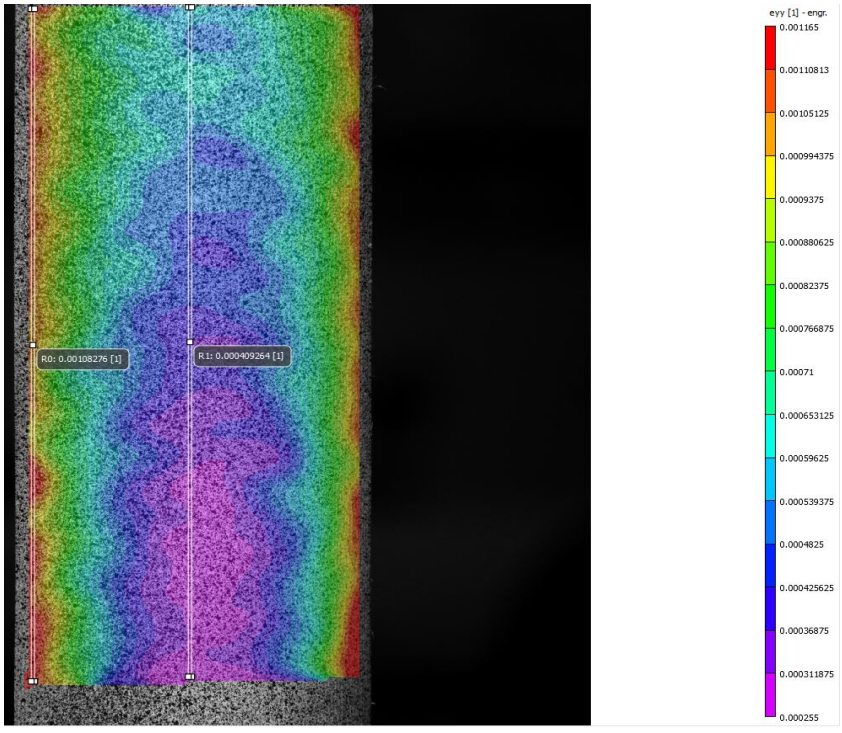

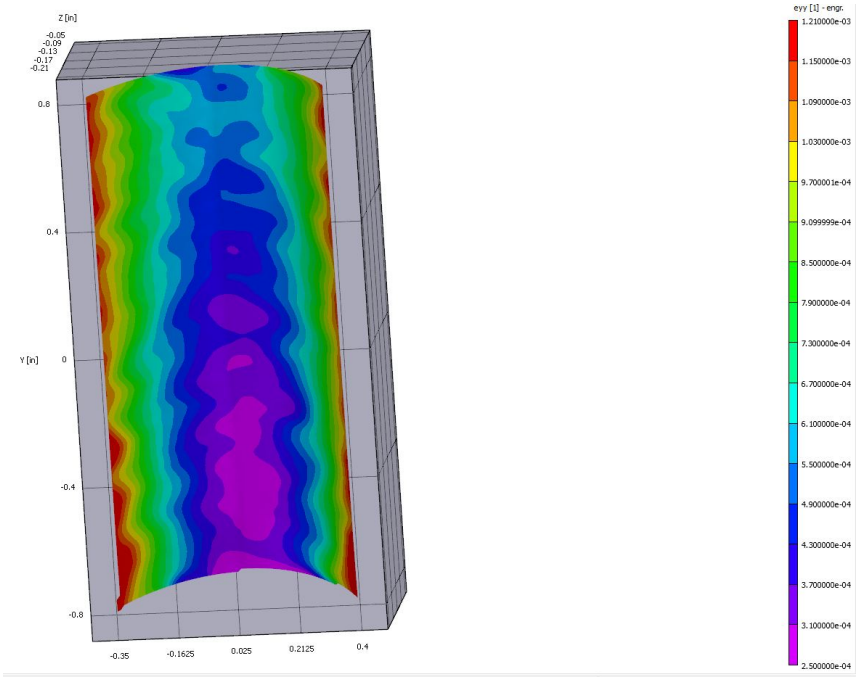

SP-3 Run-5 (-0.268 in offset)

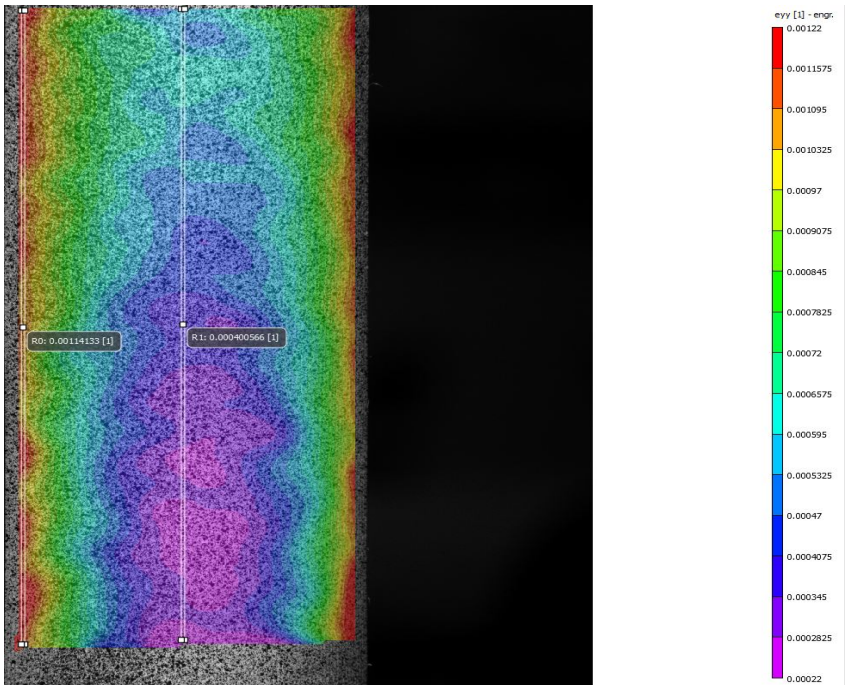

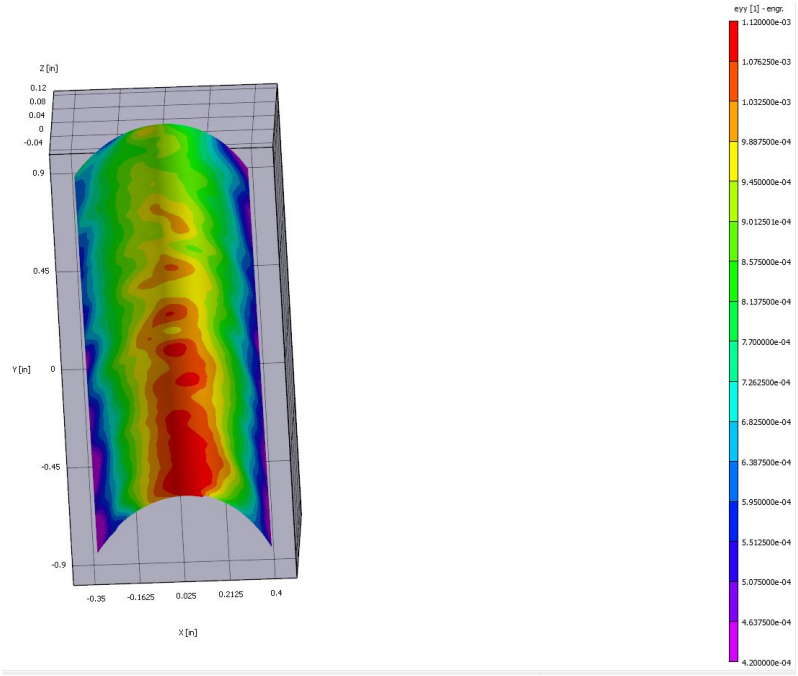

SP-4 Run-1 (+0.5 in offset)

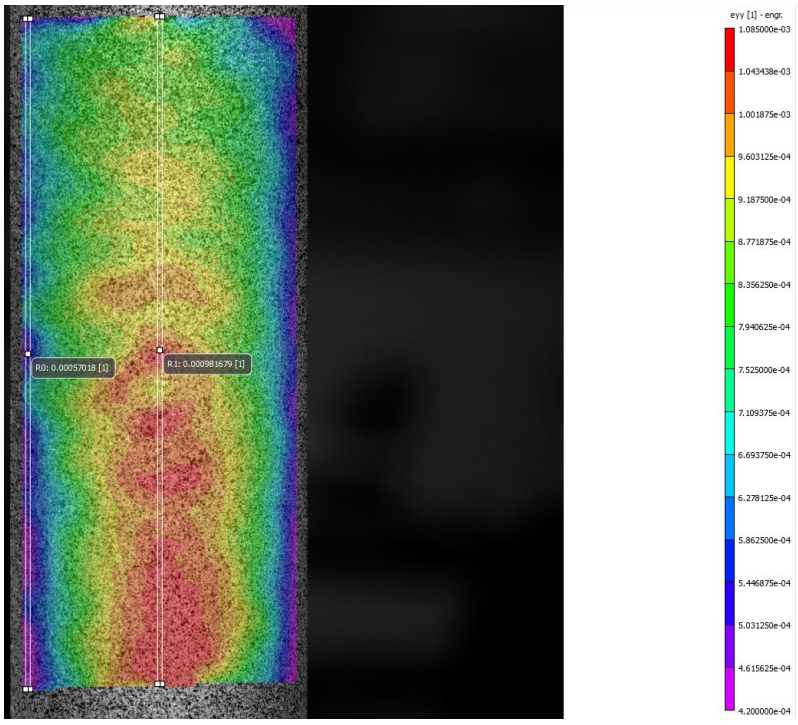

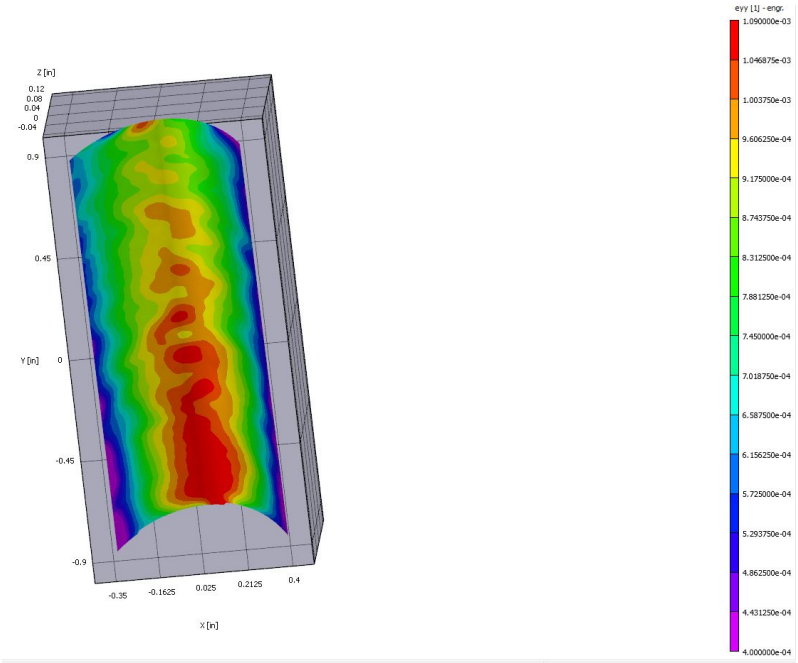

SP-4 Run-5 (+0.5 in offset)

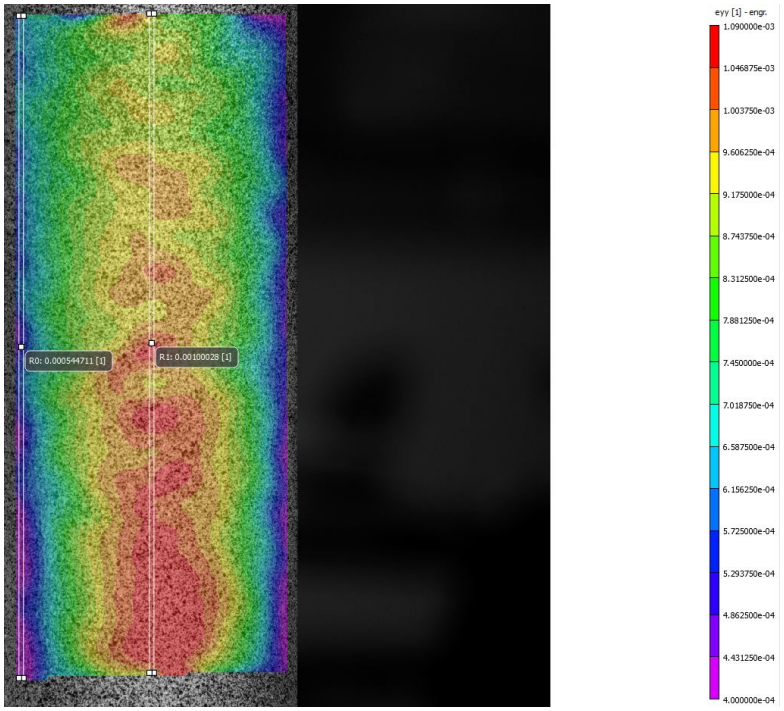

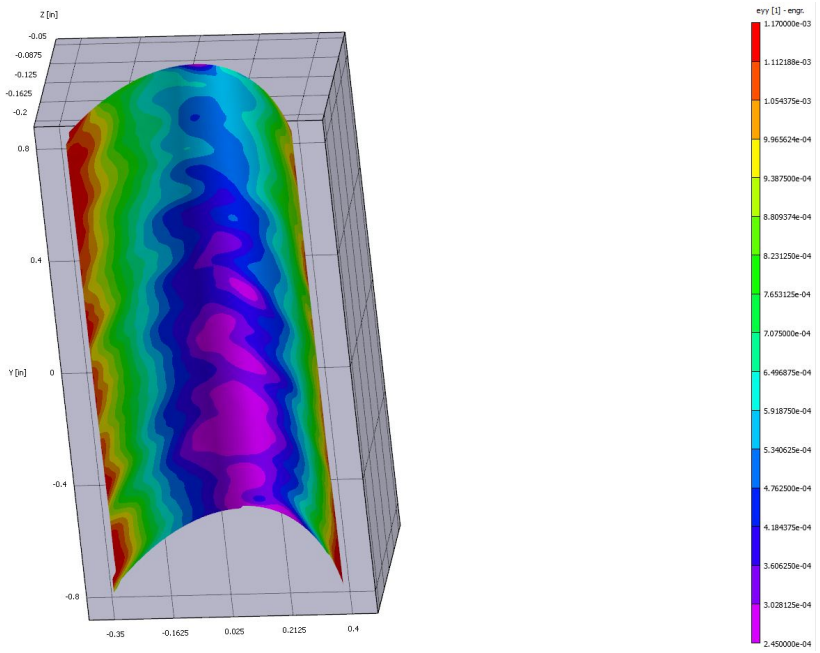

SP-4 Run-1 (-0.268 in offset)

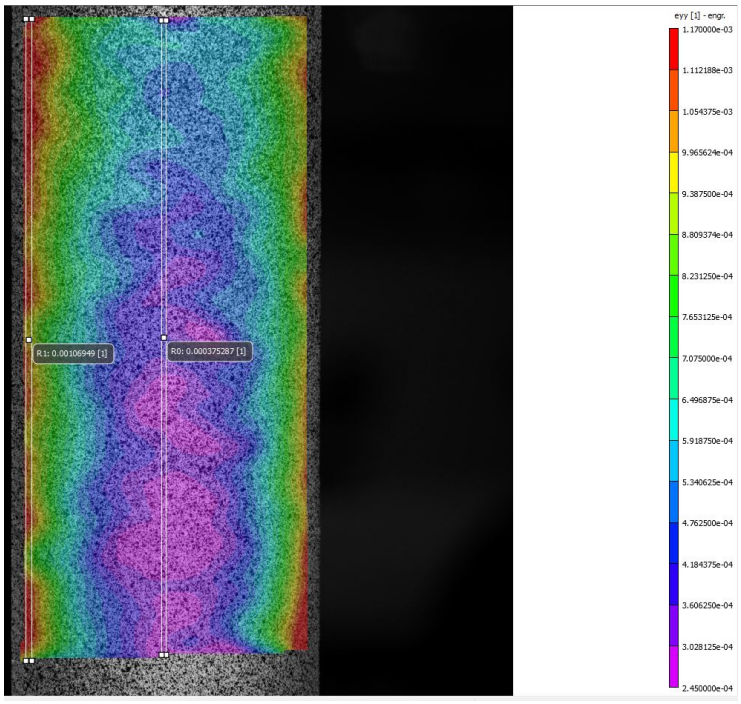

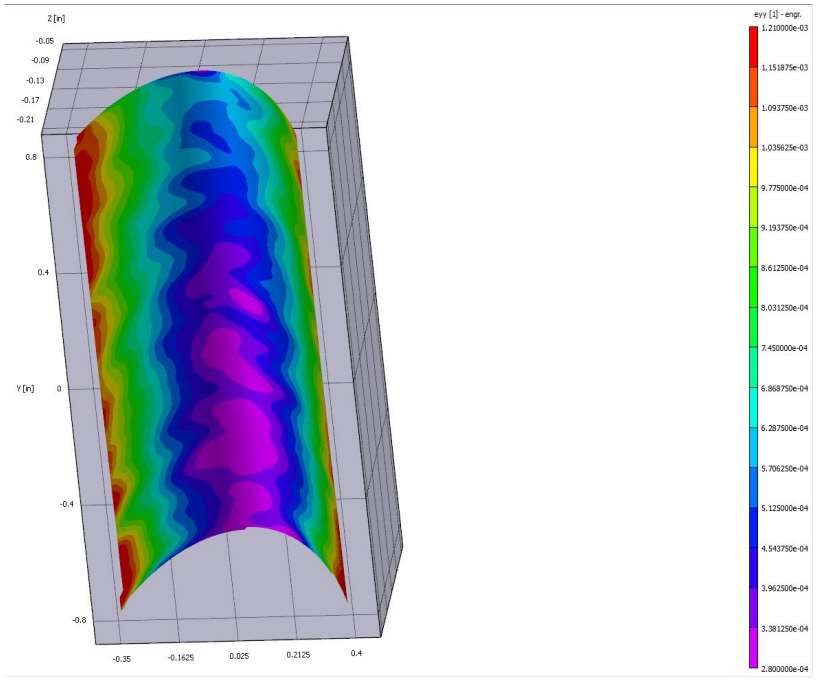

SP-4 Run-1 (-0.268 in offset)

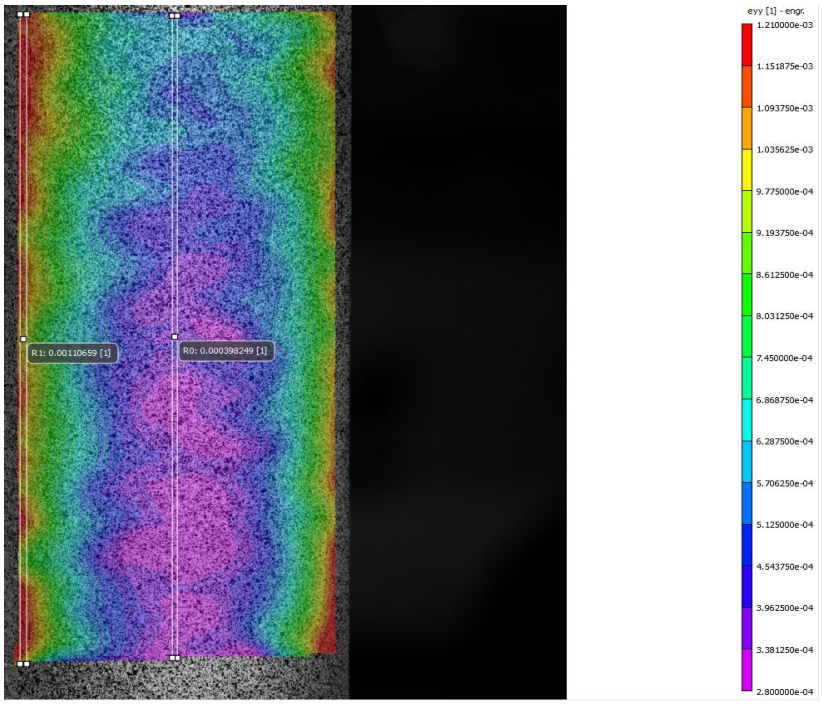

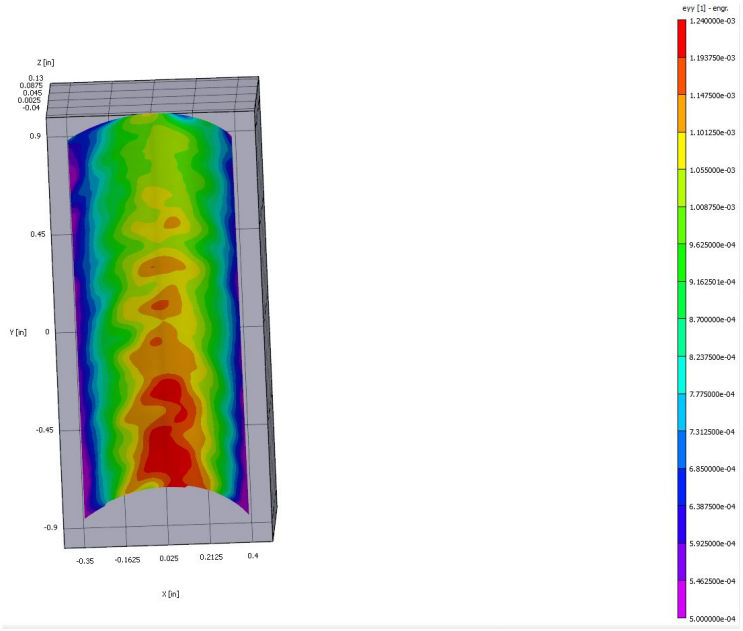

SP-5 Run-1 (+ 0.5 in offset)

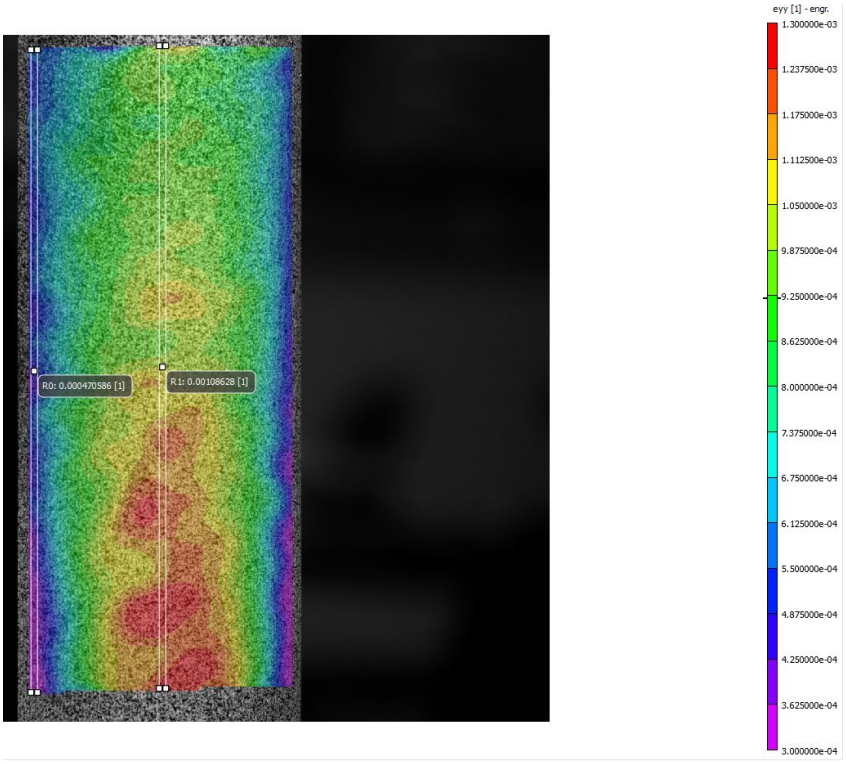

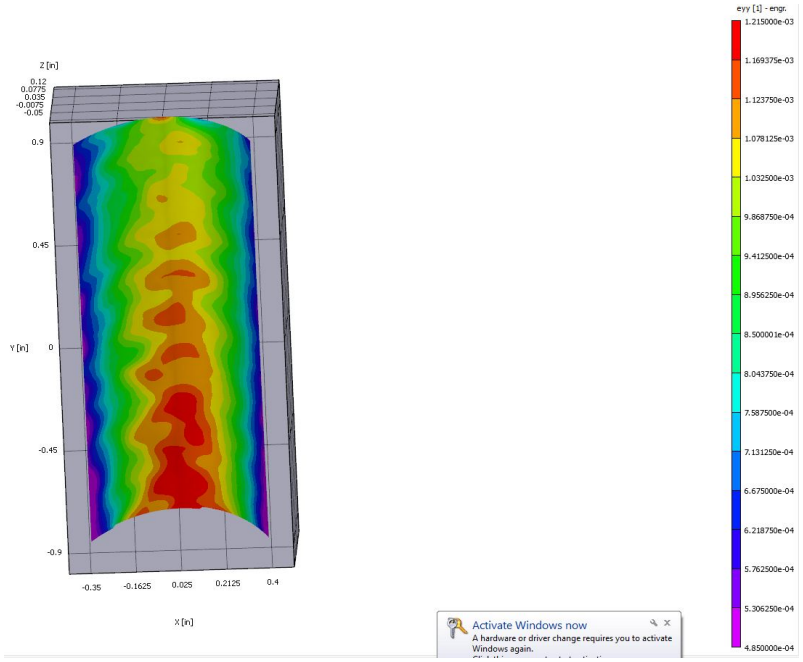

SP-5 Run-5 (+ 0.5 in offset)

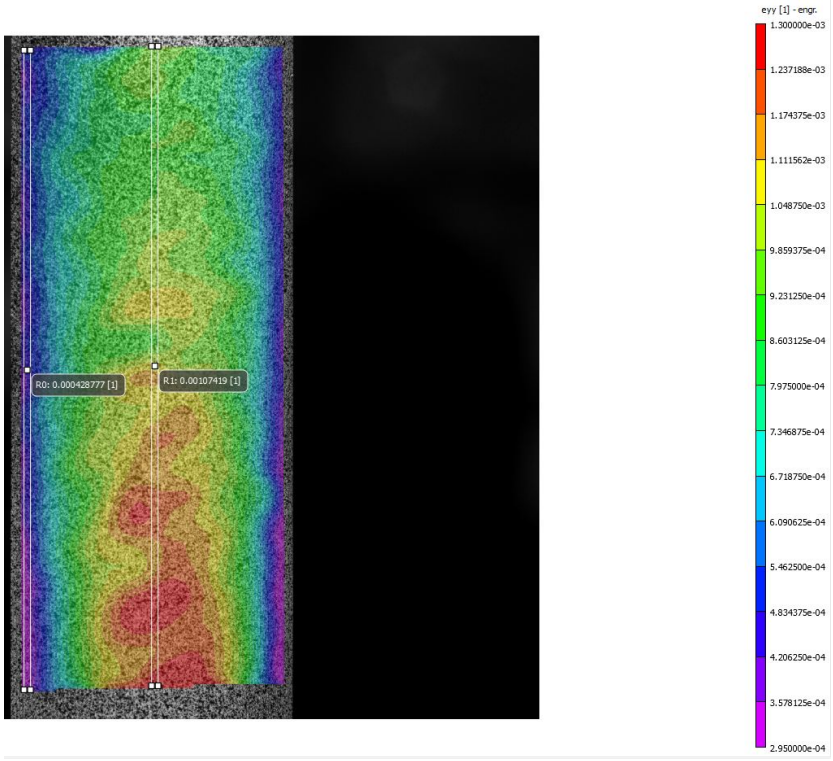

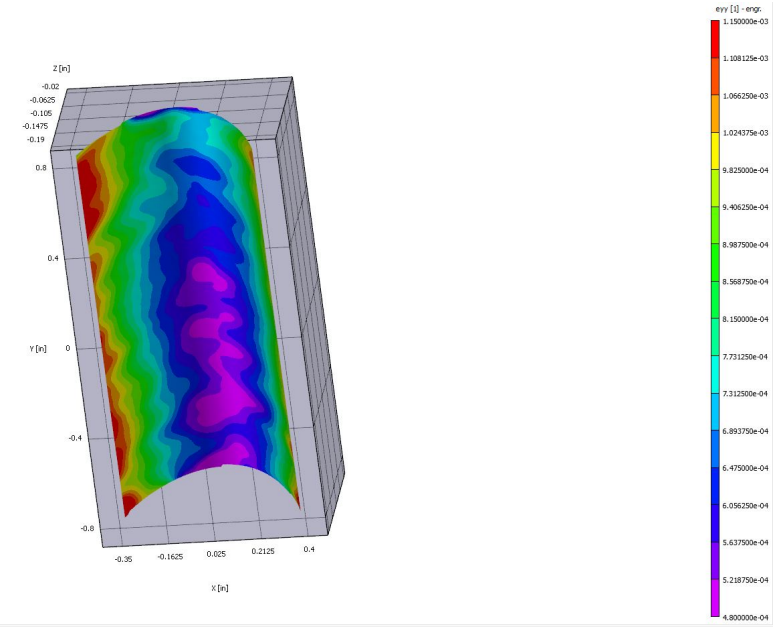

SP-5 Run-1 (- 0.268 in offset)

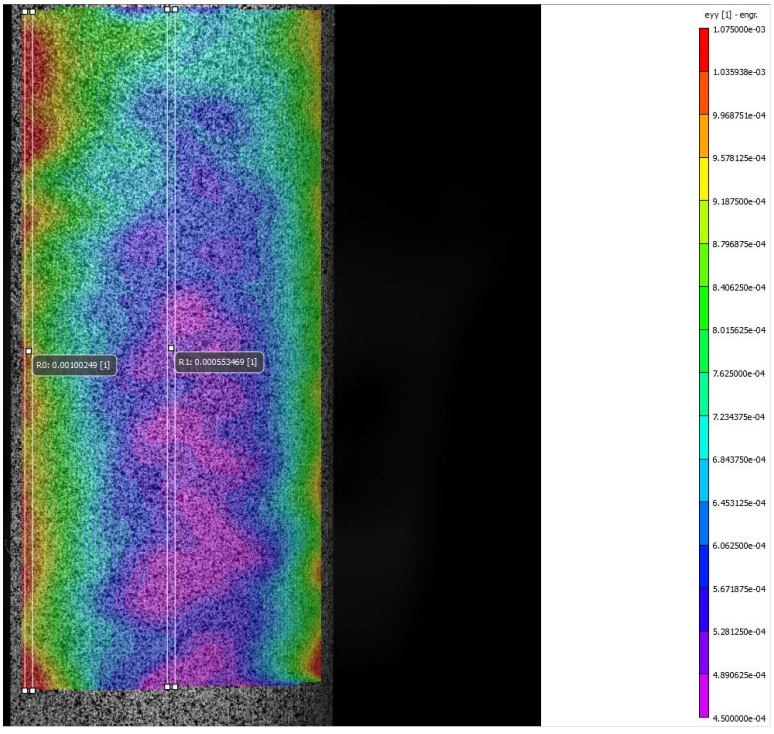

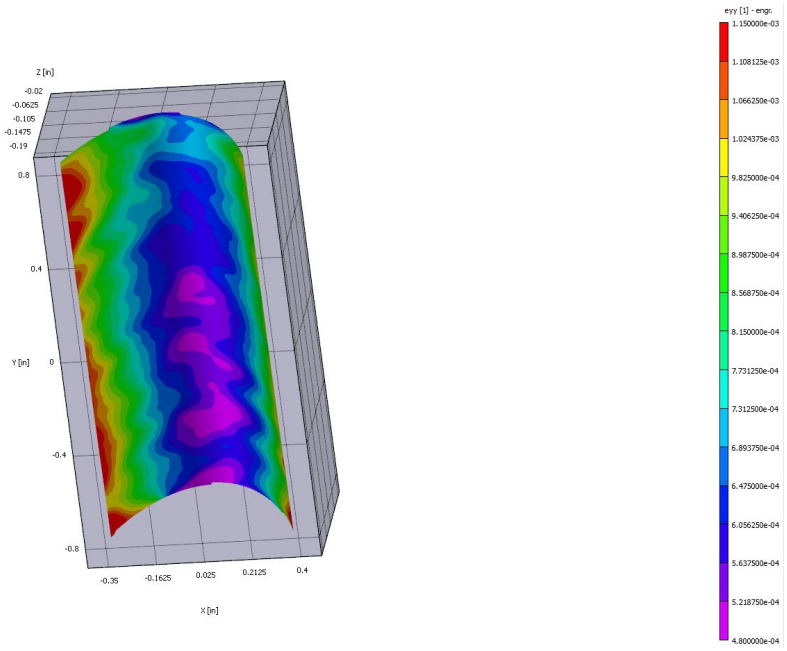

SP-5 Run-5 (- 0.268 in offset)

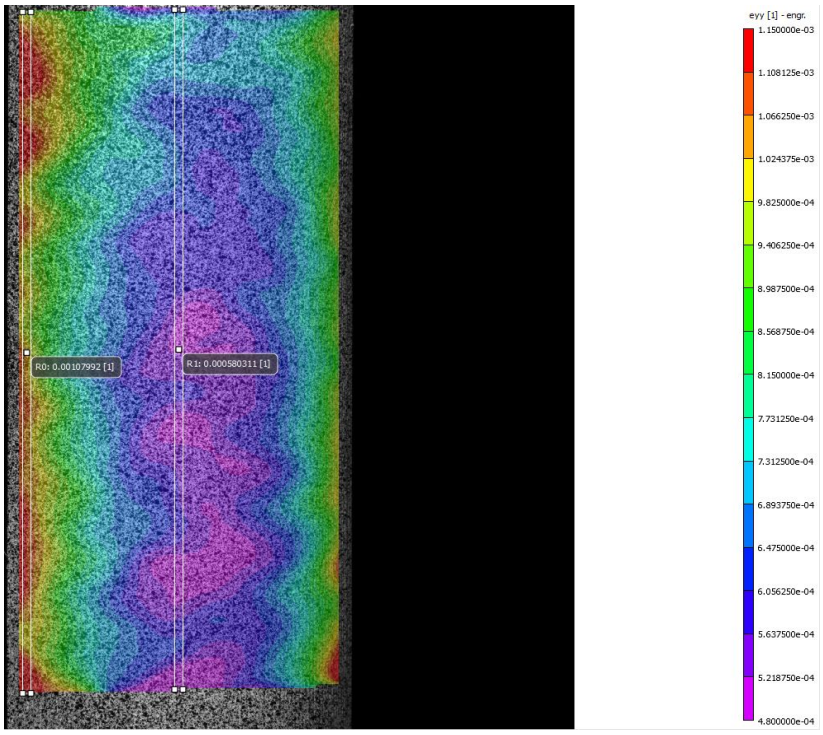

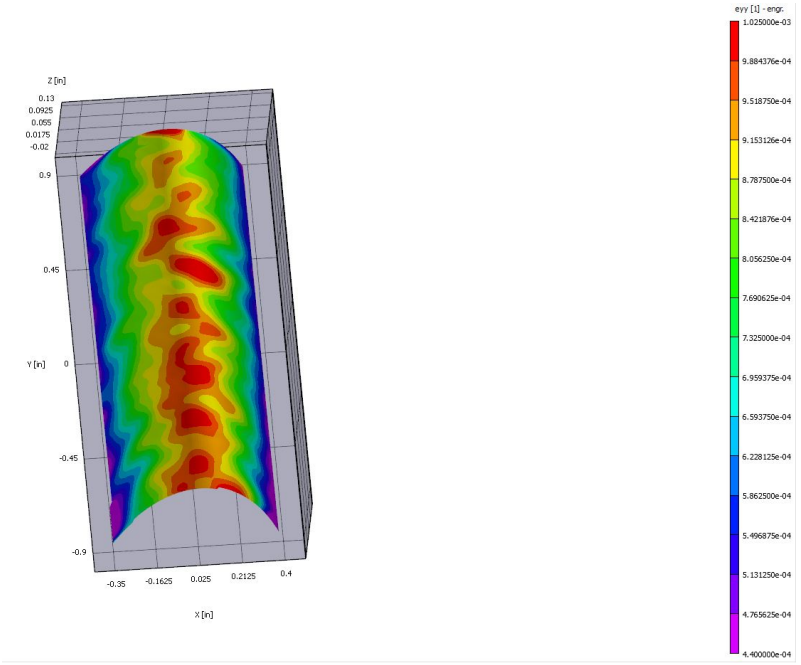

SP-6 Run-1 (+ 0.5 in offset)

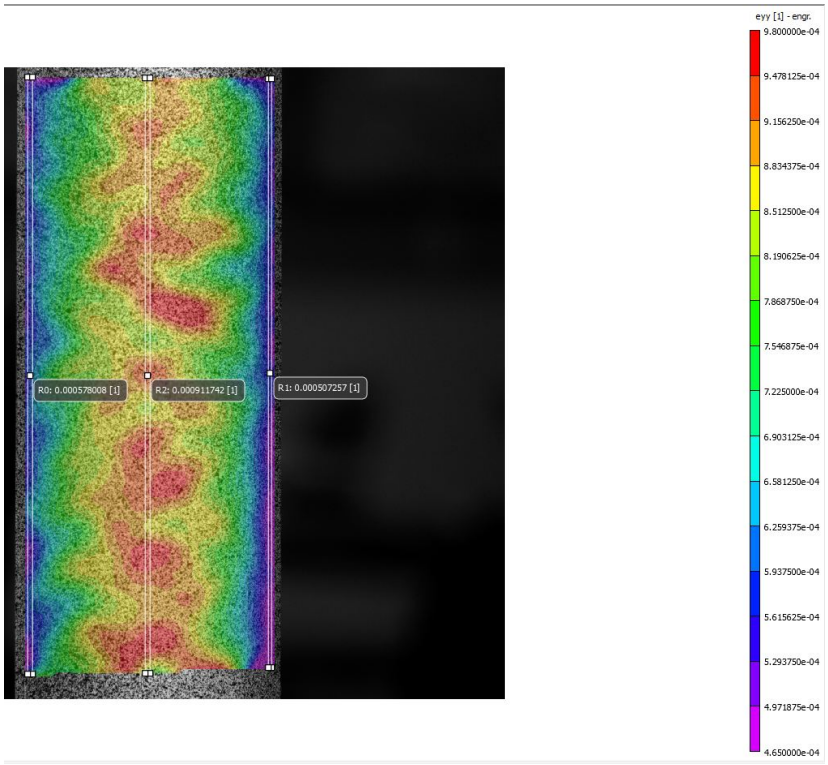

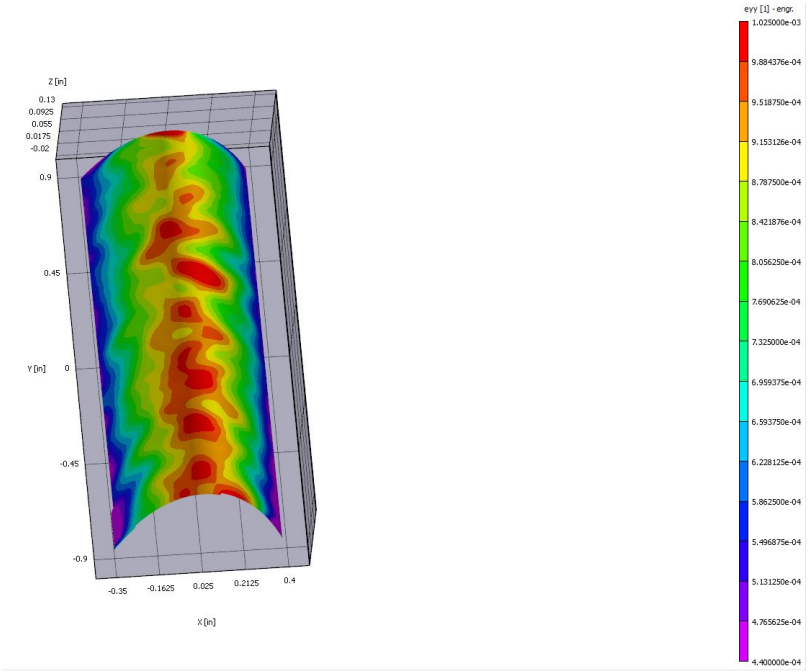

SP-6 Run-5 (+ 0.5 in offset)

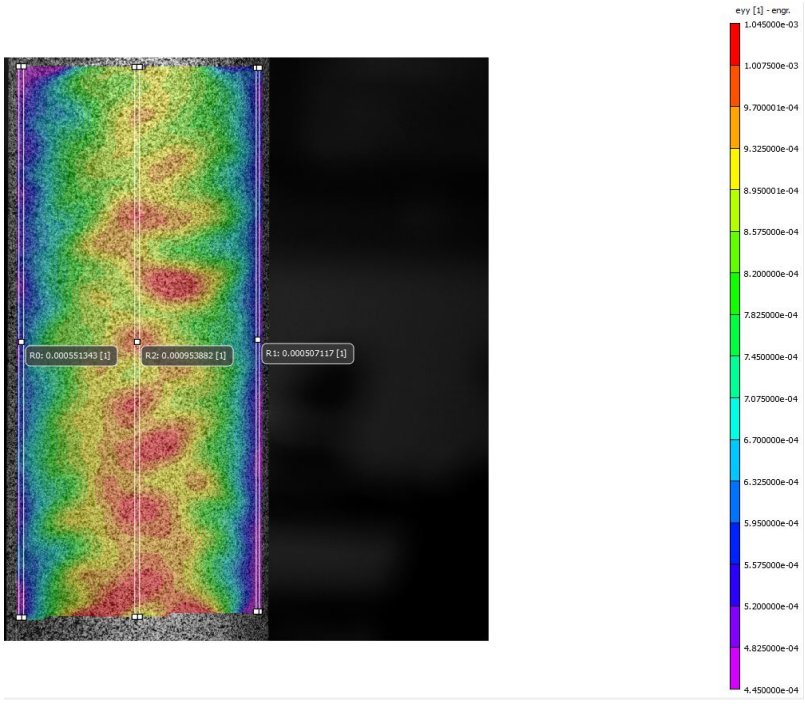

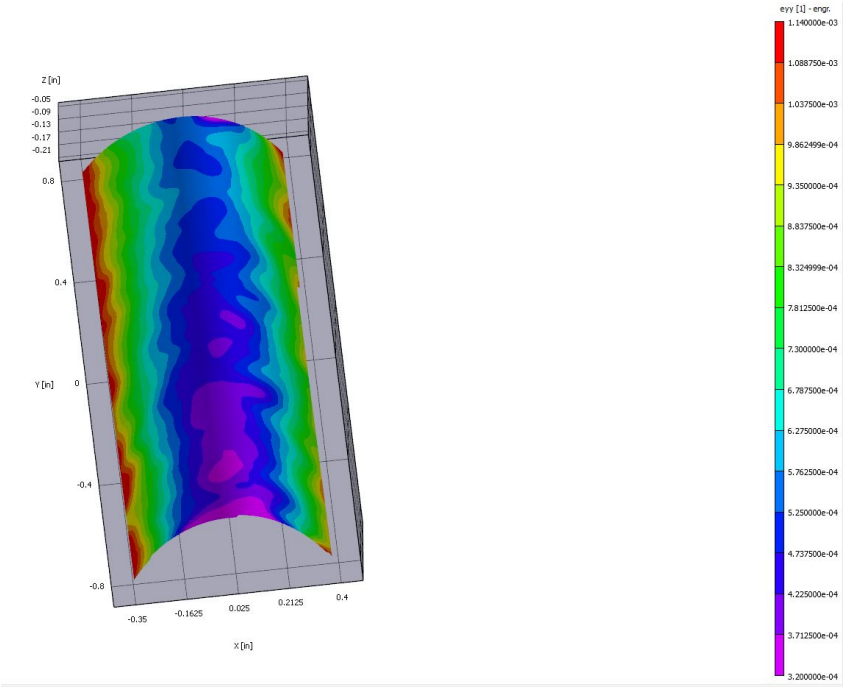

SP-6 Run-1 (- 0.268 in offset)

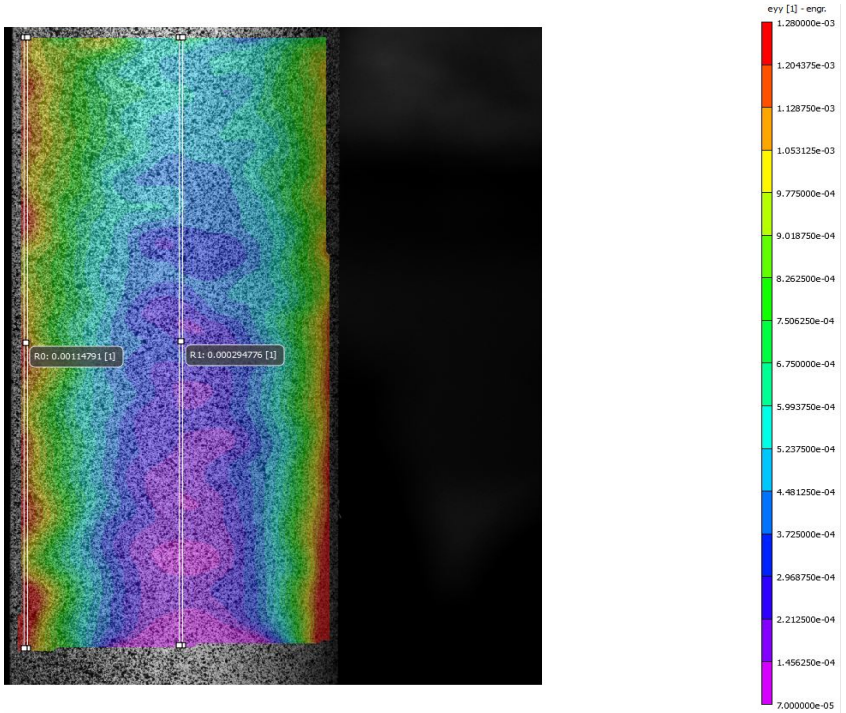

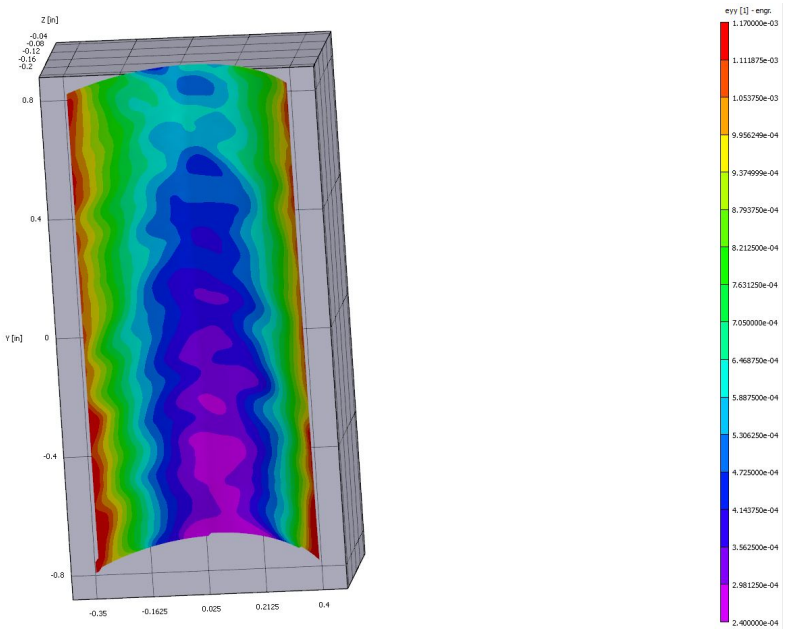

SP-6 Run-5 (- 0.268 in offset)

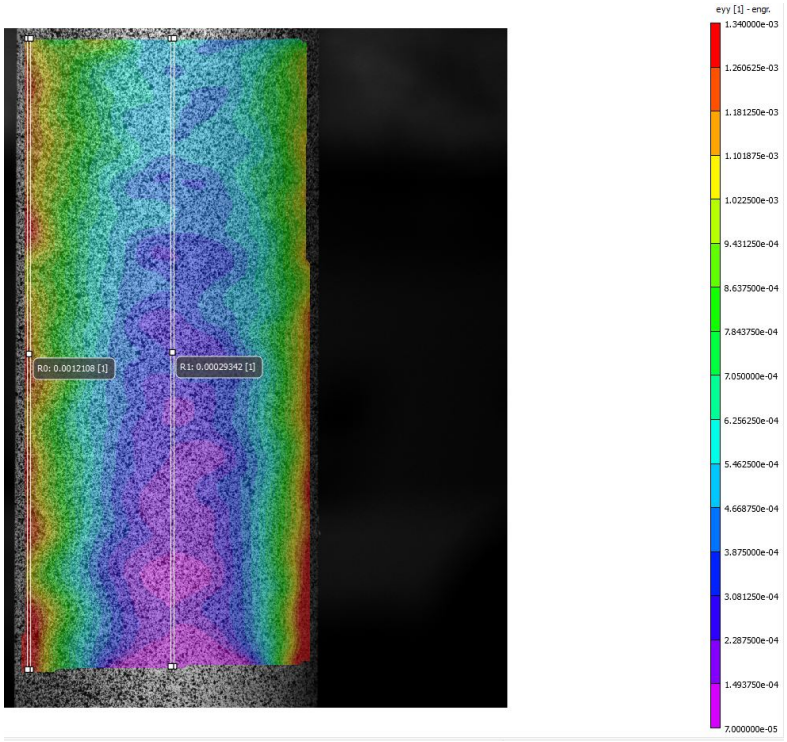

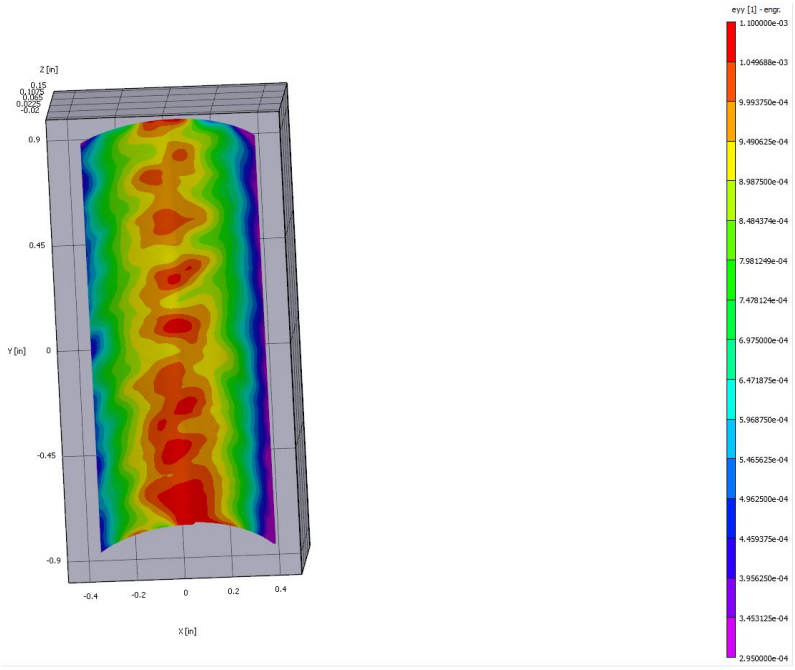

SP-7 Run-1 (+0.5 in offset)

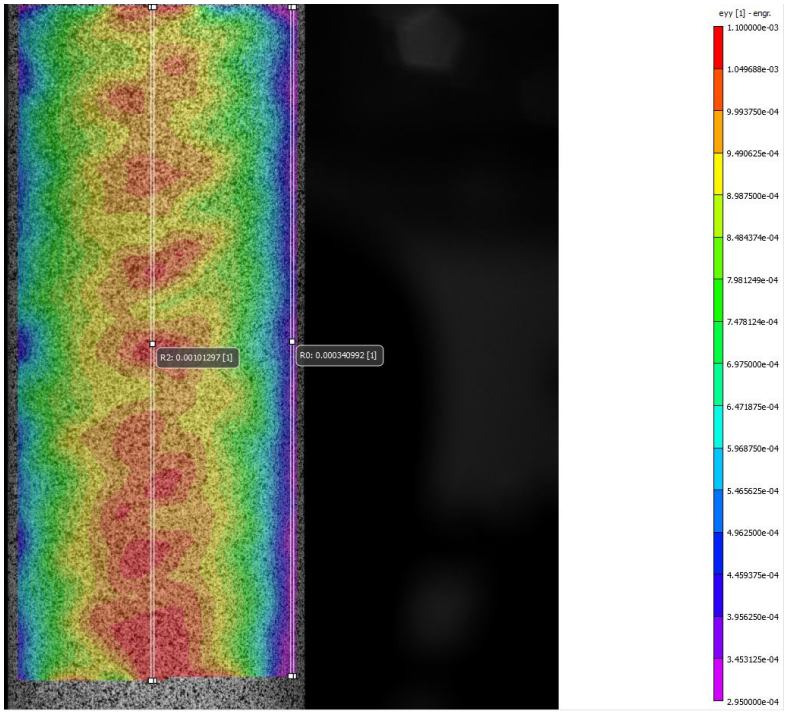

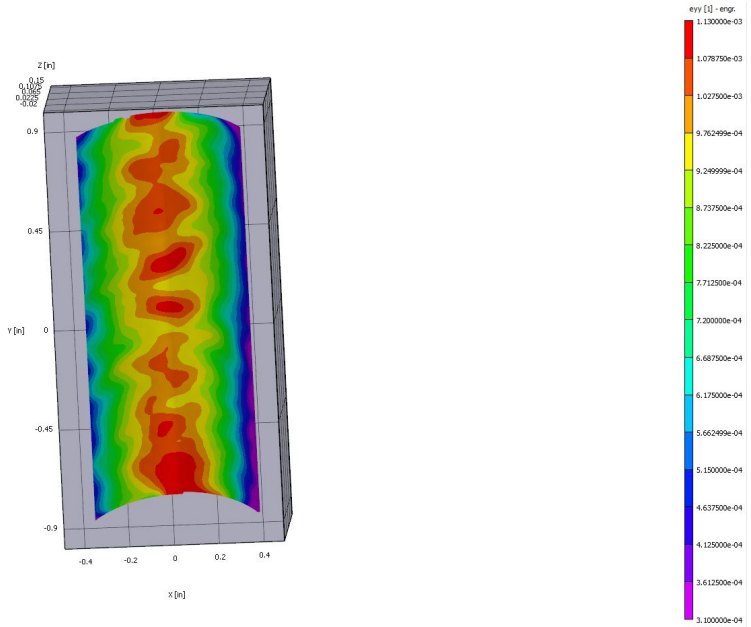

SP-7 Run-5 (+0.5 in offset)

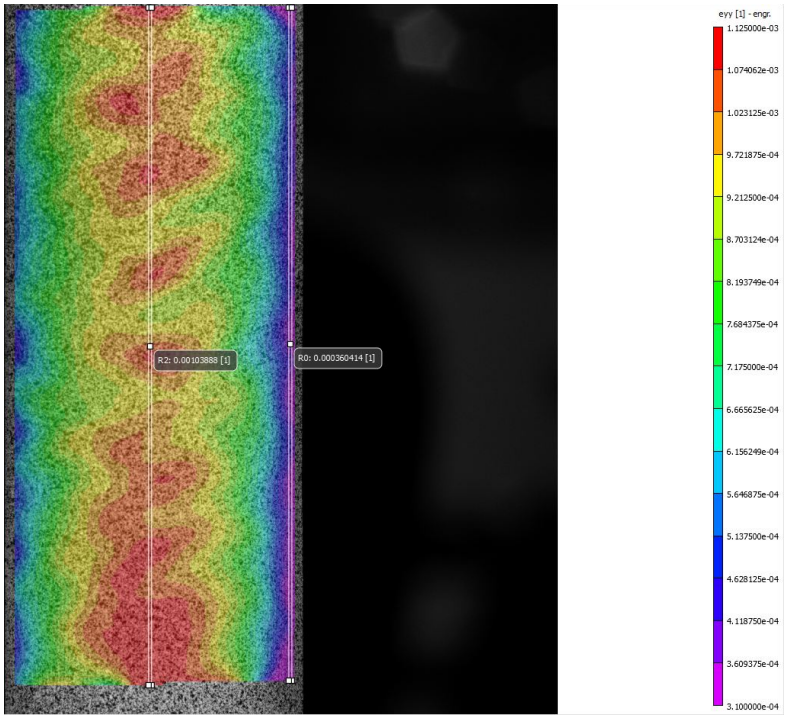

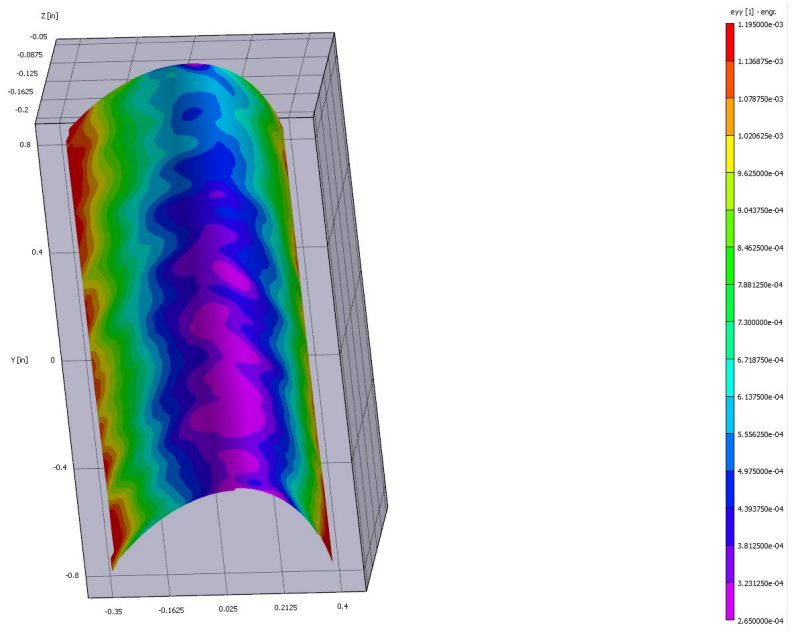

SP-7 Run-1 (-0.268 in offset)

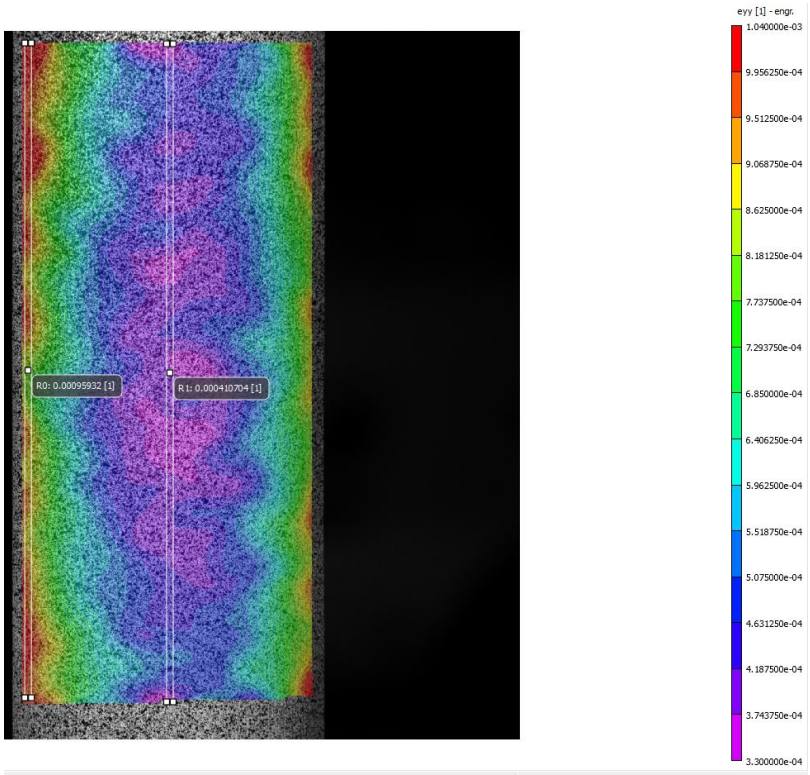

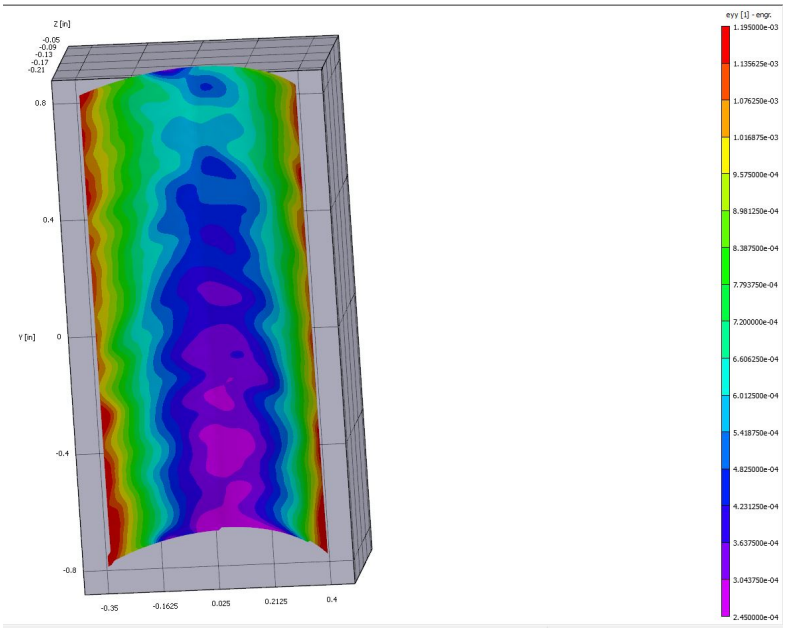

SP-7 Run-5 (-0.268 in offset)

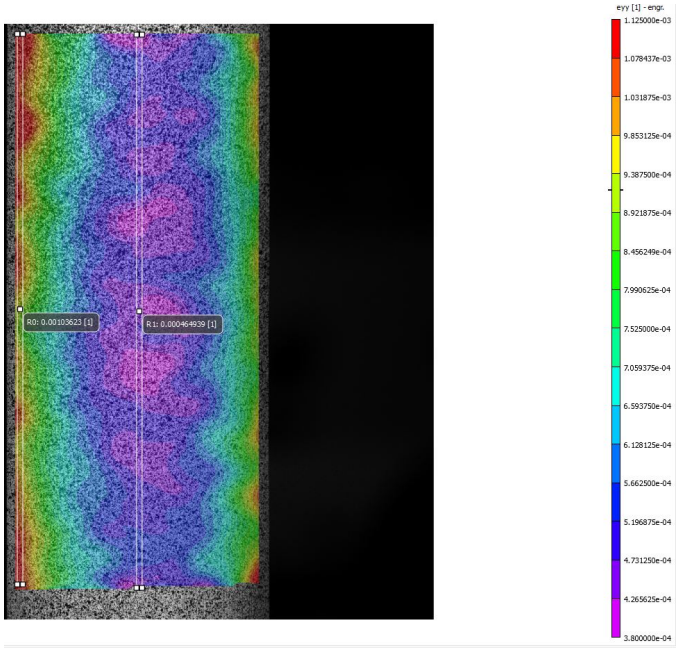

Strain Data Measured across Crown and Edge (SP-2)

Test run no:	X-crown (in)	ε_{edge} (0.5 in offset)	ε_{crown} (0.5 in offset)	ε_{edge} (-0.268 in offset)	ε_{crown} (-0.268 in offset)
Run-1	0.2	504	956	963	445
Run-2	0.2	491	1028	1062	447
Run-3	0.2	482	1021	1065	436
Run-4	0.2	433	979	1074	475
Run-5	0.2	453	994	1071	439

Strain Data Measured across Crown and Edge (SP-3)

Test run no:	X-crown (in)	ε_{edge} (0.5 in offset)	ε_{crown} (0.5 in offset)	ε_{edge} (-0.268 in offset)	ε_{crown} (-0.268 in offset)
Run-1	0.2	493	1264	1082	409
Run-2	0.2	445	1242	1093	401
Run-3	0.2	472	1266	1102	400
Run-4	0.2	486	1277	1141	391
Run-5	0.2	481	1294	1129	388

Strain Data Measured across Crown and Edge (SP-4)

Test run no:	X-crown (in)	ε_{edge} (0.5 in offset)	ε_{crown} (0.5 in offset)	ε_{edge} (-0.268 in offset)	ε_{crown} (-0.268 in offset)
Run-1	0.2	570	981	1069	376
Run-2	0.2	555	1007	1083	384
Run-3	0.2	568	1017	1081	387
Run-4	0.2	554	1002	1085	383
Run-5	0.2	544	1030	1106	398

Strain Data Measured across Crown and Edge (SP-5)

Test run no:	X-crown (in)	ε_{edge} (0.5 in offset)	ε_{crown} (0.5 in offset)	ε_{edge} (-0.268 in offset)	ε_{crown} (-0.268 in offset)
Run-1	0.2	471	1086	1002	554
Run-2	0.2	445	1082	1073	577
Run-3	0.2	422	1049	1081	585
Run-4	0.2	447	1087	1099	580
Run-5	0.2	428	1074	1079	586

Strain Data Measured across Crown and Edge (SP-6)

Test run no:	X-crown (in)	ε_{edge} (0.5 in offset)	ε_{crown} (0.5 in offset)	ε_{edge} (-0.268 in offset)	ε_{crown} (-0.268 in offset)
Run-1	0.2	507	911	1147	294
Run-2	0.2	521	961	1183	309
Run-3	0.2	497	954	1198	317
Run-4	0.2	481	931	1204	286
Run-5	0.2	508	953	1218	293

Strain Data Measured across Crown and Edge (SP-7)

Test run no:	X-crown (in)	ε_{edge} (0.5 in offset)	ε_{crown} (0.5 in offset)	ε_{edge} (-0.268 in offset)	ε_{crown} (-0.268 in offset)
Run-1	0.2	341	1012	958	411
Run-2	0.2	366	1035	1039	466
Run-3	0.2	347	1020	1042	467
Run-4	0.2	371	1046	1023	456
Run-5	0.2	361	1038	1036	464

REFERENCES

[1] Vardhan, T.K; Bhaskar, K; “Bending of laminated Orthotropic Cylindrical Shells- an Elasticity Approach”; Journal of Composite Structures; Vol: 17; pp: 141-156; May 1991.

[2] Jiarang Fan & Kewei Ding; “Analytical Solutions for Closed Laminated Cylindrical Shells”, Int. Jour. Of. Mech. Sci; Vol: 35; No; 8; 00: 657-688; June 1993.

[3] Yuan, F.G; “Exact Solutions of Laminated Composite Cylindrical Shells in Cylindrical Bending”; Journal of Reinforced Plastics and Composites; Vol: 11; pp: 340-352; May 1992.

[4] Ren, J.G; “Analysis of Laminated Circular Cylindrical Shells under Axisymmetric Loading”; Journal of Composite Structures; Vol: 30; pp: 271-281; May 1995.

[5] Cho; Ki-Ook; Min-Ho Kim; “ Efficient Higher-order Shell Theory for Laminated Composites”; Journal of Composite Structures; Vol: 34; pp: 197-212; March 1996.

[6] Wu Zhen and Chen Wanji; “A Global-Local Higher Order Theory for Multilayered Shells and the Analysis of Laminated Cylindrical Shell Panels”; Journal of Comp Struct; Vol: 84; no. 4; pp: 350—361; 2008.

[7] Bhaskar and Ganapathsaran; “Elasticity solutions for Laminated Orthotropic Cylindrical Shells Subjected to Localized Longitudinal and Circumferential Moments”; Journal of Pressure Vessels Tech; Vol: 125; no. 35; pp: 26-35, Feb 2003.

[8] Qatu M, Asadi E, Wang W. “Review of recent literature on static analyses of composite shells”: 2000–2010. J Compos Materials; Vol: 2; pp: 61–86; June 2012.

[9] Soldatos KP, Shu X; “On the stress analysis of cross-ply laminated plates and shallow shell panels”. Compos Struct, Vol:46; pp: 333–344, May 1999.

[10] Hodges and Yu; “Best Strip-Beam Properties Derivable from Classical Lamination Theory,” AIAA Journal, Vol. 46, no: 7, July 2008.

[11] Chan, W., and Demirhan, C., “A Simple Closed-Form Solution of Bending Stiffness for Laminated Composite Tubes,” Journal of Reinforced Plastics and Composites, Vol. 4, March 1, 2000.

[12] ANSYS 15.0, Technical User’s Manual.

[13] Daniel M., Ishai Ori., “ Engineering Mechanics of Composite Materials,” Oxford University Press, New York, 2006.

[14] www.Hexcel.com

[15] ABAQUS v 6.12 Technical User’s Manual.

[16] HexPly 8552 Product Data Sheet; Hexel.com.

[17] Sutton, A., “Image Correlation for Shape Motion, and Deformation Measurements,” Springer Science and Buisness Media, 2009.

[18] www.correlatedsolutions.com

[19] www.Instron.com

[20] www. McMaster.ca

[21] www.MTS.com

BIOGRAPHICAL INFORMATION

Sthanu Mahadev received his B.S degree with Honors in Aeronautical Engineering from Anna University (India) in 2008. He went ahead to gain admission for his Master's degree at The University of Texas at Arlington (U.S.A) and accomplished his M.S in Aerospace Engineering in 2011. He has been an active student member of the AIAA UTA student chapter and the honorary Phi Kappa Phi engineering Honor Society.